LEAD FREE CERAMIC POLYMER COMPOSITES FOR EMBEDDED CAPACITOR AND PIEZOELECTRIC APPLICATIONS

by

PUNYATOYA MISHRA

DEPARTMENT OF PHYSICS & ASTRONOMY
NATIONAL INSTITUTE OF TECHNOLOGY, ROURKELA
ODISHA, INDIA – 769008

July 2014

LEAD FREE CERAMIC POLYMER COMPOSITES FOR EMBEDDED CAPACITOR AND PIEZOELECTRIC APPLICATIONS

A thesis submitted by

Punyatoya Mishra

in partial fulfillment
of the requirements for the degree of

Doctor of Philosophy in **Physics**

Under the guidance of

Prof. Pawan Kumar

DEPARTMENT OF PHYSICS & ASTRONOMY
NATIONAL INSTITUTE OF TECHNOLOGY, ROURKELA
ODISHA, INDIA – 769008

July 2014

DEDICATED
TO
MY BABA AND
MY BELOVED Lt. BOU

Department of Physics & Astronomy
National Institute of Technology Rourkela
India – 769008

CERTIFICATE

This is to certify that this thesis entitled **“Lead free ceramic polymer composites for embedded capacitor and piezoelectric applications”** submitted by **Punyatoya Mishra** in partial fulfillments for the requirements for the award of degree of **Doctor of Philosophy** in **Physics** at **National Institute of Technology, Rourkela** is an authentic work carried out by her under my supervision and guidance.

To the best of my knowledge, the matter embodied in the project has not been submitted to any other University/ Institute for the award of any Degree or Diploma.

Prof. Pawan Kumar
Thesis Supervisor
Department of Physics &
Astronomy
National Institute of Technology
Rourkela - 769008

ACKNOWLEDGEMENTS

First of all, I would like to express my deep gratitude to my supervisor, Dr. Pawan Kumar. Without his help and guidance this thesis would not be possible. He provided me encouragement, motivation, sound advice, good teaching and lots of good ideas. His guidance, support, sincerity, devotion to work, simplicity and faith on the Almighty have set examples for me and are become the part of both of my academic and personal life.

I would also like to thank to my DSC members, Dr. S. Jena, Department of Physics and Astronomy, Dr. S. Bhattacharyya, Department of Ceramic Engineering and Dr. B. C. Roy, Department of Metallurgy and Material Science and Engineering for their profound knowledge, valuable suggestions and comments to make this thesis fruitful.

I express my sincere thanks to Prof. D. K. Bisoyi, Head of the Department of Physics and Astronomy, NIT, Rourkela for his guidance and suggestions. I had a pleasure to thank all the professors of Department of Physics and Astronomy, NITR for all their knowledge, skills and good communications.

It is a great honour for me to express my deep gratitude to Prof. S. C. Mishra, Department of Metallurgy and Material Science and Engineering for his valuable suggestions, advice, inspiration and blessings. I am also grateful to Dr. S. Acharya, Mechanical Engineering Department for supporting me in the composite preparation in his lab.

I am thankful to Sonia Mam for her support, suggestions, motivation, caring and help.

I would also heartful to all non-teaching staffs of the Department of Physics and Astronomy for their nice, memorable association and constant help.

I am also thankful to all the teaching and non-teaching staffs of Ceramic Engineering Department and Department of Metallurgy and Material Science and Engineering for giving me opportunity and helping me to carryout XRD, SEM and piezoelectric measurements of my samples.

I would also thankful to Mr. Uday kumar Sahoo, technical staff, XRD, Department of Metallurgy and Material Science and Engineering for his help, suggestions and support. I am heartful to Mr. Rajesh Pattnaik, technical staff, SEM, Department of Metallurgy and Material Science and Engineering for his suggestions and support.

I also wish to express my sincere thanks to my group members, Prakash, Naresh, Subrat, Mausumi, Sridevi and Chandrasekhar for their help, support, encouragements and valuable suggestions and also for giving me nice, memorable atmosphere for my work. My special thanks to Dr Tanmay Badapanda, Senthil and Satya for their valuable suggestions while writing my thesis. I would also like to thank all my friends in the department for giving me wonderful company and confidence to complete my work.

I am happy to give my gratitude to all my neighbors of SSB Hall of Residence for giving me a pleasant and memorable atmosphere while staying there.

My special thanks goes to my parents, Debendra nath Mishra and Lt. Rajalaxmi Mishra for their unconditional love, inevitable sacrifice, consistent support, right guidance, constant encouragement and the heavenly blessings from the journey of my life till now. Without their blessings and support I cannot imagine completing my Ph D. I am always grateful to them for helping me in taking care of my little daughter during all my Ph. D. work.

I received much needed love and continuous support and encouragement from my sister Punyapriya Mishra. I am very much thankful to her for being with me in the part of both of my life and my research field.

Then to *my little Angel*, ñAditiò, the most precious and blessed gift from Lord Jagannath, who also sacrified most of her beautiful childhood moments for my work. I beg extremely sorry for all those moments not being with you.

Lastly, my humble offer to Lord Jagannath, who is my source of inspiration. I am thankful to GOD for giving me all these good people, great parents and a lovely daughter.

Punyatoya Mishra

ABSTRACT

In recent years, composite materials are on the frontier row of research field due to their greater technological importance. Modern composite materials constitute a significant proportion of engineered materials market ranging from everyday product to sophisticated niche applications. These wonder materials are extensively used in space vehicle to home building, electronic packaging to medical equipments, etc.

The essence of a composite material is to combine the properties of two or more chemically and physically different phases resulting in a new material with different properties. In particular, composites based on ferroelectric ceramic as fillers in the polymer matrix have received great attention. The properties of these ceramic-polymer composites can be tailored by using different ferroelectric ceramics as fillers and different polymers as matrix for achieving the better electrical properties compared to the individual phases.

The most successful ferroelectric ceramics are based on lead zirconates and lead titanates, therefore environmental concerns have been raised to find alternative ways to substitute with ñlead-freeò ferroelectrics, particularly those with properties comparable with their lead-based counterparts. Furthermore, the necessity for using transducers with lead-free materials in therapeutic and monitoring ultrasound devices, which requires the embedded system in the human body, is another driving force for lead-free ferroelectric investigations. Among the lead free ferroelectric materials, $Ba(Zr_{0.2}Ti_{0.8})O_3$-$(Ba_{0.7}Ca_{0.3})TiO_3$/(BZT-BCT) is a lead free ferroelectric system having perovskite structure exhibiting better piezoelectric, ferroelectric and electromechanical properties compared with lead based ferroelectric materials near a morphotropic phase boundary (MPB) 50BZT-50BCT composition at room temperature (RT).

Recently miniaturization of electronic devices requires high dielectric constant materials with good temperature and frequency stability. Calcium copper titanate, $CaCu_3Ti_4O_{12}$ (CCTO) has attracted much interest due to its extraordinary high dielectric constant. CCTO is a oxide based cubic perovskite like ceramics (AAô$_3$B$_4$O$_{12}$), exhibiting gigantic dielectric permittivity of ~10^{4-5}, which is frequency independent up to 10^6 Hz and is almost constant in the temperature range 100-400K . Therefore, CCTO is a promising high dielectric constant non-ferroelectric material

which can be added within the composites for enhancing the dielectric properties without decreasing the resistivity substantially.

There have been very limited studies reported on the lead free ferroelectric ceramic-polymer composites. PMMA, polyaniline (PANI), polyurethane (PU), etc. are used as polymer matrices in the ceramic-polymer composites. Recently, the focus of research is on PVDF and epoxy based polymers. This is due to the high mechanical strength of epoxy and high dielectric constant of PVDF polymers. In our knowledge, 0-3 composites of PVDF and epoxy and (BZT-BCT) ferroelectric ceramics are not reported in the literature. Therefore, in this thesis work, various structural, dielectric and piezoelectric studies of (BZT-BCT) and PVDF & (BZT-BCT) and epoxy ceramic polymer composites are reported. With the addition of polymer to ceramics and hence forming the ceramic polymer composite, the dielectric constant of ceramics decreases drastically. In order to increase the dielectric constant and temperature stability of these (BZT-BCT) and PVDF and (BZT-BCT) and epoxy ceramic polymer composites, CCTO ceramics, having high dielectric constants and good temperature stability are further added.

Structural, Optical & Electrical Properties of (BZT-BCT) & CCTO Ceramics

The thermal analysis on (BZT-BCT) and CCTO systems hinted the phase formation of these systems to be ~ 1000 and 900^oC, respectively. XRD studies confirmed the formation of single perovskite phase in the (BZT-BCT) and CCTO systems at 1300 and 1050^oC for 4 h, respectively. The relative densities of the 0.48BZT-0.52BCT, 0.52BZT-0.48BCT and 0.50BZT-0.50BCT ceramics were found to be ~ 95, 96 and 97 %, respectively. Whereas, the relative densities of the CCTO ceramics sintered at 1050 and 1100^oC were found to be ~ 91 and 94 %, respectively. The value of band gap energy E_g ~ 3.12 eV is found for the 0.50BZT-0.50BCT ceramic sample, sintered at 1400^oC. The RT value and the temperature stability of the dielectric constant (Ụ̊$_r$) of the CCTO system were found to be better compared to the (BZT-BCT) MPB compositions. From dielectric measurements of the (BZT-BCT) MPB compositions, sintered at different temperatures, the T_c was found to vary between 96 to 115^oC. Maximum value of Ụ̊$_r$ at RT was obtained in (0.50BZT-0.50BCT) ceramics samples. The RT values of ε_r and tanδ at 1 kHz frequency of the CCTO ceramic samples sintered at 1100^oC were found to be ~ 11,537 and 0.21, respectively. Maximum value of piezoelectric coefficient (d_{33}) ~ 281 pC/N was found in the 0.50BZT-0.50BCT system. The 0.50BZT-0.50BCT system sintered at 1400^{o}C showed better microstructural, dielectric, ferroelectric and piezoelectric properties, whereas CCTO ceramics sintered at 1400^{o}C showed better dielectric properties.

Structural, Optical & Electrical Properties of the (BZT-BCT)-PVDF and (BZT-BCT)-(PVDF-CCTO) 0-3 Ceramic Polymer Composites

Φ(BZT-BCT)-(1-Φ)PVDF with (Φ = 0.05, 0.10, 0.15, 0.20 and 0.25) & 0.25(BZT-BCT)-0.75[(1-x)PVDF-xCCTO] with (x = 0.02, 0.04, 0.06, 0.08 and 0.10) 0-3 ceramic polymer composite thick films were synthesized by hot uniaxial press. From XRD study, the crystalline nature of the PVDF, (BZT-BCT) and CCTO were identified. SEM images confirmed the 0-3 connectivity of the ceramic and polymer phases in the ceramic-polymer composites. The optical band gap value increases with the increase in the (BZT-BCT) ceramic filler concentration in the (BZT-BCT)-PVDF, whereas the E_g value decreases with the increase in the (CCTO) ceramic concentration in the (BZT-BCT)-(PVDF-CCTO) composites. The values of $\mathring{U}_r$ at RT and d_{33} of both the (BZT-BCT)-PVDF and (BZT-BCT)-(PVDF-CCTO) composites are found to increase with the increase in the volume fractions of the ceramic contents.

Structural, Optical & Electrical Properties of the (BZT-BCT)-Epoxy and (BZT-BCT)-(Epoxy-CCTO) 0-3 Ceramic Polymer Composites

Φ(BZT-BCT)-(1-Φ)epoxy with (Φ = 0.05, 0.10, 0.15, 0.20 and 0.25) & 0.20(BZT-BCT)-0.80[(1-x)epoxy-xCCTO] with (x = 0.02, 0.04, o.06, 0.08 and 0.10) 0-3 ceramic polymer composite samples were fabricated by hand lay-up techniques followed by cold pressing. XRD study confirmed the presence of ceramic and polymer phases of the composite constituents. SEM images confirmed 0-3 connectivity of the ceramic and polymer phases in the ceramic-polymer composites. The optical band gap value increases with the increase in the (BZT-BCT) ceramic filler concentration in (BZT-BCT)-epoxy composites and also with the increase in the (CCTO) ceramic concentration in the (BZT-BCT)-(epoxy-CCTO) composites samples. The Φ(BZT-BCT)-(1-Φ)epoxy composite with Φ = 0.20 and 0.20(BZT-BCT)-0.80[(1-x)epoxy-xCCTO] composite with x = 0.08 exhibited highest values of ε_r and d_{33} piezoelectric coefficient, respectively.

Thesis Outline

The present thesis has been divided into 7 chapters. The brief description of each chapter is as follows:

Chapter 1 presents a short review about the phenomenon of general ferroelectricity, piezoelectricity, the need and significance of ceramic polymer composite materials and the applications, the motivation and the aim of the present work.

Chapter 2 describes about the investigated parameters.

Chapter 3 presents the detail description of the synthesis of ceramics and the ceramic polymer composites. The experimental techniques used to characterize the synthesized systems are also mentioned in this chapter.

Chapter 4 describes in details about the structural, optical and electrical properties of the (BZT-BCT), CCTO ceramics and PVDF, epoxy polymers.

Chapter 5 describes about the structural, optical and electrical properties of the (BZT-BCT)-PVDF and (BZT-BCT)-epoxy ceramic polymer composites.

Chapter 6 describes about the structural, optical and electrical properties of the (BZT-BCT)-(PVDF-CCTO) and (BZT-BCT)-(epoxy-CCTO) ceramic polymer composites.

Chapter 7 presents the major conclusions of the present work with future work recommendations.

Key words: (BZT-BCT); CCTO; PVDF; Epoxy; Composites; XRD; SEM; Dielectric properties; Ferroelectric properties; Piezoelectric properties.

CONTENTS

Chapter-1 Introduction, Literature Survey & Objective of the Work

Chapter-2 Investigated Parameters

Chapter-3 Experimental Details

Chapter-4 Structural & Electrical Properties of (BZT-BCT), CCTO ceramics and PVDF, Epoxy Polymers

Chapter-5 Structural & Electrical Properties of (BZT-BCT)-PVDF and (BZT-BCT)-epoxy Ceramic Polymer Composites

Chapter-6 Structural & Electrical Properties of (BZT-BCT)-(PVDF-CCTO) and (BZT-BCT)-(epoxy-CCTO) Ceramic Polymer Composites

Chapter-7 Conclusions & Future Works

LIST OF FIGURES

LIST OF TABLES

LIST OF SYMBOLS & ABBREVIATIONS

AFM	Atomic Force Microscopy
PMCs	Polymer Matrix Composites
CMCs	Ceramic Matrix Composites
MMCs	Metal Matrix Composites
CGMCs	Carbon and Graphite Matrix Composites
PEEK	Poly Ether Ether Ketone
VAMAS	Versailles Project on Advanced Materials and Standards
BT	Barium Titanate
PT	Lead Titanate
PZT	Lead Zirconate Titanate
PLZT	Lead Lanthanum Zirconate Titanate
PMN	Lead Magnesium Niobate
MPB	Morphotropic Phase Boundary
WEEE	Waste Electrical and Electronics Equipments
RoHS	Restriction of Hazardous Substances
T_c	Curie Temperature
P_s	Spontaneous Polarization
ε	Permittivity
$1/\varepsilon$	Inverse Permittivity
$NaKC_4H_4O_6.4H_2O$	Sodium Potassium Tartarate Tetrahydrate
KH_2PO_4, KDP	Potassium Dihydrogen Phosphate
$(NH_2CH_2COOH)_3H_2SO_4$, TGS	Triglycine Sulfate
$CaTiO_3$	Calcium Titanate
$K_xNa_{1-x}NbO_3$/KNN	Potassium Sodium Niobate
$K(Ta_xNb_{1-x})O_3$	Potassium Tantalate Niobate
$PbNb_2O_6$	Lead Niobate
BLSFs	Bismuth Layer Structure Ferroelectrics
RT	Room Temperature
FRAM	Ferroelectric Random Access Memory
$Na_{0.5}Bi_{0.5}TiO_3$	NBT
$x[Ba(Zr_{0.2}Ti_{0.8})O_3](1-x)[(Ba_{0.7}Ca_{0.3})TiO_3]$	(BZT-BCT)
P_r	Remnant Polarization
E_c	Coercive Field
ε_r	Dielectric Constant
$\tan\delta$	Dielectric Loss
d_{33}	Piezoelectric Co-efficient

XRD	X-ray Diffraction
DPT	Diffuse Phase Transition
$Ba(Fe_{1/2}Nb_{1/2})O_3$	BFN
$CaCu_3Ti_4O_{12}$, CCTO	Calcium Copper Titanate
IBLC	Internal Barrier Layer Capacitance
M-W relaxation	Maxwell Wagner relaxation
GB	Grain Boundary
T_g	Glass Transition Temperature
T_m	Melting Temperature
PVDF	Polyvinylidene Fluoride
PC	Polycarbonates
PVC	Polyvinyl Chloride
VDCN	Vinylidene Cyanide
DGEBA	Diglycidyleyher of Bisphenol A
PWB	Printed Wiring Boards
g_h	Hydrostatic Piezoelectric Co-efficient
g_{33}	Thickness mode response across a pair of electrodes in the poled 3 direction
k_t	Electromechanical Coupling Co-efficient
NRL-USRD	Naval Research Laboratoryôs Underwater Sound Reference Detachment
EMT model	Effective Medium Theory model
SEM	Scanning Electron Microscopy
TGA	Thermogravimetric Analysis
SSR	Solid State Reaction
DSC	Differential Scanning Calorimetry
DTA	Differential Thermal Analysis
DMA	Dynamic Mechanical Analysis
TOA	Thermo Optical Analysis
hkl	Miller Indices
d	Crystal plane spacing
UV-Vis	Ultraviolate-Visible
T	Transmittance
R	Reflectance
SE	Secondary Electron
BSE	Back Scattered Electron
P	Polarization
$\propto$	Polarizability
$\propto^e$	Electronic Polarizability
$\propto^i$	Ionic Polarizability

$\propto^{d}$	Dipolar Polarizability
$\propto^{f}$	Interfacial Polarizability
ε_0	Permittivity of the free space
D	Dielectric displacement
E	Electric field
T	Mechanical stress
S	Mechanical strain
P-E Loop	Polarization vs Electric field Loop
C	Curie constant
γ	Diffusivity of the material
E_d	Depolarizing field
PVA	Poly Vinyl Alcohol
ρ_{th}	Theoretical Density
$\Phi[0.50[Ba(Zr_{0.2}Ti_{0.8})O_3]-0.50[(Ba_{0.7}Ca_{0.3})TiO_3]]-(1-\Phi)PVDF$	(BZT-BCT)-PVDF
$\Phi[0.50[Ba(Zr_{0.2}Ti_{0.8})O_3]-0.50[(Ba_{0.7}Ca_{0.3})TiO_3]]-(1-\Phi)epoxy$	(BZT-BCT)-epoxy
0.25(BZT-BCT)-0.75[(1-x)PVDF-xCCTO]	[(BZT-BCT)-(PVDF-CCTO)]
0.20(BZT-BCT)-0.80[(1-x)epoxy-xCCTO]	[(BZT-BCT)-(epoxy-CCTO)]
RD	Relative Density
S.D.	Standard Deviation
d_{ex}	Experimental Density
$\propto$	Absorption Co-efficient
h	Planckôs Constant
c	Velocity of Light
$h\nu$	Energy of the Incident Photon
E_g	Optical Band Gap
ε''	Imaginary part of Relative Permittivity
ε'	Real part of Relative Permittivity
ε_{eff}	Effective Dielectric Constant
FOM	Figure of Merit

Chapter – 1

INTRODUCTION, LITERATURE SURVEY &OBJECTIVE OF THE WORK

1.1 Introduction

To meet the human needs, metals, alloys, ceramics, polymers and composites have been playing vital roles for centuries. Advances in fundamental science leads to the development of new types of functional materials. In recent years, material science has been developing as an emerging interdisciplinary field which leads us towards a new understanding of the structure and the applications of these materials.

Ceramics and polymers have been exploited as the fundamental materials in the field of material science since decades. The field of ceramics and polymers has experienced a renaissance in the past few years by the discovery of new classes of functional materials, i.e. composites. A composite material has been defined as a man made or manufactured material system consisting of two or more physically and/or chemically distinct, suitably arranged or distributed phases with an interface separating them and having properties that are not possessed by any of its components in isolation [1]. The individual components of the composites are referred to as constituent materials/phases. There are two categories of phases present in the composites; matrix phase and the reinforcement phase. The matrix phase is a continuous phase or the primary phase which surrounds and supports the reinforcement phase by maintaining their relative positions. The reinforcement phase is the second phase which is imbedded in the matrix phase in a continuous/discontinuous form. Generally, the reinforcement phase imparts the special mechanical and physical properties to the matrix phase. The zone across which the matrix phase and reinforcement phases interact is known as interface. In most of the composite materials, this region has finite thickness because of diffusion and/or chemical reactions between the filler and the matrix. A multiphase material formed from a combination of materials which differ in composition or form, remain bonded together and retain their identities and properties. Composites maintain an interface between components and act in concert to provide improved characteristics not obtainable by any of the original components acting alone. Traditional composites have been fabricated with emphasis on mechanical properties. However, the concept of the composite materials has also been extended to electronic applications. One such class of composite materials is ceramic-polymer composites.

In recent decades, a large number of ceramic-polymer composites for electronic applications have been introduced. Generally, these types of composites consist of ceramic based fillers dispersed in a polymer matrix. The concept of these composites has led to the introduction of new materials, improvements in manufacturing processes and the developments of new analytical and testing methods. The young industry of ceramic-polymer composites has been developing in the correlation with the contemporary composite industry. These materials are used in a variety of applications like: charge storage in capacitors, atomic force microscopy (AFM), medical ultrasound probes and health monitoring techniques in civil engineering, in underwater applications such as sonar in submarines, high frequency and energy harvesting applications, etc. [2-10]. Modern composite materials constitute a significant proportion of the engineered materials market ranging from everyday products to sophisticated niche devices. In this challenging era of science and technology, ceramic-polymer composites have the potential for revolutionary advances in the vibrant and exciting research field due to their excellent tailorable properties. Ceramic-polymer composites form a new class of materials of great potential applications having combined hardness and stiffness of ceramics and elasticity, flexibility, low density, and high breakdown strength of the polymers.

In recent years, the concept of miniaturization of electronic devices has stimulated the researchers to develop low loss high dielectric materials [11,12]. There is an increasing interest in the passive components of the electronic system due to their multi-functionality. To explore the capacitor applications, now interest is focused on the polymer dielectric materials due to their easy and low temperature processing. Fillers are typically used to enhance specific properties of polymers. Because of the technological importance of the ceramic-polymer composites, their electrical properties have been largely studied [5-16]. The focus of present work is primarily concerned with the electrical properties of polymer matrix composites in which ceramic phase have been randomly dispersed in particulate form.

1.2 Classification of Composites

On the basis of matrix phase, composites can be classified into polymer matrix composites (PMCs), ceramic matrix composites (CMCs), metal matrix composites (MMCs), and carbon and graphite matrix composites (CGMCs) (Fig. 1.1) [17]. According to the types of reinforcements, composites are divided into particulate composites (composed of particles), fibrous composites (composed of fibers), and structural composites. Particulate composites can be further subdivided as (i) composites with random orientation of particles and (ii) composites with preferred orientation of particles. Fibrous composites can be again subdivided into natural/biofiber and the synthetic fiber. Structural composites are divided into laminar and sandwich panels. Laminar composites are composed of two dimensional sheets or panels, while sandwich panels consist of two strong outer sheets called face sheets with a core honeycomb structure.

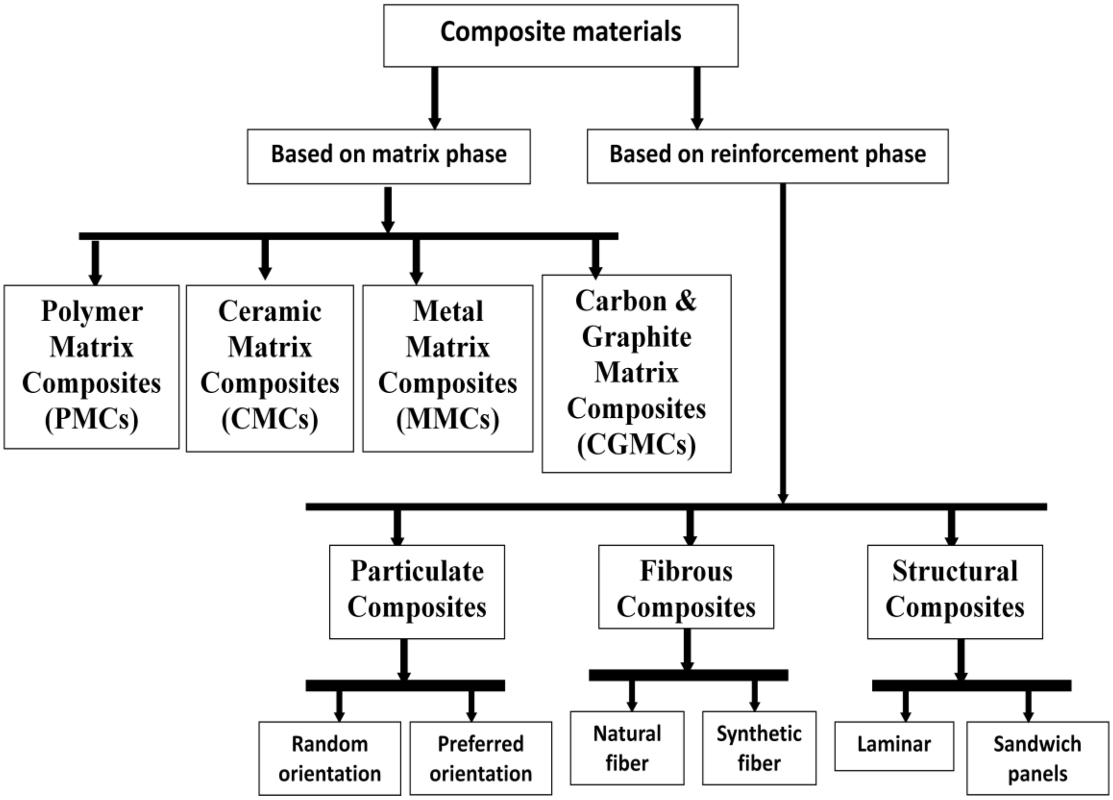

Fig. 1.1 Classification of composite materials [17].

1.2.1 Polymer Matrix Composites (PMCs)

PMCs are very popular due to their low cost and simple fabrication methods. There are different types of polymers used as polymer matrix in the PMCs, each with numerous variations. Mostly, the commercially produced composites use polymer matrix materials often called resins. The most common polymers are epoxy, polyester, phenolics, polyimide, polyamide, polypropylene, polyether ether ketone (PEEK), etc. The use of polymers is limited by their low level of mechanical properties, namely strength, modulus, and impact resistance [18,19]. Besides ceramic-polymer composites, different types of materials can also be combined to create a composite material. Within each of these classifications, materials are often further organized into groups based on their chemical composition or certain physical or mechanical properties [20,21].

1.3 Constituents of Ceramic-polymer composites

In the present work, ceramic-polymer composites for embedded capacitor and piezoelectric applications are synthesized and characterized. Therefore, next follows a brief review about the effective ceramics and polymers systems for the embedded capacitor and piezoelectric applications.

1.3.1 Ceramics

Ceramics are one of the fundamental materials playing vital roles in the advancement of material science. The word ‘ceramic’ is derived from the Greek word *‘keramos’,* which means potter’s clay. The earliest ceramics were made from clay and then fired to harden. The evolution from pottery to advanced ceramics has broadened the meaning of the word ‘ceramic’. A concise definition of ‘ceramic’ is impossible as it comprises vast array of materials. We can define ‘ceramic’ as an inorganic, refractory and non-metallic material, which acquire the mechanical strength through sintering process [22]. Ceramics can be classified into two categories, traditional ceramics and advanced ceramics. Traditional ceramics are defined as inorganic, non metallic solids, prepared from powdered raw materials and which then go through the heating process. The major characteristic properties of traditional ceramics are strength, hardness, low electrical conductivity and brittleness. The examples of traditional ceramics include clay products, pottery, silicate glasses and cement. The definition of ‘advanced ceramics’ was given by the 1993 Versailles Project on Advanced Materials and Standards (VAMAS). As per VAMAS, an advanced ceramic is “an inorganic, nonmetallic (ceramic), basically crystalline material of rigorously controlled composition and manufactured with detailed regulation from highly refined and/or characterized raw materials giving precisely specified attributes” [23]. In various parts of the world, advanced ceramics are referred to as technical ceramics, high-tech ceramics, high-performance ceramics, etc. Whereas engineering ceramics and fine ceramics terms are also used for advanced ceramics in the United Kingdom and Japan, respectively. Based on applications, advanced ceramics are classified as structural ceramics and functional ceramics. Structural ceramics are the materials used for their mechanical properties. Generally, these classes of ceramics serve as structural members when subjected to mechanical loading; therefore they are given the name structural ceramics. These structural ceramics exhibit exceptional mechanical properties which make them highly resistant to corrosion or wear, melting, stretching, and bending. Hardness, physical stability, chemical inertness, extreme heat resistance, superior electrical properties, biocompatibility and suitability for use in mass produced products make these ceramics one of the most versatile groups of materials in the world. These structural ceramics are used in mechanical, chemical, thermal, biomedical and nuclear applications. Functional ceramics are the materials; which can be used for properties other than mechanical strength, i.e. electrical, optical and magnetic, etc. This class of ceramics includes ceramic insulators, ferroelectric ceramics, piezoelectric ceramics, thermo-sensitive ceramics, pressure-sensitive ceramics and gas-sensitive ceramics, etc. The functional ceramics are used in electrical, magnetic, optical and thermal devices. Due to their unique electrical and optical properties, advanced ceramics find their use in many electronic device applications. These advanced ceramics are also referred as electroceramics and primarily used to exploit their electrical properties.

The present research work of interest partially deals with the electroceramics. Various subclasses of electroceramics are piezoelectrics, pyroelectrics and ferroelectrics. Piezoelectrics are the materials in which electrical polarization changes due to the application of mechanical stress. The piezoelectric electroceramics find their use in sonar, radar, actuators, sensors, etc. [24-26]. Pyroelectrics are the materials in which electrical polarization changes due to the application of heat. The pyroelectric electroceramics find their use in IR detectors, pyro sensors, etc. [27,28]. Ferroelectric electroceramics are the materials which exhibit both piezoelectric and pyroelectric properties and electrical polarization can follow applied external electric field and give rise to hysteresis loop. The ferroelectric electroceramics find their use in dielectric ceramics for capacitor applications, ferroelectric thin films for non-volatile memories, piezoelectric materials for medical ultrasound imaging and actuators, and electro optic materials for data storage and displays [29-35]. Fig. 1.2 shows the schematic diagram of the historical development of relative importance of materials.

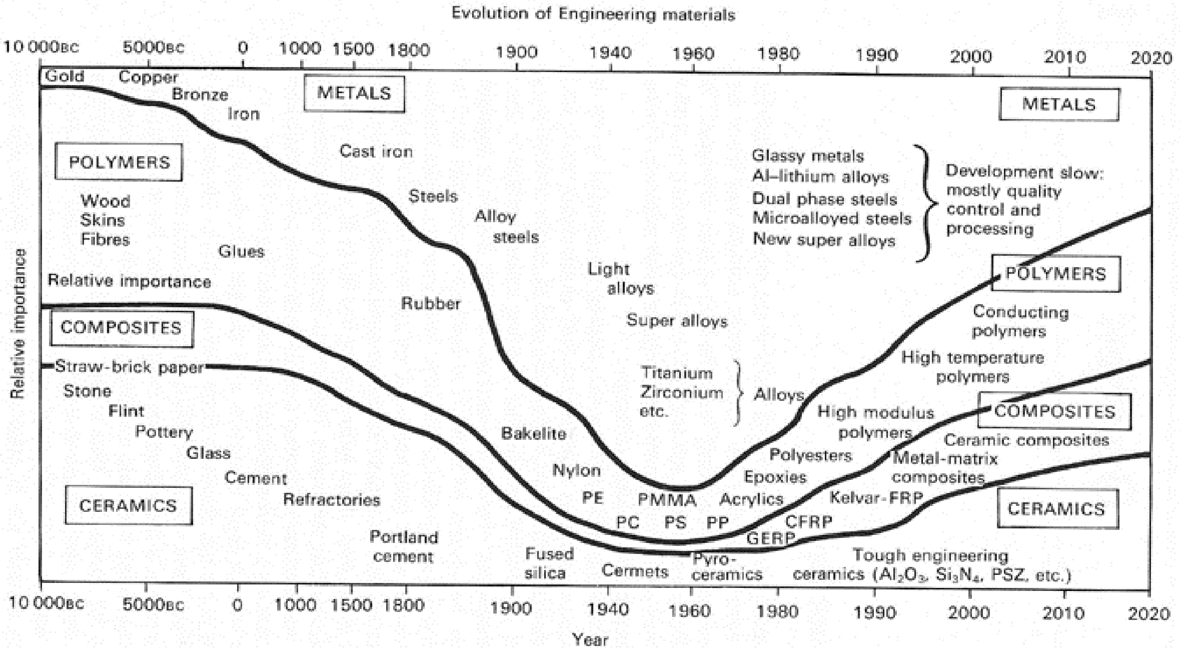

Fig. 1.2 Schematic diagram showing the relative importance of materials as a function of time [36-38].

The combination of the features of traditional ceramics and the exceptional functionality of advanced ceramics make the field of electroceramics important and these classes of materials are also named as smart materials. Smart materials detect changes in their environment and react accordingly. Smart materials can change their physical and chemical properties such as shape, volume, pH value, temperature, polarization, resistance, etc. under the influence of external stimuli, viz. atmosphere, heat, light, pressure, electric/magnetic field, etc. Ferroelectric materials are the smart materials, which exhibit both piezoelectric and pyroelectric properties in addition with high dielectric constant and electro optic effects.

1.3.1.1 Historical Development of Ferroelectric Ceramics

Before 1940, only two types of ferroelectrics namely rochelle salt and potassium dihydrogen phosphate and its isomorphous were known [39]. The birth of ferroelectric ceramics took place in the early 1940's, with the discovery of the phenomena of ferroelectricity in polycrystalline barium titanate ($BaTiO_3$/BT) [39]. The advantages of polycrystalline ceramics over single crystals are that polycrystalline ceramics can be formed into any desired shape and the orientation of polar axis can be chosen. Moreover, the synthesis process of polycrystalline ceramics is cheaper than the single crystal growth process [40]. Therefore, there is a continuous leap in the development of new ferroelectric ceramics, which are significant for technological, industrial and commercial applications [41]. BT ceramics have been the heart and soul of several billion dollar industries from high dielectric constant capacitors to the piezoelectric transducers. A huge leap in the field of research in ferroelectric materials came in the 1950's, leading to the development of many lead based ferroelectric ceramics such as lead titanate ($PbTiO_3$/PT), lead zirconate titanate (PZT), lead lanthanum zirconate titanate (PLZT) and relaxor ferroelectrics like lead magnesium niobate (PMN), etc [41].

Among these different lead oxide based ferroelectric systems, PZT is the prominent. This system shows excellent dielectric and piezoelectric properties near to the morphotropic phase boundary (MPB), which make it useful in piezoelectric transducers, actuators, transformers applications, etc [41,42]. However, generally these lead based ferroelectric materials contain more than 60 wt% of lead oxide, which can cause various environmental problems due to the recycling and disposal of the devices containing lead oxide [43-45]. An increase in the awareness about environmental issues have led WEEE (Waste Electrical and Electronic Equipment) and RoHS (Restriction of Hazardous Substances) to put ban on the use of lead oxide based materials [46]. Therefore, due to recent environmental issues research in ferroelectric materials is focused on lead free systems [47-52].

1.3.1.2 Applications of Ferroelectric Ceramics

Fig. 1.3 shows the different application regions (both near Curie temperature (T_c) and far away from T_c) of the ferroelectric ceramic materials.

Mainly, Fig. 1.3 depicts the temperature dependence of spontaneous polarization (P_s), permittivity (ε) and inverse permittivity ($1/\varepsilon$) curves of a normal ferroelectric material. P_s decreases with the increase in temperature and vanishes at T_c. ε tends to diverge near T_c, while beyond T_c, $1/\varepsilon$ is linear with respect to wide range of temperatures and obeys Curie Weiss law [53]. The materials with high permittivity are required for capacitor applications. Normally, ferroelectric materials possess high value of permittivity near T_c, hence the temperature near T_c is suitable for capacitor applications. For memory and piezoelectric applications, a stable P_s is required. For these applications, the operating temperature should be far below T_c. For pyro sensor applications, the rate of change of P_s with temperature should be high, which can be achieved by choosing the operation temperature just below T_c. Again the materials should not have any P_s value for electrostrictive and electro optic applications, which can be achieved for the ferroelectric materials above T_c.

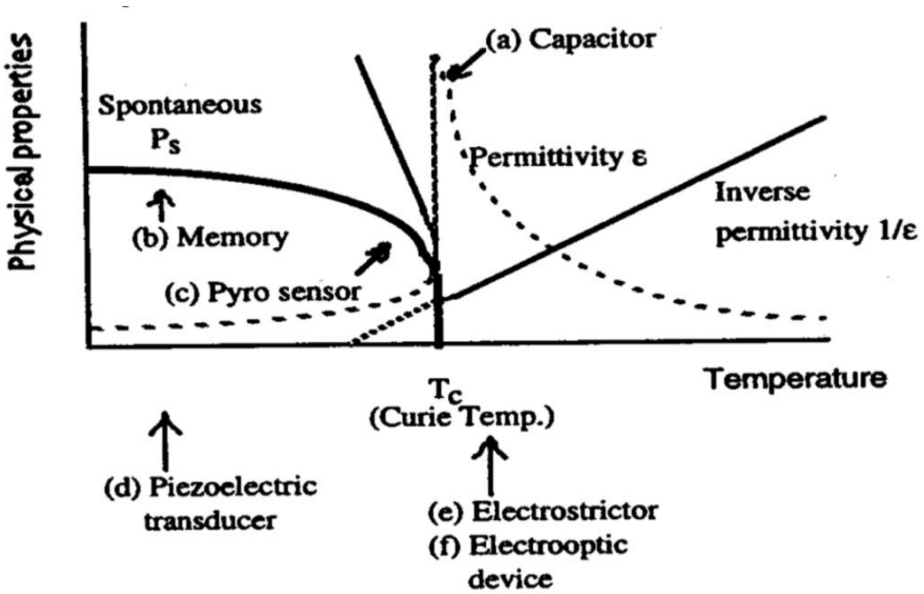

Fig. 1.3 Different application areas of ferroelectric ceramics [53].

The general category of different applications of bulk and film electroceramics is listed below in the Fig. 1.4.

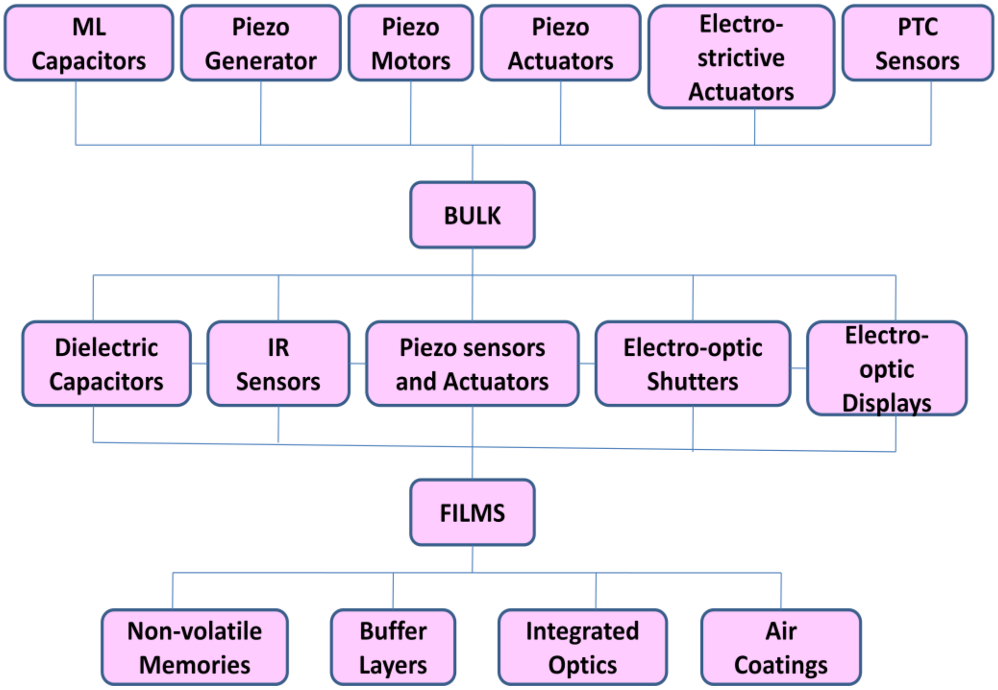

Fig. 1.4 Applications of bulk and film electroceramics [41].

1.3.1.3 Types of Ferroelectric Ceramics

1.3.1.3.1 Ferroelectrics with Hydrogen Bonded Radicals

Prior to the discovery of BT polycrystalline ceramics, researchers assumed that materials without hydrogen bond cannot show ferroelectric property. Several water soluble single crystals with hydrogen bonded radicals show ferroelectricity. The single crystals of Rochelle salt ($NaKC_4H_4O_6.4H_2O$, sodium potassium tartarate tetrahydrate), potassium dihydrogen phosphate (KH_2PO_4, KDP) and triglycine sulfate ($(NH_2CH_2COOH)_3H_2SO_4$, TGS) were the ferroelectric materials discovered before BT [54]. These materials are still in use due to their superior properties over other materials. However, there are many disadvantages associated with these materials, such as low T_c, lower mechanical properties, deliquescence and weak ferroelectricity. Because of these reasons, Rochelle salt, KDP and TGS single salts are substituted by ferroelectric polycrystalline ceramics.

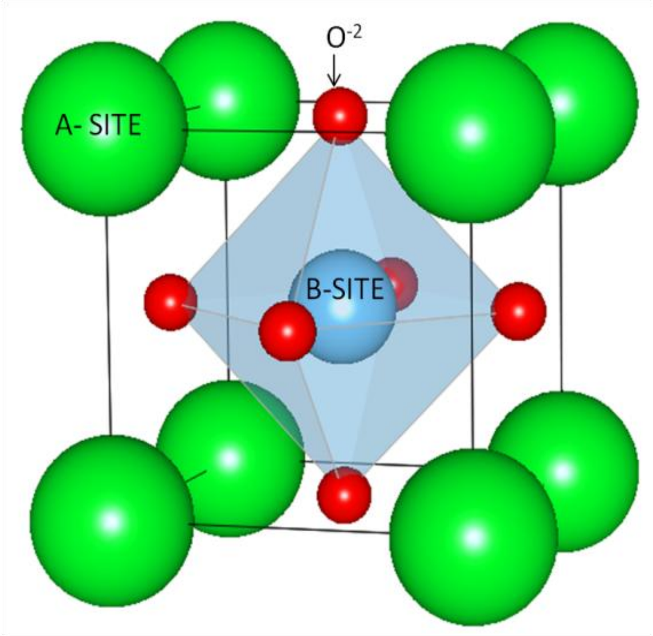

Fig. 1.5 Unit cell of a perovskite structure [54].

1.3.1.3.2 Ferroelectrics with Perovskite Structure

Perovskite is the family name of a group of materials with the same type of crystal structure as that of calcium titanate ($CaTiO_3$) [54]. The general chemical formula for a perovskite compound is ABO_3, where ‘A’ and ‘B’ are two cations of different sizes bonded with the oxygen atoms. Generally ‘A’ atoms are larger than ‘B’ atoms. The most studied ferroelectric materials with perovskite structure include barium titanate ($BaTiO_3$), lead titanate ($PbTiO_3$), lead zirconate titanate (PZT), lead magnesium niobate (PMN), lead lanthanum zirconate titanate (PLZT), potassium sodium niobate ($K_xNa_{1-x}NbO_3$/KNN) and potassium tantalate niobate ($K(Ta_xNb_{1-x})O_3$). The unit cell of a perovskite structure is shown in Fig. 1.5.

1.3.1.3.3 Ferroelectrics with Tungsten Bronze Structure

The unit cell of a perovskite structure consists of eight A-type atoms at each corner, one B-type atom at the centre and six oxygen atoms at the center of faces forming an octahedron. The B-site atom inside the oxygen octahedron is responsible for the dipole moment of the perovskite structure. A wide range of substitutions are possible in this type of structure due to the space available in the oxygen octahedron cage. Perovskite materials have many interesting properties from both theoretical and the application point of view. The commonly observed features of this family include colossal magneto resistance, ferroelectricity, superconductivity, high thermo power, spin dependent transport, etc. These compounds are used as sensors, actuators, catalytic electrodes in fuel cells and in many high temperature superconductors [54].

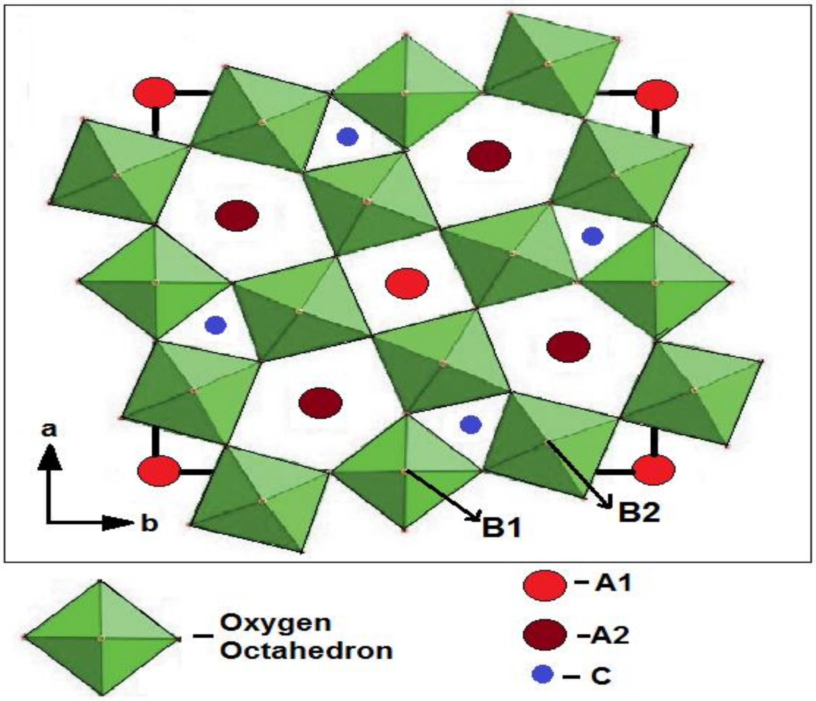

Fig. 1.6 Schematic diagram of a tungsten bronze structure [56].

The tungsten bronze type ferroelectric crystals have a structure similar to that of tetragonal tungsten bronze K_xWO_3 (x<1), the structure of which was first explained by Magneli *et al.* [55]. Lead niobate ($PbNb_2O_6$) was one of the first crystals of the tungsten bronze type structure to show useful ferroelectric properties.

The site occupancy formula for this type of structure is given by $(A_1)_2(A_2)_4(C)_4(B_1)_2(B_2)_8O_{30}$. The characteristic feature of the tungsten bronze type ferroelectric crystal is the interconnected corner sharing oxygen octahedral with three types of pseudo symmetric open channels, i.e. 3 fold, 4 fold and 5 fold. Fig. 1.6 shows the schematic of the projection of the tungsten bronze type structure on the (001) plane.

The open nature of the structure as compared to the perovskite allows a wide range of cation and anion substitutions without loss of ferroelectricity. At present, there exists more than 100 numbers of oxide ferroelectrics belonging to tungsten bronze family.

1.3.1.3.4 Ferroelectrics with Bismuth Layer Structure

Bismuth layer structure ferroelectrics (BLSFs) were first discovered by Aurivillius in the year 1949. Hence, these compounds are also called Aurivillius compounds [57]. The general formula of this family is $Bi_2A_{m-1}B_mO_{3m+3}$. It can also be written as $(Bi_2O_2)(A_{m-1}B_mO_{3m+1})$, since the phases are built up by the regular intergrowth of $(Bi_2O_2)^{2+}$ layers and perovskite $(A_{m-1}B_mO_{3m+1})^{2-}$ slabs. Here A is a combination of cations adequate for 12 co-ordinated interstices such as Na^+, K^+, Ca^{2+}, Sr^{2+}, Pb^{2+}, Ln^{3+}, Bi^{3+}, etc., B is a combination of cations well suited to octahedral coordination, like Fe^{3+}, Cr^{3+}, Ti^{4+}, Zr^{4+}, Nb^{5+}, Ta^{5+}, Mo^{6+}, W^{6+}, etc., and m is an integer corresponds to the number of two-dimensional sheets of corner-sharing octahedra forming the perovskite-like slabs.

Many compounds belonging to this family were synthesized by Smolenskii *et al.* [58] and Subbarao *et al.* [59]. At present, more than 80 compounds belonging to this category have been reported, including a considerable number of ferroelectrics. They correspond to m values ranging from 1 to 5. At room temperature (RT), their symmetry is mostly orthorhombic. The mostly studied compounds of this group are Bi_2WO_6 (m = 1), $SrBi_2Nb_20_9$ (m = 2) and $Bi_4Ti_30_{12}$ (m = 3). Ferroelectricity in these type of compounds is due to the cationic displacement along the polar a-axis and the tilting of the octahedral along ‘a’ and ‘c’ axes [59,60]. The properties of BLSF ceramics include excellent fatigue endurance, good polarization retention, fast switching speed, relatively high Curie temperature, low aging rate and low operating voltage [58-61]. These properties of BLSF ceramics make them suitable for non-volatile ferroelectric random access memory (FRAM) storage devices, sensor applications and high temperature piezoelectric device applications [62,63]. The structures of BLSF ceramics are shown in the Fig. 1.7.

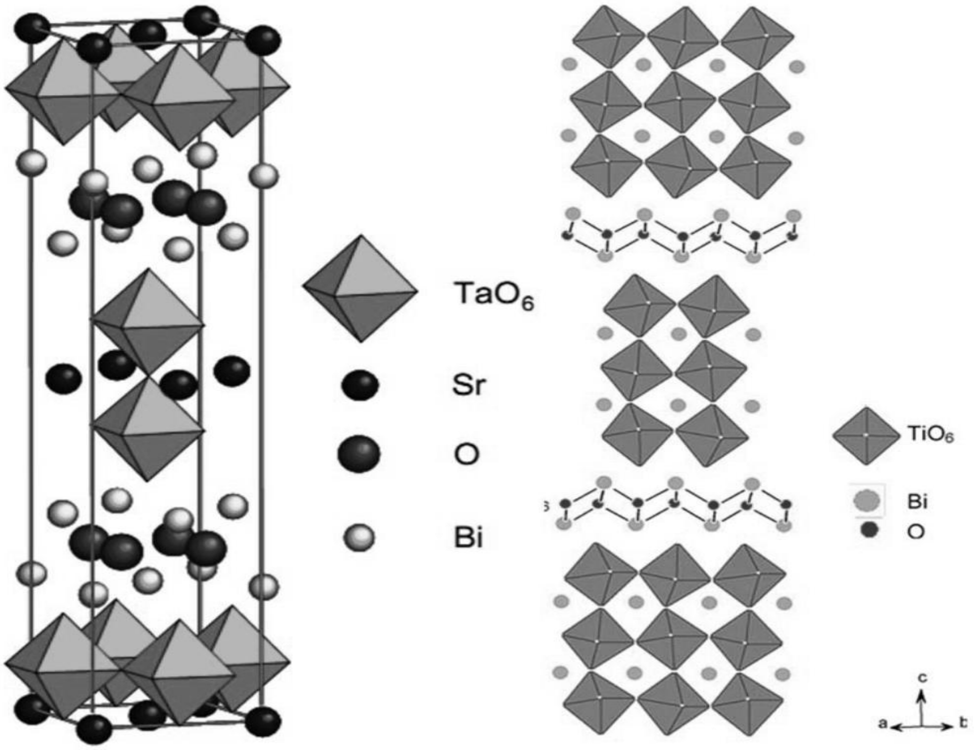

Fig. 1.7 Two layered [64] and three layered [65] BLSF structures.

1.3.1.4 Advantages of Perovskite Based Ferroelectric Ceramics

Perovskite materials exhibit many interesting properties from both the theoretical and the application point of view. The perovskite based ferroelectric ceramics show properties like ferroelectricity, piezoelectricity, superconductivity, colossal magneto resistance and high thermo power, etc. and which makes them important for various device applications. The structure of this class of materials is simple compare to other class of ferroelectric ceramics. Moreover, in this class of materials, the required modifications to obtain the desired properties for a particular device application can be made easily. Also, the synthesis of this class of material is economical.

1.3.1.5 Lead Based and Lead Free Perovskite Phase Based Ferroelectric Ceramics

Among the lead based ferroelectric materials, the perovskite family based $(Pb_{0.52}Zr_{0.48})TiO_3$ (PZT) and $Pb(Mg_{1/3}Nb_{2/3})O_3$–$PbTiO_3$ (PMN-PT) systems occupy the majority of the commercial piezoelectric market because of their excellent piezoelectric and ferroelectric properties. The excellent piezoelectric and ferroelectric properties in these lead based materials are observed near MPB between rhombohedral, tetragonal or monoclinic phases [42]. The MPB of PZT ceramics, which separate tetragonal and rhombohedral phases, is shown in Fig. 1.8.

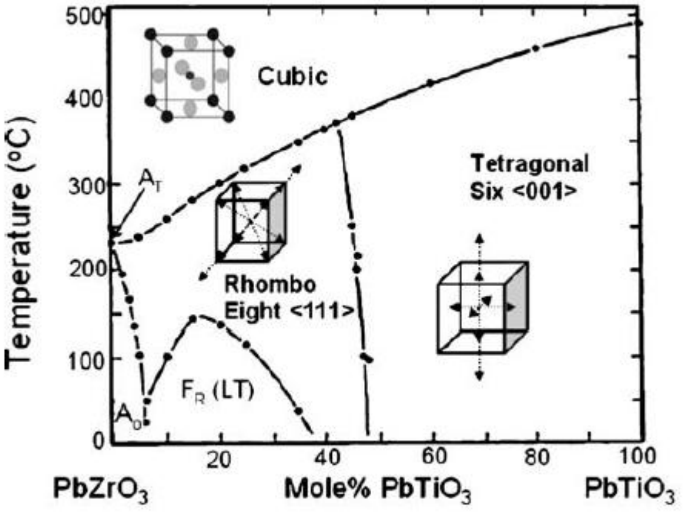

Fig. 1.8 Phase diagram of PZT [42].

MPB compositions have anomalously high dielectric and piezoelectric properties due to enhanced polarizability, which arises from the coupling between two equivalent energy states, allowing optimum domain reorientation during the poling process. The MPB of PZT ceramics is almost vertical in the phase diagram, which maintains the excellent piezoelectric properties across a wide temperature range.

A major breakthrough in the research field of lead free piezoelectric materials, as an alternative to PZT system, began within last ten years, due to the concern about environmental issues. Recent reports on lead free piezoelectrics include the following perovskite families: (i) BT, (ii) $K_{0.5}Na_{0.5}NbO_3$ (KNN), and (iii) $Na_{0.5}Bi_{0.5}TiO_3$ (NBT), based etc. [43-45, 47-52]. Fig. 1.9 (a) & (b) shows the comparison of the dielectric permittivity (ε) & the piezoelectric co-efficient (d_{33}) of lead based and lead free ceramics.

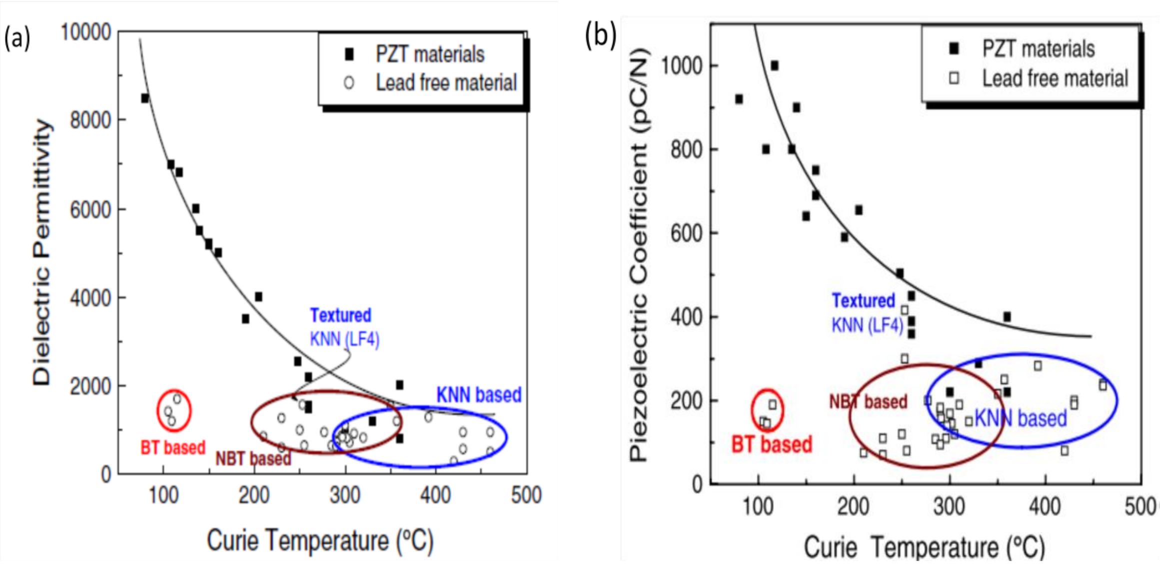

Fig. 1.9 Comparison of (a) dielectric permittivity and (b) piezoelectric coefficient of PZT and lead free materials as a function of Curie temperature [47].

As it is clear from Fig. 1.9, lead free piezoelectric ceramics generally have inferior piezoelectricity (d_{33} < 150 pC/N compared to d_{33} ~ 500 – 600 pC/N for lead based ceramics). Recently, their limit has been pushed to a higher level of d_{33} [66], but still it is halfway to the most desired PZT based systems. Liu *et al.* first reported a lead free pseudo binary $x[Ba(Zr_{0.2}Ti_{0.8})O_3]-(1-x)[(Ba_{0.7}Ca_{0.3})TiO_3]$/[BZT–BCT] ferroelectric system to replace PZT based systems [67].

Table – 1.1 Comparisons of Properties of Lead Based and Lead Free Ceramics

Properties of the materials	**Materials**				
	Lead based ceramics	**Lead free ceramics**			
	PZT	**BT**	**KNN**	**BNT-BT**	**BZT-BCT**
ε_r at 1 kHz	3400	2200	290	1900	3060
tanδ at 1 kHz	0.02	1.4	0.04	0.1	-
d_{33} in pC/N	590	260	80	110	560-720
T_c in ^oC	190	139	420	-	93
Ref.	2007[47]	2007[68]	2007[47]	2008[69]	2009[61]

This system possesses a MPB similar to PZT near (BZT-BCT) 50/50 composition. The piezoelectric, ferroelectric and electro mechanical properties for this composition are expected to be the best for this system. They reported (BZT-BCT) 50/50 ferroelectric system with surprisingly high piezoelectric properties at this optimal composition [67]. This suggests that (BZT-BCT) 50/50 ceramic system can be an effective alternative to lead oxide based PZT systems. Table – 1.1 shows the comparisons of various properties of lead based and lead free ceramics.

1.3.1.5.1 Literature Survey of Lead Free Perovskite Based Piezoelectric Materials

BT was the first lead free piezoelectric material that came into picture to replace the lead based counterparts. BT with RT d_{33} value ~ 190 pC/N was reported by Berlincourt *et al.* in the year 1971 [70]. BT based piezoelectrics have been extensively studied by different researchers by implementing different synthesis routes. Simon-Seveyrat *et al*. reported the RT d_{33} ~ 260 pC/N, higher than the values reported in the literature through the synthesis of BT powder by solid state reaction route [68].

Recent reports on lead free piezoelectrics can be divided into two main perovskite families; $K_{0.5}Na_{0.5}NbO_3$ (KNN) and $Na_{0.5}Bi_{0.5}TiO_3$ (NBT). Many studies have been carried out on various KNN-based families, such as KNN−$LiTaO_3$ [71], KNN−$LiNbO_3$ [72], KNN−$LiSbO_3$ [73] and Li-Sr-Sb-KNN [74], etc. The reported values of d_{33} of $(K_{0.5-x/2},Na_{0.5-x/2},Li_x)(Nb_{1-y},Ta_y)O_3$ ~ 300 pm/V [71], $\{[Li_x(Na_{0.5}K_{0.5})_{1-x}]NbO_3\}$ (x = 0.04–0.20) ~ 200–235 pC/N [72], $CaTiO_3$ modified $[(K_{0.5}Na_{0.5})_{0.96}Li_{0.04}](Nb_{0.91}Sb_{0.05}Ta_{0.04})O_3$ ~ 263 pC/N [73] and $(K_{0.5}Na_{0.5})_{0.96-x}Li_xSr_{0.02}Nb_{0.098}Sb_{0.02}O_3$ ~ 142 pC/N [74], respectively. Saito *et al.* successfully synthesized $(K_{0.5}Na_{0.5})NbO_3$ (KNN)-based textured ceramics with high d_{33} (~ 416 pC/N) and attributed the high piezoelectric properties to a polymorphic phase transition between orthorhombic and tetragonal phases in this system [66]. Also, studies on the structural and electrical properties of NBT and its dopants have been performed. The reported values of d_{33} of $(Na_{0.5}Bi_{0.5})_{1-x}Ba_xTiO_3$ ~ 180 pC/N [75], $(Na_{1/2}Bi_{1/2})TiO_3$ doped with 11 mol% $BaTiO_3$ (NBT–$BT_{0.11}$) ~ 13 pC/N [76], $(Na_{0.5}Bi_{0.5})TiO_3$ doped with 5 mol% $BaTiO_3$ (NBT-$BT_{0.05}$) ~ 77 pC/N [77], $(1-x)(0.98K_{0.5}Na_{0.5}NbO_3–0.02LiTaO_3)–x(0.96Bi_{0.5}Na_{0.5}TiO_3–0.04BaTiO_3)$ (KNN–LT–BNT–BT) ~ 155 pC/N [78], $(1-x)Bi_{0.47}Na_{0.47}Ba_{0.06}TiO_3–xKNbO_3$ (BNBT–xKN, x = 0–0.08) ~ 195 pC/N [79], La_2O_3 (0–0.8 wt.%)-doped $(Bi_{0.5}Na_{0.5})_{0.94}Ba_{0.06}TiO_3$ ~ 167 pC/N [80], respectively. These reported values of d_{33} are far less than the corresponding lead based ceramics. The basic approach of high piezoelectricity in lead based materials is the presence of MPB. Liu *et al.* first reported a lead free pseudo binary x[Ba($Zr_{0.2}Ti_{0.8}$)O_3]-(1-x)[($Ba_{0.7}Ca_{0.3}$)TiO_3][BZT–BCT] ferroelectric system to replace PZT based systems with surprisingly high d_{33} ~ 620 pC/N [67].

1.3.1.6 Lead Free (BZT-BCT) Ceramics

x[Ba($Zr_{0.2}Ti_{0.8}$)O_3]-(1-x)[($Ba_{0.7}Ca_{0.3}$)TiO_3]/(BZT-BCT) is a promising lead free piezoelectric system showing the highest value of d_{33} among the studied lead free piezoelectric ceramics till now. This system possesses a MPB similar to PZT near (BZT–BCT) 50/50 composition. Hence, the ferroelectric, piezoelectric, and electro mechanical properties for this composition are expected to be the best for this system. Fig. 1.10 shows the phase diagram of the (BZT-BCT) system.

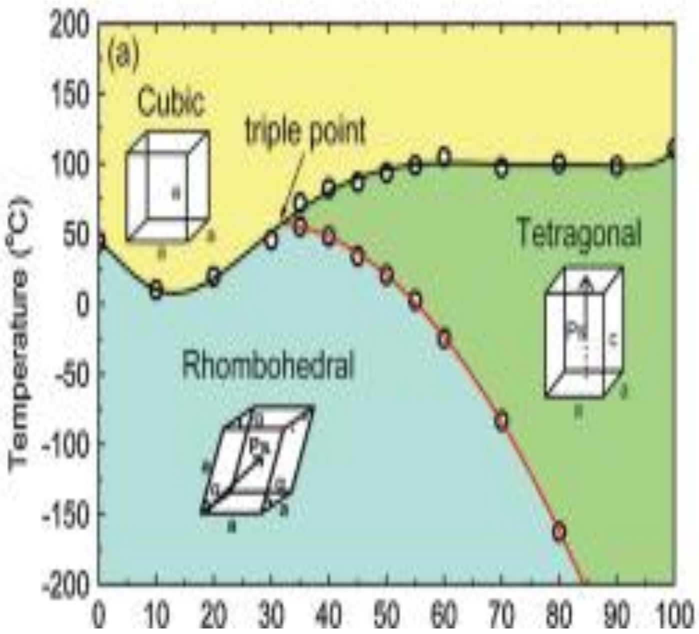

Fig. 1.10 Phase diagram of the (BZT-BCT) system [67].

The phase diagram of (BZT-BCT) ceramic system shows the presence of MPB, separating a ferroelectric rhombohedral (BZT side) and tetragonal (BCT side) phases. The most important characteristic of the (BZT-BCT) system is the presence of C-R-T triple point in the phase diagram at x ~ 32% and T_c ~ 57°C. The existence of C-R-T triple point characterizes many highly piezoelectric Pb-based systems such as PZT and PMN-PT [42]. Several researchers have put their effort to prepare (BZT-BCT) piezoelectric system using different conditions and different synthesis routes. In this section, a few examples of such efforts are briefly outlined.

Liu *et al*. [67] first reported the lead free piezoelectric $Ba(Zr_{0.2}Ti_{0.8})O_3$-x$(Ba_{0.7}Ca_{0.3})TiO_3$/BZT-xBCT system, where x is the molar percentage of BCT. The samples were prepared by solid state reaction route with $BaZrO_3$, $CaCO_3$, $BaCO_3$ and TiO_2 as the starting materials. The reported calcination and sintering temperatures were 1350^{o}C and 1450-1500^{o}C, respectively. 50BZT-50BCT at RT (20^{o}C) separating the rhombohedral and tetragonal phases with Curie temperature, T_c = 93^{o}C was reported as the MPB composition with highest spontaneous polarization P_m, highest remnant polarization P_r, lowest coercive field E_c = 168 V/mm, highest dielectric permittivity ~ 3060 and the most surprisingly high value of d_{33} ~ 560-620 pC/N.

B. Li *et al*. [81] discovered a high temperature poling method to improve the piezoelectric properties of the recently discovered lead free $Ba(Zr_{0.2}Ti_{0.8})O_3$-x$(Ba_{0.7}Ca_{0.3})TiO_3$/(BZT-BCT) system. They prepared BZT-60BCT system at a calcination temperature of 1350^{o}C/2h and a sintering temperature of 1450^{o}C/3h. RT X-ray diffraction (XRD) pattern shows the presence of tetragonal phase. The reported value of piezoelectric co-efficient, d_{33}, at 30^{o}C is ~ 360 pm/V [81]. The effective d_{33} value and the strain level have been increased by 40 % when the samples were cooled under the electric field through the Curie temperature. B. Li *et al.* interpreted it in terms of an internal bias field, induced by defect charge carriers accumulations at the grain boundaries, which may facilitate the intergranular interactions and results in large lattice strains.

J. Gao *et al*. [82] have investigated the microstructure basis for strong piezoelectricity in the lead free $Ba(Zr_{0.2}Ti_{0.8})O_3$-0.5$(Ba_{0.7}Ca_{0.3})TiO_3$ ceramics by varying compositions and temperature. The co-existence of rhombohedral and tetragonal crystal symmetries was reported among the miniaturized domains. The strong piezoelectricity in such a system was attributed to easy polarization rotation between the co-existing nano-scale tetragonal and rhombohedral domains.

M. C. Ehmke *et al*. [83] studied the effect of a uniaxial compressive stress on the properties of BZT-BCT samples across the MPB using direct piezoelectric coefficient measurements.

Y. Xifeng *et al*. [84] have compared the structure and properties of lead free BZT-BCT piezoelectric ceramics under two different sintering temperatures of 1240^{o}C and 1350^{o}C synthesized by solid state reaction route. The results showed that the lead free (BZT-BCT) ceramics had excellent piezoelectric properties and can be used for energy harvesting applications.

Revised structural phase diagram of $(Ba_{0.7}Ca_{0.3}TiO_3)$-$(BaZr_{0.2}Ti_{0.8}O_3)$ polycrystalline samples were investigated by D. S. Keeble, *et al*. [85]. The calcination temperature for BZT-BCT samples was 1350^{o}C for 15 h in oxygen atmosphere. They have reported an intermediate orthorhombic phase in contrary to the previously reported rhombohedral- tetragonal phases by Liu *et al*.

V. S. Puli *et al*. [86] synthesized lead free $[(BaZr_{0.2}Ti_{0.8})O_3]_{(1-x)}[(Ba_{0.7}Ca_{0.3})TiO_3]_x$ (x = 0.10, 0.15, 0.20) ceramics by sol-gel technique. XRD patterns revealed tetragonal crystal structure. Frequency dependent dielectric spectra confirmed the ferroelectric diffuse phase transition (DPT) near RT.

M. Wang *et al*. [87] prepared the lead free perovskite $0.5Ba(Zr_{0.2}Ti_{0.8})O_3$-$0.5(Ba_{0.7}Ca_{0.3})TiO_3$ ceramics by citrate precursor route. The results showed that the crystallization temperature of the gel was reduced by ~ 700^{o}C as compared to that in a mixed oxide route. Crystallites with pure perovskite structure and a particle size of ~ 30-60 nm were obtained by using appropriate calcination temperature.

$(1-x)Ba(Zr_{0.2}Ti_{0.8})O_3$-$x(Ba_{0.7}Ca_{0.3})TiO_3$ ferroelectric thin films on $Pt/Ti/SiO_2/Si$ substrate by G. Kang *et al.* were prepared using chemical solution approach [88]. The optimized thin film exhibited a high dielectric constant (ε_r) of ~ 2913 with a low dielectric loss (tanδ) of ~ 0.06, a high remnant polarization of 15.8 μC/cm^2, large coercive field of 58 kV/cm & an effective piezoelectric co-efficient, d_{33}, of 71.7 pm/V under substrate clamping.

The above literature survey highlights the importance of (BZT-BCT) system in the lead free ferroelectric ceramics category with effective dielectric and piezoelectric properties. This motivated us to choose the (BZT-BCT) system as our material of research for this work.

1.3.1.7 Advantages & Disadvantages of Ferroelectric Ceramics

Ferroelectric ceramics possess higher dielectric constant than ordinary insulating substances, making them useful for capacitor and energy storage applications. They have relatively low tanδ and positive temperature co-efficient of capacitance. Again ferroelectric ceramics are characterized by high specific electrical resistivity (> 10^{13} Ω–cm), moderate dielectric breakdown (100-200 kV/cm for bulk and 500-800 kV/cm for thin films) and nonlinear electrical, electromechanical and electro optic behavior. Ferroelectric ceramics also possess high piezoelectric and electromechanical coupling coefficients. These properties make ferroelectric ceramics potential candidate for high dielectric constant capacitors, piezoelectric transducers, and medical ultrasonic applications and for positive temperature coefficient devices, electro optic light valves and ferroelectric thin film memories, etc.

Despite of many advantages, ferroelectric ceramics possess the following disadvantages. High ε_r in ferroelectric ceramics is obtained near T_c. Therefore, to exploit the high capacitance of the ferroelectric materials, the operational temperature should be near T_c. But, near T_c, there is a huge variation in the dielectric properties of the ferroelectric materials, which makes them not useful for capacitor applications for a wide temperature range. Ferroelectric ceramics also exhibit low dielectric strength. As the ferroelectric ceramics are mechanically rigid, they lack flexibility/elasticity and tend to be brittle. They generally need high processing temperatures. They possess high value of acoustic impedance which does not match with water or human body tissue. Also polycrystalline ferroelectrics may lose piezoelectricity at high temperatures by depoling. These disadvantages become detrimental for various device applications.

1.3.2 High Dielectric Constant Non Ferroelectric Ceramics

Recently, high dielectric response has been observed in non ferroelectric materials. Ba $(Fe_{1/2}Nb_{1/2})O_3$/(BFN), $CaCu_3Ti_4O_{12}$/(CCTO) & NiO-based ceramics are some of the recently discovered non ferroelectric systems showing excellent dielectric properties [89-91]. A slight detail of these three ceramic systems is as follows:

Wang *et. al.* [92] reported dielectric characteristics of $Ba(Fe_{1/2}Nb_{1/2})O_3$ (BFN) ceramics over a broad temperature and frequency range. Two dielectric relaxations were observed in the range of 150–400^{o}K and 406–650^{o}K, respectively. Giant dielectric behavior (ε_r ~ 2,02,270 at 5 Hz, ε_r ~ 91,930 at 1 kHz, and ε_r ~ 37,030 at 100 kHz) with very strong frequency dispersion was observed in 406–650^{o}K range [92].

Calcium copper titanate, $CaCu_3Ti_4O_{12}$ (CCTO) has also attracted much interest due to its extraordinary high dielectric constant [90]. It exhibits gigantic dielectric permittivity of ~ 10^{4-5}, which is frequency independent up to 10^6 Hz and is almost constant in the temperature range 100-400°K [90]. Below 100°K, the dielectric constant drops rapidly to less than 100. Until now, the origin of the giant dielectric response in CCTO has not been fully understood. In CCTO, neither a phase transition nor a crystal structure change is detected in the temperature range of 35–1273°K [90]. Therefore, the high dielectric constant in CCTO is considered to be extrinsic not intrinsic. The widely accepted mechanism is an internal barrier layer capacitance (IBLC) model. In this model, the high dielectric phenomenon of CCTO ceramics is attributed to the existence of a grain-boundary IBLC effect [93].

NiO-based ceramics, the non-perovskite and non-ferroelectric material with a formula $A_xB_yNi_{1-x-y}O$ (where 'A' are mono-valents of Li, Na, K and 'B' are Ti, Al, Ta, Si) [91] have also attracted considerable attentions due to their impressive apparent high dielectric permittivity value (10^3–10^5). Moreover, the dielectric properties of NiO-based ceramics can be tuned by changing the compositions of the additives at A and B sites. The overall dielectric behavior of NiO-based ceramics is similar to those observed in CCTO. The high ε_r response in NiO-based ceramics is attributed to Maxwell–Wagner (M–W) relaxation model as a result of semiconducting properties inside grain and insulating properties at grain boundary (GB) [91].

The grain size and density of the functional ceramics depends on the processing route, which ultimately affects the material properties. In turn, electrical properties are greatly dependent on the phase, density and microstructure of the materials [94]. Also, for increasing the volume efficiency, the dielectric layers of functional ceramics and inner electrodes are stacked layer by layer to form a multilayered structures.

High dielectric response in these non-ferroelectric systems is accounted in terms of various models proposed so far from both intrinsic and extrinsic viewpoints, which still remain controversial [90,93]. These interpretations include (i) fluctuations of lattice-distortion-induced dipoles in nano size domains, (ii) electrode polarization effects due to the different work functions of an electrode and a sample, (iii) inhomogeneous conduction within the crystal due to the occurrence of defects in the grains, (iv) internal barrier layer capacitor (IBLC) effects originating from the insulating grain boundaries surrounding semiconducting grains, and (v) intra-grain insulating barrier effects [90]. In these various models, the charge dynamics inside the grain and at the grain boundary is the main factor accounted for giant dielectric response in these materials.

From the above observations for the present study, CCTO has been chosen as a high dielectric constant non ferroelectric ceramic system.

1.3.2.1 Non Ferroelectric High Dielectric Constant CCTO Ceramics

Non ferroelectric CCTO ceramic with perovskite related structure was first reported by M. A. Subramanian [95]. Neutron powder diffraction of CCTO indicates a cubic-perovskite structure with Im3 group symmetry and cubic lattice parameter a = 7.391 Å [96]. Fig. 1.11 shows the structure of $CaCu_3Ti_4O_{12}$.

In comparison with ferroelectric ceramics, the high dielectric constant originates from the tilting of Ti^{4+} ion within the TiO_6 octahedron. Moreover, CCTO exhibits more constraint than ferroelectrics. The TiO_6 octahedra tilt and form a square planar arrangement around Cu^{2+}. Based on structure calculations, it is found that the Ti-O bonds are under tension and increase the polarization of the TiO_6 octahedra [95].

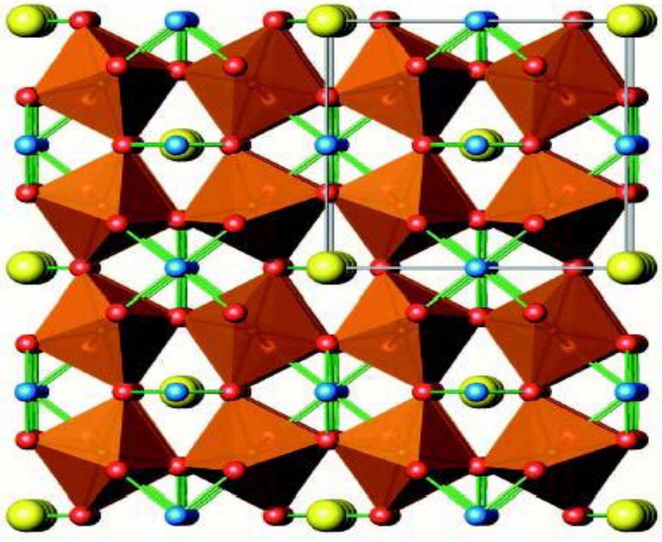

Fig. 1.11 The structure of $CaCu_3Ti_4O_{12}$ (Cu-blue, Oxygen-red, Ca-yellow) [96].

1.3.2.2 Advantages of Non Ferroelectric High Dielectric Constant Ceramics

Non ferroelectric high dielectric constant ceramics do not exhibit the time dependence of the dielectric constant and therefore does not experience a variation in capacitance from inter crystalline aging. These ceramics also have constant capacitance regardless of the applied voltage. These ceramics also experience virtually no change in capacitance with temperature.

1.3.2.3 Disadvantages of Non Ferroelectric High Dielectric Constant Ceramics

One of the major disadvantages of the non-ferroelectric high dielectric constant ceramics is that they do not have ferroelectric, pyroelectric and piezoelectric properties. Also, in spite of having high dielectric properties, the dielectric loss of high dielectric constant ceramics is high which is detrimental for their use in capacitor applications.

1.3.3 Polymers

In spite of the large dielectric constant, high piezoelectric charge co-efficient and high acoustic impedance, ceramics lack the flexibility and elasticity. These properties of the ceramics can be tailored by combining the ceramics with the polymer matrix, having elasticity, flexibility, low density and high breakdown strength. However, the choice of the polymer matrix depends on the physical, chemical and thermal properties required in the applications as well as on the economics.

Polymer is defined as a large molecule of repeating structural units connected by co-valent bonds. Hermann Staudinger was awarded with Nobel Prize for the structure of polymer in 1922 [97]. In polymers, with chemically saturated structures, the electrons are tightly bound in the σ-bonds between the atoms. Since all the available electrons are fixed in the σ-bonds, there are no electrons free to carry an electric current. Hence, solid, saturated polymers are characteristically electrical insulators. Because of this, any electrostatic charges that polymers acquire are retained for a long time. Low level conduction in insulating materials usually takes place in a variety of forms. It may be attributed to impurities that provide a small concentration of charge carriers in the form of electrons and ions. At high fields, the electrodes may also inject new carriers into the polymer, causing the current to increase more rapidly with voltage which is in accordance with the Ohm’s law.

1.3.3.1 Classifications of Polymers

Polymers are broadly divided into two categories.

- Plastics

    1. Thermoplastics

    2. Thermosets

- Elastomers

1.3.3.1.1 Thermoplastics

Thermoplastics are the polymers which become moldable above a specific temperature and return to solid state upon cooling [98]. The thermoplastic polymers are made up of long, unlinked polymer molecules, with high molecular weight. Because of the unlinked molecular chains, these polymers rely on other types of interactions, such as dipole-dipole interactions, aromatic ring stacking or Van der Waals forces. These are either amorphous or semi-crystalline in nature and have both glass transition temperature T_g and melting temperature T_m. They soften on heating and can be converted into any shape, which can be retained on cooling. They have varying degree of ductility. Processibility of these polymers is difficult. These polymers can be recycled but cannot withstand high temperatures. These are linear polymers and having poor dimensional stability. They have long storage life.

Polyvinylidene fluorides (PVDF), polycarbonates (PC), polyvinyl chlorides (PVC), Teflon, polyethylene, and polypropylene, etc. are the examples of thermoplastic polymers.

1.3.3.1.2 Thermosets

Thermosets are the polymers which usually exist in liquid or viscous state at low temperatures, but change irreversibly into infusible, insoluble hard state at high temperatures [99]. These polymers are made up of lines of molecules, which are heavily cross-linked. These polymers are amorphous and have only glass transition temperature T_g. Theses polymers become permanently hard after the initial heating-cooling cycle. These polymers are easily processible but generally brittle and cannot be recycled. These polymers can withstand high temperatures, form 3-D networks, dimensionally stable but with short storage life. Epoxy, phenolics, polyesters and silicones, etc. are the examples of thermosetting polymers.

1.3.3.1.3 Elastomers

Elastomers are the polymers with the property of visco elasticity and having low Young’s modulus and high yield strain compared with other materials. These polymers are also called rubber. These polymers are generally amorphous and exist above T_g. Natural rubbers, synthetic polyisoprene, butyl rubber and polybutadiene, etc. are some of the examples of elastomers.

In general, the advantages of polymers are following: cheap, easily processible and flexible, resistant to chemical attacks, low density and low acoustic impedance, which can match with water and human body tissues.

1.3.3.2 Ferroelectric Polymers

Ferroelectric polymers are the sub class of polymers, crystalline in nature and have permanent electric polarization, which can be switched in direction on the application of applied external electric field. The existence of piezoelectricity in natural and synthetic polymers has been known since a long time. The examples of natural piezoelectric polymers are wood and tendon. Kawai *et. al* reported that the substantial piezoelectric and pyroelectric activity can be generated in synthetic polymers after being subjected to a strong DC electric field at an elevated temperature [100]. Polymers have superior mechanical flexibility property, which makes them a subject of interest for the scientists. Till now, four classes of polymers: PVDF and its copolymers with trifluoroethylene (TrFE) and tetrafluoroethylene (TFE), the odd numbered nylons, various VDCN (vinylidene cyanide) copolymers and aromatic and aliphatic polyurea are known to have ferroelectric properties. Among these different ferroelectric class of polymers, poly(vinylidene fluoride) PVDF is the most commercially active ferroelectric polymer.

1.3.3.2.1 PVDF

PVDF is a thermoplastic fluoro-polymer. PVDF was the first polymer, which exhibited both piezoelectric and ferroelectric properties, as well as high dielectric constant, ε_r, ~ 10 [101]. The monomer unit of PVDF is CH_2-CF_2. The high electronegative fluorine atom with a Van der Waals radius of ~ 1.5 Å, is slightly larger than that of hydrogen ~ 1.2 Å, so the monomer unit has a net dipole moment of about 7.06×10^{-30} cm [102]. In 1969, the strong piezoelectricity of PVDF was observed by Kawai *et al.* [100]. The d_{33} of poled thin films of the PVDF was reported to be as large as 6-7 pC/N, which is 10 times larger than that observed in any other polymer. PVDF has T_g of about -35°C and is typically 50-60% crystalline in nature. To give PVDF its piezoelectric properties, it is mechanically stretched to orient the molecular chains in it and then poled under tension. The ferroelectric and piezoelectric properties of PVDF are due to the interaction of charges and dipoles, charge injection, charge trapping and detrapping and the influence of different crystal phases on the physical and electrical properties. PVDF has also been found to remain ferroelectrically stable after many years of preservation [103].

PVDF exists in several forms: alpha (TGTG'), beta (TTTT), gamma (TTTGTTTG') and delta (polar version of alpha) phases, depending on the chain conformations as trans (T) or gauche (G) linkages [104]. The nonpolar α phase is the most stable phase at RT. Therefore, PVDF films crystallize into α-phase from the melt. The crystallization of α phase forms a T-G chain configuration with a unit cell that has two parallel chains. The T-G chain configuration is a “cross-linked, non-planar” chain formation. Two of these chains make up one unit cell of PVDF [105]. The CH_2-CF_2 molecules of PVDF polymer have net dipole moments, pointing from the relatively electronegative fluorine atom to the hydrogen atom and can crystallize in an arrangement having macroscopic polarization. Fig. 1.12(a) shows ‘all-trans’ or TTTT configuration of polar β phase of PVDF. The ‘trans-gauche’ or TGTG conformation of α phase is shown in the Fig. 1.12(b). The β phase crystallizes into a simulated hexagonal polar packing as shown in the Fig. 1.12(c). This conforms into the paraelectric α-phase as shown in the Fig. 1.12(d) and has no net polarization [106].

The dipole moments of the crystallites of α phase PVDF are oriented in opposite directions, resulting in a net zero polarization. By the application of an electric field greater than, or equal to, 130 MV/m, the non-polar α phase can be transformed into the polar δ phase [107]. This applied electric field rotates every second chain axis, resulting in a parallel orientation of all the dipoles in the crystallites, but the chain conformation and unit cell remain the same.

To produce the β phase of PVDF, PVDF is mechanically stretched about 300 % of its original length at around 100^oC temperature. This causes an overall flip of the molecular chains and produces spontaneous polarization (ferroelectricity) in the crystallites. β phase of PVDF consists of a hexagonal unit cell with parallel oriented dipole moments. The highest dipole moment of the β phase of PVDF is perpendicular to the chain axis [108]. The γ phase has similar structure to β phase, however slightly different TTTGTTTG conformation. In addition, some observations demonstrate that electron beams can affect the relative polarization in ferroelectric materials. PVDF is a semi crystalline polymer that has morphology of crystallites in which ferroelectric phase (β phase) can be induced in the crystalline region [109].

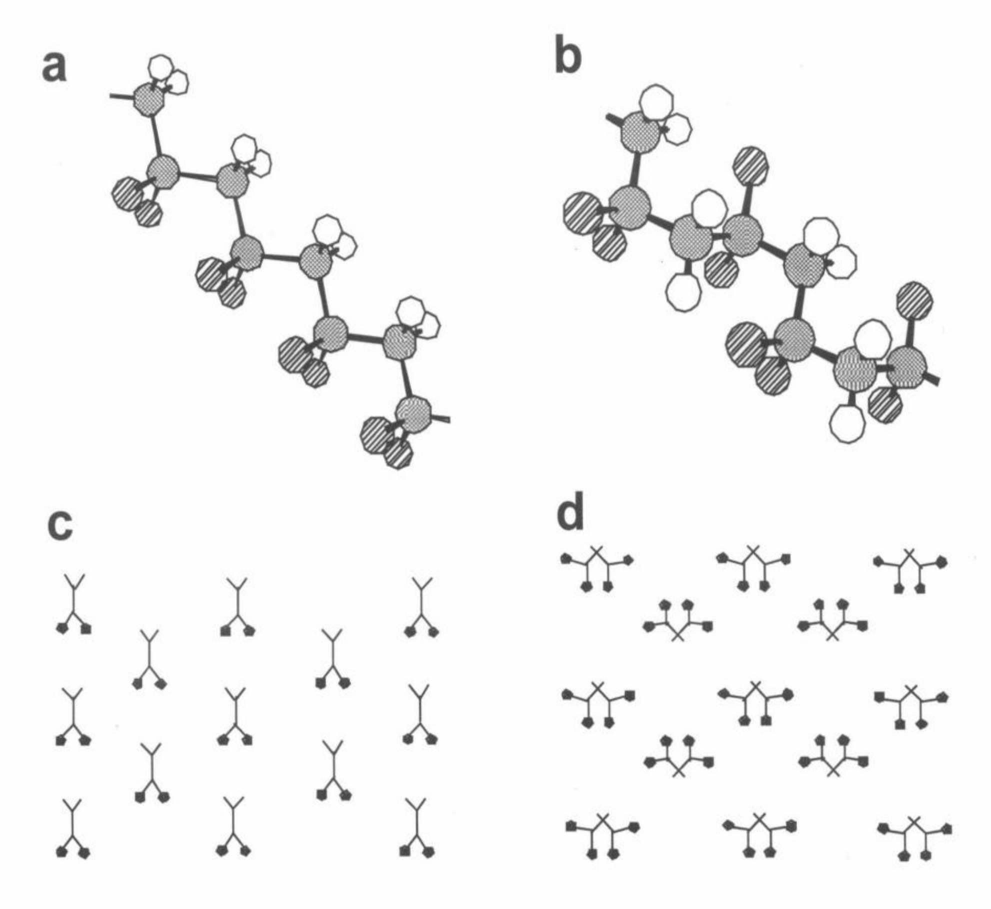

Fig. 1.12 The atomic structure of PVDF. Carbon atoms are grey, fluorine atoms are stripes and hydrogen atoms are white. (a) 'all trans' conformation of β phase of PVDF, (b) 'trans-gauche' conformation of α phase of PVDF, (c) crystal structure of β phase PVDF and (d) crystal structure of α phase PVDF [106].

1.3.3.3 Advantages & Disadvantages of Ferroelectric Polymers

Ferroelectric polymers have generated much interest since last 20 years because of their potential as functional materials for energy transduction and information recording. Ferroelectric polymers have been used as soft transducer materials due to their piezoelectric and pyroelectric properties. As sensors, these devices have better sensitivity and detectivity than oxide based ferroelectric detectors. Also the ferroelectric polymers have the advantages that they are flexible and involve simple fabrication techniques than ceramics. They can be easily fabricated into thin films by solvent casting or spinning techniques. They also exhibit relatively high voltage responsivity due to their low dielectric constant coupled with a reasonable pyroelectric co-efficient. These polymers also have low acoustic impedance which matches with water and human skin. It has been discovered that ferroelectric polymers exhibit piezoluminescence (i.e. emission of light in the elastic regime) upon the application of stress and can be used for high pressure and shock compression sensors. These types of polymers also play important roles in biomedical and robotic applications.

Ferroelectric polymers have found many new and interesting applications, which piezoelectric ceramics alone cannot fulfill. But, the disadvantages associated with this class of polymers are that they have relatively low melting point (150^oC-200^oC), low stiffness, low dielectric constant and low piezoelectric, pyroelectric properties in comparison to the piezoelectric ceramics.

1.3.3.4 Non Ferroelectric Polymers

Non ferroelectric polymers are the subclass of polymers which are amorphous in nature. Non ferroelectric polymers mainly include thermosets. These polymers are dimensionally more stable than ferroelectric polymers. They have excellent combination of mechanical properties and corrosion resistance. They also have good thermal stability and electrical properties. These polymers are relatively inexpensive than the ferroelectric polymers. Now-a-days the most commercially active examples of non-ferroelectric polymers include epoxy and phenolic thermosetting polymers.

1.3.3.4.1 Epoxy

Epoxies are a class of epoxide based polymers which are widely used as structural components and adhesives. The first production of epoxy resin occurred simultaneously in Europe and in the United States in the early 1940s. Today, a wide variety of epoxy resins of varying consistency are available. Mainly, it is composed of a two-component system, a liquid resin and a hardener/cross-linker. Upon mixing, the hardener reacts with epoxide groups in the resin to create a densely cross-linked network. Epoxy is a thermoset polymer, which means it cures into a stronger form by supplying energy. In contrast to so-called thermoplastics, thermosets cannot be melted or significantly softened by heating and are typically much stronger.

The functional group in epoxy resins is called the oxirane, which is a three-membered ring, formed between two carbon atoms and one oxygen atom, as shown in the Fig. 1.13. This atomic arrangement shows enhanced reactivity when compared with common ethers because of its high strain. Due to the different electro negativity of carbon and oxygen, the carbon atoms of the ring are electrophilic. Thus epoxies can undergo ring opening reactions towards nucleophiles. Also the polarity of the oxirane ring makes possible detection by IR spectroscopy [110].

Epoxy resins, depending on their backbone structure, may be low or high viscosity liquids or solids. In low viscosity resin, it is possible to achieve a good wetting of fibres by the resin without using high temperature or pressure. The impregnation of fibres with high viscosity resins is done by using high temperature and pressure.

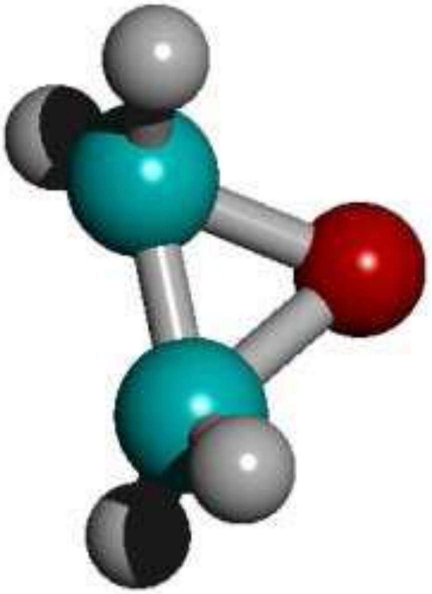

Fig. 1.13 An oxirane ring [110].

There are mainly two families of epoxies: the glycidyl epoxies and non-glycidyl epoxies (also called aliphatic or cycloaliphatic epoxy resins). The absence of aromatic rings in aliphatic epoxies makes them UV resistant and suitable for outdoor applications and also reduces viscosity. The most common epoxy monomers of each family are diglycidylether of bisphenol A (known as DGEBA) and 3,4-Epoxycyclohexyl-3’4’-epoxycyclohexane carboxylate (ECC), respectively. For the preparation of epoxy resins, a wide range of starting materials can be used.

Cycloaliphatic resins are usually found in the form of pure chemicals with a definite molecular mass. But DGEBA-based resins are synthesized by the addition of epichlorohydrine and bisphenol A and thus produce high viscosity. The nature and functionality of the epoxy monomer determines its reactivity as well as the properties and performance of the final material. The presence of glycidyl units in these resins enhances the processability but reduces thermal resistance. Fig. 1.14 shows the chemical structure of DGEBA.

The most common resin systems used worldwide in making printed wiring boards (PWB) are based on epoxies. Epoxies are relatively low in raw material cost, yet are capable of a wide range of formulation variations. T_g is a good frame of reference for traditional epoxy materials. A wide variety of epoxy systems with T_g values ranging from 110^{o}C to 170^{o}C, are very compatible with most PWB fabrication processes. In the last few years, there has been renewed interest in the epoxy based products because of their use in automotive applications, having good stiffness and strength. For many high speed digital applications, modified epoxy systems with dielectric constants in the range of 3.0 to 3.5 have been found to offer good cost performance values.

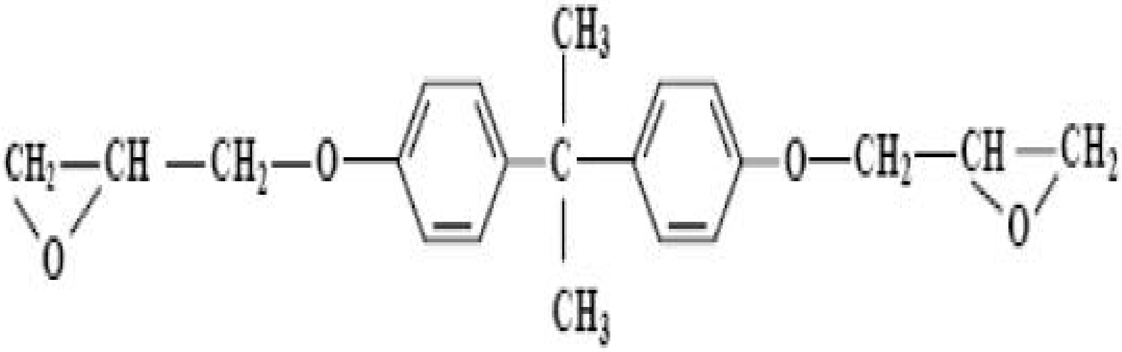

Fig. 1.14 Chemical structure of DGEBA [111].

The choice of both the resin and the hardener depends on the application, the process selected, and the properties desired. It is worthy to note that the reaction mechanism, the curing kinetics and the glass transition temperature (T_g) of the final material are also dependent on the molecular structure of the hardener.

Epoxy resins find a large number of uses because of their remarkable mechanical, chemical resistance, good heat resistance, high electrical resistance and good adhesion properties.

1.3.3.5 Advantages & Disadvantages of Non Ferroelectric Polymers

The advantages of non-ferroelectric polymers, particularly the epoxy resins include good mechanical strength, excellent resistance to chemicals and solvents, good heat resistance, good electrical resistance and excellent adhesion properties. The epoxy molecules at its centre contains two ring groups, which are able to absorb both mechanical and thermal stresses better than linear groups, giving epoxy resin very good stiffness, toughness and heat resistance. Thermoset materials are generally stronger than the thermoplastic materials and are better suited to high- temperature applications.

However, there are also some problems associated with these polymers including very low dielectric constant, which could lead to electrical impedance matching problems with the electronics. Also the primary disadvantages of the epoxy resins are that they require long curing times and in general, their mould release characteristics are poor.

1.3.4 Ceramic-Polymer Composites

Both advantages and disadvantages of ceramic and polymer have been discussed in previous sections. The drive for ceramic-polymer composites stems from the fact that desirable properties could not be obtained from single phase materials such as ceramics or polymers. In order to combine superior properties of both ceramic and polymer, flexible hybrid materials such as ceramic-polymer composites have been fabricated and studied. Compatibility of the matrix and the filler must be considered to prepare a composite. The amount of filler that can be incorporated is limited (sometimes the addition of higher amount of filler does not improve the mechanical properties of the material) and the filler should be uniformly dispersed in the polymer matrix. The efficiency of the filler to modify the properties of the polymer is primarily determined by the degree of dispersion in the polymer matrix. The phase in a heterogeneous material can be crystalline (either isotropic or anisotropic), amorphous, glassy or pore. The relative amount of each phase can be expressed by mole fraction, weight fraction, or volume fraction. The properties depend on the connectivity of the phases, volume percent of ceramic, and the spatial distribution of the active phase in the ceramic-polymer composites [49].

1.3.4.1 Connectivity Patterns for Composites

The concept of connectivity was developed by Newnham *et al*. [112]. Connectivity describes the arrangement of the component phases within a composite. It is a critical parameter in composites designed for use as piezoelectric transducers. Connectivity of the individual phases is of utmost importance, because this controls the electric flux pattern as well as the mechanical properties. Any phase in a mixture can be self connected in zero, one, two, and three dimensions. There are 10 important connectivity patterns in diphasic composites: 0-0, 0-1, 0-2, 0-3, 1-1, 1-2, 1-3, 2-2, 2-3 and 3-3, shown in Fig. 1.15 [112,113].

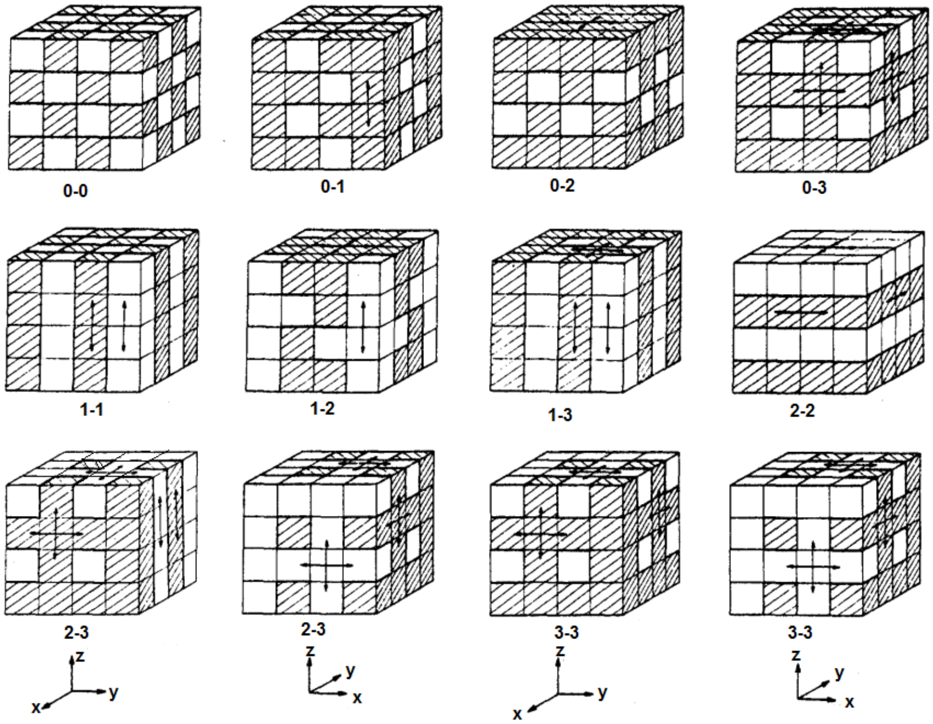

Fig. 1.15 Connectivity patterns for diphasic composites [112].

The connectivity pattern is shown in the form A-B, where 'A' refers to the number of directions in which the active phase is self-connected or continuous and 'B' refers to the continuity directions of the passive phase. The type of connectivity plays a critical role in determining the various properties of the composite.

The introduction of an inert polymeric phase in multiphase materials essentially decouples the planar Poisson stresses in the bulk ceramic, resulting in a reduction of the contributions of the g_{31} and g_{32} terms in the Eqn (1.1) [114]

$$g_h = g_{33} + g_{32} + g_{31} \tag{1.1}$$

where, g_h is the hydrostatic piezoelectric co-efficient.

g_{33} is the thickness mode response across a pair of electrodes in the poled 3-direction.

g_{32} and g_{31} are the responses in the plane.

Based on this concept, ceramic-polymer composites having connectivities of “3-1”, “3-2,” “3-3,” “1-3,” and “0-3” have been shown to exhibit good hydrostatic piezoelectric properties [114]. Recent research efforts at the Naval Research Laboratory’s Underwater Sound Reference Detachment (NRL-USRD) have further demonstrated the potential of “1-3” and “0-3” composites for future planar hydrophone applications [114].

The density, acoustic impedance, dielectric constant, ferroelectric and the piezoelectric properties like the electromechanical coupling coefficient k_t change with the volume fraction of the ceramic. Optimum material and piezoelectric parameters for medical ultrasound applications are obtained for ~ 20-25 vol% of ceramic in the composite [49].

In order to increase the dielectric constant, ceramics with high dielectric constants were added in the composites. However, even at maximum filler loading the dielectric constant of ferroelectric ceramics/polymer composites rarely exceeded 100, because the ferroelectric ceramic/polymer composites with 0-3 type of connectivity (i.e., the composites where the filler particles are distributed at random in the polymer matrix [112]) follow closely an exponential relationship between their dielectric constant and the volume fraction of the filler [11, 115-117]. Logarithm of the dielectric constant of such composites ($\varepsilon'_{\text{composite}}$) is linearly proportional to the volume fraction of the filler (φ_{filler}) with the slope dependent of the dielectric properties of both the components given in Eqn (1.2) [115].

$$\log\varepsilon'_{\text{composite}} = \varphi_{\text{filler}} \log\left(\frac{\varepsilon'_{\text{filler}}}{\varepsilon'_{\text{polymer}}}\right) + \log\varepsilon'_{\text{polymer}} \tag{1.2}$$

As the packing of a ceramic powder into a polymer matrix is limited, therefore usually the content of the filler cannot exceed 40 vol% or less, depending on the grain size distribution. The ceramic-polymer composites, with higher than 40 vol% filler loading are hard to process into the form of thin films, required for high-density capacitors. Moreover, such composites exhibit extremely poor mechanical properties, which disqualify them for application as embedded capacitor dielectrics. Hence, to obtain easily processible polymer composites with the dielectric constant higher than 100 based on typical polymers with the dielectric constant of the order of 5, the dielectric constant of the fillers must be higher than 9000.

1.3.4.2 Current Developments in Polymer Matrix Composites

1.3.4.2.1 Ferroelectric Ceramic-Polymer Composites

Several researchers have put an effort to prepare polymer based composites, especially 0-3 composites, using different ferroelectric ceramics as fillers and polymers as matrix. In this section, a few examples of such efforts are briefly outlined. 0–3 ceramic-polymer composites based on perovskite type ferroelectric ceramics, such as $BaTiO_3$ (BT), $PbZrO_3$ (PZT), $Pb(Mg_{1/3}Nb_{2/3})O_3–PbTiO_3$ (PMN–PT) and $(K_{0.44}Na_{0.52}\ Li_{0.04})(Nb_{0.86}\ Ta_{0.10}Sb_{0.04})O_3$ (KNN), etc have been well studied [118-124]. Due to environmental issues, recent focus of research is on lead free ceramic fillers. There have been limited studies on lead free ferroelectric ceramic-polymer composites [118-120,124-127]. For the better performance of 0-3 composites, polymer matrix plays a key role. Various polymers have been used based on their processibility, flexibility, melting temperature, glass transition temperature, dielectric response, and dielectric strength. Most of this research is based on polymer matrices, such as poly(methyl methacrylate) (PMMA), polyaniline (PANI), polyurethane (PU), etc. Recently, the focus of research is on Epoxy based polymers, due to their high mechanical strength and also more on PVDF based polymers due to their high dielectric constant [125-128].

Pant *et al*. [118] have investigated a comparative study of complex dielectric properties of composites of barium titanate ($BaTiO_3$) with two different polymer matrices: insulating polyaniline (PANI) powder (emeraldine base) and maleic resin. From this study, it was observed that the composites of $BaTiO_3$ with maleic resin showed normal composite behavior and the dielectric constant follows the asymmetric Bruggeman model. In contrast, the composites of $BaTiO_3$ with PANI showed an unusual behavior wherein even at a low concentration of PANI (5 wt.%) there is a drastic reduction in the dielectric constant of $BaTiO_3$.

Hajeesaeh *et al.* [119] have investigated the dielectric properties of BT-PVDF 0-3 composites. At a low volume fraction of 0.3 of BT ceramics, dielectric constant and dielectric loss of the composite at RT and at 1 kHz frequency were found to be ~ 11.5 and 0.21, respectively.

Seol *et al.* [124] have synthesized (Li, Ta, Sb) modified sodium potassium niobate/poly(vinylidenefluoride) $[(K_{0.44}Na_{0.52}Li_{0.04})(Nb_{0.86}Ta_{0.10}Sb_{0.04})O_3$-PVDF] 0-3 composites and studied their piezoelectric and dielectric properties. This class of composites showed better piezoelectric and dielectric properties than the PZT–polymer based composites.

From the observations made in all the above examples it can be concluded that efforts are going on to enhance the piezoelectric property, dielectric permittivity, etc of ceramic-polymer composites. In the knowledge of the author, there have been very few efforts to improve the dielectric and piezoelectric properties of ceramic-polymer composites by using (BZT-BCT) as filler. This motivates us to prepare ceramic-polymer composites of (BZT-BCT) as filler material.

In this work, composites of (BZT-BCT) and the best known polymers, like PVDF and epoxy are prepared and their structural, dielectric and piezoelectric properties have been investigated and discussed in detail.

1.3.4.2.2 Non Ferroelectric Ceramic-Polymer Composites

From the above observations, it can be concluded that the current research is focused on improving the structural, dielectric, and piezoelectric properties of the ferroelectric ceramic-polymer composites. Despite of many advantages, ferroelectric ceramic-polymer composites exhibit low value of dielectric constant. This motivates us to further increase the dielectric by adding high dielectric constant lead free non ferroelectric ceramics within the ferroelectric ceramic-polymer composites.

From the above literature survey, CCTO can be considered as a high dielectric constant lead free non ferroelectric ceramic for further improving the dielectric properties of the ferroelectric ceramic-polymer composites. There have been limited studies on CCTO-polymer composites [129-137]. In the knowledge of author, there exist no reports on CCTO-(BZT-

BCT)-polymer composites. This motivates us to further improve the dielectric properties of (BZT-BCT)-polymer composites by adding different volume fractions of CCTO ceramics.

1.4 Material Selected

From the above literature survey, (BZT-BCT) ferroelectric ceramics near MPB is a promising lead free system. Among polymers, PVDF & epoxy are selected to make the ceramic-polymer composites. Further, for improving the dielectric properties of ferroelectric ceramic-polymer composites, CCTO is a promising system.

1.5 Objective of the Present Work

The first objective of this work is to synthesize an effective lead free ferroelectric ceramic system with good dielectric (ε_r ~ 3000, tanδ = 0.05 at 1kHz frequency) and piezoelectric (d_{33} ~ 200 pC/N) properties at room temperature. The second objective is to prepare 0-3 ferroelectric ceramic-polymer composites for embedded capacitor (ε_r ~ 30 at RT and at 1kHz frequency) and piezoelectric (d_{33} ~ 20 pC/N) applications. The third objective of the present work is to further modify the dielectric properties (ε_r ~ 60 at RT and at 1kHz frequency) of the effective 0-3 ferroelectric ceramic-polymer composites by the addition of high dielectric constant (ε_r ~ 10,000 at RT and at 1kHz frequency) ceramic like CCTO. In order to achieve these goals, the following objectives are set for this work:

- Synthesize the lead free (BZT-BCT) compositions near MPB in single perovskite phase and study their structural, dielectric, ferroelectric and piezoelectric properties.

- To suggest the best MPB composition of the (BZT-BCT) system having good dielectric (ε_r ~ 3000, tanδ = 0.05 at 1kHz frequency) and piezoelectric (d_{33} ~ 200 pC/N) properties.

- To prepare the 0-3 ceramic-polymer composites by using the ceramic powders of the best MPB composition of (BZT-BCT) system as fillers and with PVDF and epoxy as the matrices.

- To suggest the best ceramic-polymer composites among the (BZT-BCT)/PVDF, (BZT-BCT)/epoxy systems for embedded capacitor (ε_r ~ 30 at RT and at 1kHz frequency) and piezoelectric (d_{33} ~ 20 pC/N) applications.

- To further modify the dielectric properties (ε_r > 50 at RT and at 1kHz frequency) of the best (BZT-BCT)/PVDF, (BZT-BCT)/epoxy composites by the addition of CCTO ceramic particles as fillers.

The following series of ceramics and composites are synthesized and studied under this study:

(i) $x[Ba(Zr_{0.2}Ti_{0.8})O_3]$-$(1-x)[(Ba_{0.7}Ca_{0.3})TiO_3]$/[BZT-BCT] (where, x = 0.48, 0.50 & 0.52) ceramics.

(ii) $CaCu_3Ti_4O_{12}$/(CCTO) ceramics.

(iii) Φ(BZT-BCT)-(1-Φ)PVDF composites with Φ = 0.05, 0.10, 0.15, 0.20 & 0.25 volume fractions of (BZT-BCT) ceramics, respectively.

(iv) Φ(BZT-BCT)-(1-Φ)epoxy composites with Φ = 0.05, 0.10, 0.15, 0.20 & 0.25 volume fractions of (BZT-BCT) ceramics, respectively.

(v) 0.25(BZT-BCT)-0.75[(1-x)PVDF-xCCTO]/[(BZT-BCT)-(PVDF-CCTO)] composites (where, x = 0.02, 0.04, 0.06, 0.08 & 0.10 volume fractions of CCTO ceramics).

(vi) 0.20(BZT-BCT)-0.80[(1-x)epoxy-xCCTO]/[(BZT-BCT)-(epoxy-CCTO)] composites (where, x = 0.02, 0.04, 0.06, 0.08 & 0.10 volume fractions of CCTO ceramics).

References:

[1] K. K. Chawla, Composite Materials: Science and Engineering (Third Edition, Springer, New York, 2012).

[2] H. L. W. Chan, P. K. L. Ng and C. L. Choy, Appl. Phys. Lett. 74, (1999) 3029.

[3] C. J. Dias and D. K. Das-Gupta, Ferroelectric Polymer and Ceramic-Polymer Composites, edited by D. K. Das-Gupta (Trans Tech Publications Ltd., Switzerland, 1994).

[4] V. Y. Topolov and C. R. Bowen, Electromechanical Properties in Composites based on Ferroelectrics (Springer, London, 2009).

[5] K. K. Shung, J. M. Cannata and Q. F. Zhou, Journal of Electro-ceramics. 19, (2007) 141.

[6] I. Patel, E. Siores and T. Shah, Sensors and Actuators A. 159, (2010) 213.

[7] Z. Ahmad, A. Prasad and K. Prasad, Physica B: Physics of Condensed Matter. 404, (2009) 3637.

[8] W. Thamjaree, W. Nhuapeng, A. Chaipanich and T. Tunkasiri, Applied Physics A. 81, (2005) 1419.

[9] K. H. Lam and H. L. W. Chan, Composites Science and Technology. 65, (2005) 1107.

[10] A. Petchsuk, W. Supmak and A. Thanaboonsombut, Journal of Applied Polymer Science. 114, (2009) 1048.

[11] Y. Bai, Z. Y. Cheng, V. Bharti, H. S. Xu and Q. M. Zhang, Appl. Phys. Lett. 76, (2000) 3804.

[12] S. George and M. T. Sebastian, Composites Science and Technology. 69, (2009) 1298.

[13] Q. M. Zhang, W. Cao, J. Zhao and L. E. Cross, IEEE Transactions on Ultrasonics, Ferroelectrics and Frequency control. 41, (1994) 556.

[14] K. C. Cheng, C. M. Lin, S. F. Wang, S. T. Lin and C. F. Yang, Materials Letters. 61, (2007) 757.

[15] T. Tanase, Y. Kobayashi, T. Miwa and M. Konno, Thin Solid Films. 485, (2005) 22.

[16] D. Y. Wang, K. Li and H. L. W. Chan, Sensors and Actuators A. 114, (2004) 1.

[17] A. V. Kyrylyuk and V. D. S. Paul, Proc. Ntl. Acad. Sci. USA. 105, (2008) 8221.

[18] B. E. Kilbride, J. N. Coleman, J. Fraysse, P. Fournet and M. Cadek, J. Appl. Phys. 92, (2002) 4024.

[19] E. Kymakis and G. A. J. Amaratunga, J. Appl. Phys. 99, (2006) 084302.

[20] F. Dalmas, R. Dendievel, L. Chazeau, J. Y. Cavaille and C. Gauthier, Acta Mater. 54, (2006) 2923.

[21] J. Li, P. C. Ma, W. S. Chow, C. K. To and B. Z Tang, Adv. Funct. Mater. 17, (2007) 3207.

[22] A. J. Moulson and J. M. Herbert, Electroceramics: Materials, Properties, Applications, Second Edition (John Wiley & Sons Ltd., England, 2003).

[23] S. J. Schneider, Jr., Advanced ceramics, What's in a name ? Standardization News (SN). 17, (1989) 28.

[24] G. Edwards, H. L. W. Chan, A. Batten, K. H. Lam, H. S. Luo and D. A. Scott, Sensors and Actuators A. 132, (2006) 434.

[25] S. E. Park and T. R. Shrout, IEEE Trans. Ultrason. Ferroelectr. Freq. Control. 44, (1997) 1140.

[26] W. W. Wolny, Journal of the European Ceramic Society. 25, (2005) 1971.

[27] S. Chopra, A. K. Tripathi, T. C. Goel and R. G. Mendiratta, Materials Science and Engineering B. 100, (2003) 180.

[28] S. N. Kumar and P. Kumar, Physica B. 405, (2010) 2869.

[29] H. Takezoe, Ferroelectric, Antiferroelectric and Ferrielectric liquid crystals: Applications. Encyclopedia of Materials: Science and Technology (Second Edition). 3063-3074, 2001.

[30] T. Minamikawa, Y. Yonezawa, A. Heya, Y. Fujimori, T. Nakamura, A. Masuda and H. Matsumura, Thin Solid Films. 395, (2001) 284.

[31] A. I. Mardarea, C. C. Mardarea and E. Joanni, Journal of the European Ceramic Society. 25, (2005) 735.

[32] S. Y. Liu, L. Chua, K. C. Tan and S. E. Valavan, Thin Solid Films. 518, (2010) e152.

[33] C. Guerrero, J. Roldan, C. Ferrater, M. V. Garcia-Cuenca, F. Sanchez and M. Varela, Solid-State Electronics. 46, (2001) 1433.

[34] M. Noda, K. Hashimoto, R. Kubo, H. Tanaka, T. Mukaigawa, H. Xu and M. Okuyama, Sensors and Actuators. 77, (1999) 39.

[35] A. J. Bell, Journal of the European Ceramic Society. 28, (2008) 1307.

[36] J. S. Reed, Principles of Ceramic Processing (John Wiley and Sons, Inc., New York,1995).

[37] I. D. Marinescu, H. K. Tonshoff and I. Inasaki, Handbook of Ceramic Grinding and Polishing (Noyes Publications, USA, 2002).

[38] N. Setter, J. of the Euro. Ceram. Soc. 21, (2001) 1279.

[39] C. Kittel, Introduction to Solid State Physics (7th Edition, John Wiley & sons, New York, 1995).

[40] J. Fousek, Ferroelectrics. 113, (1991) 3.

[41] G. H. Haertling, J. Am. Ceram. Soc. 82, (1999) 797.

[42] B. Jaffe, W. Cook and H. Jaffe, Piezoelectric Ceramics (Academic Press, London, 1971).

[43] T. Takenaka and H. Nagata, J. Eur. Ceram. Soc. 25, (2005) 2693.

[44] G. Z. Zang, J. F. Wang, H. C. Chen, W. B. Su, C. M. Wang, P. Qi, B. Q. Ming, J. Du, L. M. Zheng, S. Zhang and T. R. Shrout, Appl. Phys. Lett. 88, (2006) 212908.

[45] J. Wu, Y. Wang, D. Xiao, J. Zhu, P. Yu, L. Wu and W. Wu, Jpn. J. Appl. Phys. 46, **(**2007) 7375.

[46] G. M. Lee, Agency for technology and standards industry and energy of the Korean Government, Seminar on EU Product-Related Regulations, 2004, pp. 6.

[47] T. R. Shrout and S. J. Zhang, J. Electroceram. 19, (2007) 111.

[48] D. U. Hong-liang, T. Fu-sheng and L. I. Zhi-min, Trans. Nonferrous Met. Soc. China. 16, (2006) 462.

[49] M. S. Moon, N. H. Khansur, B. K. Choi, Y. G. Lee and S. C. Ur, Ceram. Int. 35, (2009) 3027.

[50] W. Lin, L. Fan, D. Lin, Q. Zheng, X. Fan and H. Sun, Curr. Appl. Phys. 13, (2013) 159.

[51] P. Wang, Y. Li and Y. Lu, J. Eur. Ceram. Soc. 31, (2011) 2005.

[52] R. Rani, S. Sharma, R. Rai and A. L. Kholkin, Mater. Res. Bull. 47, (2012) 381.

[53] K. Uchino, Ferroelectric Devices (Marcel Dekker, New York, 2000).

[54] A. Safari, R. K. Panda and V. F. Janas, Ferroelectric Ceramics: Processing, Properties & Applications (http://www.rci.rutgers.edu/~ecerg/projects/ferroelectric.html) (accessed on June 15, 2012).

[55] A. Magneli, Arkiv Kemi. 1, (1949) 213.

[56] E. Castel, M. Josse, D. Michau and M. Maglione, J. Phys. Condens. Matter. 21, (2009) 452201.

[57] B. Aurivillius, Ark. Kemi. 1, (1949) 499.

[58] G. A. Smolenskii, V. A. Isupov and A. I. Agranovskaya, Sov. Phys. Solid State. 3, (1961) 651.

[59] E. C. Subbarao, J. Am. Ceram. Soc. 45, (1962) 166.

[60] R. A. Armstrong and R. E. Newnham, Mat. Res. Bul. 7, (1972) 1025.

[61] S. K. Rout, E. Sinha, A. Hussain, J. S. Lee, C. W. Ahn, I. W. Kim and S. I. Woo, J. Appl. Phys. 105, (2009) 024105.

[62] S.O. Alfaro and A. Martinez-de la Cruz, App. Catalysis Gen. A, 383, (2010) 128.

[63] S. M. M. Zawawi, R. Yahya, A. Hassan, H. N. M. E kramul Mahmud and M. N. Daud. Chemistry Central Journal. 7, (2013) 80.

[64] H.C. Gupta, Archana and V. Luthra, J. Mol. Struct. 984, (2010) 204.

[65] M. Tripathy, R. Mani and J. Gopalakrishnan, Mater. Res. Bull. 42, (2007) 950.

[66] Y. Saito, H. Takao, T. Tani, T. Nonoyama, K. Takatori, T. Homma, T. Nagaya and M. Nakamura, Nature. 432, (2004) 84.

[67] W. Liu and X. Ren, Phys. Rev. Lett. 103, (2009) 257602.

[68] L. Simon-Seveyrat, A. Hajjaji, Y. Emoziane, B. Guiffard and D. Guyomar, Ceramic International. 33, (2007) 35.

[69] S. T. Zhang, A. B. Kounga, E. Aulbach and Y. Dung, J. Am. Ceram. Soc. 91, (2008) 3950.

[70] D. Berlincourt, in Ultrasonic Transducer Materials: Piezoelectric Crystals and ceramics, edited by O. E. Mattiat (Plenum, London, 1971, Ch-2).

[71] E. Hollenstein, M. Davis, D. Damjanovic and N. Setter, Appl. Phys. Letts. 87, (2005) 182905.

[72] Y. Guo, K. Kakimoto and H. Ohsato, Appl. Phys. Lett. 85, (2004) 4121.

[73] J. Wu, D. Xiao, Y. Wang, W. Wu, B. Zhang and J. Zhu, J. Appl. Phys. 104, (2008) 024102.

[74] J. Hao, R. Chu, Z. Xu, G. Zang and G. Li, Journal of Alloys and Compounds. 479, (2009) 376.

[75] Q. Xu, S. Chen, W. Chen, S. Wu, J. Zhou, H. Sun and Y. Li, Materials Chemistry and Physics. 90, (2005) 111.

[76] M. Cernea, C. Galassi, B. S. Vasile, C. Capiani, C. Berbecaru, I. Pintilie and L. Pintilie, Journal of the European Ceramic Society. 32, (2012) 2389.

[77] M. Cernea, B. S. Vasile, C. Capiani, A. Ioncea and C. Galassi, Journal of the European Ceramic Society. 32, (2012) 133.

[78] Y. Dai and X. Zhang, Journal of the European Ceramic Society. 28, (2008) 3193.

[79] H. Ni, L. Luo, W. Li, Y. Zhu and H. Luo, Journal of Alloys and Compounds. 509, (2011) 3958.

[80] P. Fu, Z. Xu, R. Chu, W. Li, G. Zang and J. Hao, Materials & Design. 31, (2010) 796.

[81] B. Li, J. E. Blendell and K. J. Bowman, J. Am. Ceram. Soc. 94, (2011) 3192.

[82] J. Gao, D. Xue, Y. Wang, D. Wang, L. Zhang, H. Wu, S. Guo, H. Bao, C. Zhou, W. Liu, S. Hou, G. Xiao and X. Ren, Appl. Phys. Lett. 99, (2011) 092901.

[83] M. C. Ehmke, J. Daniels, J. Glaum, M. Hoffman, J. E. Blendell and K. J. Bowman, J. Appl. Phys. 112, (2012) 114108.

[84] Y. Xifeng, L. Jiangyu, X. Shuhong, G. Yueqiu and L. Lu, Piezoelectrics & Acoustics. 2012-01 (Accepted manuscript).

[85] D. S. Keeble, F. Benabdallah, P. A. Thomas, M. Maglione and J. Kreisel, Applied Physics Letters. 102, (2013) 092903.

[86] V. S. Puli, A. Kumar, D. B. Chrisey, M. Tomozawa, J. F. Scott and R. S. Katiyar, J. Phys. D: Appl. Phys. 44, (2011) 395403.

[87] M. Wang, R. Zuo, S. Qi and L. Liu, J Mater Sci: Mater Electron. 23, (2012) 753.

[88] G. Kang, K. Yao and J. Wang, J. Am. Ceram. Soc. 95, (2012) 986.

[89] I. P. Raevski, S. A. Prosandeev, A. S. Bogatin, M. A. Malitskaya and L. Jastrabik, Journal of Applied Physics. 93, (2003) 4130.

[90] M. A. Subramanian, D. Li, N. Duan, B. A. Reisner and A. W. Sleight, Journal of Solid State Chemistry. 151, (2000) 323.

[91] J. B. Wu, C. W. Nan, Y. H. Lin and Y. Deng, Physical Review Letters. 89, (2002) 217601.

[92] Z. Wang, X. M. Chen, L. Ni and X. Q. Liu, Appl. Phys. Lett. 90, (2007) 022904.

[93] B. S. Prakash, K. B. R. Varma, D. Michau and M. Maglione, Thin Solid Films. 516, (2008) 2874.

[94] J. Y. Li, T. W. Xu, S. T. Li, H. Y. Jin and W. Li, Journal of Alloys and Compounds. 506, (2010) L1.

[95] M. A. Subramanian, D. Li, N. Duan, B. A. Reisner and A. W. Sleight, J Solid State Chem. 151, (2000) 323.

[96] C. C. Homes, T. Vogt, S. M. Shapiro, S. Wakimoto and A. P. Ramirez, Science**.** 293, (2001) 673.

[97] H. Ringsdorf and Hermann Staudinger, Angewandte Chemie International Edition. 43, (2004) 1064.

[98] S. A. Baeurle, A. Hotta and A. A. Gusev, Polymer. 47, (2006) 6243.

[99] http://old.iupac.org/goldbook/TT07168.pdf

[100] H. Kawai, Jpn. J. Appl. Phys. 8, (1969) 975.

[101] C. Ang, Z. Yu and L. E. Cross, Appl. Phys. Lett**.** 83, (2003) 1821.

[102] K. C. Kao, Dielectric Phenomena in Solids. Elsevier Academic Press: San Diego, CA, 2004.

[103] R. B. Seymour and G. B. Kauffman. J. Chem. Educ. 67, (1990) 763.

[104] A. J. Lovinger, Science. 220, (1983) 1115.

[105] R. W. Schwartz, J. Ballato and G. H. Haertling, Piezoelectric and Electrooptic Ceramics, in Ceramic Materials for Electronics: Processing, Properties, and Applications, 3rd Edition, R.

C. Buchanan, Ed. (Dekker, New York, 2003).

[106] S. P. Palta, L. M. Blinor and V. M. Fridkin, Physics of two-dimensional ferroelectric polymers. Institute of Crystallography, Russian Academy of Sciences, 2003.

[107] N. Suttle, Materials and Design. 9, (1998) 318.

[108] M. Tamura, Piezoelectric polymer properties and potential applications. Ultrasonic Symposium Proceedings. 344-346, 1987.

[109] J. Ma, Z. Shi and C. W. Nan, Adv. Mater. 19, (2007) 2571.

[110] H. F. Mark, Encyclopaedia of polymer science and technology, Vol. 9, Wiley and Sons, ISBN, New Jersey. (2004).

[111] H. Fiege, H. W. Voges, T. Hamamoto, S. Umemura, T. Iwata, H. Miki, Y. Fujita, H. J. Buysch, D. Garbe and W. Paulus, Phenol Derivatives. Weinheim: Wiley-VCH, (Ullmann's Encyclopedia of Industrial Chemistry) 2002.

[112] R. E. Newnham, D. P. Skinner and L. E. Cross, Mat. Res. Bull. 13, (1978) 525.

[113] G. Zhang and M. S. Wu, International Journal of Engineering Science. 48, (2010) 37.

[114] R. Y. Ting, Ferroelectrics. 67, (1986) 143.

[115] R. Popielarz, C. K. Chiang, R. Nozaki and J. Obrzut, Macromolecules. 34, (2001) 5910.

[116] C. K. Chiang and R. Popielarz, Ferroelectrics. 275, (2002) 1.

[117] R. Gregorio , M. Cestari and F. E. Bernardino, J. Mater. Sci. 31, (1996) 2925.

[118] H. C. Pant, M. K. Patra, A. Verma, S. R. Vadera and N. Kumar, Acta Materialia. 54, (2006) 3163.

[119] S. Hajeesaeh and S. Muensit, Songklanakarin J. Sci. Technol. 29, (2007) 414.

[120] R. K. Goyal, S. S. Katkade and D. M. Mule, Composites: Part B. 44, (2013) 128.

[121] L. Dong, C. Xiong, H. Quan and G. Zhao, Scripta Materialia. 55, (2006) 835.

[122] Z. Ahmad, A. Prasad and K. Prasad, Physica B: Physics of Condensed Matter. 404, (2009) 3637.

[123] S. V. Glushanin, V. Y. Topolov and A. V. Krivoruchko, Materials Chemistry and Physics. 97, (2006) 357.

[124] V. Y. Topolov and C. R. Bowen, Electromechanical Properties in Composites based on Ferroelectrics (Springer, London, 2009).

[125] J. H. Seol, J. S. Lee, H. N. Ji, Y. P. Oka, G. P. Konga and K. S. Kima, Ceram Int. 38S, (2012) S263.

[126] K. H. Lam, X. X. Wang and H. L. W. Chan, Composties: Part A - Applied Science and Manufacturing. 36, (2005) 1595.

[127] S. Agrawal, R. Guo, D. K. Agrawal and A. S. Bhalla, Ferroelectrics. 400, (2010) 155.

[128] E. E. Shafee and S. M. Behery. Mater Chem Phys. 132, (2012) 740.

[129] M. Arbatti, X. Shan and Z. Cheng, Adv. Mater. 19, (2007) 1369.

[130] W. Yang, S. Yu, R. Sun and R. Du, Acta Mater. 59, (2011) 5593.

[131] B. Shri prakash and K. B. R. Varma, J Compos. Sci. Technol. 67, (2007) 2363.

[132] E. Tuncer, I. Sauers, D. R. James, R. Alvin, M. Ellis and P. Paranthaman, Nanotechnology. 18, (2007) 25703.

[133] F. Amaral, C. P. L. Rubinger, F. Henry, L. C. Costa, M. A. Valente and A. B. Timmons, 354, (2008) 5321.

[134] P. Thomas, K. T. Varughese, K. Dwarakanath and K. B. R. Varma, Composites Science and Technology. 70, (2010) 539.

[135] P. Thomas, S. Satapathy, K. Dwarakanath and K. B. R. Varma, eXPRESS Polymer Letters. 4, (2010) 632.

[136] P. Thomas, K. Dwarakanath and K. B. R. Varma, Synthetic Metals. 159, (2009) 2128.

[137] L. A. Ramajo, M. A. Ramirez, P. R. Bueno, M. M. Reboredo and M. S. Castro, Materials Research. 11, (2008) 85.

******

Chapter – 2

INVESTIGATED PARAMETERS

2.1 Introduction

In this chapter, the basic principles and various experimental techniques as well as the synthesis routes used in this thesis work, are described. In the present chapter, various processes taking place during the synthesis of both ceramics and composites are presented. Generally, in order to measure the structural, microstructural and electrical properties of the ceramics as well as the composite materials, various characterization techniques are used. In the present work, thermal, structural, microstructural, dielectric, ferroelectric and piezoelectric characterizations of the selected ceramics and composites are carried out. The concepts of experimental methods and techniques for these characterizations including thermogravimetric analysis (TGA), powder x-ray diffraction (XRD), scanning electron microscopy (SEM), dielectric measurements, ferroelectric hysteresis loop measurement and piezoelectric constant measurement are briefly explained.

2.2 Synthesis Routes

2.2.1 Synthesis of Ceramics

Now-a-days ceramic materials have profound applications in electrical industry, automobiles, medical industry, etc. The synthesis of ceramics plays major roles in tailoring its physical and electrical properties [1,2]. New techniques have been developed by material scientists to get high quality materials with affordable cost and minimum required time. The knowledge of crystal chemistry, thermodynamics, reaction kinematics and equilibrium of phase plays vital roles in the material synthesis [3]. There is an interrelationship between the structures and properties with the processing of ceramic materials [4]. The science behind the processing of ceramics is to identify its important properties and to understand the effect of different parameters on its structural and physical properties. The synthesis of ferroelectric ceramics involves two forms, the single crystal and the polycrystalline forms. It is relatively difficult to prepare single crystals [5]. However; the synthesis of polycrystalline form is easier. Polycrystalline ceramics are also more stable in comparison to single crystals. The ferroelectric properties of polycrystalline ceramics can also be comparable to that of the single crystal ceramics. In the present study, we have synthesized electroceramics in the polycrystalline forms.

2.2.2 Types of Synthesis Techniques

The processing of traditional ceramic materials is relatively simple with the simple heating of ceramics. Modern engineered electroceramics have superior properties, which depends upon the processing technique used. Therefore, a more sophisticated processing technique with a high purity of advanced ceramic powders and fine particle size is necessary to achieve the best potential properties of modern polycrystalline ceramics. The basic need for the development of advanced synthesis techniques is to give a uniform particle size distribution. There are various synthesis techniques for the synthesis of ceramic samples. The synthesis methods of polycrystalline ceramics can be grouped into 3 categories depending upon the starting materials, whether in a gaseous phase, a liquid phase or a solid phase [6]. Further, gaseous phase synthesis of ceramics can be divided into 3 types. First, the chemical reaction between gaseous species is by vapour deposition method. Second, the reaction between a gas and a liquid can be referred to as direct metal oxidation. Third, the reaction between a gas and a solid is by reaction bonding. In liquid phase synthesis, a solution of compound is converted into a solid body. There are 5 methods for liquid phase synthesis of ceramic powders. Among them sol-gel synthesis is considered to be the most interesting method for the production of modern ceramic oxides. In solid phase synthesis of powder ceramics, the production of solids results from the reactions between assembles of finely divided constituents' carbonates/oxides of the starting raw powders. There are 3 types of chemical reactions among solids; oxidation and reduction of a solid, thermal decomposition of a solid and solid state reaction between two types of solids [7]. Again, the synthesis of ceramic powder can be approached in the following two ways, one is the mechanical method and the other is the chemical method. The mechanical method includes solid state reaction and different ball milling processes, etc [7]. The chemical methods are sol-gel method, hydrothermal method, co-precipitation method, combustion method, liquid and gas phase reaction, etc [7]. Each method bears its own advantages and disadvantages. The advantages of chemical method are high purity, small particle size, and chemical homogeneity. But, the disadvantages are that expensive raw material, poor for non-oxides, limited applicability, and more time consumption and complex reaction procedures [8]. Among the different mechanical synthesis methods, solid state reaction method is comparatively easier and cheaper (low cost precursors are used) and it can be used for large scale production of bulk ceramic powders [9]. In the present study, we have synthesized electroceramics by solid state reaction route.

2.2.2.1 Solid State Reaction (SSR) Route

Solid state reaction (SSR) route is the most commonly used and effective method for the synthesis of polycrystalline ceramics. The raw precursors, used in the synthesis of ceramics by SSR route are normally oxides and carbonates. The starting precursors in SSR route do not react at RT and in order to facilitate the reaction, they are heated to higher temperature between 1000 to 1500^{o}C.

In the processing of ceramics through SSR route, first of all the raw materials are weighed according to the stoichiometry of the compound with due consideration for impurity and moisture contents. Then the raw materials are mechanically mixed and grinding operations are performed to control the particle size and to make the mixture homogeneous. Generally, for this purpose the milling operation is performed which can reduce the particle size down to 1-10 μm range [10]. An attempt to further reduce the size of the particles will affect the homogeneity and processing steps. Acetone is generally usually used as a milling medium since it is available with adequate purity at low cost. The phase formation temperature is decided from the TGA. Here, the weight loss of the sample is measured as a function of temperature. Next step is the solid state reaction between the constituents of starting materials at suitable temperature [11]. This process is called firing or calcination. During calcination, control over stoichiometry is essential, and for it, volatile constituents have to be compensated. Calcination causes the constituents to interact by inter diffusion of their ions and resulting in a homogeneous body. Hence, it is considered that calcination is the part of the mixing process. Calcination also controls the shrinkage during sintering. After calcination, the powder is given desired shape, known as green body and this green body is densified through sintering process [7]. The main steps involved in SSR route are further elaborated below:

2.2.2.1.1 Precursors

Precursors are the starting materials required to prepare the solid polycrystalline ceramics. Precursors should be of high purity & fine grain powders. The physical properties of the final product will affect if the reactants contain some impurities. Fine grained powders should be used as it enhances the reaction rate due to the increase in the surface area [10]. The nature of reactants also plays major roles in the properties of the final ceramic product. The reactants are selected on the basis of the nature of the product and the reaction conditions involved [12].

2.2.2.1.2 Weighing & Mixing

The raw materials are weighted in the required amounts according to the stoichiometry to form the desired compound. After weighing, the raw materials are mixed and ball milled for several hours. Acetone and distilled water are usually used as the milling medium. After ball milling, the mixture is dried and further grinded in the agate mortar to homogenize the milled particles [10]. The mixture of reactants then becomes ready for the calcination process.

2.2.2.1.3 Calcination

The calcination process is the reaction between the starting raw materials at suitable temperature [11]. Calcination process is also called the phase formation process as the constituents of the raw materials decompose by inter diffusion between the different ions. It is an endothermic reaction with the formation of solid oxide products and gases as byproduct [11]. The idea about the phase formation temperature is taken from the TGA of the milled powders. The main motive of the calcination process is to achieve the desired ceramic phase. Generally, the heating of the raw milled powders is done in air. It is necessary to use suitable refractory containers for heating the milled powder at higher temperatures, such that the reactants cannot chemically react with the containers used. Therefore for the heating process, chemically inert and high melting point containers (crucibles or boats) are used. Generally, these crucibles are made up of porcelain, alumina, magnesia, etc or nobel metals like platinum & gold, etc. For low temperature reactions (below 600-700^{o}C), nickel, zirconium, etc can also be used as crucible. The next step of solid state reaction of materials is shaping.

2.2.2.1.4 Shaping

Calcined powders are ball milled again to give suitable shaping to the powder. Generally, an organic binder is incorporated into the powder, for giving sufficient strength to dry shapes, so that handling between shaping and sintering may not be difficult. One of the most important requirements of the binder is that it should be possible to remove the binder from the pressed shapes without any disruptive effect. Various shaping methods are:

a) Dry Pressing

b) Isostatic Pressing

c) Calendering
d) Extrusion
e) Jiggering
f) Injection Moulding
g) Silk Screening
h) Slip Casting
i) Band Casting

Among these different shaping techniques, in the present study dry pressing technique is used.

Dry Pressing

Dry pressing is used for giving small simple shapes to the calcined powder. It is carried out in a die having movable top. A cavity is formed at the bottom in lower portion. This cavity is filled with free flowing granulated powder and then it is struck with the top of the die. With the help of the top-punch, pressure in the range of 70-275 MPa is applied. A lot of care at various levels of mixing is needed while using this pressing technique, as samples prepared by this technique show the mechanical cracks after sintering. The next step of solid state reaction of materials is sintering.

2.2.2.1.5 Sintering

The calcined powder is then mixed with the binder solution and pressed into uniform and compact pellet form by using a hydraulic press. These pellets are further heated to a temperature below the melting point of the material to get the desired microstructures through the sintering process. The sintering temperature should always be higher than the calcination temperature so that the binder burns out during the sintering process. Sintering process transforms the pellet to a dense, strong, compact ceramic sample with closely packed grains. Therefore, sintering is a heating process for achieving more densified and strong polycrystalline ceramics from the green powder ceramics. The temperature and duration of sintering may vary depending upon the nature and properties of the ceramic samples used. During sintering, the particles join together to reduce the porosity present in the material without melting the powder. The science behind the joining of particles can be ascribed to the atomic diffusion in the solid state as shown in Fig. 2.1. Usually, this type of sintering is known as solid state sintering, which is the simplest case of sintering [7].

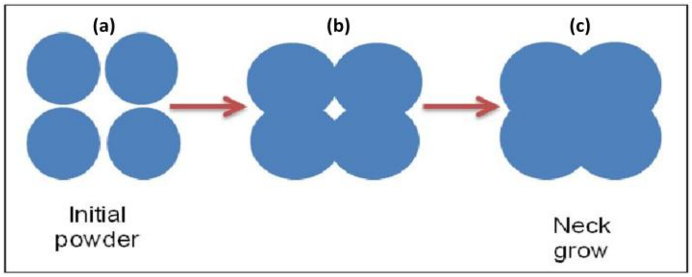

Fig. 2.1 Sintering process, (a) grains before sintering, (b) intermediate stage, (c) after sintering [7].

The reduction in the surface free energy of the particles provides the major driving force for sintering [13].

2.2.2.1.6 Electroding

The sintered pellets are polished by using a fine abrasive for achieving smooth and parallel surfaces. Generally, the sintered pellets are cleaned with the acetone and then coated with silver paste on both sides. The other conducting materials such as gold, platinum, etc can also be used as an electrode. After applying the silver paste, the samples fired in an oven for good adhesion purpose. Then the ceramic sample acts like as dielectric material between two metallic plates. The electroding of the samples can also be done by the deposition method using sputtering. After electroding the sample is ready for electrical measurements.

2.2.3 Synthesis of Ceramic-Polymer Composites

The fabrication methodology of a composite depends mainly on three factors: (i) the characteristics of constituent matrices and reinforcements, (ii) the shapes, sizes and engineering details of products and (iii) end uses. There are too many composite products and cover wide domain of applications. The fabrication technique varies from one product to the other. The matrix types (i.e., whether they are plastics, metals or ceramics) play a dominant role in the selection of a fabrication process. Similar process cannot be adapted to fabricate an engine blade made with fibre reinforced plastics and metal matrix composites. The process parameters may also have to be modified, even when one uses the same matrix type, but two different matrices. The process parameters like temperature, injection pressure and curing time vary from one method to the other.

The common methods of synthesis of polymer matrix composites include moulding methods like die mould, contact mould, filament winding and pultrusion, extrusion methods, casting, centrifugal casting, slip forming, wet lay-up and hot pressing, etc. In the present study, we have synthesized ceramic-polymer composites with PVDF matrix by hot press method and with epoxy matrix by cold press followed by hand lay-up techniques.

2.2.3.1 Hot Press Method

This process is also called compression molding or the matched die technique. In this process, the required volume fractions of both ceramic and polymer powders are stacked together and then placed between heated molds. This process is primarily used for making simple shapes such as flat laminates with constant thickness.

2.2.3.2 Hand lay-up Technique

Hand lay-up is the simplest and oldest open molding method of the composite fabrication processes. Glass or other reinforcing material or woven fabric or roving is positioned manually in the open mold, and resin is poured, brushed, or sprayed over and into the glass plies. Entrapped air is removed manually with squeegees or rollers to complete the laminates structure. RT curing polyesters and epoxies are the most commonly used matrix resins. Curing is initiated by a catalyst in the resin system, which hardens the fiber reinforced resin composite without external heat. For a high quality part surface, a pigmented gel coat is first applied to the mold surface.

2.3 Thermal Analysis

Thermal analysis is useful in studying the different properties of materials with reference to the change in temperature. The commonly used methods include differential scanning calorimetry (DSC), differential thermal analysis (DTA), dynamic mechanical analysis (DMA), thermo-optical analysis (TOA), thermo mechanical analysis (TMA) & thermogravimetric analysis (TGA). The conditions required for DSC & TGA analysis are identical.

2.3.1 Differential Scanning Calorimetry (DSC)

Differential scanning calorimetry (DSC) is a modern, more precise, sensitive, fast & reliable method used not only to measure the heat but also to measure the rate of flow of heat. DSC monitors the difference in the rate of heat flow to the sample and to a reference sample as a function of time and temperature in a controlled atmosphere [14]. During a change in temperature, DSC measures the heat quantity, which is radiated or absorbed excessively by the sample on the basis of a temperature difference between the sample and the reference material [14]. On the basis of the mechanism of operation, DSCs can be classified into two types: heat-flux DSCs and power-compensated DSCs [15]. In a heat flux DSC, the sample is enclosed in a pan and an empty reference pan is placed on a thermoelectric disk surrounded by a furnace [16]. The furnace is heated at a linear heating rate, and the heat is transferred to the sample and reference pan through the thermoelectric disk [17]. In a power-compensated DSC, the sample and reference pans are placed in separate furnaces heated by separate heaters [18]. The sample and reference are maintained at the same temperature, and the difference in thermal power required to maintain them at the same temperature is measured and plotted as a function of temperature or time [18].

2.3.2 Thermogravimetric Analysis (TGA)

Thermo gravimetric analysis (TGA) can be used to determine the materials thermal stability and volatility of the components by monitoring the weight change during heating of the specimen. The measurement is normally carried out in air or in an inert atmosphere, such as He/Ar, and the changes in weight is recorded as a function of increase of temperature of testing samples. Sometimes the measurement is performed in neon oxygen atmosphere to slow down the oxidation. Such analysis relies on a high degree of precision in three measurements: weight, temperature, and temperature change. The results from thermo gravimetric analyses are usually reported in the form of curves relating the mass lost from the sample against temperature. From this, the temperatures at which certain chemical processes begin and get completed are graphically plotted. TGA is commonly employed in research to determine degradation temperatures, absorbed moisture content of materials, the level of inorganic and organic components in materials, decomposition points of explosives, and solvent residues. It is also often used to estimate the corrosion kinetics in high temperature oxidation [19].

2.4 X-ray Diffraction (XRD)

X-ray diffraction (XRD) is an analytic non-destructive technique used to determine the structure, phase, crystallite size, percentage of crystallinity, micro-strain, crystal orientations, crystal defects, etc. In the year 1912, Max von Laue discovered that crystalline substances act as three-dimensional diffraction gratings for X-ray wavelengths. This is possible since the wavelengths of X-rays are of the order of the spacing of planes in a crystal lattice. Now-a-days XRD is a commonly used technique for the study of crystal structures and atomic spacing of a material. As the physical properties of solids (e. g., electrical, optical, magnetic, ferroelectric, etc.) depend on atomic arrangements of materials, determination of the crystal structure is a vital part of the characterization of materials.

X-ray diffraction peaks are produced by constructive interference of monochromatic beams of X-rays scattered at specific angles from each set of lattice planes in a sample. The peak intensities are determined by the atomic arrangements within the lattice planes. Consequently, the X-ray diffraction pattern is the fingerprint of periodic atomic arrangements in a given material. Generally X-rays are generated by a cathode ray tube, filtered to produce monochromatic radiation, collimated to concentrate, and directed toward the sample. The interaction of the incident rays with the sample produces constructive interference (and a diffracted ray) when conditions satisfy Bragg's law [20],

$$n\lambda = 2d\sin\theta \tag{2.1}$$

Where, 'n' is the order of diffraction, 'λ' is the wave-length of the X-rays used, 'd' is interplanar distance and 'θ' is the angle of incidence. The wavelength of the X-rays should be of the order of lattice spacing of the sample in order to produce diffraction peaks at specific angles. Fig. 2.2 shows the schematic diagram of the interaction of X-rays with crystal planes.

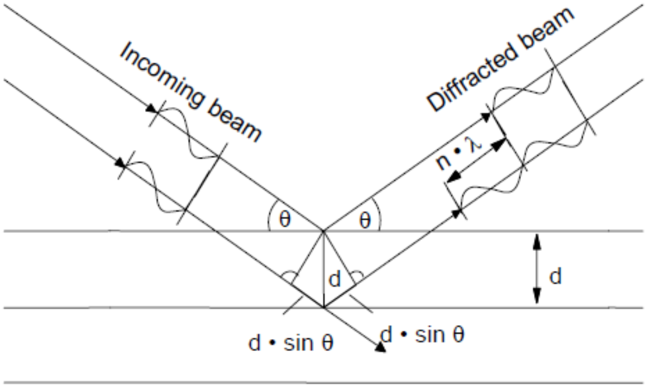

Fig. 2.2 Schematic diagram of interaction of X-rays with crystal planes [20].

The diffracted X-rays are detected and a plot of intensity as a function of the 2θ angle is obtained. This XRD pattern provides very useful information such as the d spacing of the lattice planes, which is directly related to the unit cell parameters, and the symmetry of the phase(s) present in the sample [21].

Miller indices of a plane are represented by hkl. The relation between (hkl) and crystal plane spacing (d) is given by

$$\frac{1}{d^2} = \frac{h^2}{a^2} + \frac{k^2}{b^2} + \frac{l^2}{c^2} \tag{2.2}$$

Where, a,b,c are the lattice parameters. By knowing the value of 'd', the lattice parameters can be calculated.

2.5 Ultraviolet-Visible Absorption Spectroscopy (UV-Vis) Study

The word "spectroscopy" implies to gain information about the compounds by using electromagnetic spectrum. Ultraviolet-visible absorption spectroscopy (UV-Vis) study reveals the measurement of the attenuation of a beam of light after it passes through a sample or after reflection from a sample surface in the spectral range of 190-900 nm, i.e. in the visible and ultraviolet regions of the spectrum.

When radiant energy impinges upon a sample, it may be absorbed, transmitted, or reflected. In spectrophotometery the absorbed light is determined. However, because of the difficulty of directly measuring the absorbed energy, the transmitted energy is measured and the amount absorbed is indirectly determined by subtracting the transmitted from the initial energy and by using the relationship $E = h\nu$, where E is the transition energy from the stable to excited state, h is the Planck's constant, and ν is the frequency. The energy of ultraviolet and visible radiation corresponds to that required for electronics transitions of the outer electrons. Since these are the valance electrons of the molecules or ions, the absorption spectra reflect the bonding characteristics of these particles. It is frequently impossible to obtain resolution of the numerous close absorption lines, and the plot of absorption vs wavelength yields a broad, smooth band spectrum.

If I is the intensity of the light passing through the sample, I_o is the intensity of light before it passes through the sample, then (I/I_o) is called the transmittance (%T). The absorbance is expressed as A = - log(%T/100%). And if R measures the intensity of light reflected from the sample, R_o is the intensity of light reflected from a reference material, then (R/R_o) is called the reflectance (%R).

UV-Vis spectroscopy is useful to characterize the absorption, transmission, and reflectivity of a variety of materials, such as pigments, coatings, windows, and filters, etc. This is also used in the determination of structure, the impurities present, molecular weight, presence or absence of functional groups and the qualitative & quantitative analysis of the compounds.

2.6 Scanning Electron Microscopy (SEM) Study

Scanning electron microscopy (SEM) technique is on the mainstay among the vital techniques used to reveal the information about the topography, morphology, compositions and crystallographic information of solid samples. The scanning electron microscope uses a focused beam of high energy electrons to produce the images of the sample surface by scanning in raster scan pattern with a spatial resolution greater than 1 nm. The data are collected over a selected area of the sample surface and a 2-dimensional image of the sample is generated. SEM can also be performed on the selected point locations on the sample.

The accelerated electrons in SEM carry significant amount of kinetic energy, which is dissipated to produce variety of signals due to the interaction of electrons with the atoms in the sample. The signals include secondary electrons (SE), back scattered electrons (BSE), characteristic X-rays, visible light and heat as shown in Fig. 2.3. The SEs are produced during ionization of atoms in the material due to incident electrons. BSEs are the electrons scattered either elastically or inelastically from the sample surface. The signals detected from secondary and backscattered electrons are commonly used for imaging samples. SEs are valuable for showing morphology and topography on samples and BSEs are most valuable for illustrating contrasts in composition in multiphase samples.

Another important point in SEM study is the sample preparation. The samples must be electrically conductive because the non-conductive samples get charged when scanned by the electron beam and detect faults in the secondary electron imaging mode. So the non-conducting samples are coated with a thin layer of electrically conducting material deposited on the sample surface either by low vacuum sputtering or by high vacuum evaporation. The conducting material used for specimen coating include gold/ palladium alloy, graphite, platinum, tungsten, osmium, iridium, chromium, etc. Alternatively, an electrically insulating sample can be examined without a conductive coating in an instrument capable of "low vacuum" operation. SEM analysis is considered as a "non-destructive" technique as the x-rays generated by electron interactions do not lead to volume loss of the sample. So the same material can be used to analyze repeatedly [22,23].

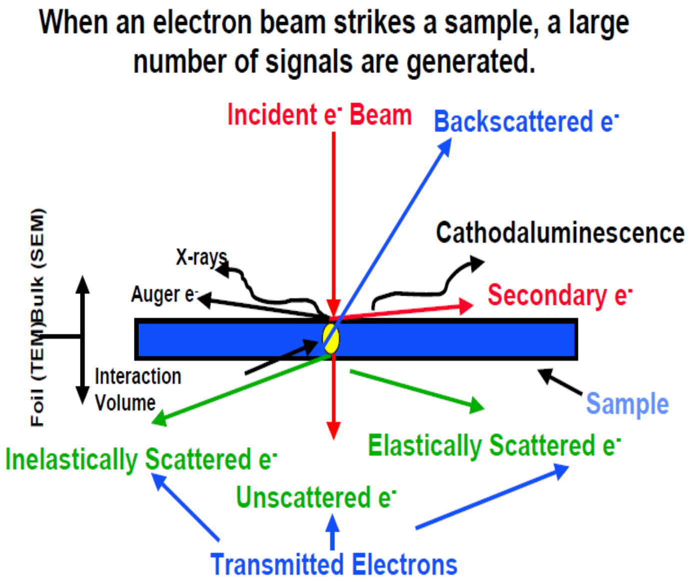

Fig. 2.3 Interaction of the electron beam with a sample [22].

2.6.1 Energy Dispersive X-ray Analysis (EDX)

EDX analysis technique is a commonly used technique in conjunction with SEM instrument to determine the chemical composition of the material. EDX analysis is based on the principle that each element has a unique atomic structure allowing unique set of peaks on its X-ray spectrum [24]. When an electron beam with energy of ~10-20 keV strikes the material, X-rays are emitted along with other electromagnetic radiations. These X-rays are generated from the atoms present in a region of material surface to a depth of 2 microns. These X-rays are detected by suitable detectors and the signals are analyzed to know the chemical composition. The limitation of EDX analysis is that elements with low atomic number (<11) cannot be detected.

2.7 Density & Porosity Measurements

For measuring the experimental bulk density of the ceramics/composite samples Archimedes principle was used.

The formulas employed for the calculation of the density & apparent porosity of the ceramic samples are as follows:

$$\text{Density} = \left[\frac{\text{Dry weight}}{\text{Soaked weight} - \text{Suspended weight}}\right] * \text{Density of the liquid used} \qquad (2.3)$$

$$\text{Apparent Porosity} = \frac{(\text{Soaked weight} - \text{Dry weight})}{(\text{Soaked weight} - \text{Suspended weight})} \qquad (2.4)$$

To measure dry weight, the sintered samples were first heated to 100°C to avoid the moisture content in the samples. Then the weights of the samples were measured by a digital electronic balance. For measuring the soaked weight, the samples were put in a beaker with kerosene oil. Kerosene oil is used as it has better wetting capacity compared to water, easier for drying and suitable for hygroscopic materials. The beaker containing the samples dipped in kerosene oil was kept in a desiccator attached with a suction pump. As the air is sucked out by the pump, vacuum is created and air trapped pores of the samples are replaced by kerosene showing bubbling. When there were no more bubbles coming out of the sample, the suction pump was stopped and the vacuum was slowly released. Then the beaker was taken out of the desiccator. The soaked weight of the samples were measured by the digital electronic balance. The suspended weight of the samples were measured by suspending the samples in kerosene oil with the help of a specially designed light weight hanging pan for holding the samples inside the kerosene oil. The experimental density and porosity of the ceramic samples was calculated by using the above formulas. The given Archimedes relation cannot account the porosity of ceramic-polymer composites due to closed pores. The porosity due to the closed pores of ceramic-polymer composites can be accounted by non-destructive techniques (NDTs).

We can also use the following formulae for calculating the density, porosity and relative density of the composite samples.

$$\rho_{cal} = \rho_f V + \rho_m (1 - V) \qquad (2.5)$$

$$P = 1 - \frac{\rho_{mea}}{\rho_{cal}} \quad (2.6)$$

$$\rho_{rel} = 1 - P \quad (2.7)$$

Where, ρ_f is the density of the filler (ceramic), ρ_m is the density of the matrix (polymer), V is the volume fraction of the filler, P is the porosity of the composites and ρ_{rel} is the relative density of the composite samples.

The experimental density can be compared with the theoretical density for better application point of view. The theoretical density can be determined by using the lattice parameters from XRD. The formula for calculating the theoretical density is as follows,

$$\rho_{th} = \frac{\sum A}{NV} \quad (2.8)$$

Where, A = nM, n is the number of atoms per unit cell and M is the atomic weight. N is the Avogadro's number and V is the volume of the unit cell. The experimental density of the sample is always less than the theoretical density as the macroscopic samples contain some cracks and pores.

2.8 Dielectric measurements

A dielectric material measurement provides the critical design parameter information for many electronic applications. The aim of dielectric measurements is to report the relative permittivity of a specimen under test for a specified orientation of electric field and frequency.

2.8.1 Dielectric Polarization

When electric field is applied to a parallel plate capacitor containing dielectric, then there will be separation of charges. This process is called polarization. Mathematically, polarization of a dielectric material is defined as dipole moment per unit volume and is given as

$$P = \propto E \quad (2.9)$$

Where, P is the polarization of the material under an applied external electric field E and $\propto$ is the polarizability of the dielectric material. Dielectric study of the materials generally deals with four major kinds of polarizations [25]. The overall polarizability, $\propto$, of a material is made up of four contributions:

$$\propto = \propto^e + \propto^i + \propto^d + \propto^f \tag{2.10}$$

Where, $\propto^e$ = Electronic polarizability, $\propto^i$ = Ionic polarizability, $\propto^d$ = Dipolar polarizability and $\propto^f$ = Interfacial polarizability. Different polarization mechanism is as shown in the Fig. 2.4.

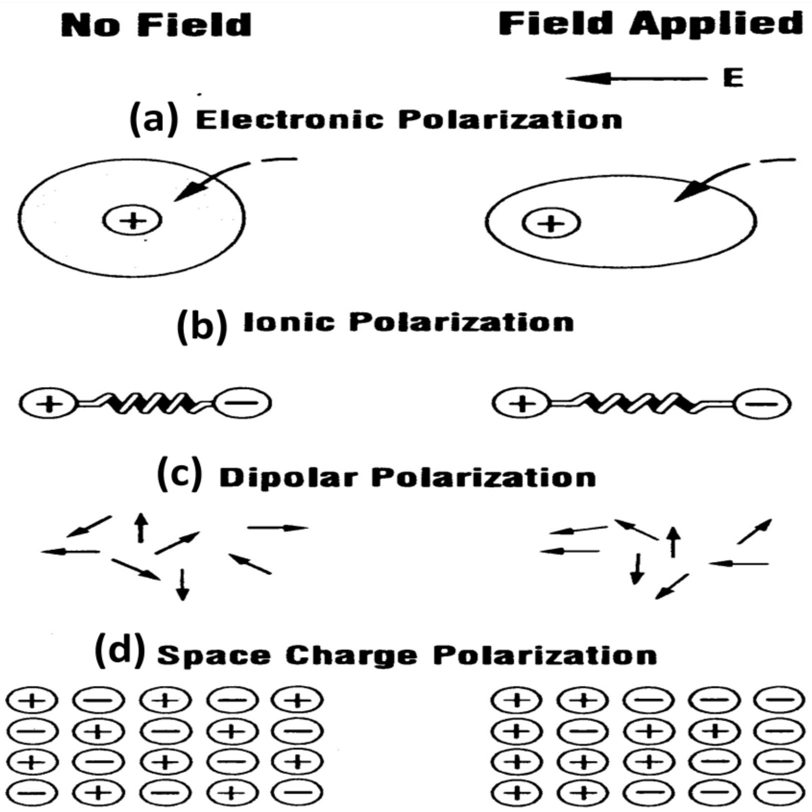

Fig. 2.4 Different polarization mechanisms; (a) electronic polarization, (b) ionic polarization, (c) dipolar polarization & (d) interfacial/space charge polarization [25].

2.8.1.1 Electronic Polarization

Electronic polarization arises due to the relative displacement of the centres of +ve charges with respect to the centres of –ve charges of an atom or ion when subjected to an external electric field. It is generally temperature independent. This type of polarization is active in the visible-ultraviolate frequency range, i.e. ~ 10^{15}-10^{16} Hz.

2.8.1.2 Ionic or Atomic Polarization

Ionic polarization arises due to the relative displacement of positive and negative ions from the equilibrium positions in an ionic crystal under an applied electric field. When an electric field is applied to an ionic material, cations and anions get displaced in opposite directions giving rise to a net dipole moment. Ionic polarization causes both ferroelectric transition and dipolar polarization. The transition, which is caused by the order of the directional orientations of permanent dipoles along a particular direction, is called order-disorder phase transition. The transition which is caused by ionic polarizations in crystals is called displacive phase transition. Since the entire ions which are heavier than electrons are displaced this mechanism is only active up to 10^{12}-10^{13} Hz (Infra-red frequencies). This mechanism is also temperature independent.

2.8.1.3 Dipolar Polarization

Dipolar polarization can either be inherent to polar molecules (orientation polarization), or can be induced in any molecule in which the asymmetric distortion of the nuclei is possible (distortion polarization).

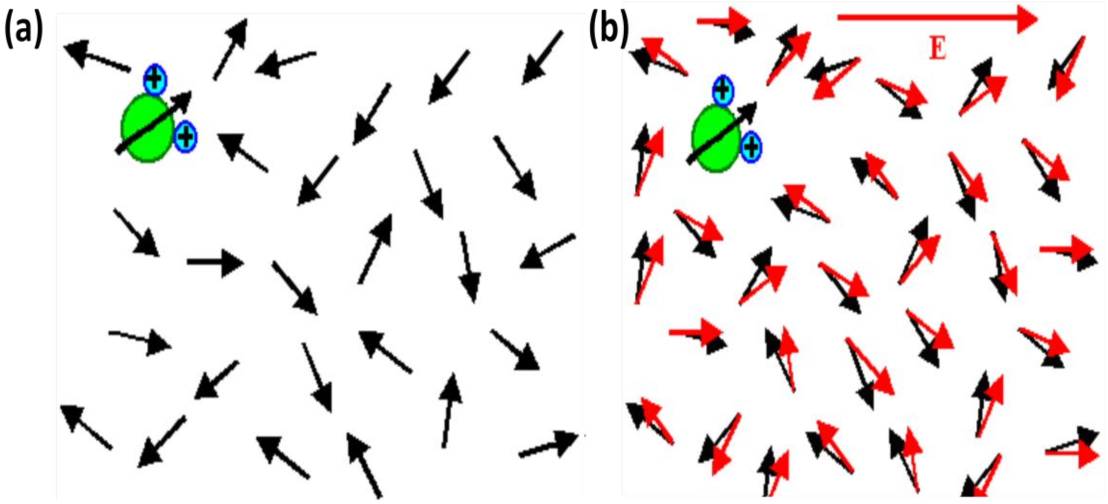

Fig. 2.5 Schematic diagram of the dipolar orientation process (a) without field**,** (b) with field [26].

In zero fields, the permanent dipoles will be randomly oriented and the system has nonet polarization. But an externally applied electric field will tend to align the dipoles and the material will acquire a net polarization, which is known as orientational polarization. Schematic diagram of the dipolar orientation process is shown in the Fig. 2.5.

Due to the randomizing effect of the thermal vibrations this type of polarization is more effective at low temperatures and decreases with the increase in temperature. Dipolar polarization is frequency dependent, and can follow the oscillations of the electric field up to 10^{11} Hz [26].

Frequency ranges of different polarizations is given in Fig. 2.6.

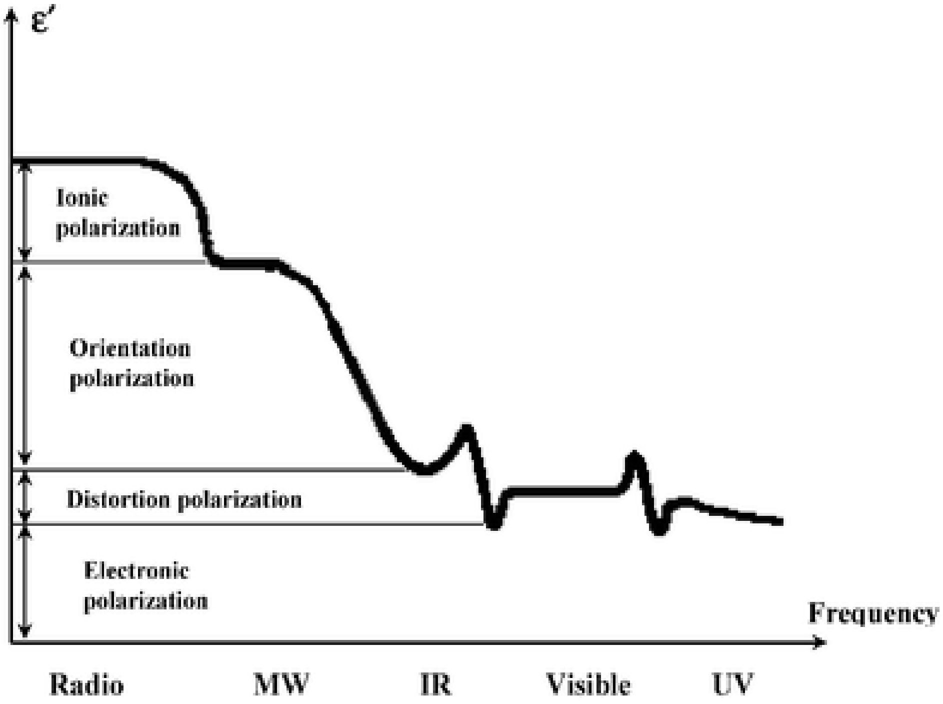

Fig. 2.6 Frequency ranges of different polarizations [27].

2.8.1.4 Interfacial or Space Charge Polarization

In polycrystalline materials, the inter-grain boundaries are zones, where free charges (interstitial ions, vacancies, injected electrons etc.) may accumulate and cause polarization of the crystallites, which is known as interfacial polarization. The notion of interface polarization is related to separate surfaces between crystallites, which act as barriers to the motion of free charges from one crystallite to the other and is a characteristics of polycrystalline materials [27]. Interfacial polarization is prominent in low frequency (10^{-3}-10^{3} Hz) and high temperature range. It is active in low frequency region, and as the frequency is increased, the time required for the interfacial charges to be polarized is delayed. At high temperatures the increase of defect or impurities gives rise to interfacial polarization.

2.8.2 Dielectric Properties

The studies of the dielectric properties provide a great deal of information about the applicability of the ferroelectric materials in various applications. For most applications of ferroelectric materials, the dielectric constant (ε_r) and dielectric loss ($\tan\delta$) are important practical parameters.

2.8.2.1 Dielectric Constant (ε_r)

The relative dielectric constant (ε_r) of a material is the ratio of the charge stored on an electroded slab of the material brought to a given voltage to the charge stored on a set of identical electrodes, separated by vacuum. Mathematically, it is defined as

$$\varepsilon_r = 1+P/\varepsilon_0 E \qquad (2.11)$$

Where, ε_r = Dielectric constant or relative permittivity of the material

E = Net electric field in the presence of dielectric material

P = Induced dipole moment / volume under an applied electric field E

ε_0 = Permittivity of the free space

And, for an alternating electric field, the dielectric constant can be written as

$$\varepsilon_r = \varepsilon' - i\varepsilon'' \qquad (2.12)$$

Where ε' is the real component of the dielectric constant/ relative permittivity, in phase with the applied external field E. ε'' is the imaginary component, 90^{o} out of phase with the applied external electric field, caused by either resistive leakage or dielectric absorption. For normal substances, the value of ε_r is low, usually under 5 for organic materials and under 20 for most inorganic solids. Ferroelectric ceramics, however generally have much higher ε_r, typically several hundred to several thousand [28].

2.8.2.2 Dielectric Loss (tanδ)

In ideal dielectrics, the charging current leads the applied voltage by Π/2 radians. However, in real dielectrics in addition to the charging current, associated with the storage of electric charge by the dipoles, a loss current must also be considered. The loss current arises from the long-range migration of charges, e.g., dc ohmic conduction and the dissipation of energy associated with the rotation or oscillation of dipoles [28]. As there is no dielectric which is a perfect insulator (is not loss free), it is generally represented by a complex dielectric constant. The total current in the real dielectric is a complex quantity which leads the voltage by an angle (90-δ), where δ is called the loss angle. Dielectric loss (tanδ), also known as dissipation factor, is defined as $\tan\delta = \varepsilon''/\varepsilon'$. The inverse of the loss tangent, $Q = (1/\tan\delta)$, is used as a figure of merit in high frequency piezoelectric applications.

2.8.2.3 Curie Temperature (T_c)

Curie temperature (T_c) is the temperature above which the spontaneous polarization (Ps) of the ferroelectric materials vanishes and the material goes into paraelectric state. A ferroelectric crystal undergoes a structural phase transition from a ferroelectric (non-centrosymmetric) to paraelectric phase (symmetric) at this temperature and above T_c the material does not exhibit ferroelectricity. Thermodynamic properties including dielectric, elastic, optical and thermal constants show an anomalous behavior near the vicinity of T_c, [29]. If there are two or more ferroelectric phases present in a material, the Curie point only specifies the temperature at which a ferroelectric - paraelectric phase transition occurs.

2.8.2.4 Phase Transitions

In case of ferroelectric materials, the spontaneous polarization, P_s, decreases with the increase in temperature and becomes zero at T_c. At T_c, transition takes place from ferroelectric phase to paraelectric phase. If this transition is a discontinuous change in P_s at T_c, then phase transition is known as first order phase transition. However, if P_s becomes zero gradually with temperature, then the transition is called second order phase transitions [28]. The first & second order phase transitions are shown in Fig. 2.7 [30].

2.8.2.5 Diffuse Phase Transition (DPT)

In case of macroscopic homogeneous materials, the observed transition temperature is not sharply defined. A diffuse phase transition (DPT) is generally characterized by broadening in ε_r

vs temperature curve. The most remarkable examples of DPT are found in ferroelectric materials.

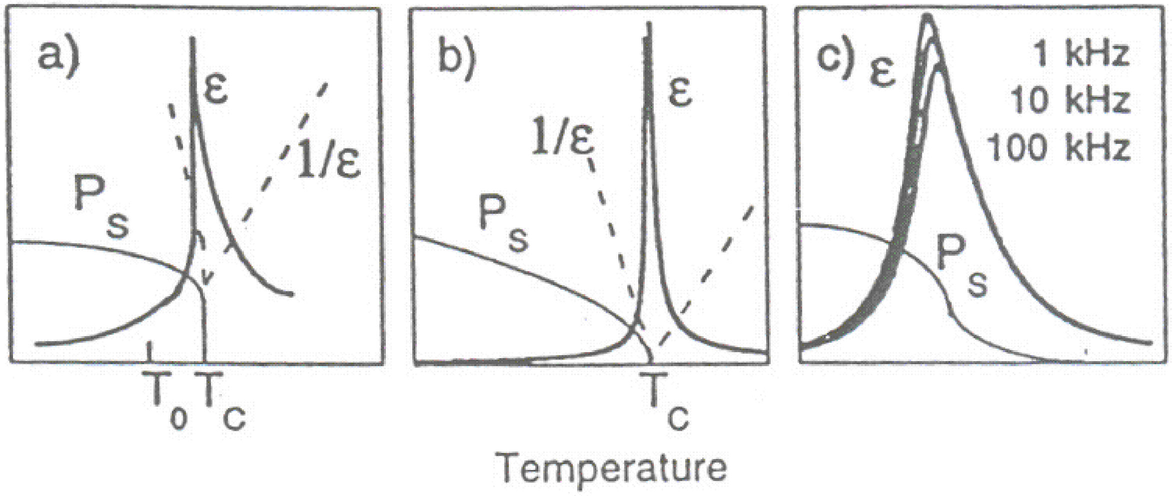

Fig. 2.7 Ferroelectric phase transition behaviors (a) first order, (b) second order, and (c) relaxor type [30].

The diffuseness of the phase transition is assumed to be due to the occurrence of fluctuations in a relatively large temperature interval around the phase transition temperature. Usually here two kinds of fluctuations are considered: (a) compositional fluctuation and (b) polarization (structural) fluctuation. From the thermodynamic point of view, it is clear that the compositional fluctuation is present in ferroelectric solid solutions and polarization fluctuation is due to the small energy difference between high and low temperature phases around the transition temperature. This small entropy difference between ferroelectric and paraelectric phases will cause a large probability of fluctuation. According to Fritsberg, *et al.* substances of less stability are expected to have a more diffuse transition [31]. For relaxor as well as other FDPT, the width of the transition region is mainly important for practical applications. Complex perovskite type ferroelectrics with distorted cation arrangements show DPT which is characterized by a broad maximum for the temperature dependence of dielectric constant (ε_r) and dielectric dispersion in the transition region. For DPT, ε_r follows modified temperature dependence Curie Weiss law [32-34].

$$\frac{1}{\varepsilon'} - \frac{1}{\varepsilon_m} = (T - T_m)^{\gamma}/C' \tag{2.13}$$

Where, T_m is the temperature at which ε_r reaches maximum (ε_m), C is the modified Curie constant and γ is the critical exponent. The γ factor explains the diffusivity of the materials, which lies in the range $1<\gamma<2$. In case of γ equals to unity, normal Curie–Weiss law is followed and it shows the normal ferroelectric phase transition [35]. Whereas on the basis of a local compositional fluctuation model, the value of $\gamma=2$ corresponds to a completely diffused system [36]. For systems exhibiting intermediate value of diffusivity ($1\leq\gamma\leq2$) the materials are complex, hence partially disordered.

2.8.3 Ferroelectric Domains

Ferroelectric domains are the regions of uniformly oriented spontaneous polarization within the material. Onset of the spontaneous polarization at T_c, leads to the formation of surface charge. These surface charges produce an electric field, called depolarizing field, E_d. The depolarizing field may be very strong of the order of several kV/cm, rendering the single–domain state of the ferroelectric energetically unfavorable [37,38]. The electrostatic energy associated with the depolarizing field may be minimized if

(i) The ferroelectric splits into domains with oppositely oriented polarization.

(ii) The depolarizing charge is compensated for by electrical conduction through the material or by charges from the material surrounding.

Splitting of a ferroelectric crystal into domains may also occur due to the influence of mechanical stresses [39].

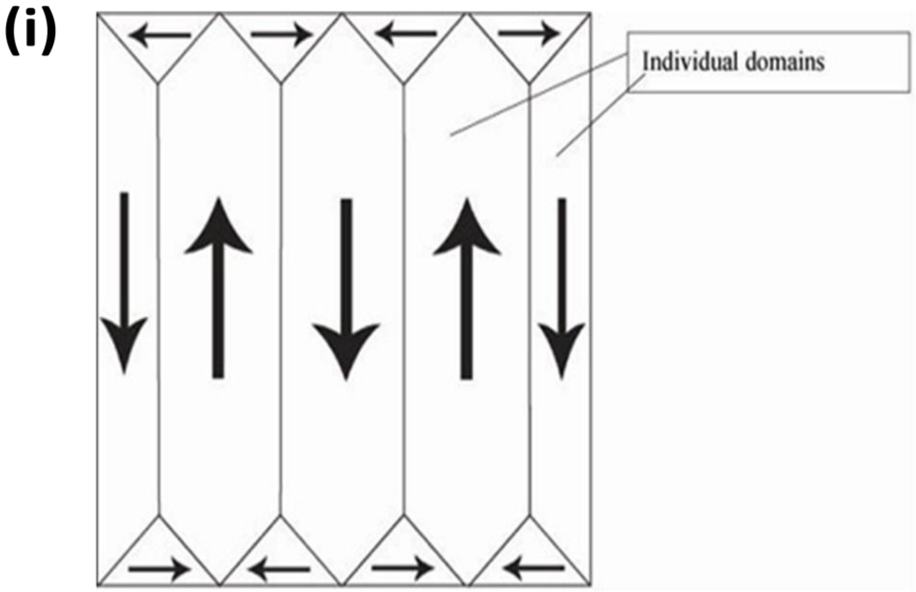

(ii)

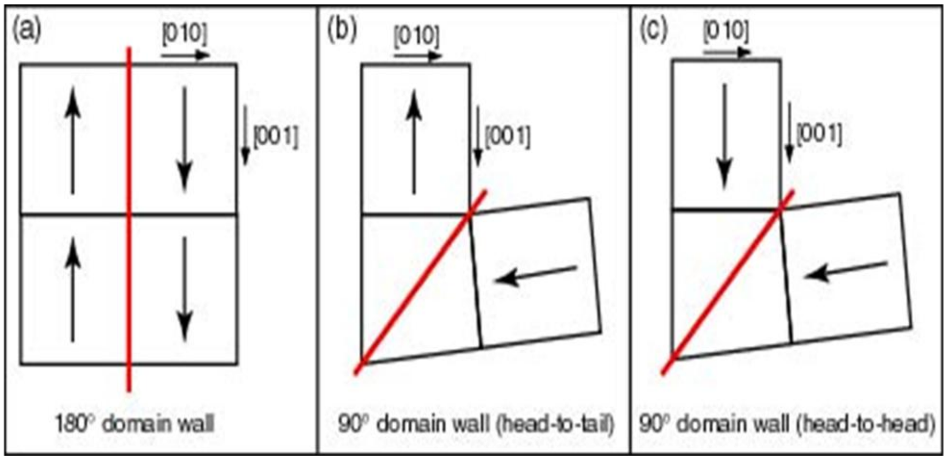

Fig. 2.8 Ferroelectric (i) individual domains and (ii) domain walls [40,41].

The walls, which separate domains with oppositely oriented polarization, are called 180^{o} walls and those, which separate regions with mutually perpendicular polarization, are called 90^{o} walls [40]. 180^{o} and 90^{o} domain walls are shown in Fig. 2.8 [41]. Both 90^{o} and 180^{o} walls may reduce the effects of depolarizing fields but only the formation of 90^{o} walls may minimize the elastic energy [41]. 90^{o} domain wall motion results in large deformation and their movements require higher fields. The types of domain walls that can occur in a ferroelectric material depend on the symmetry of both the non-ferroelectric and ferroelectric phases of the material. Ferroelectric domain walls are much narrower than domain walls in ferromagnetic materials.

2.8.4 Polarisation vs Electric field (P-E) Loop

Polarization vs electric field hysteresis is one of the defining properties of ferroelectric materials. We know that ferroelectricity is the property of certain materials that have a spontaneous polarization that can be reversed by the application of an external electric field [42]. The parameters spontaneous polarization, remanent polarization and coercive field can be measured from the P-E loop by using the principle of Sawer-Tower circuit [43].

The P-E hysteresis loop of a ferroelectric material is as shown in the Fig. 2.9. First when we are applying a small ac field, the polarization increases linearly with the field amplitude and the field is not strong enough to switch the domains with the unfavourable direction of the polarization. With the increase in the field, the polarization of domains starts to switch in the direction of applied field and rapidly increasing the measured charge density. The polarization reversal takes place by the growth of existing anti-parallel domains, by domain-wall motion [40, 41]. In this region, the polarization response is strongly nonlinear and once all the domains are aligned, the ferroelectricity again behaves linearly. With the decrease in field strength, some domains back–switch, but at zero field the polarization is non zero and to reach a zero polarization state, the field must be reversed. With the further increase of the field in the negative direction, there will be new alignment of dipoles and saturation. The field strength is then reduced to zero and reversed to complete the cycle. The value of polarization at zero fields is called the remnant polarization, P_r, and the field necessary to bring polarization to zero is called the coercive field, E_c. The spontaneous polarization, P_s, is usually taken as the intercept of the polarization axis, tangent to the saturated polarization.

An ideal hysteresis loop is generally symmetrical. But the switching mechanism depends upon many factors, the nature of the ferroelectric material used, types of electrodes used, thickness of the sample, temperature, field profile and the number of field cycles, etc [44].

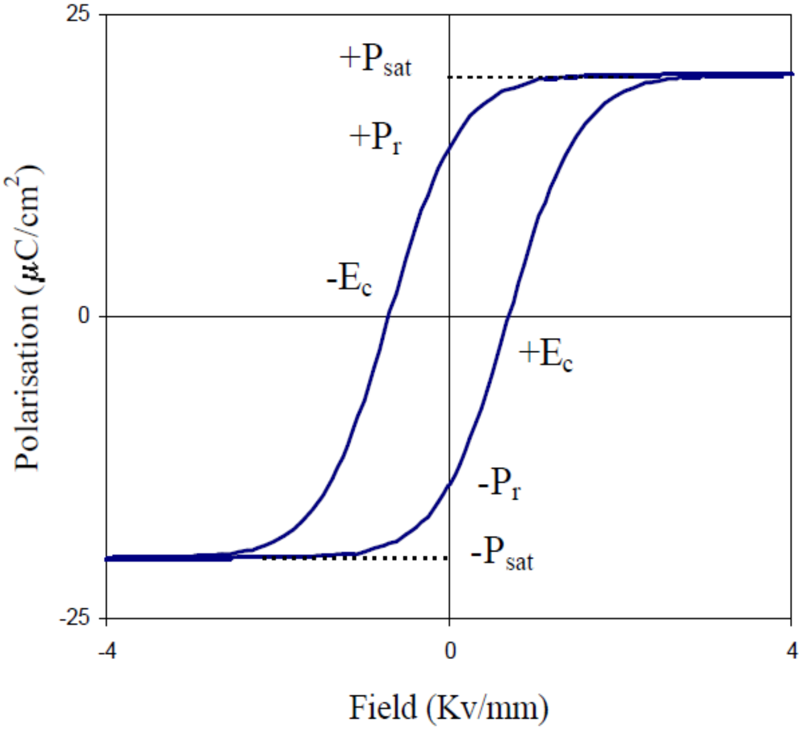

Fig. 2.9 P-E hysteresis loop [42].

2.8.5 Poling

Activation of the piezoelectric ceramic properties on a macroscopic level occurs during the “poling” process. Poling is defined as a process during which a high electric field is applied on the ferroelectric ceramic samples for a short period of time to force the randomly orientated domains to reorient in the direction of the applied electric field [45]. Different steps of poling of a ferroelectric material are shown in Fig. 2.10.

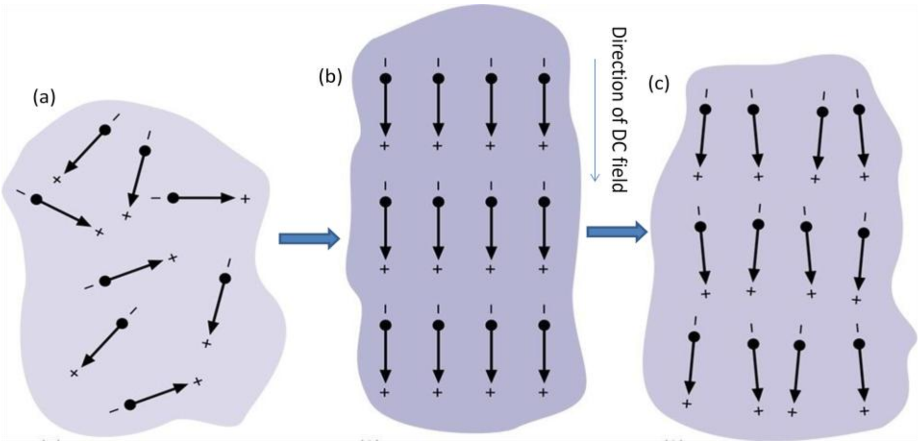

Fig. 2.10 Electric dipole moments in domains (a) before poling, (b) during poling and (c) after poling [45].

Ferroelectric materials possess uniform polarization regions known as ferroelectric domains. Within a domain, all the electric dipoles are aligned in the same direction. The crystals may possess many domains, which are separated by boundaries called domain walls. Adjacent domains may have different polarization vectors either in anti-parallel directions or at right angles. Accordingly, there are 180^o or 90^o domain walls.

Before poling, ferroelectric ceramics do not possess piezoelectric properties due to the random orientation of ferroelectric domains in the ceramics. During poling, a high DC electric field is applied on the ferroelectric samples to force the domains to be oriented. After poling, the electric field is removed and a remanent polarization and strain is maintained in the sample and the sample exhibits piezoelectricity [28].

2.8.6 Piezoelectric Co-efficients

2.8.6.1 Piezoelectric Charge Co-efficient (d_{33})

There are two types of piezoelectric effects, direct and converse piezoelectric effects. Piezoelectric coefficients can be measured using either direct piezoelectric effect or converse piezoelectric effect. Piezoelectric coefficients using direct piezoelectric effect measure the charge on the electrode, while piezoelectric coefficients using converse piezoelectric effect measure the strain in the ferroelectric materials.

The equations for the direct and converse piezoelectric effects are given below:

$$\mathrm{D} = \mathrm{dT} \text{ (Direct piezoelectric effect)} \tag{2.14}$$

$$\mathrm{S} = \mathrm{dE} \text{ (Converse piezoelectric effect)} \tag{2.15}$$

Where, “d” is piezoelectric charge coefficient, “D” is the dielectric displacement, “T” is the mechanical stress, “E” is the electric field and “S” is the mechanical strain, respectively.

The piezoelectric coefficient is direction dependent. d_{33} is the piezoelectric constant when the direction of the applied stress is along the direction of the faces of the ceramic on which charges are developed and is shown in the Fig. 2.11 [37]. d_{33} is measured in Coulomb/Newton (C/N).

High d_{33} constant is desirable for materials intended to develop motion or vibration, such as sonar or ultrasonic cleaner transducers [28]. Piezoelectric constants and strain induced by electric field behavior is desired for actuator applications [45].

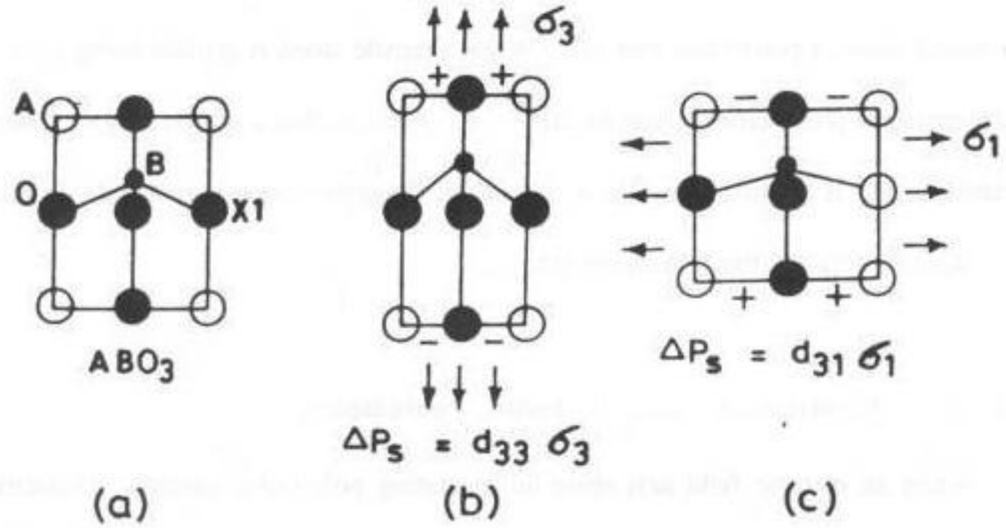

Fig. 2.11 (a) A two dimensional view of the perovskite structure (ABO_3) showing the displacement of B-ions in the x3 direction, (b) The ame structure with a tensile stress $\sigma 3$ applied along x3, and (c) A tensile stress $\sigma 1$ applied along x1 [37].

References

[1] T. Yamamoto, Am. Ceram. Soc. Bull. 71, (1992) 978.

[2] G. Arlt, Ferroelectrics. 104, (1990) 217.

[3] K. C. Patil. Chemistry of Nanocrystalline Oxide Materials-Combustion Synthesis, Properties and Applications (World Scientific Publishing Co. Pte. Ltd. 2008).

[4] C. B. Carter and M. G. Norton, Ceramic Materials: Science and Engineering (Springer. 2007).

[5] W. A. Bonner and G. J. Zydzik, J. of Crystal Growth. 7, (1970) 65.

[6] T. A. Ring, Fundamentals of Ceramic Powder Processing and Synthesis (Chapter- II, PP. 81, 1985).

[7] M. N. Rahaman, Ceramic Processing and Sintering (Second Edition, 2003).

[8] A. K. Jonscher, Journal of Physics D: Applied Physics. 32, (1999) 57.

[9] M. E. Lines and A. M. Glass, Principles and Applications of Ferroelectrics and Related Materials. (Clarendon Press, Oxford, 1977).

[10] A. J. Moulson and J. M. Herbert, Electroceramics: Materials, Properties and Application. (Chapman and Hall, 1990).

[11] G. C. C. da Costa, A. Z. Simoes, A. Ries, C. R. Foschini, M. A. Zaghete, and J. A. Varela, Mater. Lett. 21, (2004) 414.

[12] A. R. West, Solid State Chemistry and its Applications. Wiley and Sons, (2005).

[13] M. W. Barsoum, Fundamentals of Ceramic. McGraw-Hill Companies,Inc. International Edition, (1997).

[14] B. Wunderlich, Thermal Analysis (New York: Academic Press. pp. 137, 1990).

[15] P. Gill, T. T. Moghadam and B. Ranjbar, J Biomol Tech. 21, (2010) 167.

[16] P. J. Haines, M. Reading and F. W. Wilburn, Differential thermal analysis and differential scanning calorimetry. In Brown ME, editor. (ed): Handbook of Thermal Analysis and Calorimetry (Vol 1 The Netherlands: Elsevier Science BV. 279, 1998).

[17] R. L. Danley, Thermochim Acta. 395, (2002) 201.

[18] N. Zucca, G. Erriu, S. Onnis and A. Longoni, Thermochim Acta. 143, (2002) 117.

[19] J. D. Menczel and R. Bruce Prime. Thermal analysis of polymers, fundamentals and applications (John Wiley & Sons, Inc., Hoboken, New Jersey, 2009).

[20] L. E. Smart and E. A. Moore, Solid State Chemistry (Taylor & Francis, London 2005).

[21] A. R. West, Basic Solid State Chemistry (John Wiley & Sons, New York, 1999).

[22] E. Suzuki, J. of Microscopy. 208, (2002) 153.

[23] G. I. Goldstein, D. E. Newbury, P. Echlin, D. C. Joy, C. Fiori, E. Lifshin, Scanning electron microscopy and x-ray microanalysis (Plenum Press, New York 1981).

[24] J. Goldstein, D. Newbury, D. Joy, C. Lyman, P. Echlin, E. Lifshin, L. Sawyer and J. Michael, Scanning Electron Microscopy and X-ray Microanalysis (Kluwer Academic / Plenum Publishers, New York, 2002).

[25] I. Bunget and M. Popescu, Physics of Solid Dielectrics (Elsevier, New York, 1984).

[26] M. Ugine Prince and S. Perumal, Archives of Applied Science Research. 4, (2012) 508.

[27] L. L. Hench, J. K. West, Principles of Electronic Ceramics (John Wiley & Sons, New York 1989).

[28] B. Jaffe, W. Cook and H. Jaffe, Piezoelectric Ceramics (Academic Press, London, 1971).

[29] Y. Xu, Ferroelectric Materials and Their Applications (Elsevier Science Pub. Co. New York, USA, 1991).

[30] L. E. Cross, Ferroelectrics, 76**,** (1987) 241.

[31] G. H. Jonker, Mater. Res. Bull., 18, (1983) 301.

[32] J. Fritesberg, Proc. 4th Int. Meeting on Ferroelectricity, Leningrad (1977).

[33] J. Hao, Z. Xu, R. Chu, W. Li, G. Li, and Q. Yin, J. Alloy. Compd. 484, (2009) 233.

[34] X. G. Tang, J. Wang, X. X. Wang, and H. L. W. Chan, Solid State Commun. 131, (2004) 163.

[35] B. Tilak, American Journal of Materials Science. 2, (2012) 110.

[36] A. Shukla and R. N. P. Choudhary, Physica B: Condensed Matter. 405, (2010) 2508.

[37] G. H. Haertling, J. Am. Ceram. Soc. 82, (1999) 797.

[38] J. C. Burfoot and G. W. Taylor, Polar Dielectrics and Their Applications (London: Macmillan, 1979).

[39] G. Arlt, J. Mater. Sci. 25**,** (1990) 2655.

[40] S. Stemmer, S. K. Streiffer, F. Ernst and M. Ruhle, Phil. Mag. A. 71, (1995) 713.

[41] R. E. Newnham, Structure–Property Relations (Berlin: Springer 1975).

[42] G. H. Haertling, J. Am. Ceram. Soc. 50**,** (1967) 329.

[43] C. B. Sawyer and C. H. Tower, Phys. Rev. 35**,** (1930) 269.

[44] V. Shur and E. Rumyantsev, J. Korean. Phys. Soc. 32, (1988) S727.

[45] S. E. Park, T.R. Shrout, J. Appl. Phys. 82**,** (1997) 1804.

******

Chapter – 3

EXPERIMENTAL DETAILS

3.1 Introduction

This chapter describes the various steps involved in the synthesis of the ceramics and composites selected for the present work. The details about the instruments used for the various characterizations of the samples are also given in detail.

3.2 Sample Preparation

This section comprises the details of the methods used for the preparation of ceramics and composites systems by different processing techniques.

3.2.1 Preparation of Ceramic Samples

3.2.1.1 (BZT-BCT) System by Solid State Reaction (SSR) Route

The following series of (BZT-BCT) ceramic systems were synthesized by conventional solid state reaction route:

i. $x[Ba(Zr_{0.2}Ti_{0.8})O_3]$-$(1-x)[(Ba_{0.7}Ca_{0.3})TiO_3]$/(BZT-BCT) where, x = (0.48, 0.50, 0.52)

The various steps involved in conventional processing of the above mentioned ceramics are represented as a flow chart and shown in Fig. 3.1.

For synthesis of (BZT-BCT) ceramic samples, barium carbonate ($BaCO_3$, 99% purity), zirconium dioxide (ZrO_2, 99.5% purity), calcium carbonate ($CaCO_3$, 98.5% purity) and titanium dioxide (TiO_2, 99% purity) were used as precursors. All the raw powders were weighted according to stoichiometry and mixed. The mixed powders were ball milled with acetone for 8 h, using zirconia balls as the grinding media. After grinding, the thermal decomposition and crystallization of the samples were investigated by differential scanning calorimeter (TGA-DSC, STA449C, NETZSCH) to know about the calcination temperature. The calcination was carried out at 1300^{o}C for 4 h. Single perovskite phase formation was confirmed by X-ray diffraction (XRD) study. XRD analysis was performed using Philips X'PERT System X-Ray Diffractometer (PW 3020, Phillips, Eindhoven, The Netherlands) with

Cu K_α radiation (λ = 1.5405 A°). The calcined powders were thoroughly mixed with 2 wt% polyvinyl alcohol (PVA) binder solution and then pressed into disks of diameter ~10 mm and a thickness ~1.5 mm under ~ 60MPa pressure. The sintering of the samples was carried out at 1300, 1350 and 1400^{o}C for 6 h with a heating rate of 5^{o}C/min. For each composition of the ceramics, the sintering temperature was optimized to achieve better density.

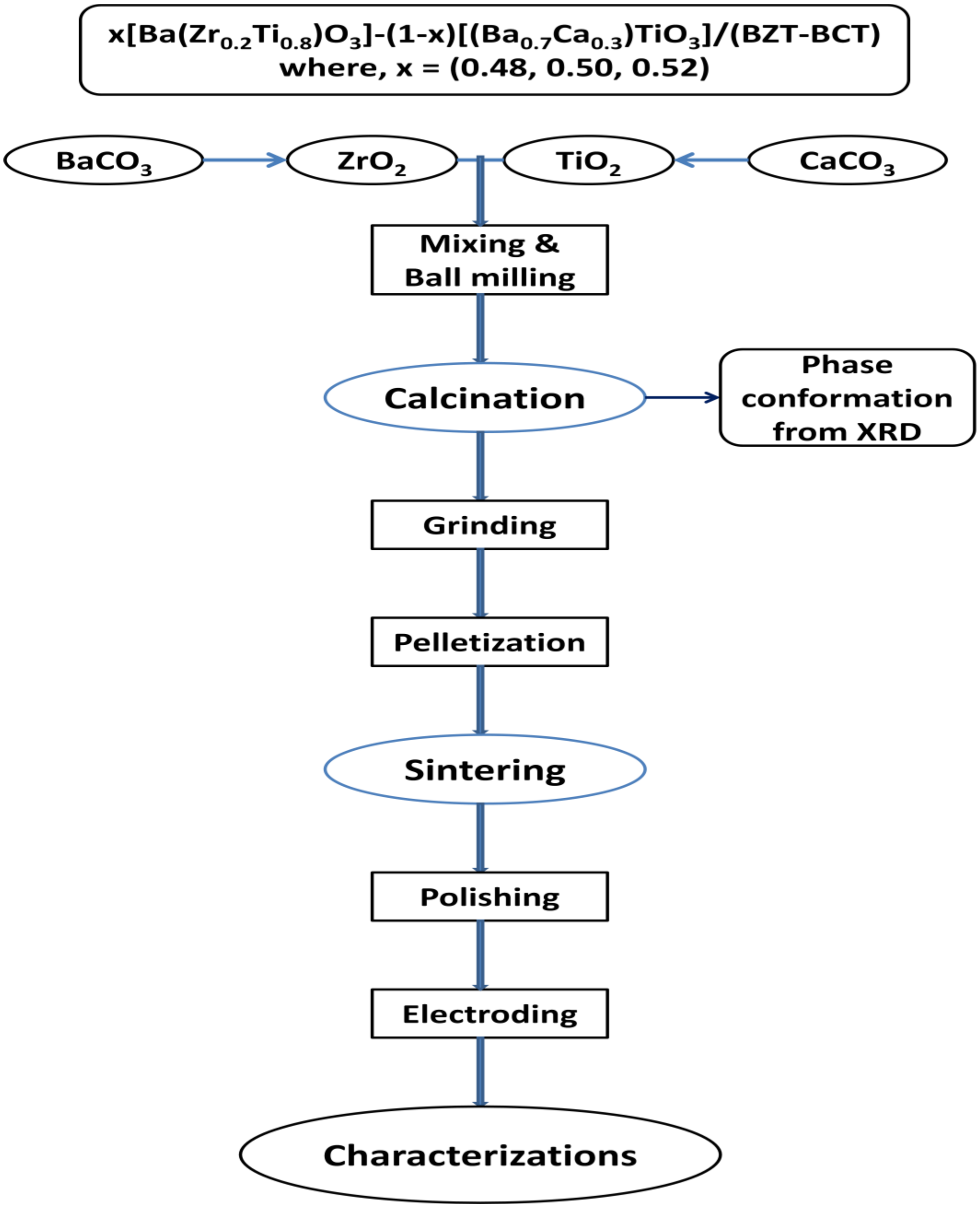

Fig. 3.1 Flow chart of synthesis of (BZT-BCT) system by SSR route.

The microstructures of the samples were observed using a JEOL JSM-6480LV scanning electron microscope (SEM). The experimental densities (d_{ex}) of the samples were measured by the Archimedes' method. The sintered samples were polished by using emery paper and electroded by applying the silver paste on both sides of the samples for electrical characterizations. The UV-Visible optical absorption and transmittance of the ceramic powders have been carried out with a view to explore their optical properties. The spectral absorption was taken out by using UV visible spectrometer (Model: Shimadzu UV, 2250) in the wavelength ranges from 200 to 800 nm using halogen and deuterium lamp as sources for visible and UV radiations, respectively at RT. Dielectric constant (ε_r) and dielectric loss (tanδ) were measured as a function of temperature using a computer interfaced HIOKI 3532-50 LCR-HITESTER. The ferroelectric property was characterized by the measurement of polarization as a function of electric field using precision premier II, a standard ferroelectric testing machine (Radiant Technology). The samples for the piezoelectric property measurements were poled by corona poling unit at RT by applying a dc electric field of 5kV/mm for 20 min. The d_{33} values of the samples were measured by Piezo meter (YE2730A d_{33} Meter, APC International Ltd.).

3.2.1.2 CCTO System by Solid State Reaction (SSR) Route

$CaCu_3Ti_4O_{12}$/CCTO ceramic systems were also synthesized by conventional solid state reaction route.

For synthesis of CCTO ceramic samples, calcium carbonate ($CaCO_3$, 98.5% purity), copper(II) oxide (CuO, 99% purity) and titanium dioxide (TiO_2, 99% purity) were used as starting materials. Stoichiometric weights of all the raw powders were mixed and ball milled with acetone for 10 h. zirconia balls were used as the grinding media. After ball milling, the mixture was dried in an agate mortar and grinded for the homogeneous mixing of the powders. The calcination temperature was decided from the differential scanning calorimeter (TGA-DSC, STA449C, NETZSCH). The CCTO powder calcined at 1050^{o}C for 4h showed single perovskite phase. The phase formation of the calcined CCTO powder was confirmed from the XRD study, performed on a Philips X'PERT System X-Ray Diffractometer (PW 3020, Phillips, Eindhoven, The Netherlands) with Cu K_α radiation (λ = 1.5405 A°). Then the calcined powder was mixed with the binder solution (2 wt% PVA) and compacted to pellet form by using a hydraulic press. The sintering of the samples was carried out at 1050 and 1100^{o}C for 8 h.

The flow chart showing the synthesis process of CCTO ceramics is as shown in the Fig. 3.2 as follows:

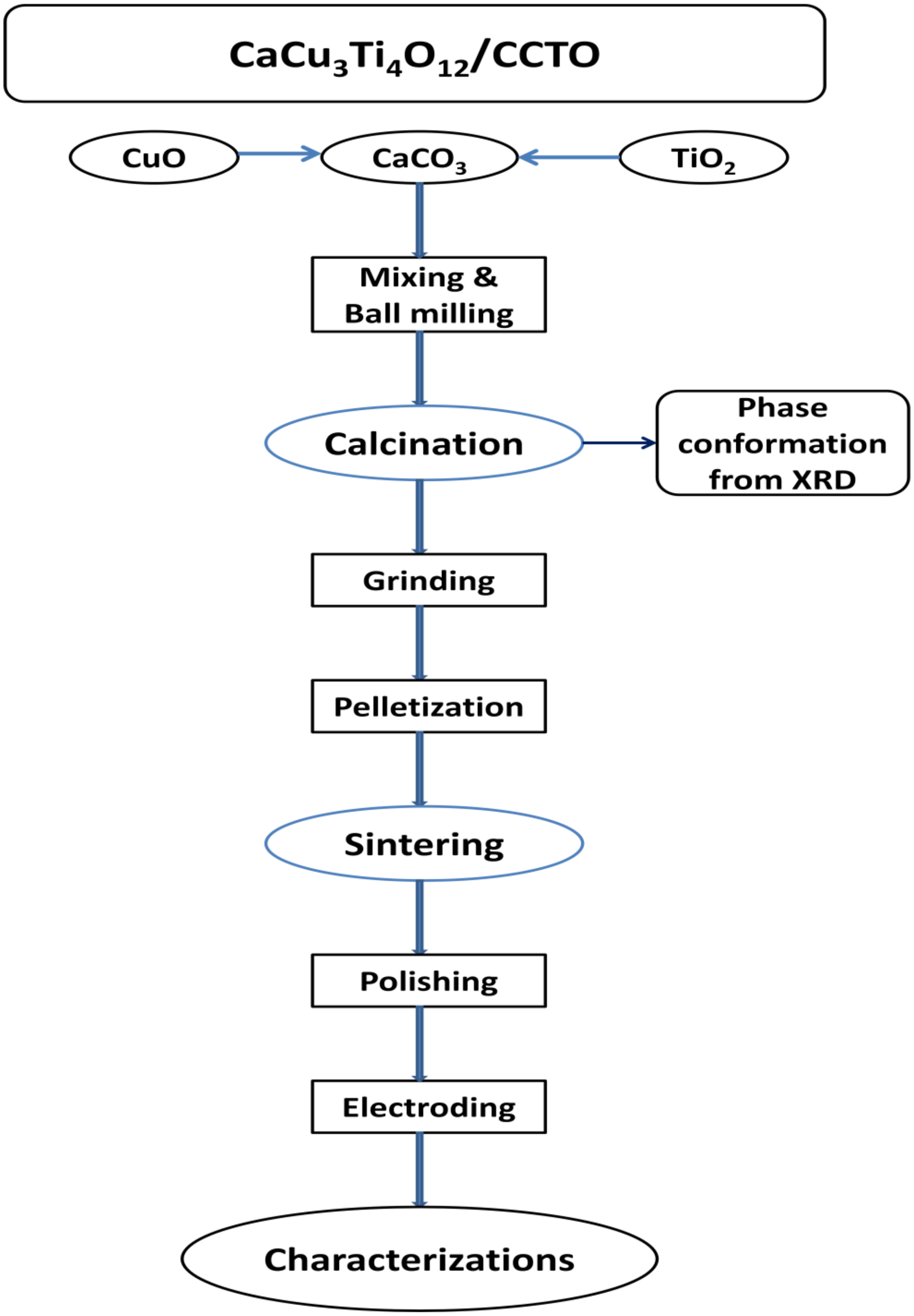

Fig. 3.2 Flow chart of synthesis of CCTO system by SSR route.

The microstructure analysis of the sintered sample was carried out using a JEOL JSM-6480LV scanning electron microscope. The experimental densities (d_{ex}) of the samples were measured by the Archimedes method. The UV-Visible optical absorption spectra of CCTO ceramic powders was taken out by using UV visible spectrometer (Model: Shimadzu UV, 2250) in the wavelength ranges from 200 to 800 nm at RT. Then silver paste was applied on both the sides of the sintered samples for different electrical measurements. ε_r and $\tan\delta$ were measured as a function of temperature using a computer interfaced HIOKI 3532-50 LCR-HITESTER.

3.2.2 Preparation of Ceramic-Polymer Composite Samples

3.2.2.1 Preparation of Ceramic PVDF Composite Samples

In the present work, the following series of 0-3 ceramic-polymer composites using PVDF as polymer phase have been synthesized by uniaxial hot pressing method.

(i) $\Phi\{0.50[Ba(Zr_{0.2}Ti_{0.8})O_3]\text{-}0.50[(Ba_{0.7}Ca_{0.3})TiO_3]\}\text{-}(1\text{-}\Phi)$PVDF/[(BZT-BCT)-PVDF] composites (where, Φ = 0.05, 0.10, 0.15, 0.20 & 0.25 volume fractions).

(ii) $0.25\{0.50[Ba(Zr_{0.2}Ti_{0.8})O_3]\text{-}0.50[(Ba_{0.7}Ca_{0.3})TiO_3]\}\text{-}0.75\{(1\text{-}x)\text{PVDF-}xCaCu_3Ti_4O_{12}\}$/[(BZT-BCT)-(PVDF-CCTO)] composites (where, x = 0.02, 0.04, 0.06, 0.08 & 0.10 volume fractions).

In the present work, PVDF of molecular weight ~ 5,34,000 (Sigma-Aldrich) was used for the preparation of PVDF, (BZT-BCT)-PVDF, and (BZT-BCT)-(PVDF-CCTO) 0-3 composite thick films.

PVDF thick films were prepared by uniaxial hot pressing of PVDF powder at 150°C and at an applied pressure of ~ 6.5 MPa for 30 mins and then cooled to RT under pressure.

For the fabrication of Φ(BZT-BCT)-(1-Φ)PVDF 0-3 composite thick films, first the (BZT-BCT) sintered pellets at 1400°C for 6 h, were crushed to powder form by using an agate mortar and pestle. Both the (BZT-BCT) sintered powder and PVDF powder with single phases were taken in required volume proportions and were mixed thoroughly using a magnetic stirrer for 1 h to get a homogeneous mixture of the composite powder. The mixture was then subjected to ultrasonic agitation for 30 min to avoid agglomeration of ceramic phase. (BZT-BCT)-PVDF composite thick films were prepared by hot uniaxial pressing of (BZT-BCT)-PVDF powder at 150^{o}C and an applied pressure of ~ 6.5 MPa for 30 mins and then cooled to RT under pressure. A series of (BZT-BCT)-PVDF composites with different ceramic volume fractions ranging from 0.05 to 0.25 were fabricated. The samples were cut into rectangular shapes for different characterizations. Silver paste was applied on both the sides of the samples for electrical measurements.

Among the series of (BZT-BCT)-PVDF composites, 0.25[BZT-BCT]-0.75[PVDF] composite has been reported as showing the best properties with a highest relative permittivity ε_r ~ 41 at RT and at 1 kHz frequency [1]. Still, there is a need of enhancing the dielectric properties of these composites further. Hence the 0.25[BZT-BCT]-0.75[PVDF] composite was combined with different volume fractions of PVDF polymer and CCTO ceramics to form [(BZT-BCT)-(PVDF-CCTO)] composite thick films.

Therefore, in this work, 0.25(BZT-BCT)-0.75[(1-x)PVDF-xCCTO]/[(BZT-BCT)-(PVDF-CCTO)] (where x = 0.02, 0.04, 0.06, 0.08 & 0.10 volume fractions) composites were fabricated by the hot press method with different volume fractions of CCTO ceramics incorporated into (BZT-BCT)-PVDF composites.

For the fabrication of [(BZT-BCT)-(PVDF-CCTO)] 0-3 composite thick films, again the sintered CCTO pellets at 1100^{o}C for 8 h were crushed into powder forms using mortar and pestle. Then the 0.25[BZT-BCT]-0.75[PVDF] composite powder, sintered CCTO powder and PVDF powder with single phases were taken in required volume proportions and mixed thoroughly using a magnetic stirrer for 1 h to get a homogeneous mixture of the composite powder. The mixture was then subjected to ultrasonic agitation for 30 min to avoid agglomeration of ceramic phase. [(BZT-BCT)-(PVDF-CCTO)] composite thick films were prepared by hot uniaxial pressing of [(BZT-BCT)-(PVDF-CCTO)] powder at 150^{o}C and an applied pressure of ~ 6.5 MPa for 30 mins and then cooled to RT under pressure. A series of [(BZT-BCT)-(PVDF-CCTO)] composites with different CCTO ceramic volume fractions ranging from 0.02 to 0.10 were fabricated. The samples were cut into rectangular shapes for different characterizations. Silver paste was applied on both the sides of the samples for electrical measurements. The hot press used for the fabrication of 0-3 ceramic PVDF composites and the composites are as shown in Fig. 3.3 as follows:

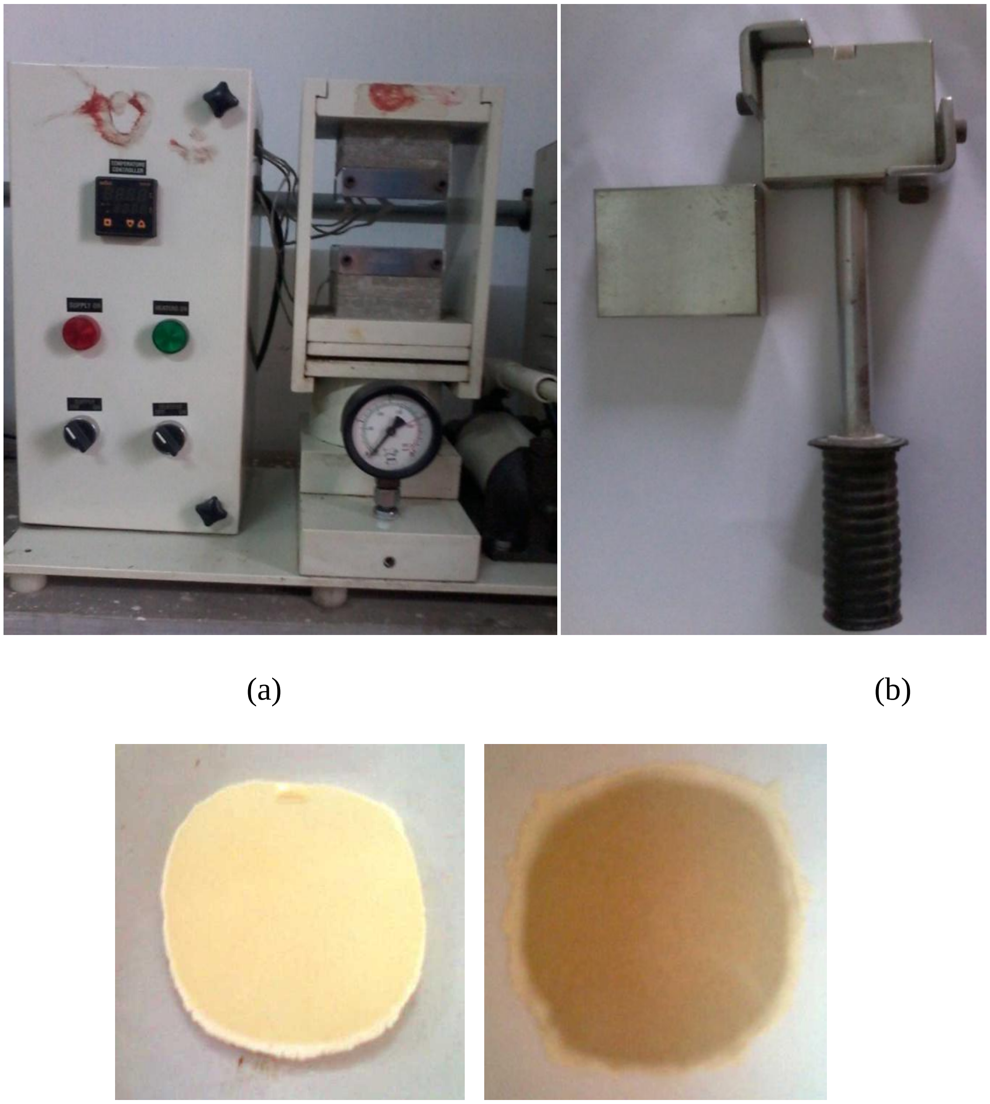

(a) (b)

(c) (d)

Fig 3.3 (a) Hot press used for the fabrication of 0-3 ceramic PVDF composites, (b) Sample holder, (c) (BZT-BCT)-PVDF composite sample & (d) (BZT-BCT)-(PVDF-CCTO) composite sample.

3.2.2.2 Preparation of Ceramic Epoxy Composite Samples

In the present work, the following series of 0-3 ceramic-polymer composites using epoxy as polymer phase have been synthesized by cold pressing and hand lay-up methods.

(i) $\Phi\{0.50[Ba(Zr_{0.2}Ti_{0.8})O_3]$-$0.50[(Ba_{0.7}Ca_{0.3})TiO_3]\}$-$(1-\Phi)$epoxy/[(BZT-BCT)-epoxy] composites (where, $\Phi = 0.05, 0.10, 0.15, 0.20$ & 0.25 volume fractions).

(ii) $0.20\{0.50[Ba(Zr_{0.2}Ti_{0.8})O_3]$-$0.50[(Ba_{0.7}Ca_{0.3})TiO_3]\}$-$0.80\{(1-x)$epoxy-$xCaCu_3Ti_4O_{12}\}$/[(BZT-BCT)-(epoxy-CCTO)] composites (where, $x = 0.02, 0.04, 0.06, 0.08$ & 0.10 volume fractions).

In the present work, the type of epoxy resin used, is Araldite-AW-106, which chemically belongs to epoxide family. Its common name is Bisphenol A Diglycidyl Ether. 1, 3-propanediamine (HV- 953-IN) has been used as hardener.

The 0-3 (BZT-BCT)-epoxy composites were prepared by cold pressing and hand lay-up techniques. For the fabrication of the composites, (BZT-BCT) sintered pellets at 1400°C for 6 h were first grinded to powder form by using an agate mortar and pestle for the homogeneous mixing of the ceramic powder with the polymer matrix. The sintered powder was then mixed with the epoxy resin and hardener in required volume proportions. For different volume fractions of ceramics, a calculated amount of epoxy resin and hardener (in the weight ratio of 15:1) was used. The mixture was then thoroughly mixed with gentle stirring to minimize the air entrapment. For the fabrication of the composite samples, a steel mould was fabricated in the work shop as shown in the Fig. 3.4. The steel mould was used for the preparation of cylindrical (pin) type specimen of length ~ 35 mm and diameter of ~ 10 mm. The mixture of sintered (BZT-BCT) powder and epoxy resin was poured into the cylindrical cavity of the mould and the two halves of the mould were fixed properly. It required proper care during the fixing of moulds, as some of the resins may squeeze out. After closing the mould properly, the specimens were allowed to solidify inside the moulds at RT for 24 h.

A series of (BZT-BCT)-epoxy composites with different volume fractions of (BZT-BCT) ceramics ranging from 0.05 to 0.25 were fabricated. For the purpose of comparison, the pure epoxy matrix material was also cast under similar conditions. After curing, the cylindrical samples were taken out from the mould and cut into required shapes and sizes for different measurements and characterizations. Silver paste was applied on both the sides of the samples for electrical measurements.

Among the series of (BZT-BCT)-epoxy composites, 0.20[BZT-BCT]-0.80[epoxy] composite has shown the best property with a highest relative permittivity ε_r ~ 34 at RT and at 1 kHz frequency [2]. To enhance the dielectric properties of these composites, the 0.20[BZT-BCT]-0.80[epoxy] composite was combined with different volume fractions of epoxy polymer and CCTO ceramics to form [(BZT-BCT)-(epoxy-CCTO)] composite samples.

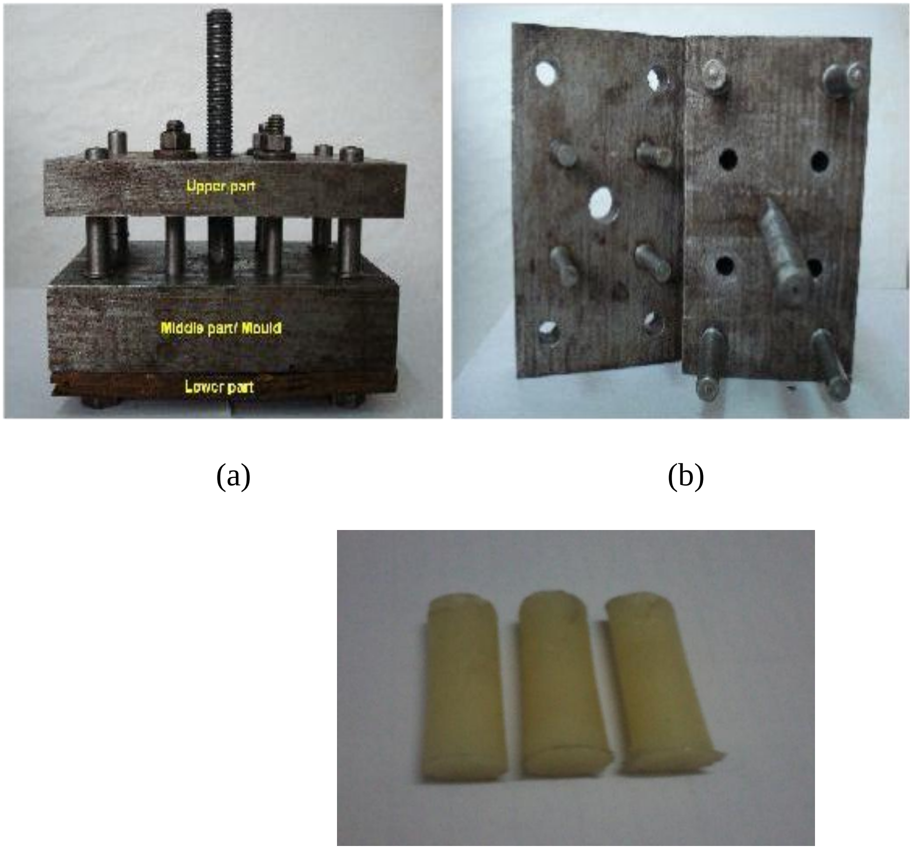

(a) (b)

(c)

Fig 3.4 (a) Steel moulds designed for the preparation of cylindrical (pin) type specimens, (b) Two halves of the mould & (c) Fabricated cylindrical samples.

Therefore, in the present work, 0.20(BZT-BCT)-0.80[(1-x)epoxy-xCCTO]/[(BZT-BCT)-(epoxy-CCTO)] (where, x = 0.02, 0.04, 0.06, 0.08 & 0.10 volume fractions) composites were fabricated by the cold pressing and hand lay-up methods with different volume fractions of CCTO ceramics incorporated into (BZT-BCT)-epoxy composites.

Again for the fabrication of [(BZT-BCT)-(epoxy-CCTO)] composites, the sintered CCTO pellets at 1100°C for 8 h, were crushed into powder forms using mortar and pestle. The sintered (BZT-BCT) and CCTO powders were mixed with the required volume proportions of epoxy resin and hardener. The weight ratio of epoxy resin and hardener used was 15:1, same as that of used for the preparation of (BZT-BCT)-epoxy composites. The mixture of ceramic powders and epoxy resin was continuously mixed with gentle stirring to minimize the air entrapment. For the fabrication of [(BZT-BCT)-(epoxy-CCTO)] composite samples, the same steel mould was used. The mixture of sintered (BZT-BCT), CCTO powders and epoxy resin was poured into the cylindrical cavity of the mould and the two halves of the mould were fixed properly with adequate care. After closing the mould properly, the specimens were allowed to solidify inside the moulds at RT for 24 h.

A series of [(BZT-BCT)-(epoxy-CCTO)] composites with different volume fractions of (CCTO) ceramics ranging from 0.02 to 0.10 were fabricated. After curing, the cylindrical samples were taken out from the mould and cut into required shapes and sizes for different measurements and characterizations. Silver paste was applied on both the sides of the samples for electrical measurements.

3.3 Studied Parameters and Characterization Techniques Used

This section describes the details about the measurement of various structural, microstructural and electrical properties.

3.3.1 TG/DSC

Thermal decomposition and crystallization of the sample was investigated by differential scanning calorimeter (TGA-DSC, STA449C, NETZSCH). These devices have a disk (constantan alloy) on which the sample and reference pans rest symmetrically placed platform. Thermocouple (chromel alloy) is welded to the underside of each platform. The chromel constantan junctions make up the differential thermocouple junctions with the constantan disk acting as one leg of the thermocouple pair. A calibration constant within the computer software converts the amplified differential thermocouple voltage to energy per unit time which is plotted on y-axis of the DSC output.

In TGA experiment, specimen powder is placed on refractory pan (porcelain or platinum). The pan in the hot zone of the furnace is suspended from a high precision balance. A thermocouple is in the close proximity to the specimen but not in contact, so as not to interfere with the free float of the balance. The balances are electronically compensated so that the specimen pan does not move when the specimen gains or losses weight. The effect of particle packing affects both DSC and TGA analysis therefore this is taken into account while doing the experiments.

3.3.2 X-ray Diffraction (XRD)

XRD study was performed on a Philips X'PERT System X-Ray Diffractometer (PW 3020, Phillips, Eindhoven, The Netherlands) with Cu K_{α} radiation (λ = 1.5405 A°). The diffraction data was taken in the 2θ range from 10^{o} to 70^{o}. The XRD data were used to find out the crystal structure and the unit cell parameters of the ceramic samples. Cu $K_{\alpha 2}$ radiation was stripped from the collected XRD data by using standard software "X'pert high score". The 2θ values, corresponding to the peaks were noted from the diffraction patterns. The crystal structure and unit cell parameters were obtained, using a computer program package "POWD" [3].

3.3.3 Ultraviolet-visible (UV-Vis) Absorption Spectroscopy Study

The UV-Visible optical absorption and transmittance of both the ceramic & composite powder samples have been carried out by using UV visible spectrometer (Model: Shimadzu UV, 2250) in the wavelength ranges from 200 to 800 nm using halogen and deuterium lamp as sources for visible and UV radiations, respectively at RT.

3.3.4 Scanning Electron Microscopy (SEM) Study

In the present work, the topographical and morphological study was carried out by using JEOL JSM-6480LV Scanning Electron Microscope. The average grain size of the samples was calculated by diagonal intercept method with the help of the "Image J" software. The average grain size was measured by drawing lines of known length diagonally on the micrograph. The numbers of grains intersected by the lines were counted. Then the average grain sizes were calculated by dividing the length of the line by the number of grain coming under that line.

3.3.5 Electroding of the Samples

The samples were polished by emery paper to achieve a thickness of ~ 1mm and cleaned with acetone. Sufficient care was taken to keep the faces of the pellets parallel. Then thin layer of silver paste was applied on both side of the ceramic samples and fired in an oven at 300°C for 30 min to ensure good adhesion. The pellets now act as dielectric medium between the two parallel metallic plates. Now, the samples are ready for electrical measurements.

3.3.6 Dielectric Measurements

In the present work, the dielectric measurements of the samples were carried out by using a computer interfaced LCR Hitester (Hioki 3532-50, Japan), as shown in the Fig. 3.5.

Fig. 3.5 Diagram of the Hioki 3532-50 LCR Hitester.

The electrode samples were used for this measurement. The interfacing of the instrument was done by using Lab view software. The LCR meter measures different electrical parameters of the samples at low frequencies employing the auto balancing bridge. The dielectric constant and dielectric loss was measured as a function of both frequency and temperature. The dielectric constant and dielectric loss can be measured as a function of temperature to calculate the Curie temperature (T_c) at four different frequencies. For this measurement, the sample was kept in a holder in a computer controlled heating furnace. The data were collected with a heating rate of 2°C/min and at an interval of 1°C.

The schematic diagram of auto balancing bridge method is shown in Fig. 3.6.

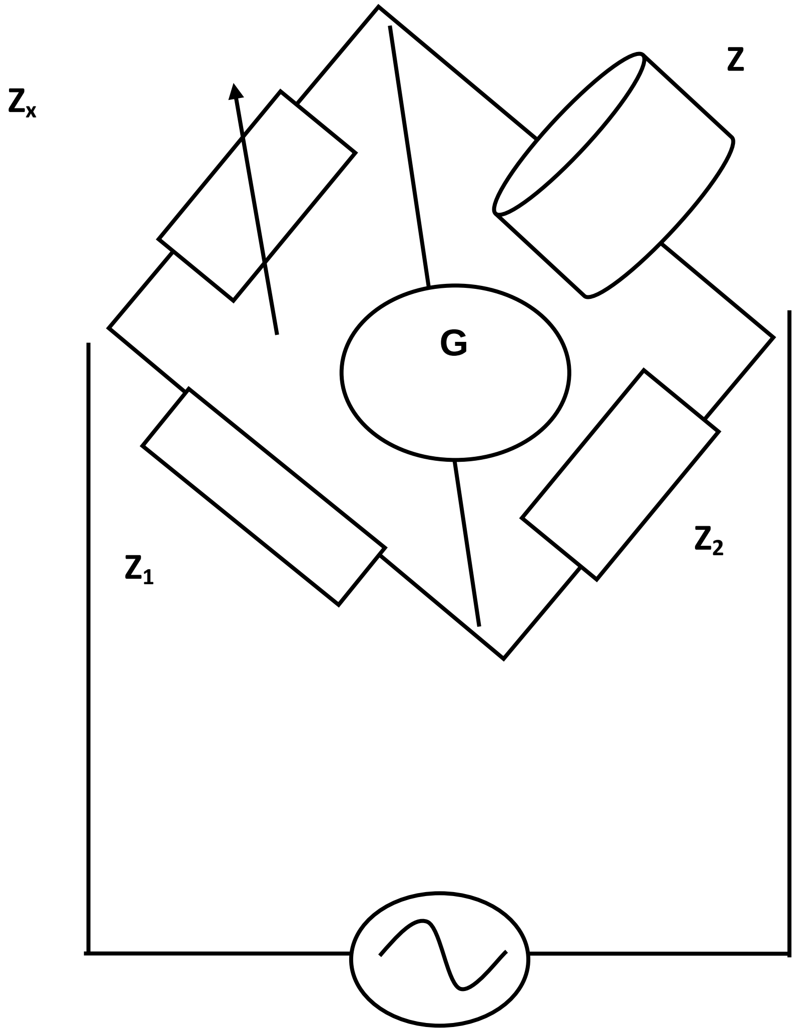

Fig. 3.6 Schematic diagram of auto balancing bridge.

Here Z represents the impedance of the material (i.e. the pellet), Z_1 and Z_2 are known impedances and Z_x is the variable impedance. Z_x varies until no current flows through G. Under balanced condition, Z can be calculated as follows:

$$Z = (Z_2/Z_1)\, Z_X \tag{3.1}$$

If the Z value is known, then the resistance component (R) and reactance component (X) can be calculated. Capacitance (C) and dielectric loss (tanδ) can be calculated using the following formula $C = 1 / 2\pi f X$ and dielectric loss: $\tan\delta = R / X$.

Knowing the capacitance C, dielectric constant can be calculated as [4]

$$\varepsilon_r = \frac{C\, d}{\varepsilon_0 A} \tag{3.2}$$

Where, ε_0: Permittivity of free space in farad per meter ($8.854 \times 10^{-12} F/m$) [5]

ε_r: Dielectric constant or relative permittivity of the sample.

A : Area of each plane electrode in square meters (m^2)

d : Thickness of the electrode ceramic sample in meters (m)

3.3.7 Polarization vs Electric field (P-E) Measurements

(P-E) loops at RT for all the (BZT-BCT) ceramic samples were recorded using precision premier II, a standard ferroelectric testing machine (Radiant Technology). P-E hysteresis is one of the defining properties of ferroelectric materials. The parameters spontaneous polarization, remanent polarization and coercive field can be measured from the P-E loop by using the principle of Sawer-Tower circuit as shown in the Fig. 3.7 [6]. For this measurement, the sample should be kept in the silicone oil.

In this circuit, a sinusoidal voltage U_{ac} is connected to the sample capacitor C_x. C_1 is the reference capacitor of a known capacity and it is independent of the applied voltage.

The x-channel of the oscilloscope is connected to the supply voltage U_{ac} through the voltage dividers R_1 and R_2. If $C_1 >> C_x$, the voltage drop at C_1 is neglected and the voltage at C_x is nearly equal to the supply voltage U_{ac}. Due to the proportionality between the voltage and the electric field, the voltage at x-channel is considered as the measure of the electric field inside the sample C_x.

The y-channel gets voltage proportional to the polarization of the sample C_x. As the capacitors C_x & C_1 are connected in series, therefore same current flows through both the elements. Hence both C_x & C_1 carry the same charge at any time. Due to the proportionality between voltage and charge, the voltage at C_1 is the measure of the charge capacity C_x or the polarization.

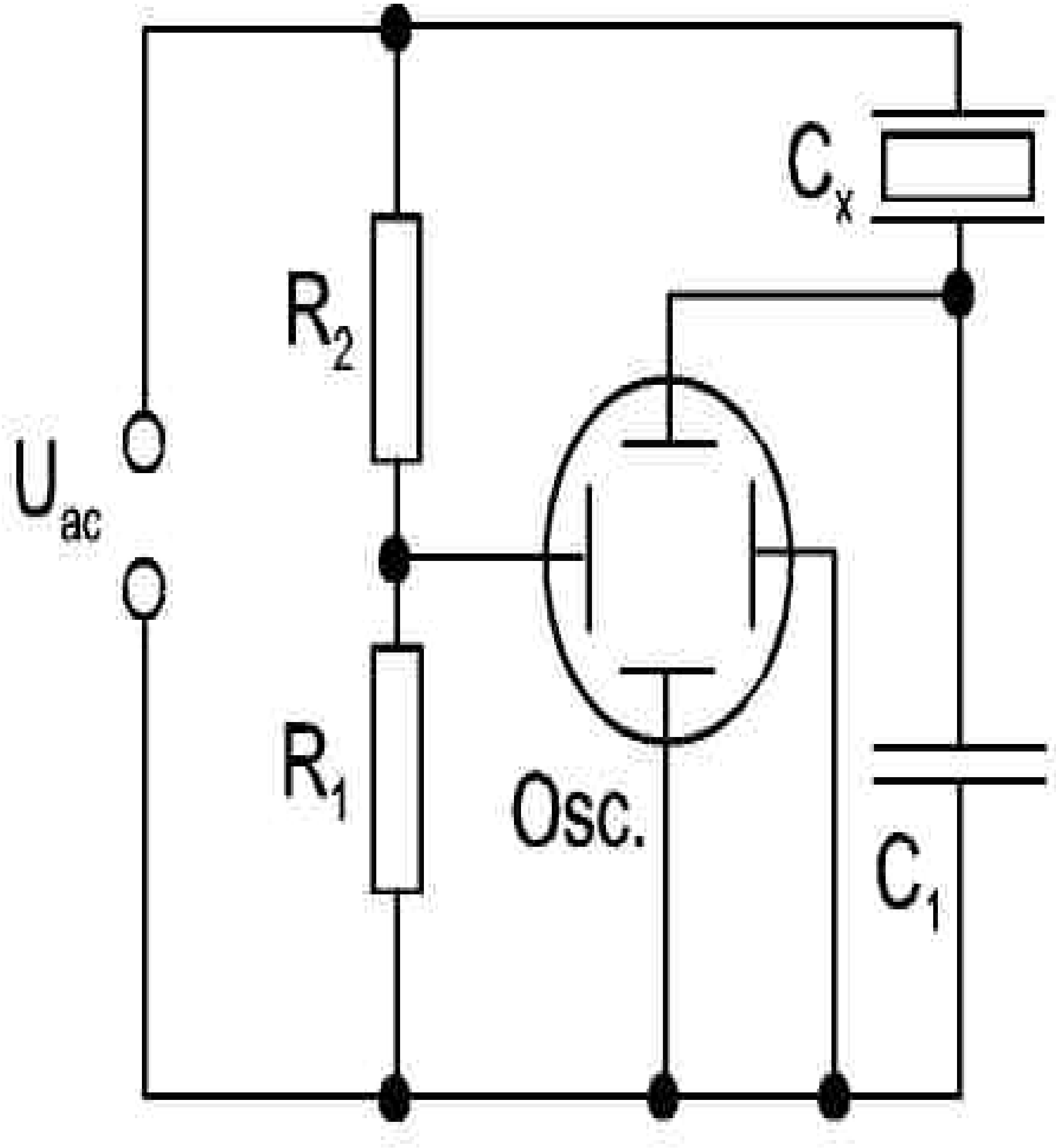

Fig. 3.7 Schematic diagram of Sawer-Tower circuit [7].

Once the charge on the sample is known, the polarization can be determined using relation given below.

$$P = Q/A \tag{3.3}$$

Where, Q is the charge developed on the electrodes of the ferroelectric capacitor and A is the area of the electrodes.

3.3.8 Poling

There are different methods of poling, viz. thermal poling, corona charging and electron beam injection. In the present study, corona charging method is employed for poling the ferroelectric samples. Fig. 3.8 shows the set up used in this work for corona charging technique.

The corona poling unit consists of a corona needle, a grid, hot plate temperature controller unit and a high voltage power supply system. The sample to be poled was placed on a conducting hot plate connected to a temperature controller. Before poling, the (BZT-BCT) ferroelectric ceramic sample was preheated at a temperature ~ 90^{o}C. The unit consists of a sharp corona needle made up of brass of ~ 2 mm diameter. A ring shaped grid of ~ 12 mm diameter made up of copper wire was kept between the tip of the corona needle and the conducting hot plate in such a way that the tip of the needle is 1 mm above the centre of the grid. A high voltage (~ 5 kV) was applied between the corona needle and the hot plate. This voltage should be slightly higher than the voltage at which corona discharge starts. A bias voltage (~ 1.5 kV) was applied between the grid and the conducting hot plate to accelerate the ions caused by the breakdown of the air. Then the preheated sample was subjected to corona discharge for 20 min maintaining the temperature. The onset of the corona was seen as a spray of blue flame from the tip of corona needle towards the sample surface. Then the heater was turned off while maintaining the corona discharge till the temperature of sample reached RT. Finally the field was removed. In this study, the composite samples were poled by the same procedure, but at RT.

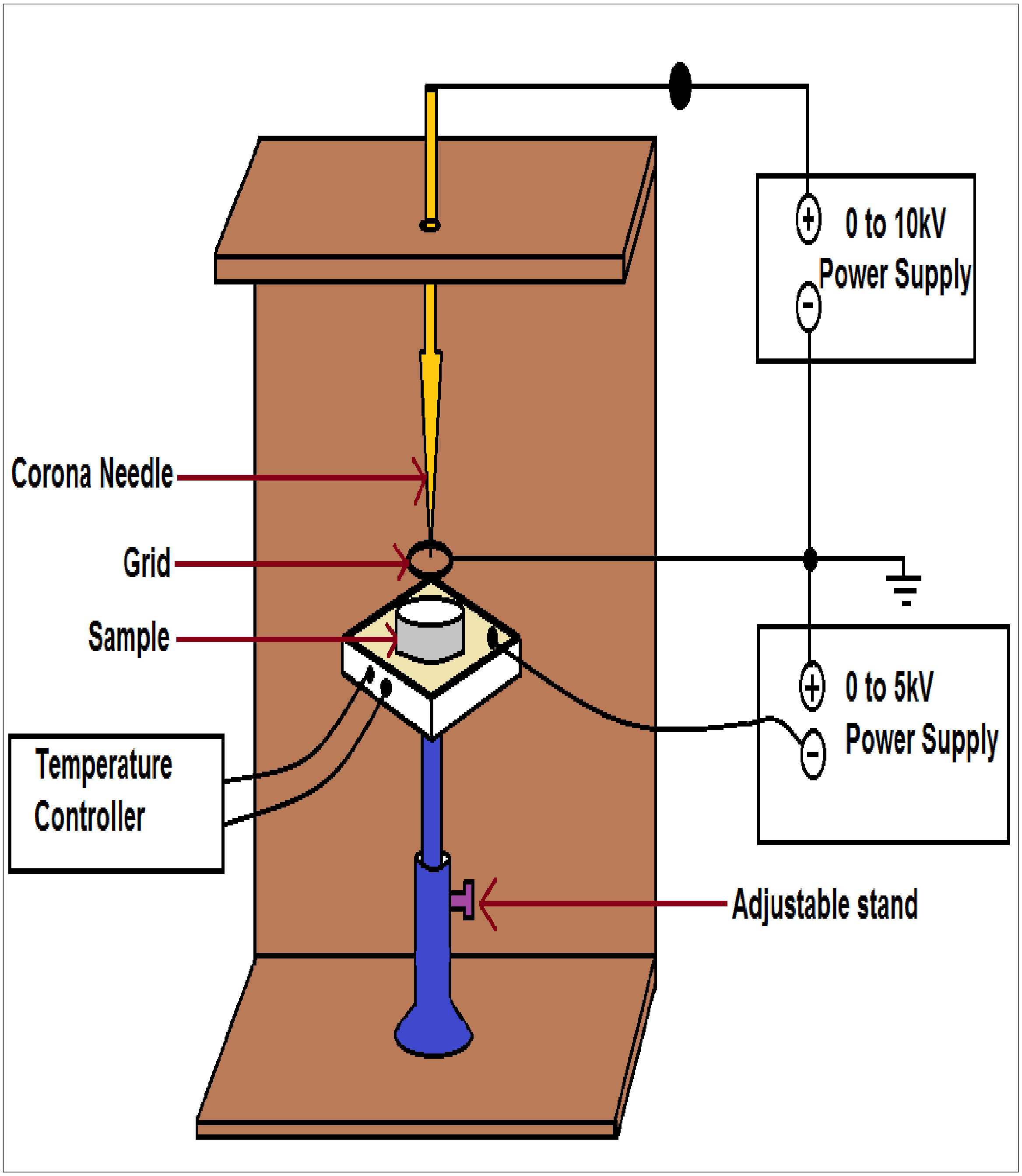

Fig. 3.8 Schematic diagram of corona poling unit.

3.3.9 d_{33} Measurements

The d_{33} of the samples was measured by a quasi-static method using a Piezometer (YE2730A d_{33} Meter, APC International Ltd.). The piezoelectric coefficient is defined by the following equation:

$$d_{33} = \left(\frac{D_s}{T_s}\right)_E \tag{3.4}$$

Where, D_s is the charge density (C/m^2) and T_s is the mechanical stress (N/m^2) at constant electric field (E). Fig. 3.9 shows a schematic diagram for the d_{33} measurement using the Piezo-Meter.

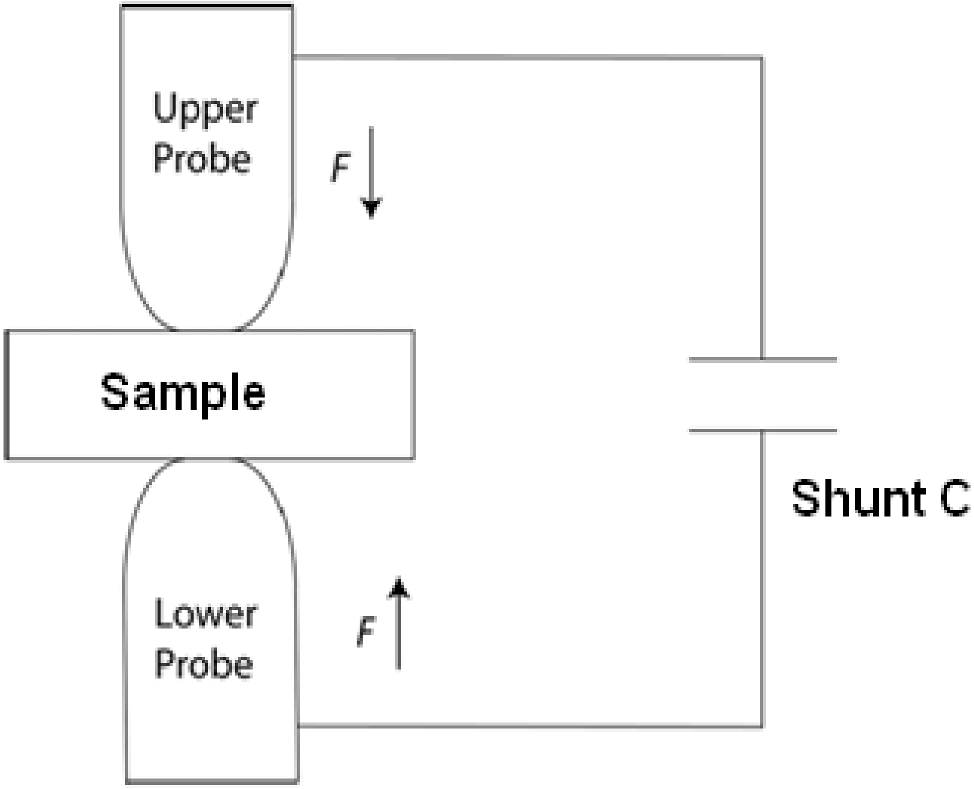

Fig. 3.9 Schematic diagram for d_{33} measurement.

When a force (F) was applied on an area (A) of a poled sample by the upper and lower probes, a piezoelectric charge (Q) was produced due to the piezoelectric effect on the contact area (A). Hence, piezoelectric charge coefficient (d_{33}) was measured by measuring the charge developed on the surface of the sample. Eqn 3.4 can be simplified as follows:

$$d_{33} = \left(\frac{D_s}{T_s}\right)_E = \frac{(Q/A)}{(F/A)} = \frac{Q}{F} = \frac{CV}{F} \tag{3.5}$$

Where, C is the shunt capacitance and V is the potential difference across the shunt capacitor. The Piezometer measures this potential difference, calculates the d_{33} (in pC/N) of the sample and displays the value digitally. Average d_{33} values are taken after taking measurements from various areas across a ceramic sample.

References

[1] P. Kumar, P. Mishra and S. Sonia, J. Inorg. Organomet. Polym. 23, (2013) 539.

[2] P. Mishra and P. Kumar, Hindawi Publishing Corporation: Advances in Condensed Matter Physics. 2013, (2013) 1.

[3] E. Wu. POWD, an interactive powder diffraction data interpretation and indexing program ver.2.1. School of Physical Science, Finder's University of South Australia Bedford Park.

[4] E. Barsoukov, and J. R. Macdonald, Impedance Spectroscopy: Theory, Experiment, and Applications (Wiley-Interscience, Hoboken, 2005).

[5] K. C. Kao, Dielectric phenomena in Solids (Elsevier Academic Press, London 1990).

[6] C. B. Sawyer and C. H. Tower, Phys. Rev. 35, (1930) 269.

******

Chapter – 4

STRUCTURAL & ELECTRICAL PROPERTIES OF (BZT-BCT), CCTO CERAMICS AND PVDF, EPOXY POLYMERS

In this chapter, the structural, optical and electrical properties of (BZT-BCT), CCTO ceramics and PVDF, epoxy polymers are discussed in details.

4.1 Structural & Electrical Properties of (BZT-BCT) Ceramics

4.1.1 Introduction

From the literature survey, x[Ba($Zr_{0.2}Ti_{0.8}$)O_3]-(1-x)[($Ba_{0.7}Ca_{0.3}$)TiO_3]/(BZT-BCT) system is found to be the first reported lead free pseudo binary ferroelectric MPB system to replace the PZT based systems [1]. (BZT-BCT) was first synthesized and identified as a ferroelectric system in the year 2009 by W. Liu *et.al.* [1]. This system possesses a MPB near 50/50 composition similar to that of the PZT system. W. Liu *et.al.* reported (BZT-BCT) 50/50 ferroelectric system with surprisingly high piezoelectric properties at this optimal composition [1]. Also, at this 50/50 composition, the ferroelectric and electro mechanical properties are expected to be the best for (BZT-BCT) system [1]. At RT, this MPB composition (50BZT-50BCT) is found to exist in a ferroelectric rhombohedral-tetragonal structure with $T_c = 93^oC$ [1]. Because of its excellent piezoelectric properties [1], (BZT-BCT) system has many technological applications and can be a successful alternative to the lead based ferroelectric-piezoelectric systems.

In the present work, three different compositions in the MPB region of the xBZT-(1-x)BCT system, where x = 0.48, 0.50 & 0.52, have been synthesized by the conventional solid state reaction route. The structural, microstructural, optical, dielectric, ferroelectric and piezoelectric properties of these compositions, sintered at different temperatures have been investigated and discussed in detail.

4.1.2 Optimization of Calcination and Sintering Temperatures

It is very important to develop single perovskite phase in the synthesized (BZT-BCT) ferroelectric ceramics. Since, the presence of secondary phase in the ferroelectric ceramics always increase the conductivity and decreases the piezoelectric properties, which is undesirable for practical applications. Therefore, to ensure the single perovskite phase formation, the calcination temperature of the parent (BZT-BCT) ceramics has been optimized. It is well known that a dense ceramic body is necessary to achieve maximum dielectric and piezoelectric properties. Therefore, in the present section, the optimization of the sintering process is also discussed in detail.

4.1.2.1 Thermal Analysis

Fig. 4.1 shows the thermogravimetric and differential scanning calorimetry (TG-DSC) curves of the uncalcined xBZT-(1-x)BCT (x = 0.48, 0.50, 0.52) ceramics. The TG curves of all the 3 MPB compositions show overall weight loss of ~ 18 % from RT to 1200^{o}C. For 0.48BZT-0.52BCT composition, the DSC curve shows major endothermic peaks at ~ 729 and 816^{o}C. While for 0.50BZT-0.50BCT composition, the maximum weight loss of around ~ 12 % is observed between 800 and 1000^{o}C, which are correlated with endothermic and exothermic peaks in the DSC curve. For 0.52BZT-0.48BCT composition, the DSC curve has endothermic peaks at ~ 820 and 964^{o}C. The overall weight loss processes of the uncalcined (BZT-BCT) powders are divided into three steps in the TG curve. The first step of weight loss ~ 2% is observed between 26 and 200^{o}C. This weight loss could be due to the evaporation of water and decomposition of thermally unstable organic compounds [2]. In the same temperature range the DSC curve shows an endothermic peak, which is correlated to the decomposition of water during the thermal decomposition of the precursors. Second weight loss of ~ 4% is observed between 600 and 800^{o}C. Maximum weight loss of around ~ 12% is observed between 800 and 1000^{o}C. These weight losses are correlated with an endothermic and an exothermic peak in accordance to the DSC curve. The endothermic peak, observed between 600 and 800^{o}C can be correlated to the elimination of CO and CO_2 molecules originated from the decomposition of carbonate groups. For all the three compositions, the appearance of exothermic peaks at ~ 1012^{o}C in the DSC curves can be correlated to the crystallization process of (BZT-BCT) powder [3,4]. No further significant weight loss is observed above 1012^{o}C temperature, indicating an absence of further decompositions beyond this temperature [5]. Hence, from the DSC curves, it can be concluded that the calcinations of the MPB (BZT-BCT) ceramic samples can be carried out ~1000^{o}C.

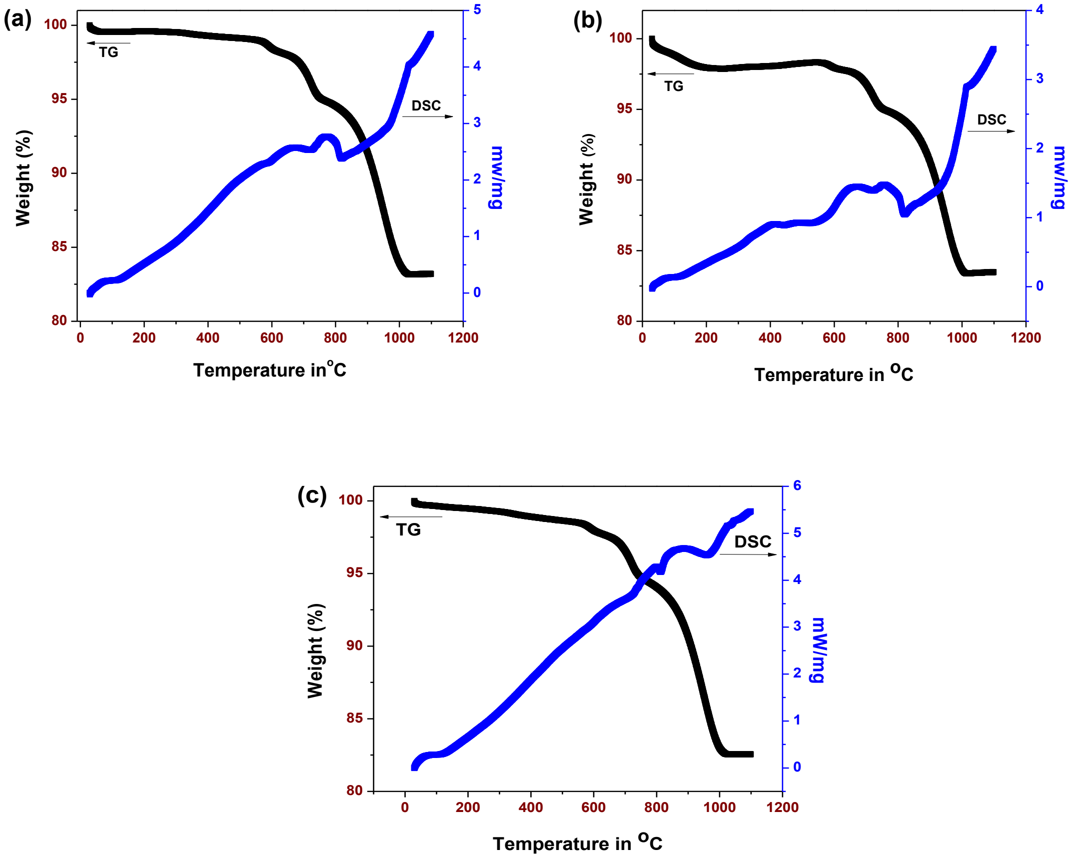

Fig. 4.1 TG-DSC curves of the uncalcined xBZT-(1-x)BCT powders with (a) x = 0.48, (b) x = 0.50 and (c) x = 0.52.

4.1.2.2 Single Perovskite Phase Formation

Fig. 4.2 shows the RT XRD patterns of the (BZT-BCT) ceramic powders calcined at 1100, 1200 & 1300°C for 4 h, respectively. XRD patterns of all the samples calcined at 1300°C show the development of single perovskite phase without any secondary phase peaks. Thus 1300°C has been optimized as the calcination temperature for the single perovskite phase in the (BZT-BCT) ceramics near MPB.

4.1.2.3 Sintering and Density Study

The sintering of all the (BZT-BCT) ceramic samples has been carried out at1300, 1350 & 1400°C for 6 h, respectively. The optimum sintering temperature for all the compositions of (BZT-BCT) system is found to be 1400°C for 6 h. The variation of relative density (RD) of the xBZT-(1-x)BCT ceramics as a function of different sintering temperature is shown in Fig. 4.3.

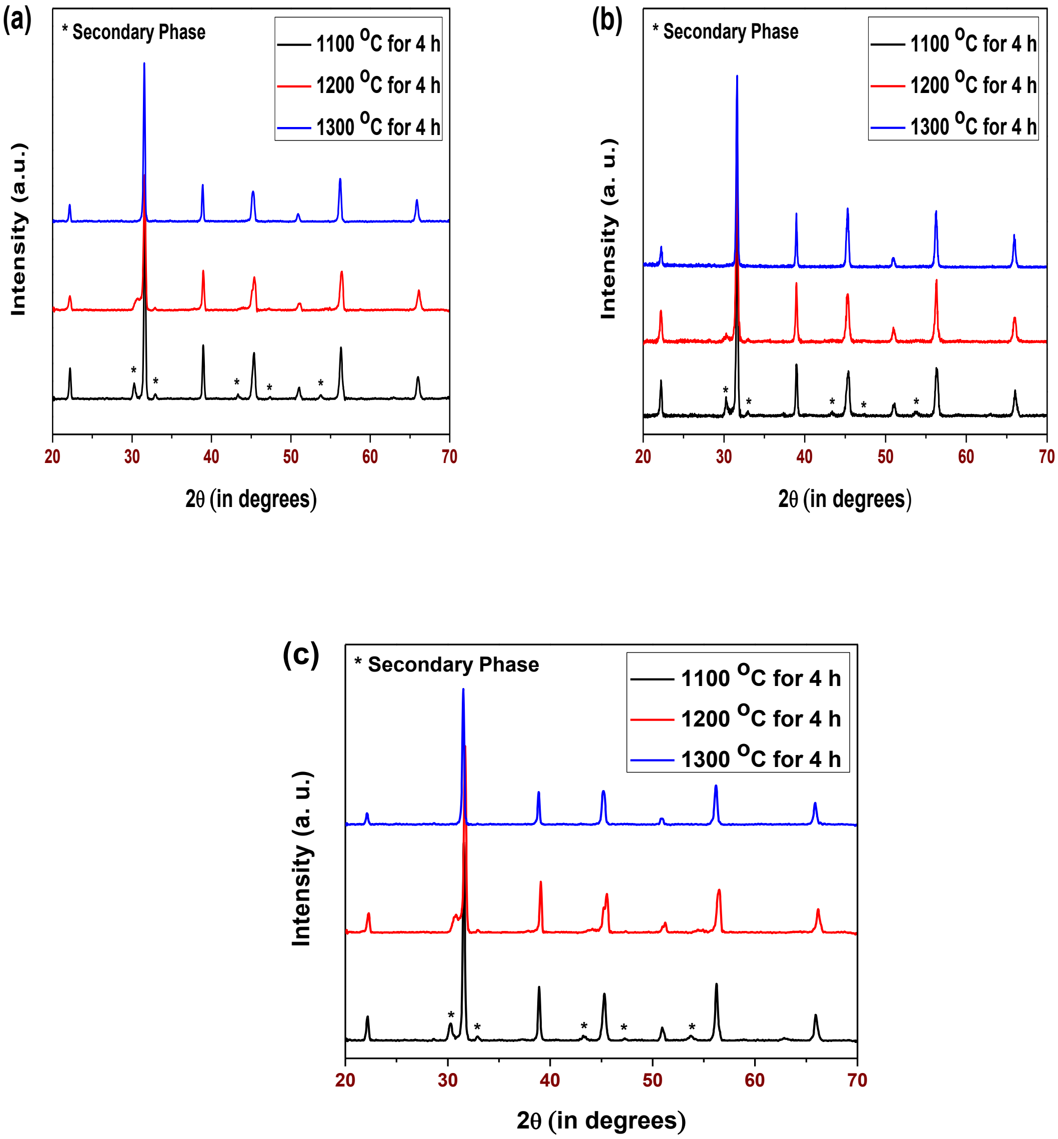

Fig. 4.2 XRD patterns of the calcined xBZT-(1-x)BCT ceramics for (a) x = 0.48, (b) x = 0.50 and (c) x = 0.52.

Here, at all sintering temperatures with the increase in x in the xBZT-(1-x)BCT ceramics, initially the RD (Relative Density) increases and becomes maximum at x = 0.50, but with the further increase in x the RD decreases. This lowering of RD in the xBZT-(1-x)BCT at x = 0.52 ceramics may be due to the lower melting point of $BaCO_3$ (~ 811°C) and $CaCO_3$ (~ 825°C), which improves the densification with the formation of liquid phase at high temperature [6]. It is known that the formation of liquid phase, which leads to rearrangement of particles and providing more effective packing, is a critical parameter for densification of the perovskite based ceramics. The RD at 1400°C sintering temperature of the 0.48BZT-0.52BCT & 0.52BZT-0.48BCT ceramics is found to be ~ 95 and 96 %, respectively, whereas the RD of 0.50BZT-0.50BCT ceramic is ~ 97 %. With the increase in sintering temperature beyond 1400°C, the RD decreases which may be due to the formation of excess liquid phase in the ceramics. Therefore, based on this study, 1400°C for 6 h has been optimized as the sintering temperature of the MPB compositions of the (BZT-BCT) systems.

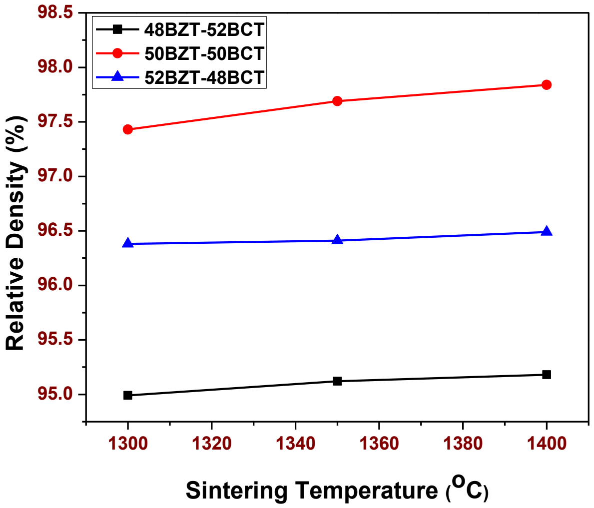

Fig.4.3 Relative density (RD) of xBZT-(1-x)BCT ceramics sintered at different temperatures.

4.1.3 Structural Study

Fig. 4.4 shows the XRD patterns of the xBZT-(1-x)BCT ceramics sintered at optimum temperature. XRD peaks of 0.48BZT-0.52BCT and 0.50BZT-0.50BCT samples reveal the development of single perovskite phase without any secondary phase peaks, while 0.52BZT-0.48BCT system shows the presence of secondary phases. The XRD peaks are also found to be sharp and distinct indicating good homogeneity and crystallinity of the samples. The diffraction lines of different compositions of the (BZT-BCT) system, calcined at 1300°C, are indexed in different crystal systems and unit cell configurations using a computer program package 'Powdmult' [7]. Standard deviations (S.D, $\sum \Delta d$ = (d_{obs} - d_{cal}), where, 'd' is inter-plane spacing) is found to be minimum for different crystal structures. Both the compositions of the

(BZT-BCT) system, corresponding to x = 0.48 and x = 0.52 exhibit tetragonal crystal structures, whereas coexistence of tetragonal (T) and monoclinic (M) structures are found in the composition corresponding to x = 0.50.

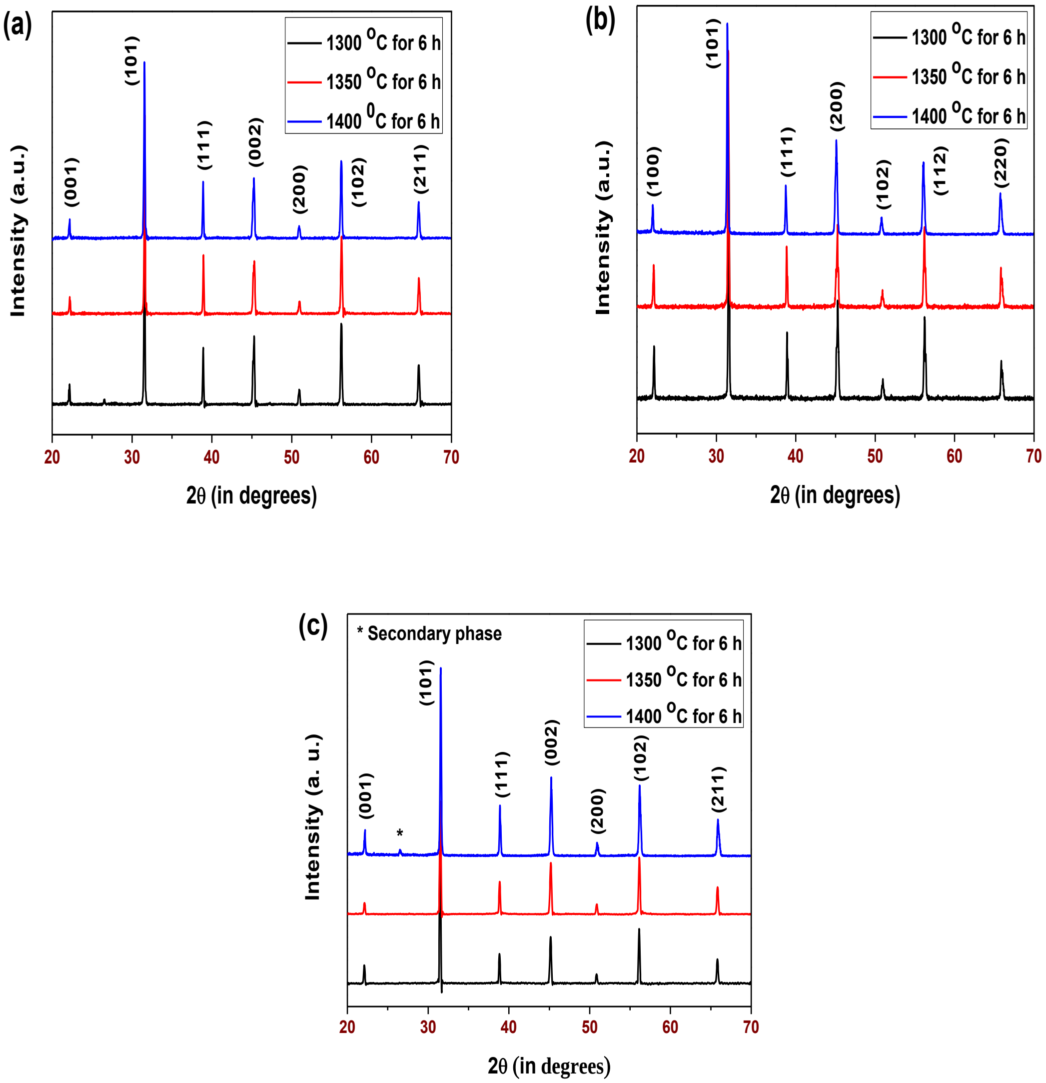

Fig. 4.4 XRD patterns of sintered xBZT-(1-x)BCT ceramics for (a) x = 0.48, (b) x = 0.50 and (c) x = 0.52.

The enlarged view of the XRD pattern of the 0.50BZT-0.50BCT composition, calcined at 1300^{o}C, in the 45^o to 46^o range is shown in the Fig. 4.5. Fig. 4.5 shows a splitting at ~ 45.5^o, confirming the presence of both monoclinic and tetragonal structures [8]. The appearance of the M phase can be explained as the follows. After sintering, when a poly twinned tetragonal (T) domain structure is further cooled, the Landau free energy of the rhombohedral (R) phase becomes lower and lower as compared to that of the T phase. The R phase has a tendency to nucleate in these T domains by developing polarization in the direction where the T domains have zero polarization value. Since the polarization anisotropy is small near MPB, the free energy of monoclinic (M) phase is close to that of R phase, the difference in the long-range elastic and electrostatic interaction energies of the two different M and R nano-domain structures can outweigh that in the chemical free energy and the total free energy of the M nano-domain structure could be lower than that of R nano-domain structure. As a consequence, the polarization in the new direction may not develop fully into that of R phase, but rather into M phase [9-11].

The existence of double structures suggests that the composition corresponding to x = 0.50 is the actual MPB composition of the (BZT-BCT) system [12-14]. The calculated values of the lattice parameters of the (BZT-BCT) samples, calcined at 1300°C, are listed in Table – 4.1.

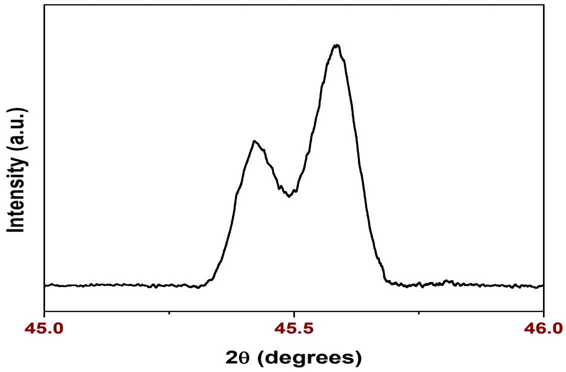

Fig. 4.5 Enlarged view of the XRD pattern of the 0.50BZT-0.50BCT composition, calcined at 1300°C.

Table – 4.1 Various physical parameters of (BZT-BCT) ceramics

Compositions of (BZT-BCT) system	**Structure**	**Lattice parameters (Å)**	**Volume (Å^3)**
48-52	Tetragonal	a = 3.991 b = 3.991 c = 4.016	V = 63.97
50-50	Tetragonal	a = 3.996 c = 4.017	V = 64.16
	Monoclinic	a = 5.645 b = 4.015 c = 3.994	V = 64.13
52-48	Tetragonal	a = b = 4.005 c = 4.008	V = 64.28

4.1.4 UV-Vis Absorption Spectroscopy Study

UV–Visible absorption spectroscopy is one of the important and commonly employed techniques for finding out the band gap of a material. In this technique, photons of selected wavelengths are directed at the sample and their relative transmittance is observed. Since the photons with energies greater than the band gap are absorbed while photons with energies less than the band gap are transmitted, the technique serves to provide an accurate measurement of the energy band gap. The optical band gap is dependent upon the particle shape, particle size and defect concentration in the crystal. The absorption spectrum of the (0.50BZT-0.50BCT) sample has been recorded in the 200 to 800 nm wavelength ranges and is shown in Fig. 4.6.

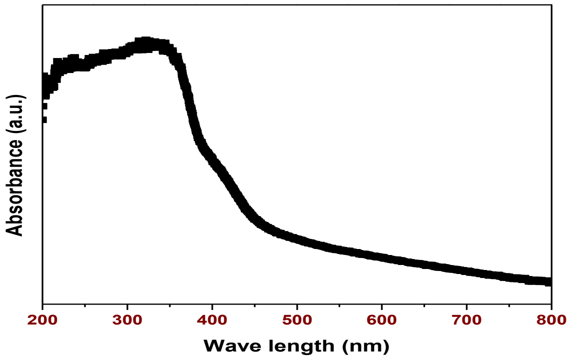

Fig. 4.6 UV-Visible absorption spectra of (BZT-BCT) ceramics

To know the nature of the transition, whether direct or indirect can be determined by using the following relation proposed by Tauc, Davis & Mott [15]

$$\text{Absorption coefficient } (\propto) = \frac{A(h\nu - E_g)^n}{h\nu} \qquad (4.1)$$

Where, hν is the energy of the incident photon, A is a constant, E_g is the optical band gap of the material & the exponent 'n' denotes the nature of the sample transition. The value of the exponent 'n' denotes the nature of the sample transition. For direct allowed transition, n=1/2. For direct forbidden transition, n=3/2. For indirect allowed transition, n=2. And for indirect forbidden transition, n=3. Since in this experiment, the indirect allowed transition is used, we can take the value of n=2.

The energy gap estimated by plotting $(\propto h\nu)^2$ vs hν is shown in Fig. 4.7. The value of hν extrapolated to $\propto = 0$ gives an absorption energy, which corresponds to a band gap E_g. The value of band gap energy ~ 3.12 eV is found for the 0.50BZT-0.50BCT ceramic sample, sintered at 1400°C.

4.1.5 Morphological Study

Fig. 4.8 shows the SEM micrographs of the xBZT-(1-x)BCT (x = 0.48, 0.50, 0.52) ceramic samples sintered at 1300, 1350 and 1400°C for 6 h, respectively. The (BZT-BCT) ceramic samples exhibit regular shaped grains with clear grain boundaries. The average grain size of the (BZT-BCT) ceramic samples, sintered at different temperatures, is calculated by linear intercept method and given in the Table – 4.2. It is distinctly observed that as the sintering temperature increases from 1300°C to 1400°C, the grain size increases and the pore size decreases. Less porosity is observed at 1400°C sintering temperature. The increase of grain size with the increase in sintering temperature can be explained based on the phenomenological kinetic grain growth [16].

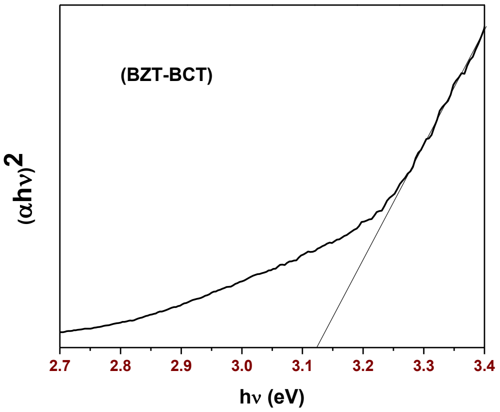

Fig. 4.7 The $(\propto h\nu)^2$ vs hν curves for (BZT-BCT) ceramics.

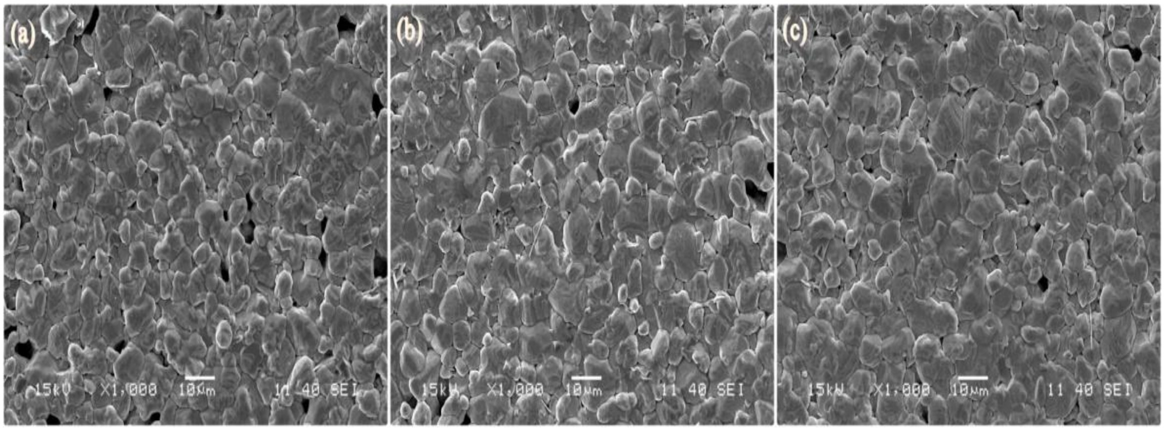

Fig. 4. 8(i) SEM micrographs of 0.48BZT-0.52BCT ceramics sintered at (a) 1300, (b) 1350 and (c) 1400°C, respectively.

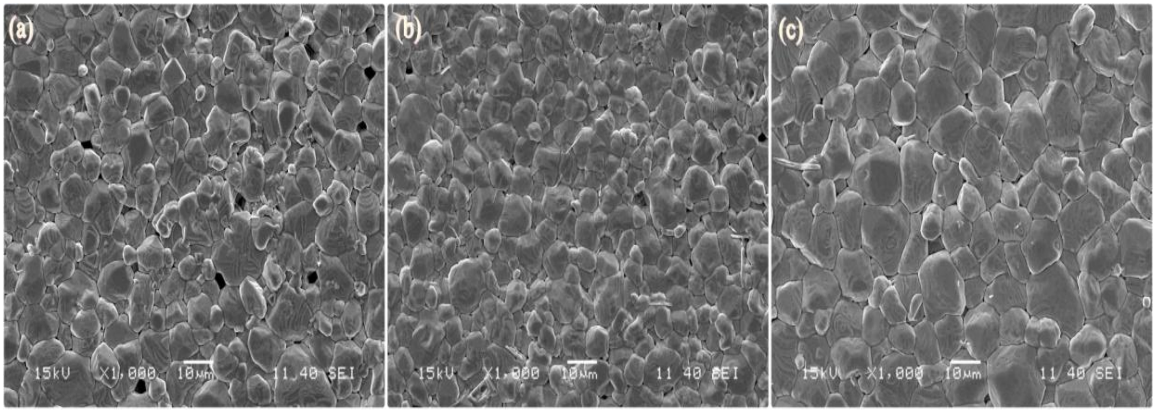

Fig. 4. 8(ii) SEM micrographs of 0.50BZT-0.50BCT ceramics sintered at (a) 1300, (b) 1350 and (c) 1400°C, respectively.

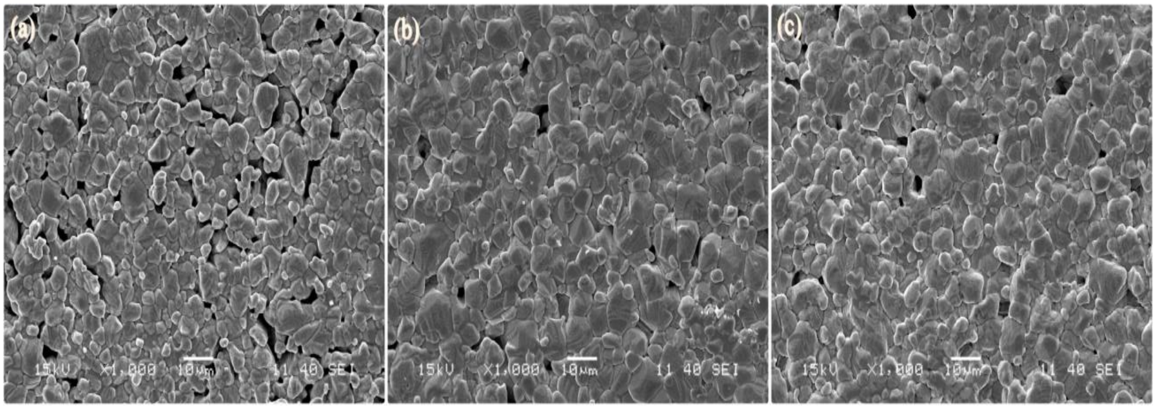

Fig. 4. 8(iii) SEM micrographs of 0.52BZT-0.48BCT ceramics sintered at (a) 1300, (b) 1350 and (c) 1400°C, respectively.

4.1.5.1 Density & Porosity Measurements

The experimental density (d_{ex}) of different compositions of the (BZT-BCT) ceramic samples, sintered at different temperatures, is measured by Archimedes' method. It is clearly observed that, for all the compositions, the density increases with the increase in sintering temperature. This is also confirmed by SEM study (shown in Fig. 4.8), where the distribution of pores decreases through diffusion kinetics with the increase in sintering temperature. The highest density ~ 5.29 gm/cc is observed in the 0.50BZT-0.50BCT ceramics, sintered at 1400°C

[17]. The values of experimental densities and porosity of the (BZT-BCT) ceramic samples are listed in the Table – 4.2.

Table – 4.2 Density, porosity & average grain size of (BZT-BCT) ceramics

Compositions of (BZT-BCT) system	Sintering temperature in °C	d_{ex} in gm/cm^3	Porosity in %	Average grain size in μm
48-52	1300	4.88	5.01	7.6
	1350	4.97	4.88	7.7
	1400	4.99	4.82	7.7
50-50	1300	5.04	2.57	7.3
	1350	5.18	2.31	7.3
	1400	5.29	2.16	7.7
52-48	1300	5.01	3.62	6.2
	1350	5.07	3.59	6.4
	1400	5.09	3.51	6.9

4.1.6 Dielectric Properties

4.1.6.1 Frequency Dependence of Dielectric Constant (ε_r) and Dielectric Loss (tanδ)

Fig. 4.9 shows the frequency dependence of dielectric constant (ε_r) for different MPB compositions of the (BZT-BCT) system, sintered at 1400°C. The RT value of ε_r at 1kHz frequency of sintered (BZT-BCT) ceramic samples are listed in Table – 4.3. Initially, ε_r decreases slowly with the increase in frequency and at higher frequencies it decreases rapidly. It is observed that at higher frequencies ε_r decreases more rapidly for 0.50BZT-0.50BCT composition. The decrease in the value of ε_r can be explained on the basis of decrease in net polarization with the increase in frequency. Polarization of a dielectric material is the sum of the contributions of dipolar, electronic, ionic and interfacial polarizations [18]. At low frequencies, all the polarizations respond easily to the time varying electric field but as the frequency of the electric field increases different polarization contributions filters out. As a result, the net polarization of the material decreases which leads to the decrease in the value of ε_r. Among different MPB compositions of the (BZT-BCT) system, the x = 0.50 composition, sintered at 1400°C has the highest $\varepsilon_{r.}$ This can be explained on the basis of the presence of mixed structures in this x = 0.50 MPB composition. The presence of mixed structure increases the number of polarization orientations in this composition, which leads to higher polarization and hence higher dielectric constant.

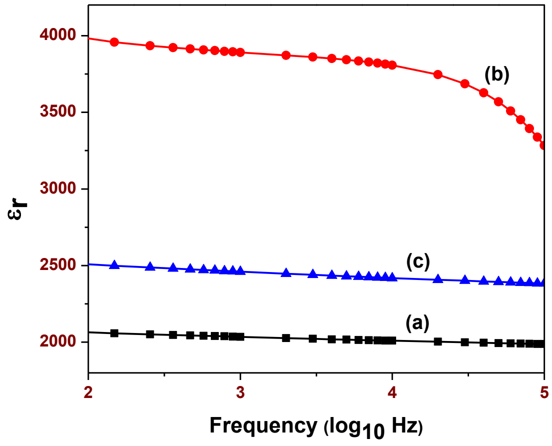

Fig. 4. 9 RT frequency dependence of ε_r of xBZT-(1-x)BCT, with x = (a) 0.48, (b) 0.50 and (c) 0.52 samples sintered at 1400^{o}C.

Fig. 4.10 shows the frequency dependence of dielectric loss (tanδ) at RT and at 1kHz frequency of the (BZT-BCT) MPB compositions, sintered at 1400^{o}C. The RT value of tanδ of sintered (BZT-BCT) ceramic samples are listed in Table – 4.3.

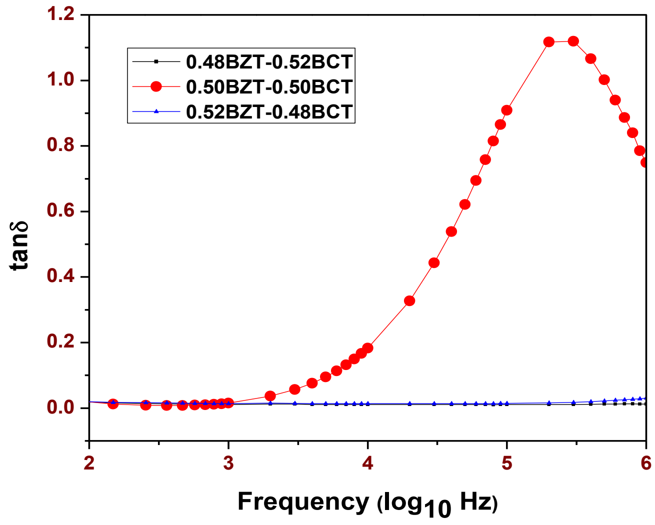

Fig. 4. 10 RT frequency dependence of tanδ of 0.48BZT-0.52BCT, 0.50BZT-0.50BCT & 0.52BZT-0.48BCT samples sintered at 1400^{o}C.

It is observed from Fig. 4.10 that there exists a maximum in the tanδ vs. frequency graph for the 0.50BZT-0.50BCT MPB composition. In a ferroelectric material there can exist several resonance peaks, which hints that in 0.50BZT-0.50BCT ceramic samples, a resonance phenomenon is taking place near the frequency at which tanδ becomes maximum [19].

4.1.6.2 Temperature Dependence of Dielectric Constant (ε_r) and Dielectric Loss (tanδ)

Fig. 4.11 (i-ix) shows the temperature dependence of dielectric constant (ε_r) at four different frequencies of (BZT-BCT) ceramics, sintered at different sintering. The values of ε_r and tanδ for the (BZT-BCT) ceramic system at four different applied frequencies are given in Table - 4.4. The plots of ε_r vs. temperature are a typical behaviour of a ferroelectric system, which confirms phase transition of that material at a temperature called as Curie temperature (T_c). It can be seen that with the increase in x content, T_c of the xBZT-(1-x)BCT ceramics decreases. The dielectric broadening at the paraelectric-ferroelectric phase transition in (BZT-BCT) system is due to compositional fluctuations and microscopic inhomogeneity [20-22]. Therefore, this decrease in T_c with increase in x content suggests the decrease in compositional fluctuations and microscopic inhomogeneity.

Fig. 4.12 shows the temperature dependence of ε_r at 1 kHz frequency of xBZT-(1-x)BCT ceramics with (x = 0.48, 0.50 & 0.52) sintered at optimum temperature. It is evident from the Fig. 4.12 that the phase transition is observed near T_c. The highest permittivity ($\varepsilon_r \sim 5529$) at T_c is observed for the 0.50BZT-0.50BCT ceramics. The ε_r value of (BZT-BCT) ceramic samples increases with the increase in temperature and near T_c it shows strong anomalies in the value of ε_r. This can be explained on the basis of increase in domain wall mobility with the increase in temperature. Also, the phase transition in perovskite materials generally occurs due to instability of temperature dependent low frequency optical soft mode [23, 24]. At T_c, frequency of the soft mode tends to zero and the lattice displacement associated with it becomes unstable and leads to phase transition. A transverse radiation field derives the soft transverse optical mode of the material in a forced vibration. Energy is transferred from the electromagnetic field to this lattice mode and is then degraded into other vibrational modes. Therefore, the sharp rise of ε_r value near T_c can be due to the presence of soft mode frequency in the system [25]. Again, the T_c decreases with the increase in Zr content and decrease in Ca content due to the changes in crystal structure. Addition of Zr^{4+} ions substituent has more prominent effect on T_c than the addition of Ca^{2+} ions. A small increment in Zr^{4+} addition lowers the T_c more rapidly than that of Ca^{2+} addition [26]. The obtained Curie temperatures are ~ 115, 108 & 96°C for 0.48BZT-0.52BCT, 0.50BZT-0.50BCT and 0.52BZT-0.48BCT ceramics, respectively. From the Fig. 4.12, it can also be seen that all (BZT-BCT) ceramics have broad peak at around Curie temperature. The dielectric broadening is maximum for 0.48BZT-0.52BCT samples and it decreases with the increase in Zr content in the (BZT-BCT) system. This dielectric broadening at the phase transition in the (BZT-BCT) system is due to compositional fluctuations and micro-inhomogeneity [20]. Decrease in dielectric broadening with the increase in Zr content suggests that the microscopic inhomogeneity is decreasing with the increase in Zr content.

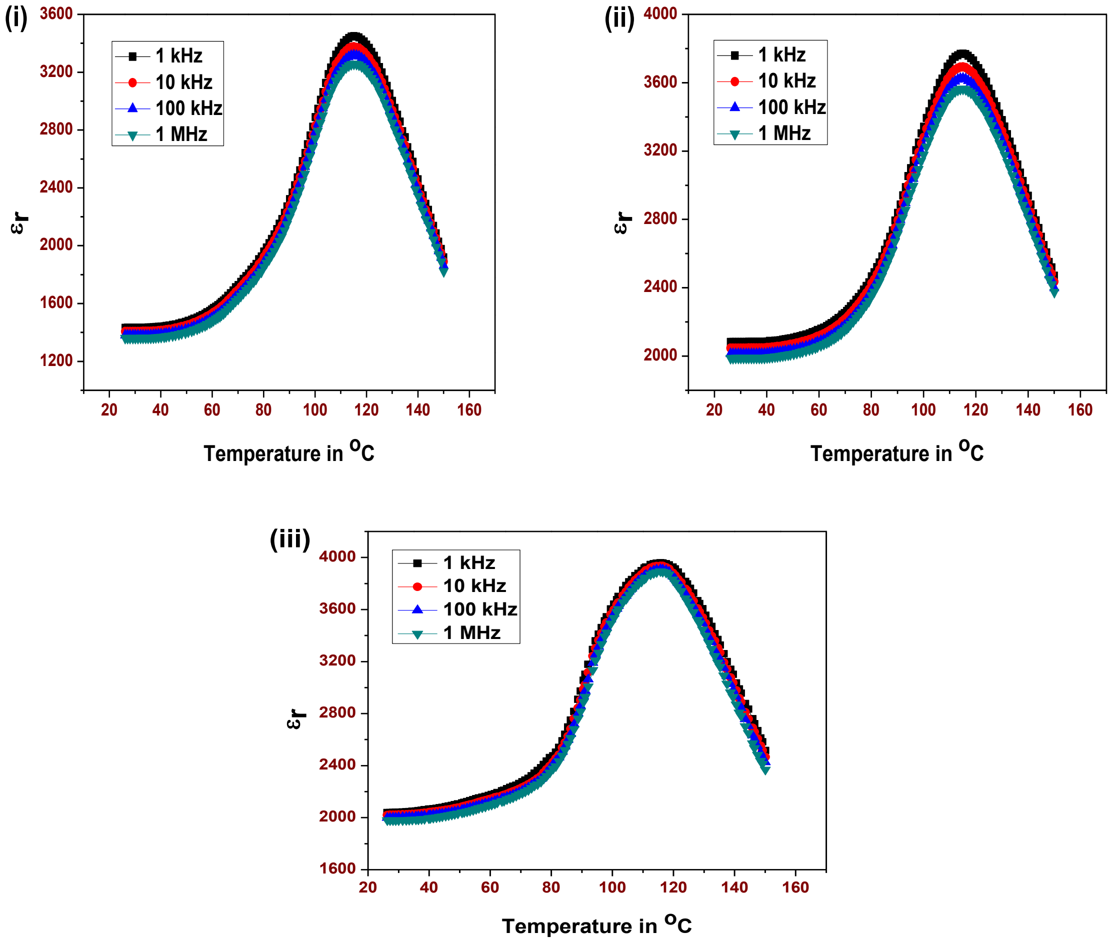

Fig. 4.11(i-iii) Temperature dependence of ε_r of 0.48BZT-0.52BCT ceramics sintered at (i) 1300, (ii) 1350 & (iii) 1400°C, respectively.

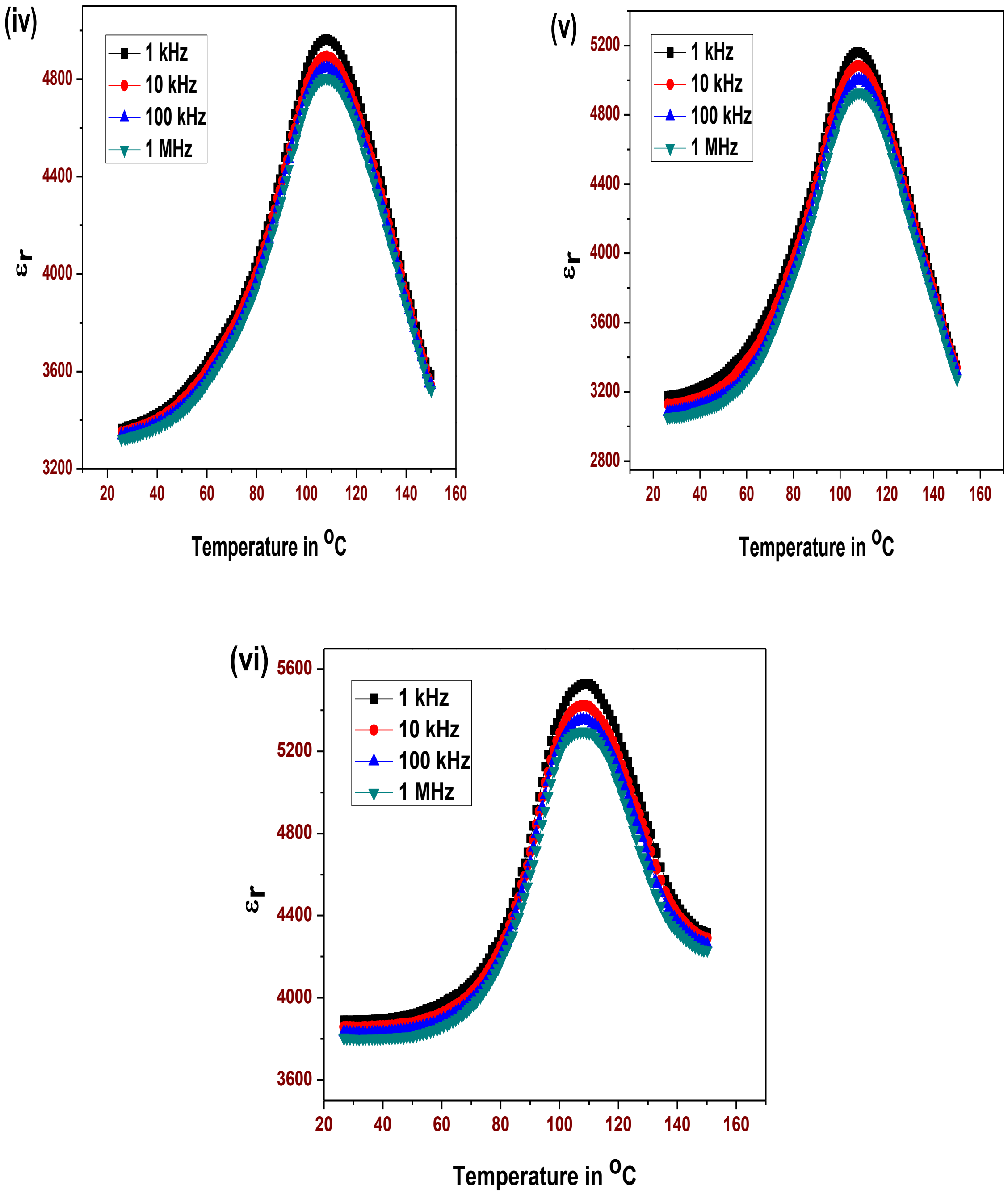

Fig. 4.11(iv-vi) Temperature dependence of ε_r of 0.50BZT-0.50BCT ceramics sintered at (iv) 1300, (v) 1350 & (vi) 1400^{o}C, respectively.

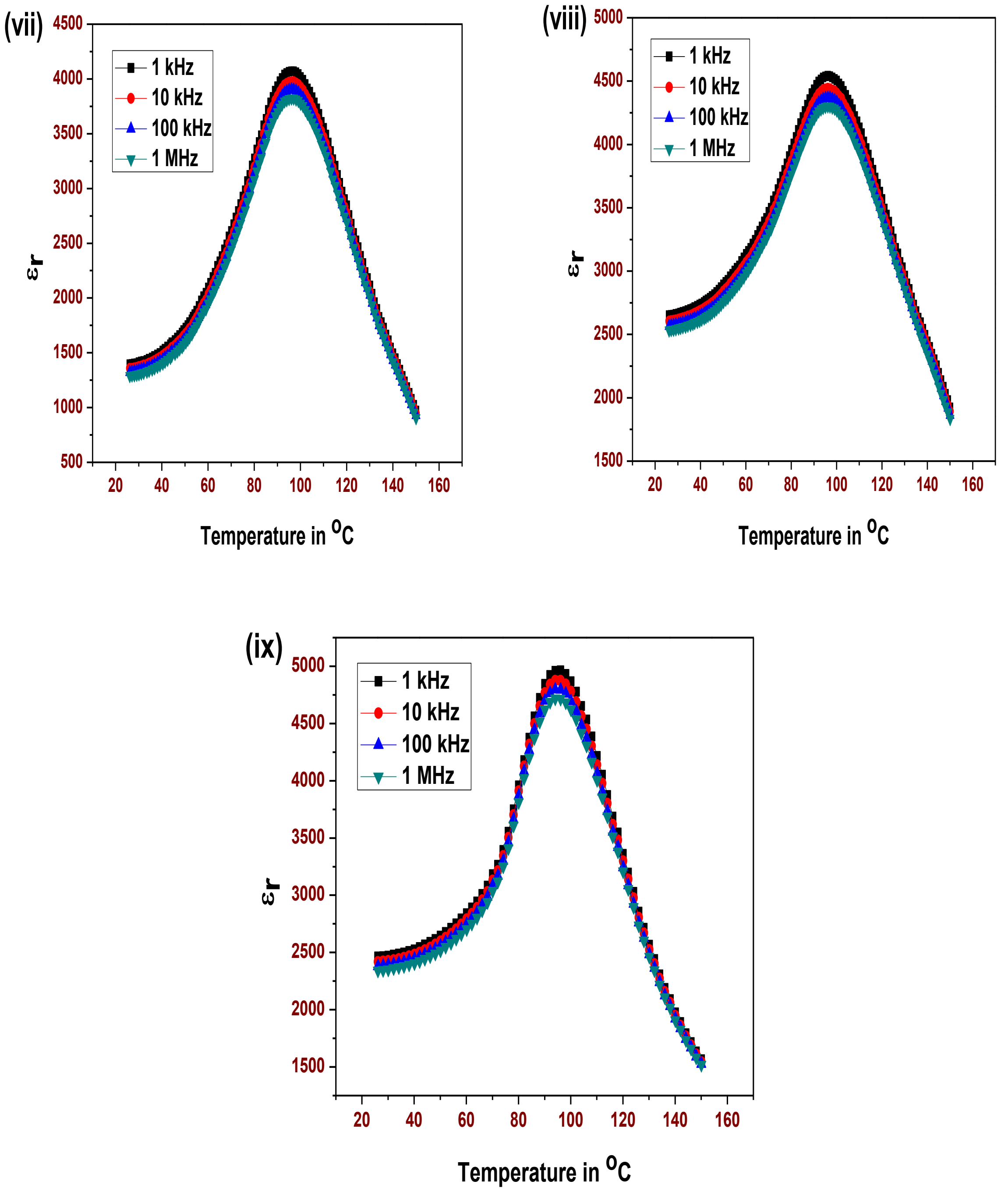

Fig. 4.11(vii-ix) Temperature dependence of ε_r of 0.52BZT-0.48BCT ceramics sintered at (vii) 1300, (viii) 1350 & (ix) 1400°C, respectively.

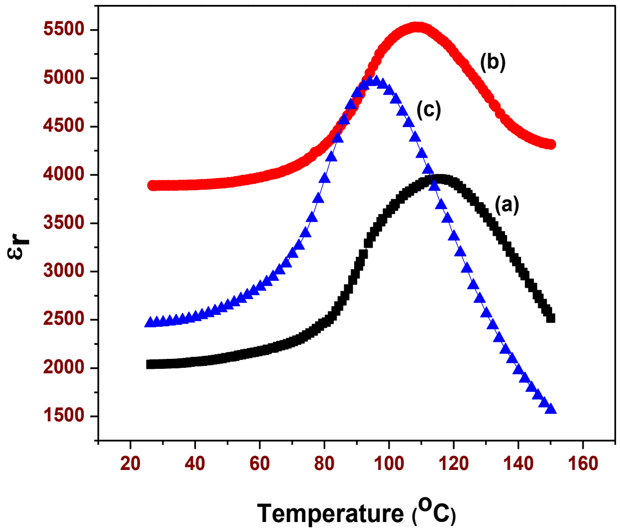

Fig. 4.12 Variation of ε_r with temperature of xBZT-(1-x)BCT samples at 1 kHz sintered at optimum temperature for (a) x = 0.48, (b) x = 0.50 and (c) x = 0.52.

Fig. 4.13 (i-ix) show the temperature dependence of dielectric loss (tanδ) at four different frequencies of (BZT-BCT) ceramic systems, sintered at different temperatures. It is observed that the tanδ increases with the increase in temperature at all the frequencies. The increase in tanδ value of the (BZT-BCT) is very small up to 60°C and above this temperature there is a sudden increase in the tanδ value. A clear peak has been observed at 110-130°C for 1 MHz and this peak is more broadened and shifted to higher temperature side with an increase in frequency. The peak positions are observed to be in the temperature between 100°C to 130°C. The increasing trend in tanδ (at different frequencies) at higher temperatures may be due to space charge polarization [27]. This may also be due to the increase in the mobility of ions and imperfections in the ceramics [27]. It can also be seen that the temperatures of peak dielectric loss and peak dielectric constant do not coincide. Kramers–Kronig relation indicates that this can be the consequence of temperature dependent relaxation near Curie temperature [27].

Fig. 4.14 show the temperature dependence of dielectric loss (tanδ) at 1 kHz frequency of xBZT-(1-x)BCT ceramics with (x = 0.48, 0.50 & 0.52) sintered at optimum temperature.

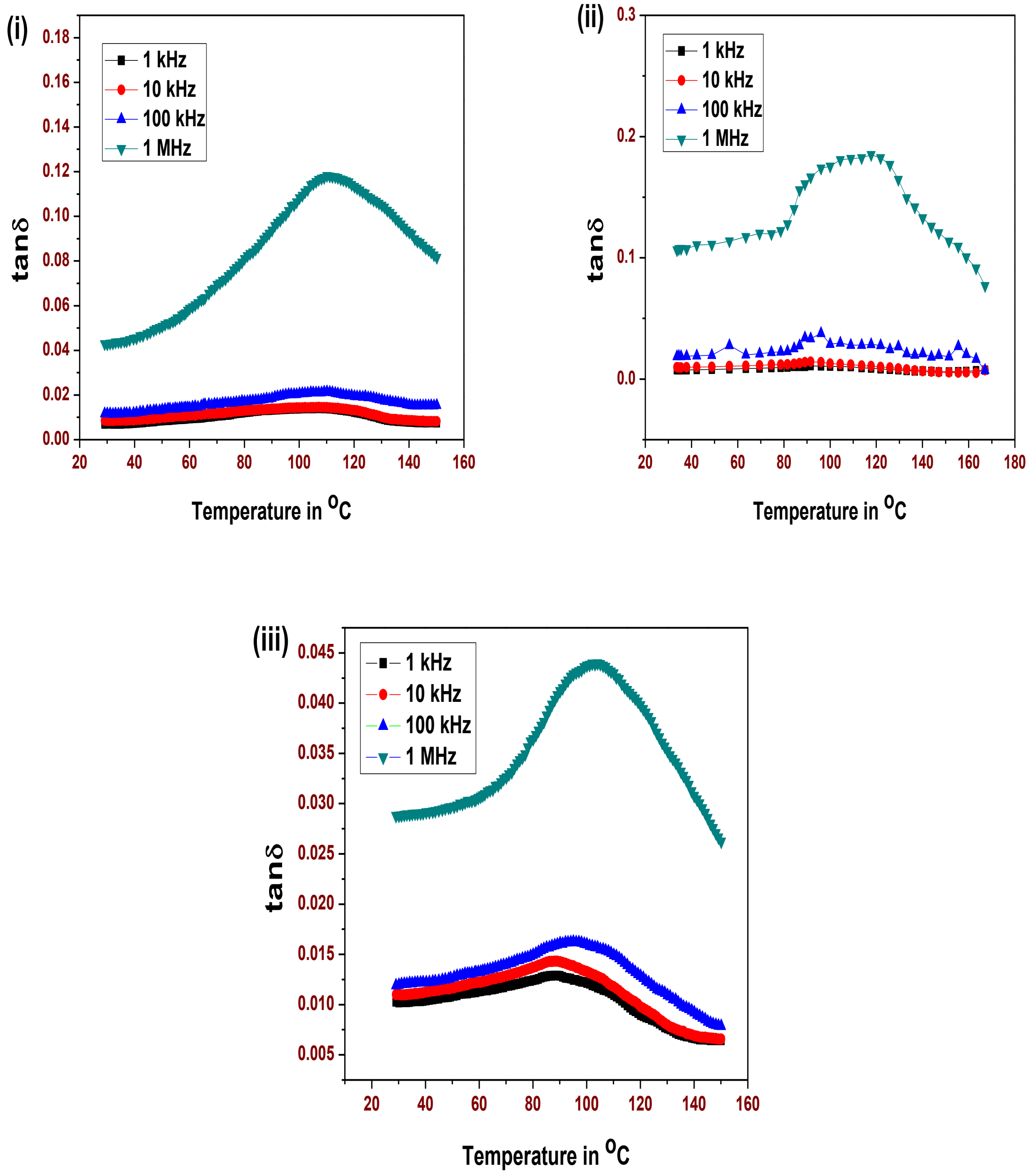

Fig. 4.13(i-iii) Temperature dependence of tanδ of 0.48BZT-0.52BCT ceramics sintered at (i) 1300, (ii) 1350 & (iii) 1400°C, respectively.

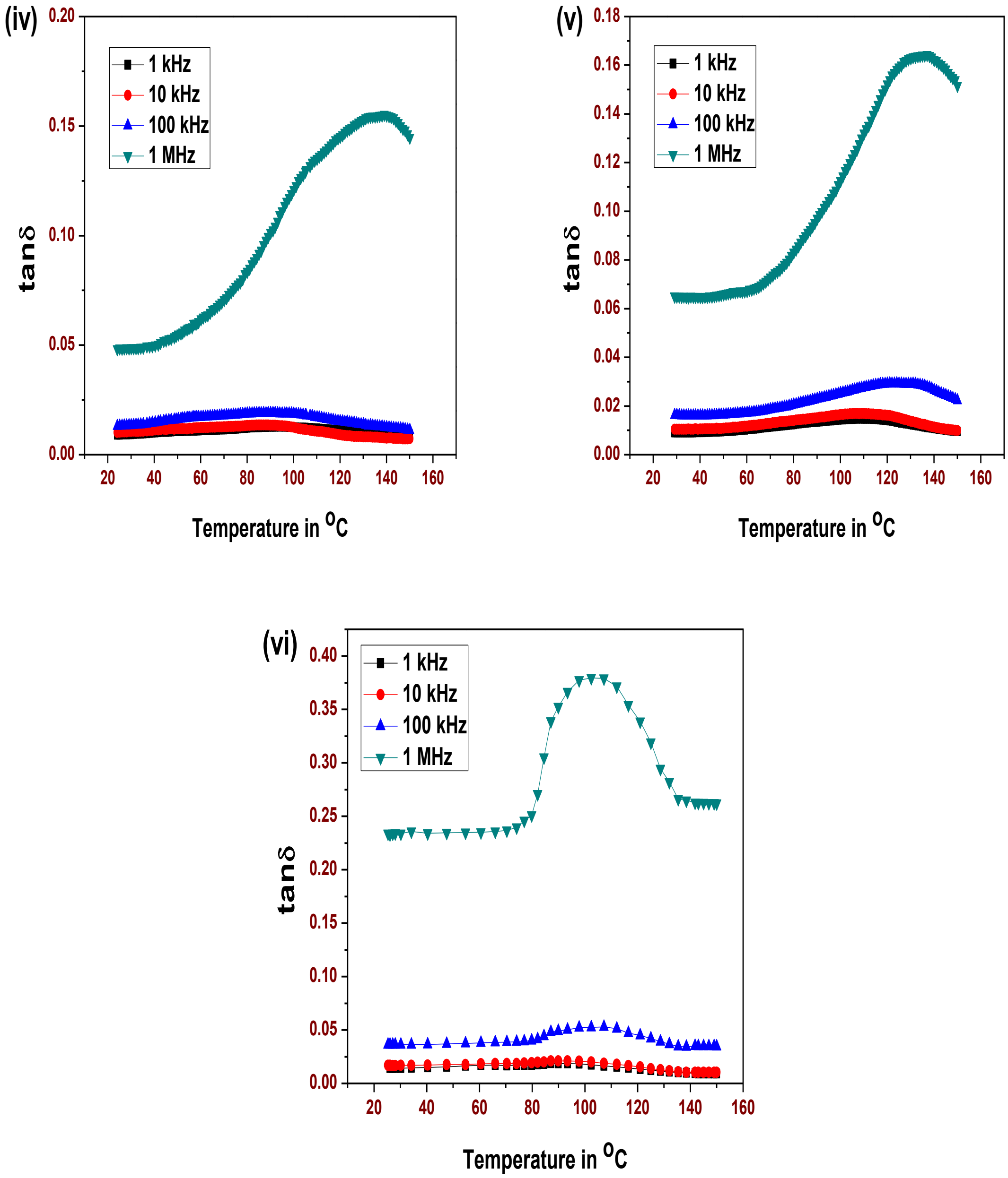

Fig. 4.13(iv-vi) Temperature dependence of tanδ of 0.50BZT-0.50BCT ceramics sintered at (iv) 1300, (v) 1350 & (vi) 1400^{o}C, respectively.

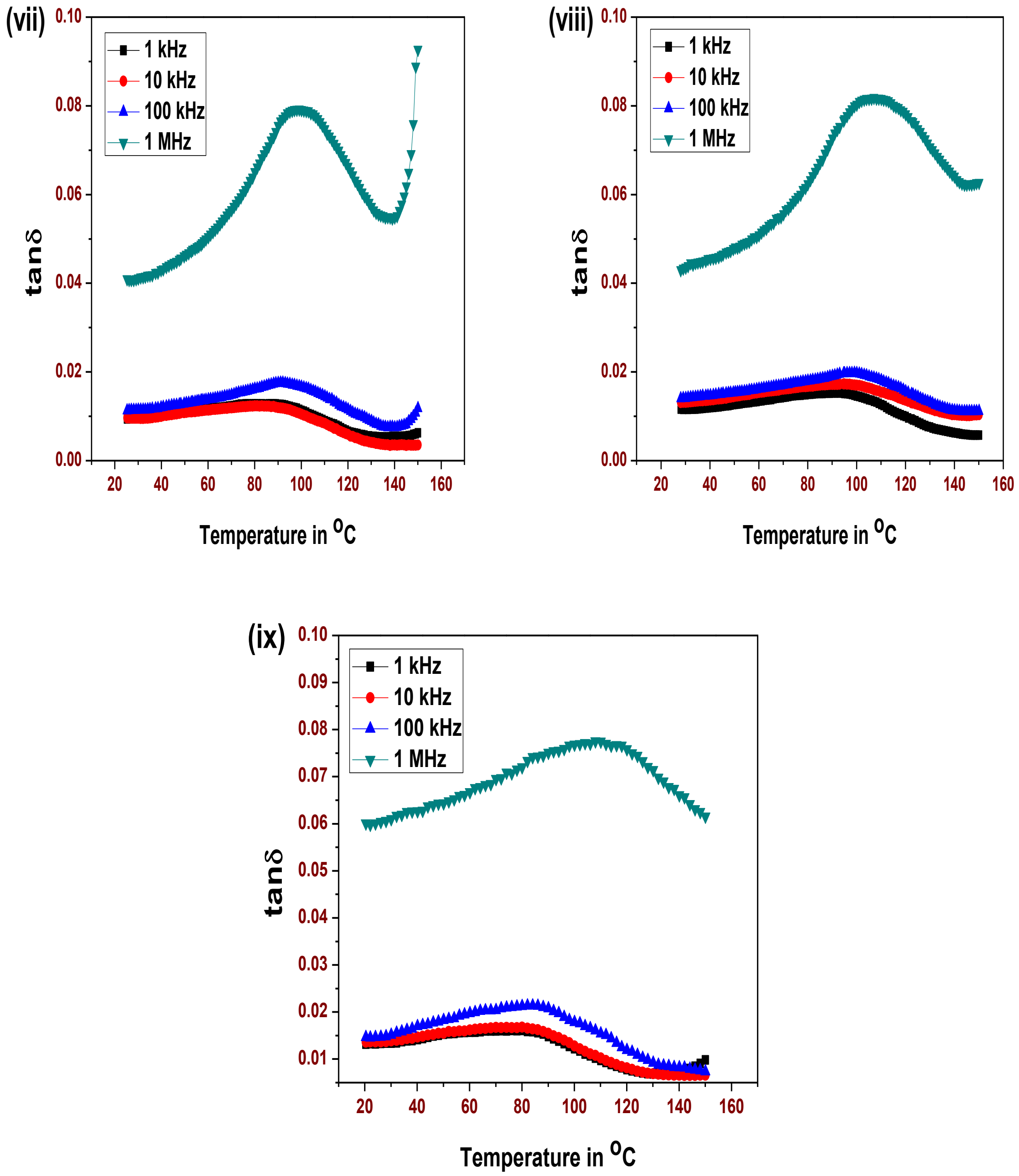

Fig. 4.13(vii-ix) Temperature dependence of tanδ of 0.52BZT-0.48BCT ceramics sintered at (vii) 1300, (viii) 1350 & (ix) 1400°C, respectively.

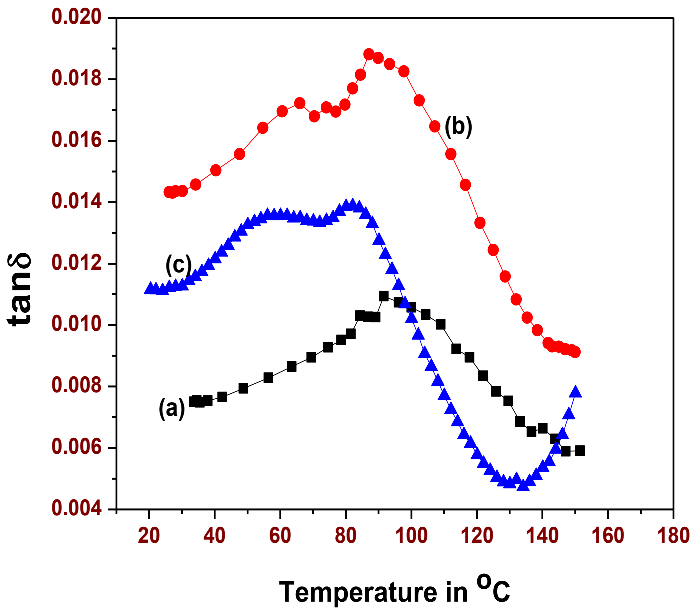

Fig. 4.14 Variation of tanδ with temperature of xBZT-(1-x)BCT samples at 1 kHz sintered at optimum temperature for (a) x = 0.48, (b) x = 0.50 and (c) x = 0.52.

Table – 4.3 Variation of dielectric properties & diffusivity of sintered (BZT-BCT) system at different temperatures

Compositions of (BZT-BCT) system	**Sintering temperature in °C**	**T_c in °C**	**ε_r at RT (at 1kHz)**	**tanδ at RT (at 1kHz)**	**ε_r at T_c (at 1kHz)**	**Diffusivity factor (γ)**
48-52	1300	115	1432	0.006	3449	1.9
	1350	115	2082	0.007	3769	1.9
	1400	115	2038	0.010	3958	1.9
50-50	1300	108	3367	0.008	4962	1.7
	1350	108	3176	0.009	5162	1.8
	1400	108	3888	0.014	5529	1.8
52-48	1300	96	1396	0.009	4070	2.0
	1350	96	2652	0.011	4541	2.0
	1400	96	2463	0.013	4962	1.9

Table - 4.4 Details of dielectric properties of sintered (BZT-BCT) system

Compositions of (BZT-BCT) system	**48-52**			**50-50**			**52-48**		
Sintering temperature in °C	1300	1350	1400	1300	1350	1400	1300	1350	1400
ε_r at RT at 1 kHz	1432	2082	2038	3367	3176	3888	1396	2652	2463
ε_r at RT at 10 kHz	1406	2046	2020	3351	3127	3857	1356	2605	2418
ε_r at RT at 100 kHz	1381	2013	1999	3338	3083	3830	1323	2566	2381
ε_r at RT at 1 MHz	1360	1988	1980	3322	3051	3806	1289	2533	2341
tanδ at RT at 1 kHz	0.006	0.007	0.010	0.008	0.009	0.014	0.009	0.011	0.013
tanδ at RT at 10 kHz	0.008	0.009	0.010	0.010	0.010	0.016	0.009	0.013	0.013
tanδ at RT at 100 kHz	0.011	0.018	0.011	0.013	0.016	0.036	0.011	0.014	0.014
tanδ at RT at 1 MHz	0.042	0.106	0.028	0.048	0.064	0.233	0.040	0.042	0.060

4.1.7 Diffusivity Study

All the (BZT-BCT) ceramic samples show broad and diffuse phase transitions. Generally, the diffuse phase transition is attributed to inhomogeniety in the chemical composition at nano or micro scale region [28, 29]. The modified empirical expression, proposed by Uchino and Nomura [30], is used to describe the diffuseness of ferroelectric phase transition, given as follows:

$$1/\varepsilon_r - 1/\varepsilon_{r(max)} = (T - T_{max})^{\gamma} / C \qquad (4.2)$$

Where, ε_r is dielectric constant, $\varepsilon_{r(max)}$ is the maximum dielectric constant, T is temperature, T_{max} is the temperature (corresponding to $\varepsilon_{r(max)}$) at which ε_r value reaches the maximum, and γ

is diffusivity. γ and C are assumed to be constants. The values of γ can be estimated from the slope of linear fitting of the data points obtained from the plot of log($1/\varepsilon_r$–$1/\varepsilon_{r(max)}$) vs. log(T–T_{max}). The value of γ is the expression of degree of dielectric relaxation (diffusivity factor) & is a material constant depending on the composition and structure of the material [31]. The limiting value γ = 1 makes the equation fit for the conventional Curie-Weiss law which is valid for the normal ferroelectrics and the limiting value γ = 2 makes the equation fit for the material having diffusive phase transition, normally for relaxor ferroelectric systems [32]. γ value between 1 and 2 corresponds to the incomplete diffuse phase transition where the correlated ferroelectric clusters are hypothesized [33].

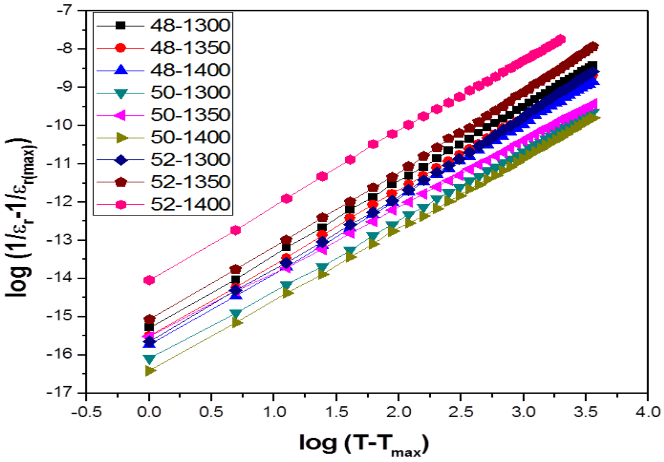

Fig. 4.15 Plot between log ($1/\varepsilon_r$-$1/\varepsilon_{r(max)}$) vs log (T-T_{max}) for sintered (BZT–BCT) ceramic samples.

Fig. 4.15 shows the plot between log ($1/\varepsilon_r$-$1/\varepsilon_{r(max)}$) versus log (T-T_{max}) for the (BZT-BCT) ceramic samples sintered at different temperatures. The values of diffusivity factor (γ), calculated from the slope of the plot are given in Table – 4.3. From the value of γ of different compositions of the (BZT-BCT) systems, sintered at different temperatures, the phase transitions are of diffusive nature. Diffuse phase transition in the (BZT-BCT) systems, sintered at different temperatures, can be explained based on different theories. As per Smolensky–Isupov theory, diffuse phase transition can be explained on the basis of composition fluctuations of different polar micro regions where different B′ and B″ ions try to occupy the same crystallographic B site, in a simple perovskite structure (ABO_3) [30]. Based on this theory, it can be concluded that at higher sintering temperature, the competition between Ti and Zr ions increases to occupy the same crystallographic site B, which leads to an increase in composition fluctuations [34] of different polar micro-regions and hence increase in diffuse phase transition nature in (BZT-BCT) system.

4.1.8 Piezoelectric Study

The piezoelectric constant (d_{33}) of the xBZT-(1-x)BCT (x = 0.48, 0.50, 0.52) ceramic samples, sintered at 1300, 1350 and 1400^{o}C, respectively are given in Table – 4.5. Maximum value of d_{33} (~ 281 pC/N) is obtained in case of 0.50BZT-0.50BCT ceramics sintered at 1400^{o}C, which may be due to the exact MPB nature of the this composition.

4.1.9 P-E Loop Study

In order to examine the ferroelectric nature of the (BZT-BCT) ceramics, the polarization vs. electric field (P-E) loops are measured and shown in Fig. 4.16. Saturated hysteresis loops are developed in all the (BZT-BCT) ceramics which is a clear evidence of the ferroelectric nature of the (BZT-BCT) ceramic samples under study. The remnant polarization (P_r) and coercive field (E_c) of the (BZT-BCT) ceramic samples sintered at 1300, 1350 and 1400^{o}C are listed in Table – 4.5. From the Fig. 4.16, it is observed that P_r and E_c values of all the MPB compositions do not follow a particular trend.

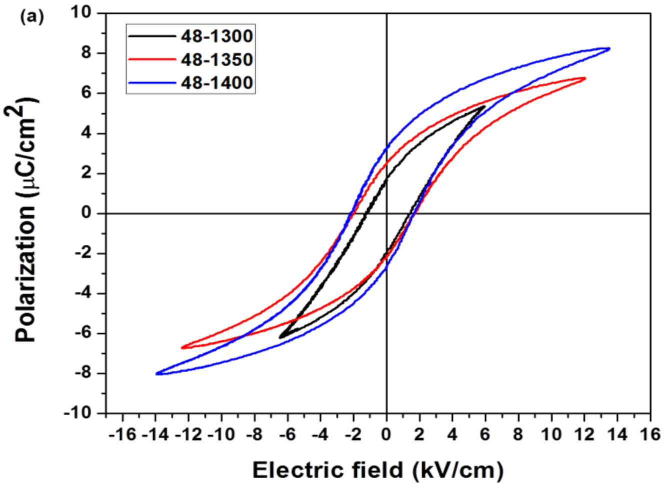

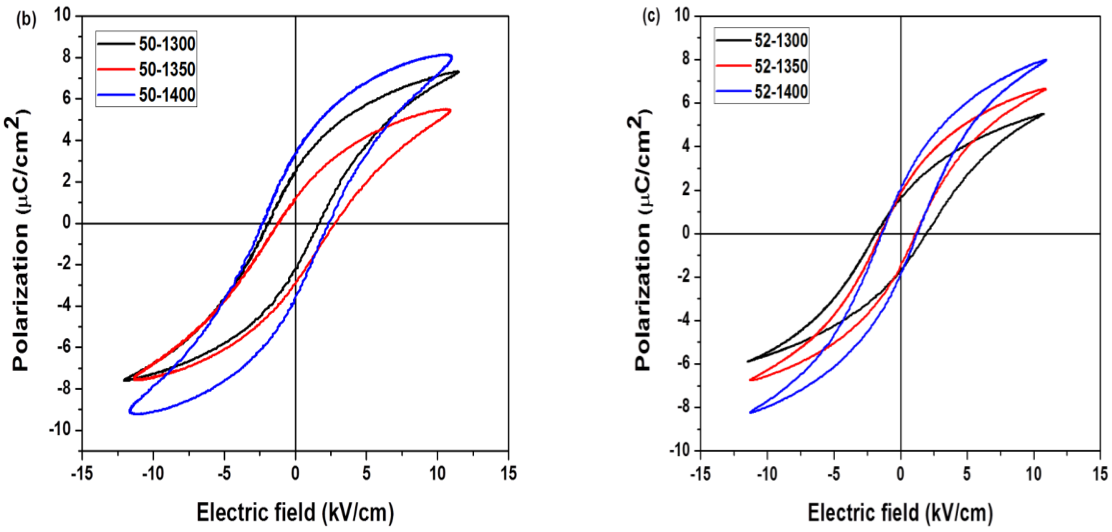

Fig. 4.16 Ferroelectric hysteresis loops of sintered (a) 0.48BZT–0.52BCT, (b) 0.50BZT-0.50BCT and (c) 0.52BZT-0.48BCT ceramic samples.

Table – 4.5 Variation of P_r, E_c and d_{33} values of (BZT-BCT) ceramics as a function of sintering temperature

Compositions of (BZT-BCT) system	**Sintering temperature in °C**	**P_r value in μC/cm^2**	**E_c value in kV/cm**	**d_{33} values in pC/N**
48-52	1300	0.01	1.33	208
	1350	1.60	1.83	215
	1400	2.95	1.92	270
50-50	1300	2.34	1.77	224
	1350	2.01	1.96	258
	1400	1.78	1.53	281
52-48	1300	1.62	1.89	170
	1350	1.65	1.32	178
	1400	1.92	1.32	186

4.1.10 Summary

Ferroelectric (BZT-BCT) ceramic systems near MPB region were synthesized by solid state reaction route. Single perovskite phase formation in all the (BZT-BCT) samples has been confirmed from XRD analysis at 1300°C for 4h. The optimum sintering temperature for all the MPB compositions of the (BZT-BCT) system was found to be 1400°C for 6 h. The maximum relative density ~ 97% was obtained in 0.50BZT-0.50BCT ceramic system at optimized sintering temperature. The co-existence of the tetragonal and monoclinic structures was found in the 0.50BZT-0.50BCT composition, which confirmed its MPB nature. The value of band gap energy E_g ~ 3.12 eV is found for the 0.50BZT-0.50BCT ceramic sample, sintered at 1400°C. SEM micrographs of the (BZT-BCT) ceramic samples exhibited regular shaped grains with clear grain boundaries. Maximum value of ε_r at RT was obtained in 0.50BZT-0.50BCT ceramics samples. P–E hysteresis loops confirmed the ferroelectric nature of the ceramic system. Maximum value of piezoelectric coefficient (d_{33}) ~ 281 pC/N was found in the 0.50BZT-0.50BCT system sintered at 1400°C for 6 h. The 0.50BZT-0.50BCT system sintered at 1400°C showed better structural, microstructural, dielectric, ferroelectric and piezoelectric properties, which are in accordance with the pre-determined objectives and comparable with the lead based counterparts [1]. The results in this study indicate that ferroelectric lead free 0.50BZT-0.50BCT system can be a suitable candidate to replace the lead-based materials and also for piezoelectric applications.

4.2 Structural & Electrical Properties of CCTO Ceramics

4.2.1 Introduction

Oxides with the perovskite based structure are well known for their ability to possess high dielectric constants. However, dielectric constants higher than 1,000 at RT have always been associated with ferroelectric or relaxor properties in the perovskite based structure materials. In ferroelectric and relaxor materials, the dielectric constant increases with the increase in temperature and becomes maximum at Curie transition temperature (T_c). This temperature dependence of the dielectric constant in the ferroelectric and relaxor materials is undesirable for many applications.

There are also classes of compounds, with a perovskite related structure, which have dielectric properties very different from those of the ferroelectric or relaxor materials. Their high dielectric constants show only a small dependence on temperature and frequency. Calcium copper titanate ($CaCu_3Ti_4O_{12}$)/CCTO is one such compound which has attracted the attention of many researchers because of its high dielectric constant (ε_r) at RT [35, 36]. CCTO was first discovered by Subramanian *et al*. in the year 2000 [37]. It is an oxide based cubic perovskite like ceramics ($AA'_3B_4O_{12}$). It exhibited an extremely high ε_r value (up to 10^5) at RT in the frequency range between 100 Hz and 1 MHz [35]. Again this high value of ε_r was found to be independent in the temperature range of 100-600K [38]. The drive for ultra miniaturization of the electronic devices in automobiles and air craft requires the development of high ε_r materials that are stable over a wide range of temperatures. Generally, high ε_r in perovskite materials such as $BaTiO_3$ and $PbTiO_3$ systems (ferroelectric ceramics) is associated with the atomic displacements within the non-centrosymmetric structures [39]. However, these dielectric oxides lack either temperature and/or high voltage stability, or do not possess giant dielectric permittivity. The large value of ε_r in the CCTO ceramics is ascribed to the grain boundary barrier layer capacitance effects [40, 41]. ε_r of the CCTO ceramics is reported to be highly dependent on the processing conditions such as milling time, sintering temperature and its duration along with sintering atmosphere [42-44]. The value of ε_r in the CCTO ceramics, ranging from 2000 to 80,000 can be achieved by varying the processing conditions [42-44].

In the present work, CCTO ceramics have been synthesized by the conventional solid state reaction route. The structural, microstructural, optical, and dielectric properties of the CCTO ceramics, sintered at different temperatures, have been investigated and discussed in detail.

4.2.2 Optimization of Calcination and Sintering Temperatures

For better dielectric properties CCTO ceramics should be in single perovskite phase. Therefore, to ensure the single perovskite phase formation in the CCTO ceramics the calcination temperature was optimized. In the present section optimization of the calcination and sintering processes of the CCTO ceramics are discussed in detail.

4.2.2.1 Thermal Analysis

Fig. 4.17 shows the TG-DSC curves of the uncalcined CCTO powder. The TG curve shows that from RT to 1100°C the overall weight loss is ~ 11%. The major weight loss processes in the TG curve of the CCTO ceramics are divided into three steps. The first major step of weight loss, which is ~ 7%, is observed between 600-750°C. This weight loss can be associated with the decomposition of the thermally unstable organic compounds [2]. In the same temperature range the DSC curve shows an exothermic peak. The second major step of the weight loss, which is ~ 4 %, is observed between 750-950^{o}C. The last step of major weight loss is observed after 950^{o}C. In the same temperature range the DSC curve shows a major exothermic peak. The appearance of exothermic peak in the DSC curves at ~ 950^{o}C can be correlated with the crystallization process in the CCTO powder. No further significant weight loss is observed above 950^{o}C temperature, indicating an absence of further decompositions beyond this temperature. Hence, from the TG-DSC study, it can be concluded that for the single perovskite phase formation, the calcination of the CCTO ceramic samples can be carried out above 900^{o}C.

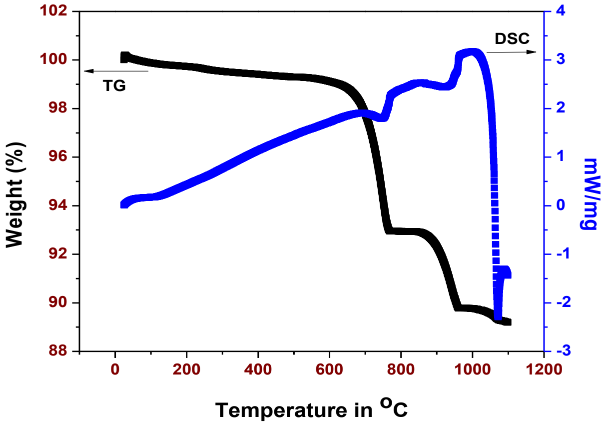

Fig. 4.17 TG-DSC curves of the uncalcined CCTO powders.

4.2.2.2 Single Perovskite Phase Formation

Fig. 4.18 shows the RT XRD patterns of the CCTO samples calcined at 900, 950, 1000 & 1050^{o}C for 4 h, respectively. Single perovskite phase is formed at 1050^{o}C for 4 h. Thus the calcination temperature for the CCTO ceramics is optimized as 1050^{o}C for 4 h.

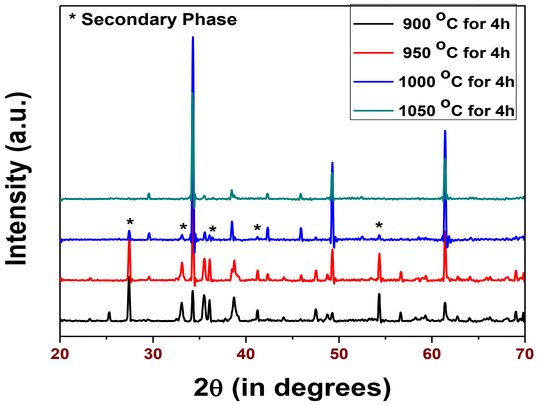

Fig. 4.18 XRD patterns of the CCTO ceramics calcined at different temperatures.

4.2.2.3 Sintering and Density Study

The sintering of the CCTO ceramic samples has been carried out at 1050 & 1100°C for 8 h, respectively. The optimum sintering temperature is found to be 1100°C, for 8 h. The variation of RD of the CCTO ceramics as a function of sintering temperature is shown in Fig. 4.19. The RD is found to increase with the increase in the sintering temperature. The RD of the CCTO ceramic samples sintered at 1050 and 1100°C is found to be ~ 91.93 and 94.67 %, respectively.

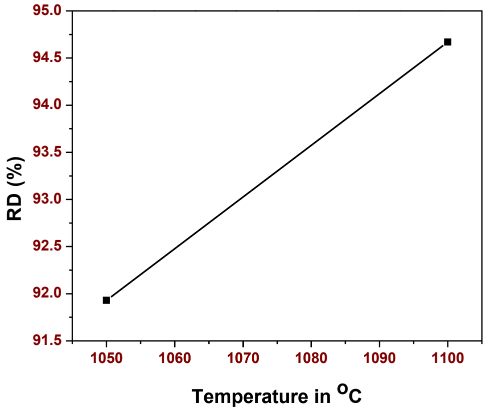

Fig. 4.19 RD of the CCTO ceramics sintered at different temperatures.

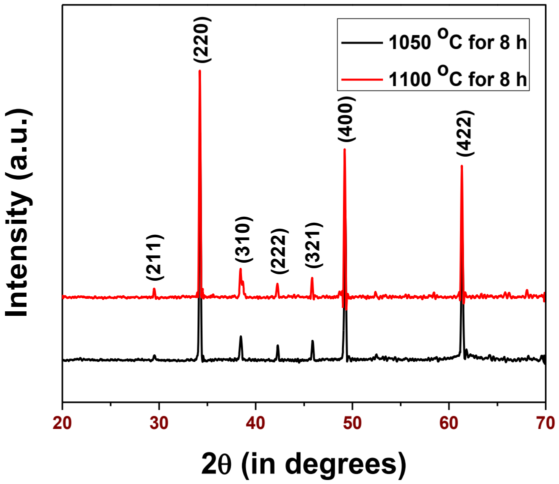

Fig. 4.20 XRD patterns of the sintered CCTO ceramics.

4.2.3 Structural Study

Fig. 4.20 shows the XRD patterns of the CCTO ceramic samples sintered at 1050 & 1100°C for 8h, respectively. The XRD peaks of the sintered CCTO ceramics show good crystallinity and homogeneity. The XRD shows the formation of a single phase of the CCTO ceramics with peaks observed when 2θ angles are ~29.5863°, 34.3047°, 38.4132°, 42.2924°, 45.8465°, 49.2863°, and 61.3605°, respectively. The same formation for single perovskite phase formation is also reported by Valim *et al*. (2004) and Almeida *et al*. (2002) [45]. All the diffraction peaks appeared in the XRD patterns matched with the peaks of the pseudo-cubic CCTO system by comparing with the standard powder diffraction file database (JCPDF File No. 75-2188), with no traces from other impurity phases, indicating that a solid solution of the CCTO system has been formed [45].

4.2.4 UV-Vis Absorption Spectroscopy Study

The absorption spectrum of the CCTO samples has also been recorded in the 200 to 800 nm wavelength range and is shown in Fig. 4.21. The absorption spectra of the CCTO samples show two broad bands: (i) around 220-550 nm and (ii) around 700 nm. The first band can be resolved by curve-fitting into 3-components with the maxima around 330, 370 and 470nm. The intensity of these components is much higher than that of the 700 nm band.

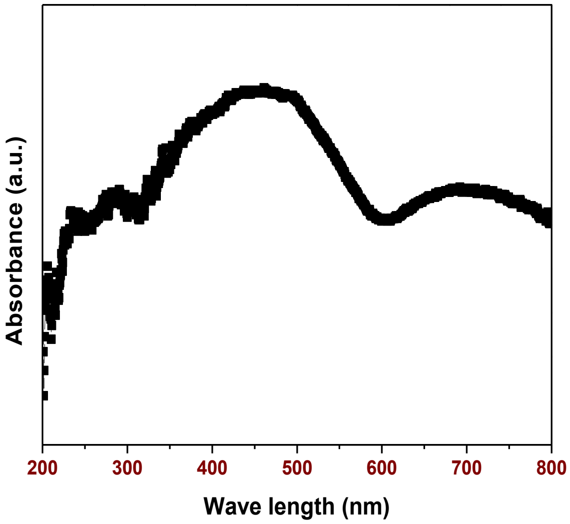

Fig. 4.21 UV-Visible absorption spectra of CCTO ceramics.

The E_g value of CCTO ceramic is estimated by plotting the $(\propto h\nu)^2$ vs hν curve (shown in Fig. 4.22) and by extrapolating the linear portion of the absorption edge to find the intercept with energy axis. The value of E_g of the CCTO ceramic samples is found to be ~ 2.22 eV.

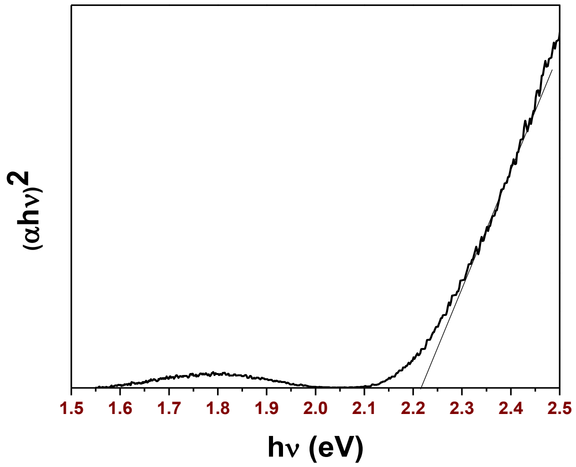

Fig. 4.22 The $(\propto h\nu)^2$ vs hν curve for CCTO ceramics.

4.2.5 Morphological Study

Fig. 4.23 shows the SEM of the CCTO ceramic samples, sintered at 1050 and 1100°C for 8 h, respectively. CCTO ceramic samples, sintered at 1100°C for 8 h, exhibit a reasonably uniform microstructure with clear grain boundaries. The average grain size of the CCTO ceramic samples, sintered at different temperatures, is calculated by linear intercept method and is found to be in between 10-20 μm. SEM of the CCTO samples sintered at 1050°C shows incomplete grain growth.

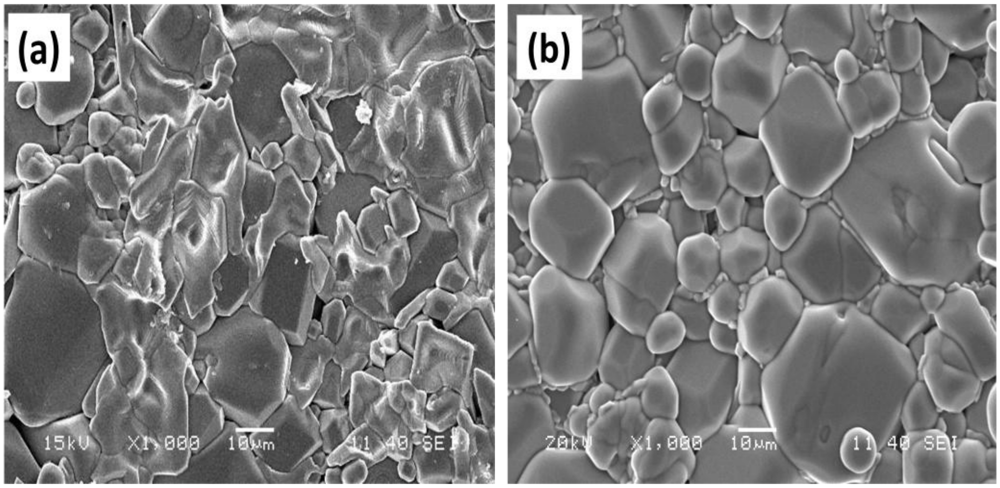

Fig. 4.23 SEM micrographs of CCTO ceramics sintered at (a) 1050 and (b) 1100°C, respectively.

4.2.5.1 Density & Porosity Measurements

The experimental densities (d_{ex}) of the CCTO ceramic samples, sintered at different temperatures, are measured by Archimedes' method. The density increases with the increase in sintering temperature [17]. This is also supported by the pore free and dense gain morphology of CCTO ceramics sintered at 1100^oC (shown in Fig. 4.23). The highest density ~ 4.76 gm/cc is achieved in the CCTO ceramics, sintered at 1100^oC. The values of the experimental density and porosity of the CCTO ceramic samples is listed in Table – 4.6.

Table – 4.6 Different Parameters of the sintered CCTO ceramics

Different Parameters	**Sintering Temperatures in ^oC**	
	1050	**1100**
d_{ex} in gm/cc	4.64	4.76
Porosity in %	4.05	2.49
ε_r at RT	11498	11537
tanδ at RT	0.181	0.213

4.2.6 Dielectric Properties

4.2.6.1 Frequency Dependence of Dielectric Constant (ε_r) and Dielectric Loss (tanδ)

The frequency dependence of both ε_r and tanδ of CCTO ceramic samples sintered at 1050 and 1100^oC is shown in Fig. 4.24. The RT values of the ε_r and tanδ at 1 kHz frequency of the CCTO ceramic samples are listed in Table – 4.7. ε_r values of the sintered CCTO ceramic samples are found to decrease with the increase in frequency. The highest value of ε_r ~ 11537 at RT and at 1 kHz frequency is observed in the CCTO ceramic samples, sintered at 1100^oC for 8 h. The reason for the highest ε_r can be explained by considering that the charge carriers accumulate at the interface between the semiconducting grains and the insulating grain boundary, which results in interfacial space charge polarization and hence large ε_r [19]. The tanδ value of the CCTO sample is obviously frequency dependent and begins to increase quickly above 10^5 Hz. The variation of tanδ above 10^5 Hz signifies that the relaxation process does not lie within the studied frequency range.

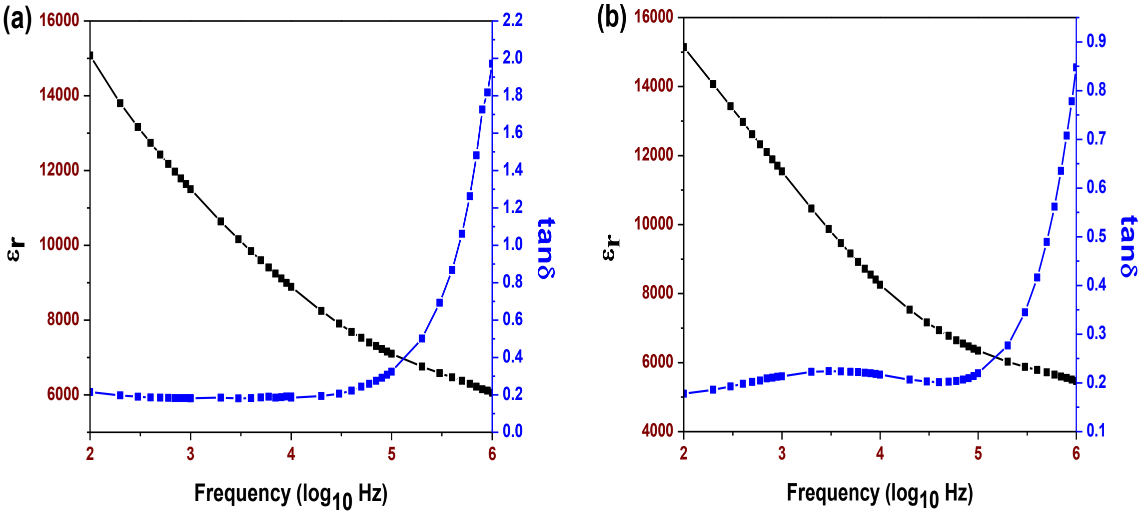

Fig. 4.24 RT frequency dependence of ε_r and tanδ of the CCTO ceramics sintered at (a) 1050, and (b) 1100°C, respectively.

4.2.6.2 Temperature Dependence of Dielectric Constant (ε_r) and Dielectric Loss (tanδ)

Fig. 4.25 shows the temperature dependence of ε_r at 1 kHz, 10 kHz, 100 kHz and 1 MHz frequencies, respectively of the sintered CCTO ceramic samples. This dielectric behavior suggests that some type of dielectric relaxation process is present in the CCTO ceramics as indicated by the step like increase in ε_r with the increase of temperature, which shift to higher temperatures with increasing frequency. This behavior of dielectric relaxation is of Debye-type [46]. It can also be seen that the ε_r is comparatively higher than that of the (BZT-BCT) ceramics and almost temperature independent in the temperature range of 30-70°C, which signifies the importance of the CCTO ceramics as an additive to enhance the dielectric properties of the composites in the present study. Beyond 70°C, there is an increase in ε_r with the increase in temperature.

Fig. 4.26 shows the temperature dependence of tanδ at 1 kHz, 10 kHz, 100 kHz and 1 MHz frequencies of the sintered CCTO ceramic samples, respectively. The tanδ value is almost temperature independent in RT-120°C temperature range. The appearance of tanδ peak at

~160°C in the CCTO ceramics, sintered at 1100°C, can be associated with the dielectric relaxation process, which can further be associated with the surface layers interfacial polarization [47].

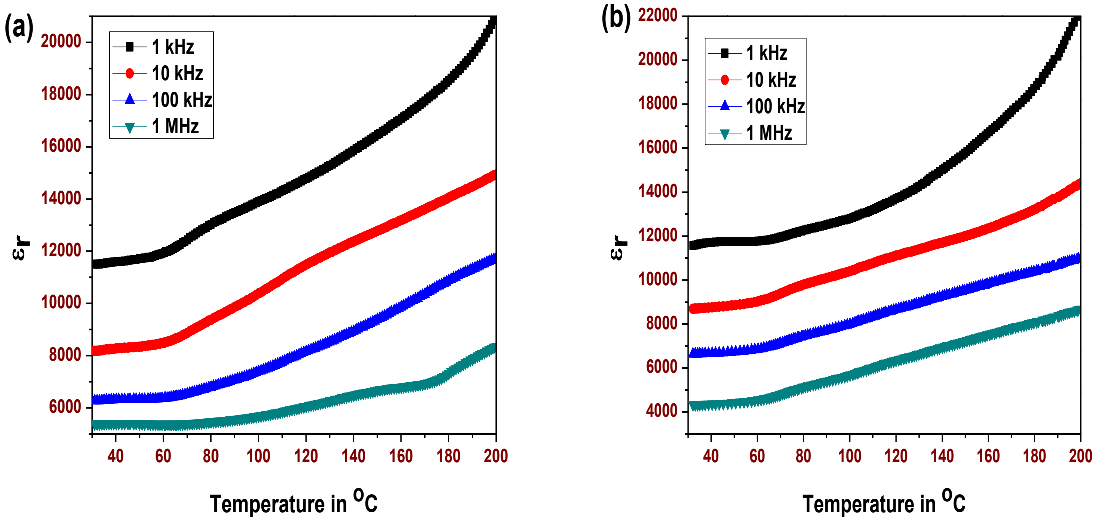

Fig. 4.25 Temperature dependence of ε_r at different frequencies of the CCTO ceramics sintered at (a) 1050, and (b) 1100°C, respectively.

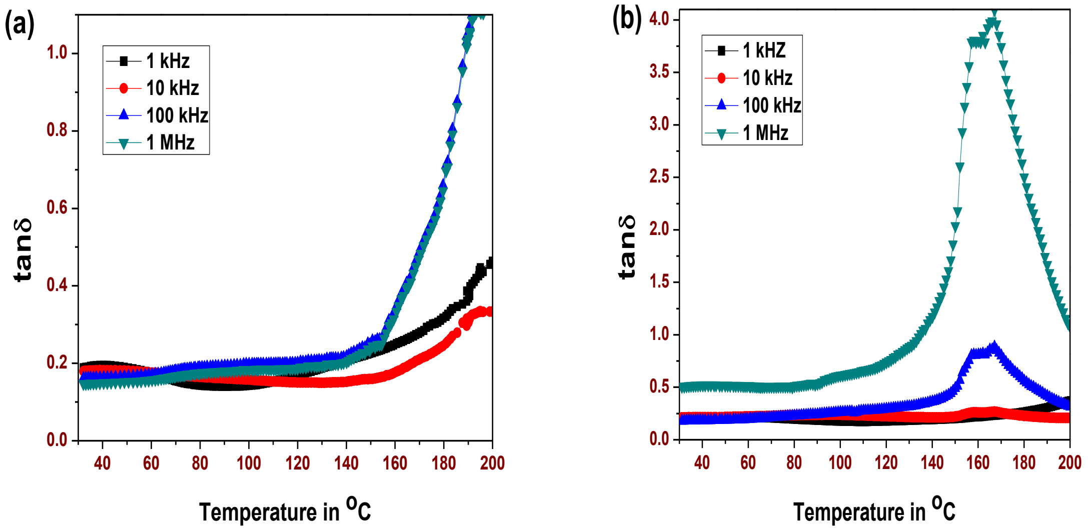

Fig. 4.26 Temperature dependence of tanδ of CCTO ceramics sintered at (a) 1050, and (b) 1100°C, respectively.

Table – 4.7 Details of dielectric properties of sintered CCTO ceramic samples at different temperatures

ε_r & tanδ values at different frequencies	Sintering Temperatures in °C	
	1050	**1100**
ε_r at RT at 1 kHz	11498	11537
ε_r at RT at 10 kHz	8186	8697
ε_r at RT at 100 kHz	6272	6641
ε_r at RT at 1 MHz	5384	4329
tanδ at RT at 1 kHz	0.18	0.21
tanδ at RT at 10 kHz	0.17	0.21
tanδ at RT at 100 kHz	0.16	0.18
tanδ at RT at 1 MHz	0.14	0.50

4.2.7 Summary

CCTO ceramic samples were synthesized by solid state reaction route. XRD analysis confirmed the formation of single perovskite phase at 1050°C for 4 h. The CCTO ceramic samples, sintered at 1100°C showed better microstructural and dielectric properties. The RT values of ε_r and tanδ at 1 kHz frequency of the CCTO ceramic samples sintered at 1100°C were found to be ~ 11,537 and 0.21, respectively. CCTO is a suitable non-ferroelectric high dielectric constant ceramic with the dielectric constant values as per the pre-determined objectives and comparable with the previous reports on high dielectric constant ceramics [32-35].

4.3 Structural & Electrical Properties of PVDF & Epoxy Polymers

4.3.1 Introduction

Polyvinylidene fluoride (PVDF) is a semicrystalline polymer with best piezoelectric, pyroelectric and ferroelectric properties among ferroelectric polymers [48]. PVDF exists in five phases with different conformations of the (–CH_2–CF_2–) monomer units [49]. Five crystalline phases are identified based on different conformations between trans (T) or gauche (G) linkages. PVDF with all trans (TTT) planar zigzag conformation is identified as β-phase, TGTG′ is identified as α and δ phases and T_3GT_3G' is identified as γ and ε phases [49, 50]. Among these five different phases, the phase with all trans linking i.e. β phase is highly polar. The electrical properties are found to vary with the amount of β phase present in PVDF [51]. The addition of ferroelectric ceramics to PVDF promises to enhance the electrical properties of PVDF while preserving its flexural properties.

Epoxies are a class of epoxide based polymers which are widely used as structural components and adhesives. Mainly, it is composed of a two-component system, a liquid resin and a hardener/cross-linker. Upon mixing, the hardener reacts with epoxide groups in the resin to create a densely cross-linked network. The functional group in epoxy resins is called the oxirane, which is a three-membered ring formed between two carbon atoms and one oxygen atom. In the last few years, there has been renewed interest in the epoxy based products for their use in automotive applications, having good stiffness and strength. For many high speed digital applications, modified epoxy systems with dielectric constants in the range of 3.0 to 3.5 have been found to offer good cost performance values.

In the present work, the structural, optical, and dielectric properties of both PVDF & epoxy polymers have been investigated and discussed in detail.

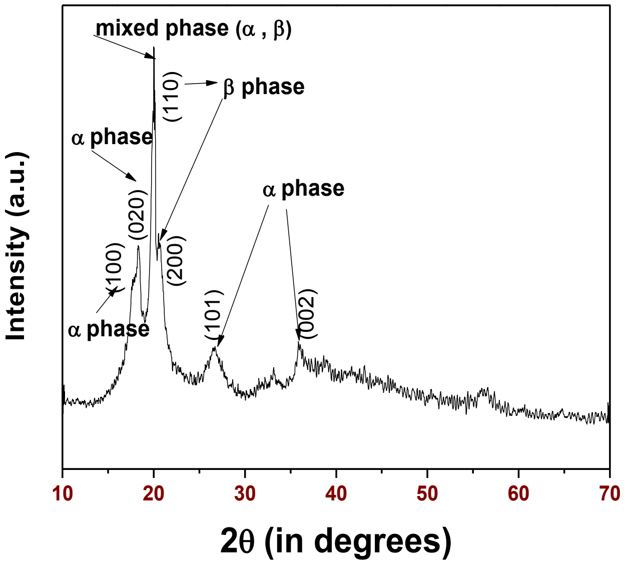

Fig. 4.27 XRD pattern of PVDF polymer.

4.3.2 Structural Study

Fig. 4.27 shows the RT XRD pattern of pure PVDF polymer. The XRD pattern of the PVDF polymer shows peaks at 2θ ~ 17.7^o, 18.3^o, 19.8^o, 20^o, 26.3^o, and 38.0^o, respectively. Generally, the reflections observed at 2θ ~ 17.8^o, 18.4^o, 19.9^o, 26.5^o and 38.0^o are assigned to the (100), (020), (110), (021) and (002) reflections, respectively, of the α-phase of the PVDF [49]. The peaks at 2θ ~20^o and 20.5^o are assigned to the (110) and (200) reflections, respectively, of the β-phase of PVDF [49]. Further, the XRD peak near 2θ ~20^o can be resolved into distinct peaks. This confirms the presence of α and β phases together.

Fig. 4.28 shows the RT XRD pattern of pure epoxy polymer. The XRD pattern of epoxy polymer shows the amorphous phase without any distinct peaks.

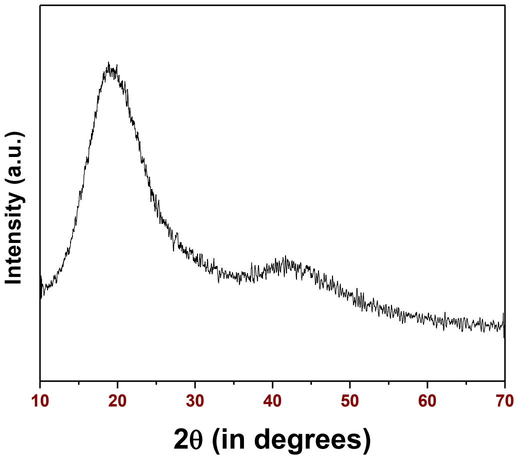

Fig. 4.28 XRD pattern of epoxy polymer.

4.3.3 UV-Vis Absorption Spectroscopy Study

The absorption spectrum of the PVDF polymer powder samples has been recorded in the 200 to 800 nm wavelength ranges and is shown in Fig. 4.29. The spectra show strong polymer broadening in the 250 to 350 nm wave length range. The broadening of the UV band may be due to the mean free path effect [52].

The E_g of the PVDF polymer sample can be obtained by plotting $(\propto h\nu)^2$ vs hν using the Tauc Eqn (4.1) and by extrapolating the linear portion of the absorption edge to find the intercept with energy axis. The E_g estimated by plotting $(\propto h\nu)^2$ vs hν is as shown in Fig. 4.30.

The E_g value for PVDF polymer was found to be 3.19 eV. The absorption spectra of the epoxy polymer samples have also been recorded in the 200 to 800 nm wavelength ranges and are shown in Fig. 4.31. The E_g of the epoxy polymer is estimated by plotting $(\propto h\nu)^2$ vs hν (as shown in Fig. 4.32). The E_g value of the epoxy polymer is found to be ~ 4.12 eV.

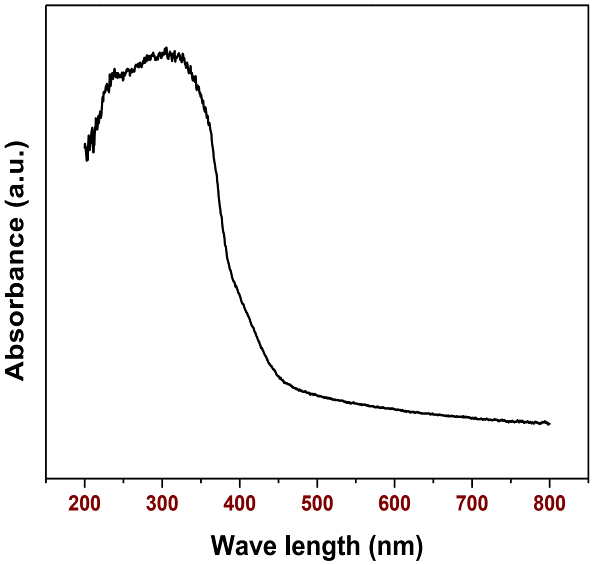

Fig. 4.29 UV-Visible absorption spectra of PVDF.

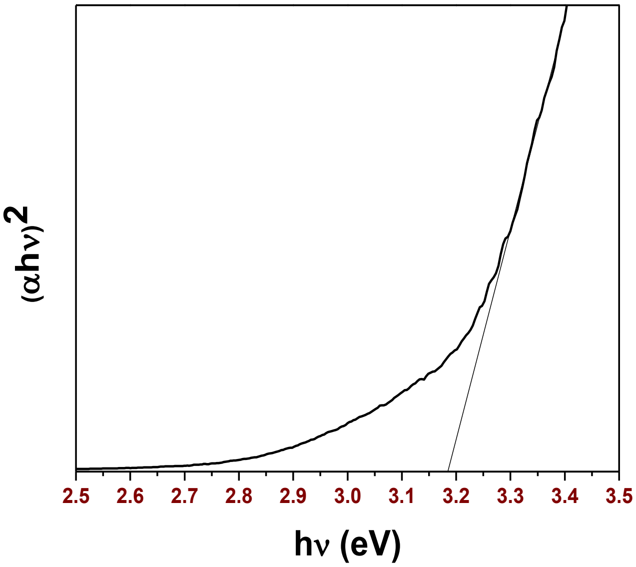

Fig. 4.30 The $(\propto h\nu)^2$ vs hν curve for PVDF polymer.

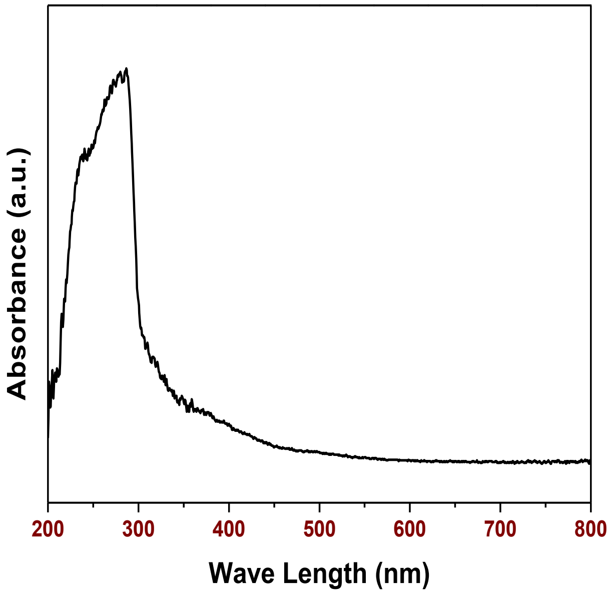

Fig. 4.31 UV-Visible absorption spectra of epoxy.

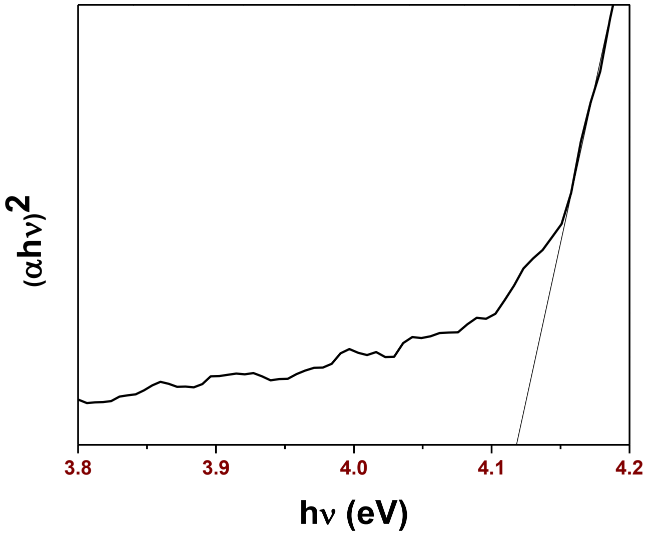

Fig. 4.32 The $(\propto h\nu)^2$ vs hν curve for epoxy polymer.

4.3.4 Dielectric Properties

4.3.4.1 Frequency Dependence of Dielectric Constant (ε_r) and Dielectric Loss (tanδ)

The frequency dependence of ε_r and tanδ of the PVDF polymer thick films is shown in Fig. 4.33. ε_r ~ 17 and tanδ ~ 0.018 at RT and at 1 kHz frequency is achieved for the PVDF polymer.

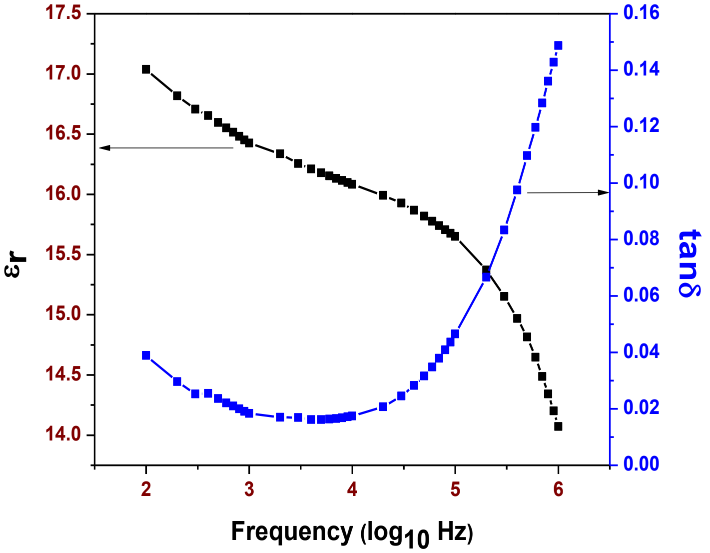

Fig. 4.33 Frequency dependence of ε_r and tanδ of PVDF polymer.

Fig. 4.34 depicts the frequency dependence of ε_r and tanδ for the epoxy polymer. ε_r ~ 7 and tanδ ~ 0.005 at RT and 1 kHz frequency is achieved for the epoxy polymer.

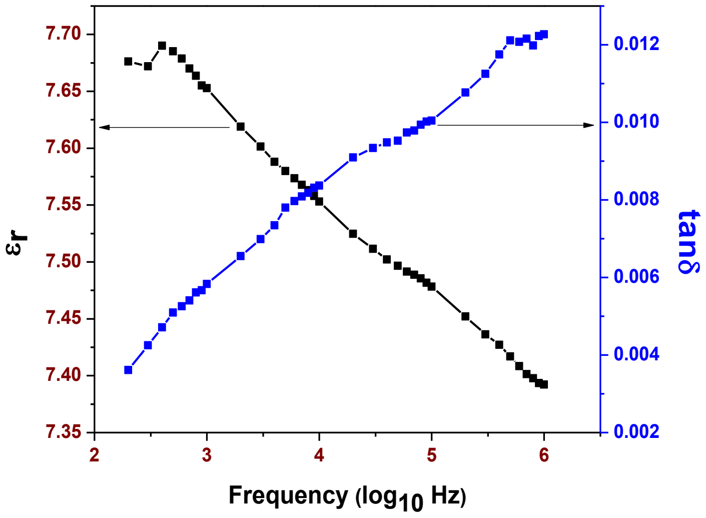

Fig. 4.34 Frequency dependence of ε_r and tanδ of epoxy polymer.

4.3.4.2 Temperature Dependence of Dielectric Constant (ε_r) and Dielectric Loss (tanδ)

Fig. 4.35(a) shows the temperature dependence of ε_r at 1 kHz, 10 kHz, 100 kHz & 1 MHz frequencies, respectively of the PVDF polymer samples. The values of ε_r and tanδ for the PVDF specimens at four different applied frequencies are given in Table - 4.9.

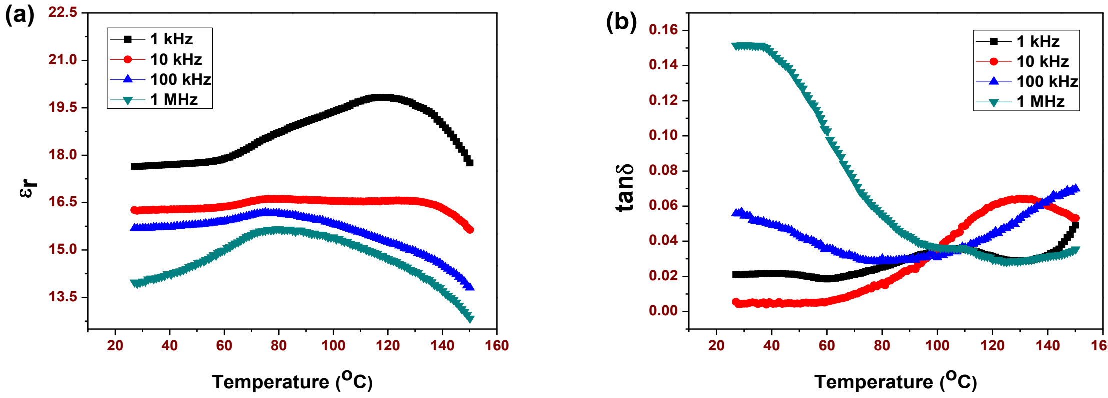

Fig. 4.35 Temperature dependence of (a) ε_r and (b) tanδ at different frequencies of the PVDF polymer.

Table – 4.8 Different calculated parameters of PVDF & epoxy polymers

Polymers Properties	PVDF	Epoxy
E_g in eV	3.19	4.12
ε_r at RT at 1 kHz	17	7
tanδ at RT at 1 kHz	0.018	0.005
Density in gm/cc	1.74	1.1

Fig. 4.36(a) shows the temperature dependence of ε_r at 1 kHz, 10 kHz, 100 kHz & 1 MHz frequencies, respectively of the epoxy polymer samples. The values of ε_r and tanδ for epoxy specimens at four different applied frequencies are given in Table – 4.9.

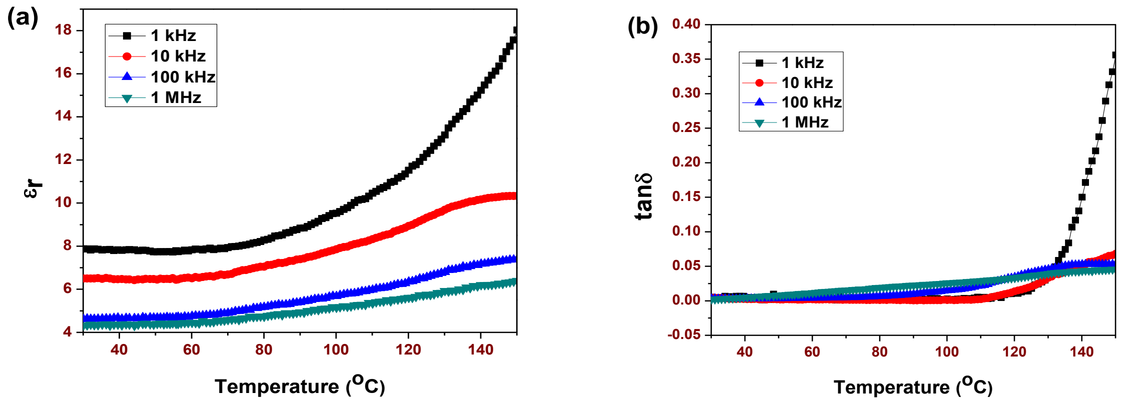

Fig. 4.36 Temperature dependence of (a) ε_r and (b) tanδ at different frequencies of the epoxy polymer.

Table – 4.9 Details of dielectric properties of PVDF & epoxy polymers

Polymers Properties	PVDF	Epoxy
ε_r at RT at 1 kHz	17.63	7.70
ε_r at RT at 10 kHz	16.26	6.55
ε_r at RT at 100 kHz	15.68	4.68
ε_r at RT at 1 MHz	13.97	4.39
tanδ at RT at 1 kHz	0.020	0.009
tanδ at RT at 10 kHz	0.005	0.004
tanδ at RT at 100 kHz	0.055	0.003
tanδ at RT at 1 MHz	0.151	0.002

4.3.5 Summary

Pure thermoplastic PVDF and thermoset epoxy polymer samples have been fabricated for comparison with composite samples. The structural, optical and dielectric properties of both the polymer samples have been studied. The XRD pattern of PVDF polymers shows crystalline phase while XRD pattern of the epoxy shows amorphous phase. The E_g values for the PVDF and epoxy polymers are found to be ~ 3.19 and 4.12, respectively. The ε_r and tanδ values at RT and at 1 kHz frequency for PVDF and epoxy polymer are found to be ~ 17, 7 and 0.018, 0.0052, respectively. The obtained dielectric properties of these polymers are better (as reported in chapter 1) than the earlier reports. For embedded capacitor and piezoelectric applications (such as energy harvesting) the dielectric (ε_r >50 at 1kHz and at RT) and piezoelectric properties (d_{33}~20pC/N at RT) of these polymers should be increased.

References:

[1] W. Liu and X. Ren, Physical Review Letters. 103, (2009) 257602.

[2] R. Ramaraghavulu, S. Buddhudu and G. Bhaskar Kumar, Ceram. Int. 37, (2011) 1245.

[3] H. Guihua, W. Zhanhong and Z. Feng, J. Rare Earths. 29, (2011) 160.

[4] A. R. James, R. Kumar, M. Prem Kumar, K. Srinivas, V. Radha, M. Vithal and M. Vijaya kumar, J. Alloys Comp. 496, (2010) 624.

[5] R. Yang, W. Fu, X. Deng, Z. Tan, Y. Zhang, L. Han, C. Lu and X. Guan, Adv. Mater. Res. 148, (2011) 1062.

[6] F. Rubio-Marcos, P. Ochoa and J. F. Fernandez, J. Eur. Ceram. Soc. 27, (2007) 4125.

[7] E. Wu. POWD, an interactive powder diffraction data interpretation and indexing program ver.2.1. School of Physical Science, Finder's University of South Australia Bedford Park.

[8] B. Parija, T. Badapanda, P. K. Sahoo, M. Kar, P. Kumar and S. Panigrahi, Processing and Application of Ceramics. 7, (2013) 73.

[9] J. Rodel, W. Jo, K. T. P. Seifert, E. M. Anton, T. Granzow and D. Damjanovic, Journal of the American Ceramic Society. 92, (2009) 1153.

[10] W. Wang, W. L. Li, D. Xu, W. P. Cao, Y. F. Hou and W. D. Fei, Ceramics International. 40, (2014) 3933.

[11] X. Q. Ke, D. Wang, X. Ren and Y. Wang, Physical Review B. 88, (2013) 214105

[12] N. Chaiyo, A. Ruangphanit, R. Muanhlua, S. Niemcharoen, A. Sangseub, S. Taopen, S. Leelapattana, W. C. Vittayakoran and N. Vittayakoran, Ferroelectrics. 383, (2009) 8.

[13] H. Du, F. Tang, F. Luo, D. Zhu, S. Qu, Z. Pei and W. Zhou, Mater. Res. Bull. 42, (2007) 1594.

[14] B. Noheda, J. A. Gonzalo, L. E. Cross, R. Guo, S. E. Park, D. E. Cox and G. Shirane, Physical Review B. 61, (2000) 8687.

[15] H. G. Tompkins and E. A. Irene, Handbook of Ellipsometry (William Andrew, Inc. 2005).

[16] T. Chen, S. Chu and Y. Juang, Sens. Actuator A Phys. 102, (2002) 6.

[17] S. Choudhury, M. A. Bhuiyan and S. M. Hoque, Int. Nano Lett. 1, (2011) 111.

[18] A. K. Singh, T. C. Goel, R. G. Mendiratta, O. P. Thakur and C. Prakash, J. Appl. Phys. 91, (2002) 6626.

[19] S. F. Mansour, Egypt. J. Solids. 28, (2005) 263.

[20] A. D. Hilton, C. A. Randall, D. J. Barber and T. R. Shrout, Ferroelectrics, 93, (1989) 379.

[21] J. Kelly, M. Leonard, C. Tantigate and A. Safari, J. Am. Ceram. Soc. 80, (1997) 379.

[22] P. Kumar, C. Prakash and T. C. Goel, Science and Technology of Advanced Materials. 8, (2007) 463.

[23] E. Tasarkuyu, A. Coskun, A. E. Irmark, S. Akturk, G. Unlu, Y. Samancioglu, A. Yucel, C. Sarikurkcu, S. Aksoy and M. Acet, J. Alloys Comp. 509, (2011) 3717.

[24] K. V. R. Prasad, A. R. Raju and K. B. R. Varma, J. Mater. Sci. 29, (1994) 2691.

[25] T. Maiti, R. Guo and A. S. Bhalla, Journal of the American Ceramic Society. 91, (2008) 1769.

[26] P. Victor, R. Ranjith and S. B. Krupanidhi, J Appl. Phys. 94, (2003) 7702.

[27] P. K. Palei and P. Kumar, Jpn. J. Appl. Phys. 51, (2012) 011503.

[28] W. Chaisan, R. Yimnirun, S. Ananta and D. P. Cann, Mat. Chem. Phy. 104, (2007) 113.

[29] I. W. Chen, P. Li and Y. Wang, J. Phys. Chem. Solids. 57, (1996) 1525.

[30] K. Uchino and S. Nomura, Ferroelectr. Lett. 44, (1982) 55.

[31] K. A. Singh, A. Bauria and N. S. Panwar, Ferroelectrics. 386, (2009) 139.

[32] K. Singh, M. Uniyal, S. C. Bhatt and B. S. Semwal, Sri Lankan J. Phys. 2, (2001) 13.

[33] A. Fundora, A. Vazquez, J. Portelles, F. Calderon and J. M. Siqueiros, J. Non-Crystalline Solids. 235 (1998) 567.

[34] Z. Yang, Y. Chang, B. Liu and L. Wei, J. Mater. Sci. Eng. A. 432, (2006) 292.

[35] C. Masingboon, P. Thongbai and S. Maensiri, Mater Chem Phys. 109, (2008) 262.

[36] J. Zhao, J. Liu and G. Ma, Ceram Int. 38, (2012) 1221.

[37] M. A. Subramanian, D. Li, N. Duan, B. A. Reisner and A. W. Sleight, J. Solid State Chem. 151, (2000) 323.

[38] L. He, J. B. Neaton, M. H. Cohen and D. Vanderbilt, Physical Review B. 65, (2002) 214112.

[39] B. Jaffe, W. Cook and H. Jaffe, Piezoelectric Ceramics (Academic Press, London, 1971).

[40] F. Tsang-Tse and S. Hsu-Kai, Journal of the American Ceramic Society. 87, (2004) 2072.

[41] J. L. Zhang, P. Zheng, C L. Wang, M. L. Zhao, J. C. Li and J. F. Wang, Applied Physics Letters. 87, (2005) 142901.

[42] J. Li, M. A. Subramanian, H. D. Rosenfeld, C. Y. Jones, B. H. Toby and A. W. Sleight, *Chem. Mater.* 16, (2004) 5223.

[43] B. A. Bender and M. J. Pan, Materials Science and Engineering: B. 117, (2005) 339.

[44] S. F. Shao, J. L. Zhang, P. Zheng, W. L. Zhong and C. L. Wang, J. Appl. Phys. 99, (2006) 084106.

[45] J. J. Mohamed, S. D. Hutagalung and Z. A. Ahmad, Journal of King Saud University – Engineering Sciences. 25, (2013) 35.

[46] M. Chunhong, Z. Huaiwu, H. Ying and L. Peng, Physica B. 405, (2010) 386.

[47] B. S. Prakash and K. B. R. Varma, J. Phys. Chem. Solids. 68, (2007) 490.

[48] Z. M. Dang, Y. H. Lin and C. W. Nan, Adv. Mater. 15, (2003) 1625.

[49] A. J. Lovinger, Macromolecules. 15, (1982) 40.

[50] M. G. Broahurst, G. T. Davis, J. E. McKinney and R. E. Collins, J. Appl. Phys. 49, (1978) 4992.

[51] A. Salimi and A. A. Yousefi, Polym. Testing. 22, (2003) 699.

[52] A. Moroz, Virtual Journal for Biomedical Optics. 6, (2011) 1130.

******

Chapter – 5

STRUCTURAL & ELECTRICAL PROPERTIES OF (BZT-BCT)-PVDF AND (BZT-BCT)-EPOXY CERAMIC-POLYMER COMPOSITES

In this chapter, the structural, optical, morphological, dielectric and piezoelectric properties of $\Phi\{0.50[Ba(Zr_{0.2}Ti_{0.8})O_3]\text{-}0.50[(Ba_{0.7}Ca_{0.3})TiO_3]\}\text{-}(1\text{-}\Phi)$PVDF/[(BZT-BCT)-PVDF] & $\Phi\{0.50[Ba(Zr_{0.2}Ti_{0.8})O_3]\text{-}0.50[(Ba_{0.7}Ca_{0.3})TiO_3]\}\text{-}(1\text{-}\Phi)$epoxy/[(BZT-BCT)-epoxy] (where Φ = 0.05, 0.10, 0.15, 0.20 & 0.25 volume fractions) ceramic-polymer composites with 0-3 connectivity are discussed. (BZT-BCT)-PVDF composites are prepared by hot uniaxial press method, whereas (BZT-BCT)-epoxy composites are prepared by cold press followed by hand lay-up technique. The detailed description of preparation and the experimental procedure of the composite samples are discussed in Chapter-3.

5.1 XRD Studies

5.1.1 XRD Studies of $\Phi\{0.50[Ba(Zr_{0.2}Ti_{0.8})O_3]\text{-}0.50[(Ba_{0.7}Ca_{0.3})TiO_3]\}\text{-}(1\text{-}\Phi)$PVDF/(BZT-BCT)-PVDF (where, Φ = 0.05, 0.10, 0.15, 0.20 & 0.25 Volume Fractions) Composites

Fig. 5.1 shows the XRD patterns of (BZT-BCT)-PVDF composite samples. The XRD patterns of the (BZT-BCT)-PVDF composite specimens show the presence of peaks corresponding to both the PVDF polymer and the (BZT-BCT) ceramic separately. With the increase in (BZT-BCT) ceramic volume content in the (BZT-BCT)-PVDF composites, the resemblance of the XRD patterns of the composites with pure (BZT-BCT) ceramic increases.

5.1.2 XRD Studies of $\Phi\{0.50[Ba(Zr_{0.2}Ti_{0.8})O_3]\text{-}0.50[(Ba_{0.7}Ca_{0.3})TiO_3]\}\text{-}(1\text{-}\Phi)$epoxy/(BZT-BCT)-epoxy (where, Φ = 0.05, 0.10, 0.15, 0.20 & 0.25 Volume Fractions) Composites

Fig. 5.2 shows the XRD patterns of (BZT-BCT)-epoxy composite samples. The XRD patterns of the composites reveal the presence of both (BZT-BCT) ceramics and epoxy polymer phases separately. With the increase of (BZT-BCT) ceramic powder in the (BZT-BCT)-epoxy composites, the relative intensity of amorphous phase of epoxy decreases in the low 2θ angle range (20–30^o). It suggests that as the content of (BZT-BCT) ceramic powder increases, the (BZT-BCT) ceramic phases start dominating the crystal properties of (BZT-BCT)-epoxy composites.

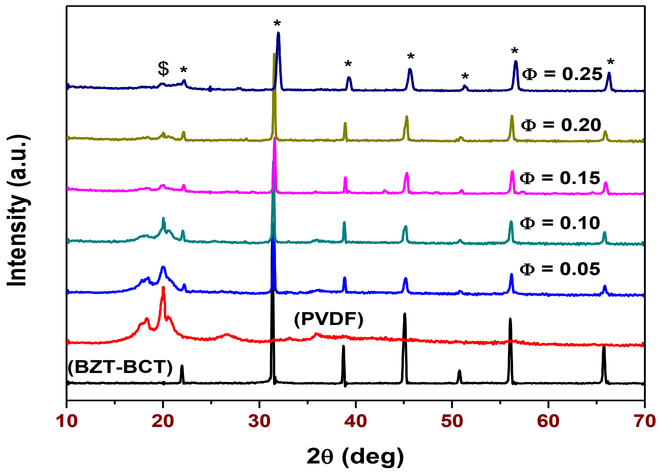

Fig. 5.1 XRD patterns of Φ(BZT-BCT)-(1-Φ)PVDF composites, where $, and * represent PVDF, and (BZT-BCT) phases, respectively.

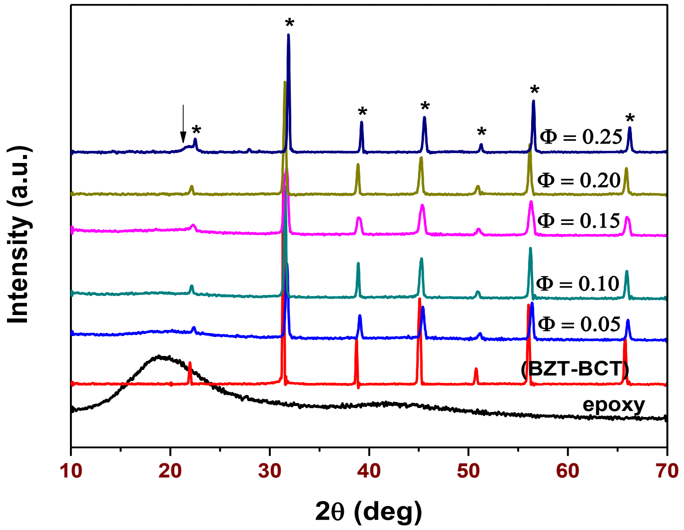

Fig. 5.2 XRD patterns of Φ(BZT-BCT)-(1-Φ)epoxy composites, where ↓, and * represent epoxy, and (BZT-BCT) phases, respectively.

5.2 UV–Visible Absorption Spectroscopy Studies

5.2.1 UV–Visible Absorption Spectroscopy Studies of (BZT-BCT)-PVDF Composites

UV–Visible absorption spectroscopy is a powerful technique to explore the optical properties of the samples. It is one of the direct methods to investigate the band structure of the materials. In the absorption process, an electron is excited from a lower energy state to a higher energy state by the absorption of energy. The changes in the transmitted radiation can decide the types of possible electron transitions. Fundamental absorption refers to band-to-band or exciton transition. The fundamental absorption shows a sudden rise in absorption, known as absorption edge, which can be used to determine the optical band gap ($E_g = hc/\lambda$).

The absorption spectra of the (BZT-BCT)-PVDF composite samples have been recorded in the wavelength ranges from 200 to 800 nm and are shown in Fig. 5.3. The UV data shows that the intensity of absorption spectra of the (BZT-BCT)-PVDF composite samples increases with the increase in (BZT-BCT) ceramic volume concentration from $\Phi = 0.05$ to 0.25 [1]. The increase in volume fractions of ceramics does not change the chemical structures of the components of the composites. The UV spectra of the composites are much broader due to the strong polymer broadening and show a kind of red shift as the volume fractions of the ceramics is increased. The broadening of the UV band may be due to the mean free path effect as well as the influence of conduction electron collisions with the particle surfaces in the composite [2].

The absorption co-efficient ($\propto$) helps us to know the nature of the electronic transition. When the values of $\propto > 10^4$ cm^{-1} at high energies, we expect direct electronic transitions and the energy and momentum are preserved for both the electron and photon. When the values of $\propto < 10^4$ cm^{-1} at low energies, in that case, we expect indirect electronic transitions and the momentum of the electron and photon are preserved by the help of phonons [3]. The results showed that the values of the absorption coefficient of the (BZT-BCT)-PVDF composites is less than 10^4 cm^{-1}, which indicates the indirect electronic transition.

The nature of the transition, whether direct or indirect can be determined by using the following relation proposed by Tauc, Davis & Mott [4]

$$Absorption\ coefficient\ (\propto) = \frac{A(h\nu - E_g)^n}{h\nu} \tag{5.1}$$

Where, hν is the energy of the incident photon, A is a constant, E_g is the optical band gap of the material & the exponent ‘n’ denotes the nature of the sample transition. For direct allowed transition n=1/2, and for direct forbidden transition n=3/2. For indirect allowed transition n=2, and for indirect forbidden transition n=3. Since in this experiment, the indirect allowed transition is used, we have taken the value of n=2.

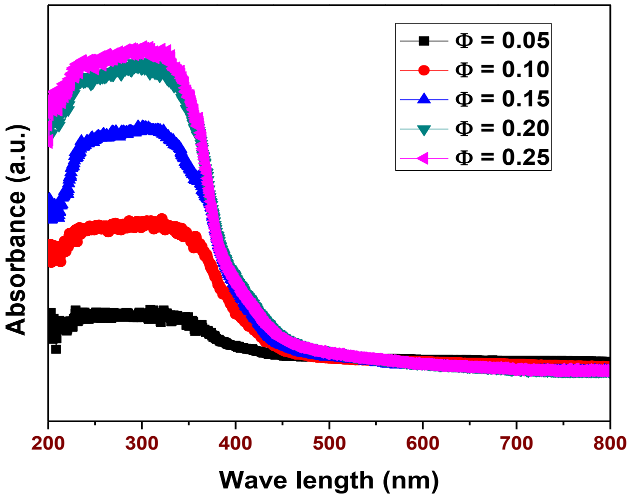

Fig. 5.3 UV-Visible absorption spectra of Φ(BZT-BCT)-(1-Φ)PVDF composites.

The energy band gap (E_g) of the (BZT-BCT)-PVDF composite samples can be obtained by plotting $(\propto h\nu)^2$ vs hν and by extrapolating the linear portion of the absorption edge to find the intercept with energy axis. The energy gap estimated by plotting $(\propto h\nu)^2$ vs hν is shown in Fig. 5.4.

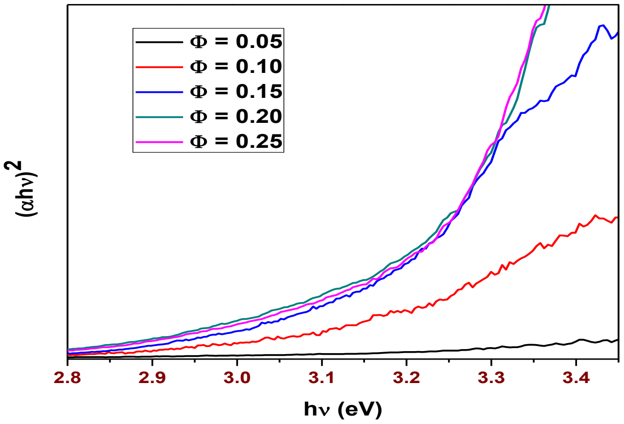

Fig. 5.4 The $(\propto h\nu)^2$ vs hν curves for Φ(BZT-BCT)-(1-Φ)PVDF composites.

The individual graphs of each composition of the (BZT-BCT)-PVDF composite samples are shown in the Fig. 5.5 (a)-(e). The band gap values of the composite materials are found to increase from 2.96 to 3.24 eV as the (BZT-BCT) volume fraction increases from 0.05 to 0.25. Table – 5.1 gives the values of band gap energy of the (BZT-BCT)-PVDF composite samples.

It has been reported that E_g is associated with the presence of intermediary energy levels within the band-gap of the materials [5]. These energy levels are also dependent of the degree of structural order–disorder in the lattice. Therefore, the increase in structural organization in the lattice leads to formation of intermediary energy levels and consequently increases the band gap. The E_g values can also be related to the other factors such as; preparation method, processing time and temperature, particles shape and morphology. These factors affect the different structural organizations like oxygen vacancies, bond distortions leading to affect the formation of intermediary energy levels within the band gap.

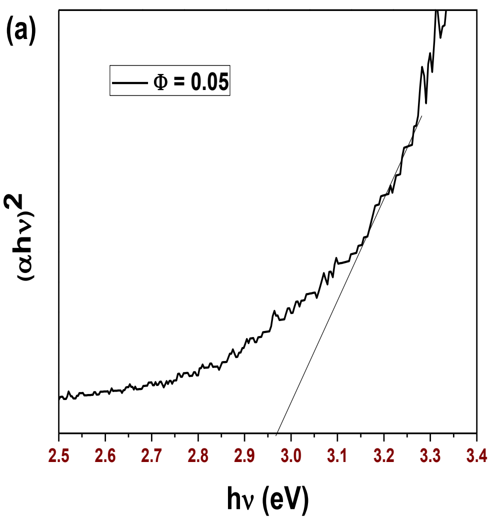

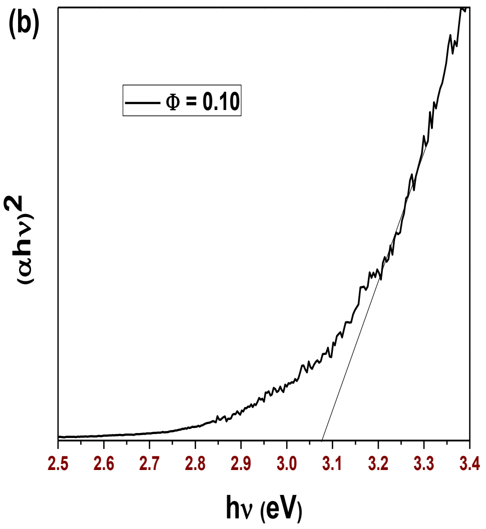

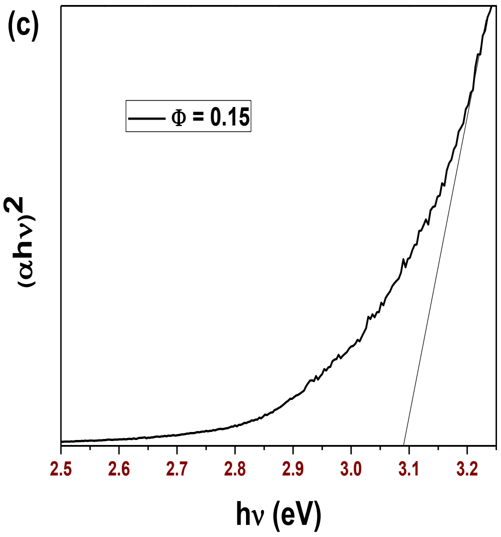

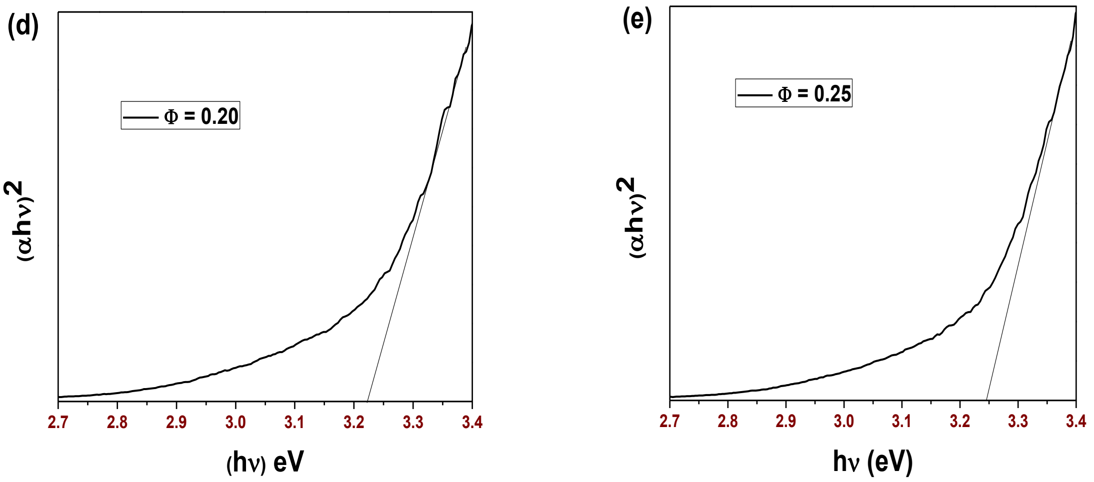

Fig. 5.5 The $(\propto h\nu)^2$ vs hν curves for Φ(BZT-BCT)-(1-Φ)PVDF composites with (a) Φ = 0.05, (b) Φ = 0.10, (c) Φ = 0.15, (d) Φ = 0.20 & (e) Φ = 0.25, respectively.

5.2.2 UV–Visible Absorption Spectroscopy Studies of (BZT-BCT)-epoxy Composites

Fig. 5.6 shows the UV absorption spectra of (BZT-BCT)-epoxy composites in the wavelength ranges from 200 to 800 nm. Increase in the intensity of absorption peaks with the increase in the volume fractions of (BZT-BCT) ceramics from 0.05 to 0.25 can be seen in Fig. 5.6. All the composites have the broad absorption peaks in the 280 to 350 nm wavelength ranges. The broadening of the bands can be ascribed to the mean free path effect and also the conduction electron collisions with the particle surfaces [2]. The absorption edge of the composites was shifted towards higher wavelengths with increasing the (BZT-BCT) ceramic concentrations. The optical properties of the materials are strongly dependent on particle size. Therefore the increase in absorption and absorption peak shift may be due to particle size effect of ceramic fillers [6].

The absorption coefficient helps to know the nature of the electronic transition. The results showed that the values of absorption coefficient of the (BZT-BCT)-epoxy composites is less than 10^4 cm^{-1}, which indicates the indirect electronic transition. Again the nature of transition, whether direct or indirect can also be determined by using the relation proposed by Tauc, Davis & Mott [4]. Since in this experiment, indirect allowed transition is used, we have taken the value of n = 2.

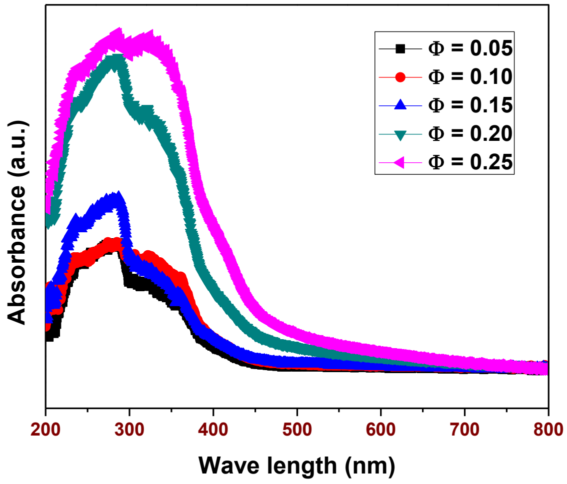

Fig. 5.6 UV-Visible absorption spectra of Φ(BZT-BCT)-(1-Φ)epoxy composites.

Fig. 5.7 depicts $(\propto h\nu)^2$ versus hν graph of (BZT-BCT)-epoxy composites and Fig. 5.8 (a)-(e) shows the $(\propto h\nu)^2$ versus hν graph of Φ(BZT-BCT)-(1-Φ)epoxy composites with Φ = 0.05, 0.10, 0.15, 0.20 and 0.25, respectively.

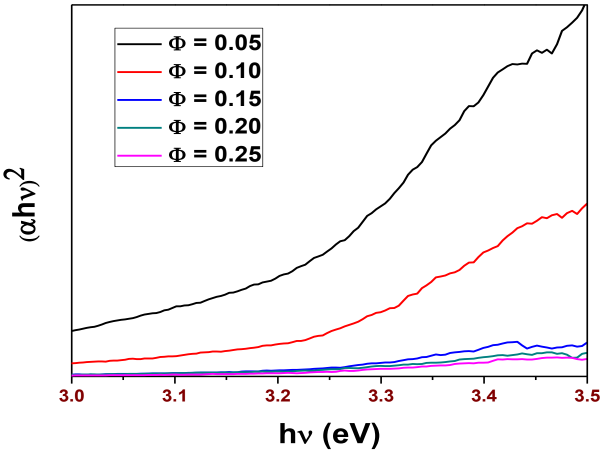

Fig. 5.7 The $(\propto h\nu)^2$ vs hν curves for Φ(BZT-BCT)-(1-Φ) epoxy composites.

The energy band gap (E_g) of the (BZT-BCT)-epoxy composites is obtained from the intercept of the extrapolation of linear portion of the absorption edge with energy axis. The band gap values are found to increase from 3.14 to 3.23 eV with the increase in the volume fractions of ceramics in the composite samples. This increase in can be ascribed to the

Burstein–Moss effect [7], in which the donor electrons occupy the states at the bottom of the conduction band. Since the Pauli principle prevents states from being doubly occupied, the optical band gap is given by the energy difference between states with Fermi momentum in the conduction and valence bands. Hence, the increase in the volume fractions of (BZT-BCT) ceramics induces the shift of the Fermi level into the conduction band of the composites. The energy band gap (E_g) values of the (BZT-BCT)-epoxy composites are given in Table – 5.1.

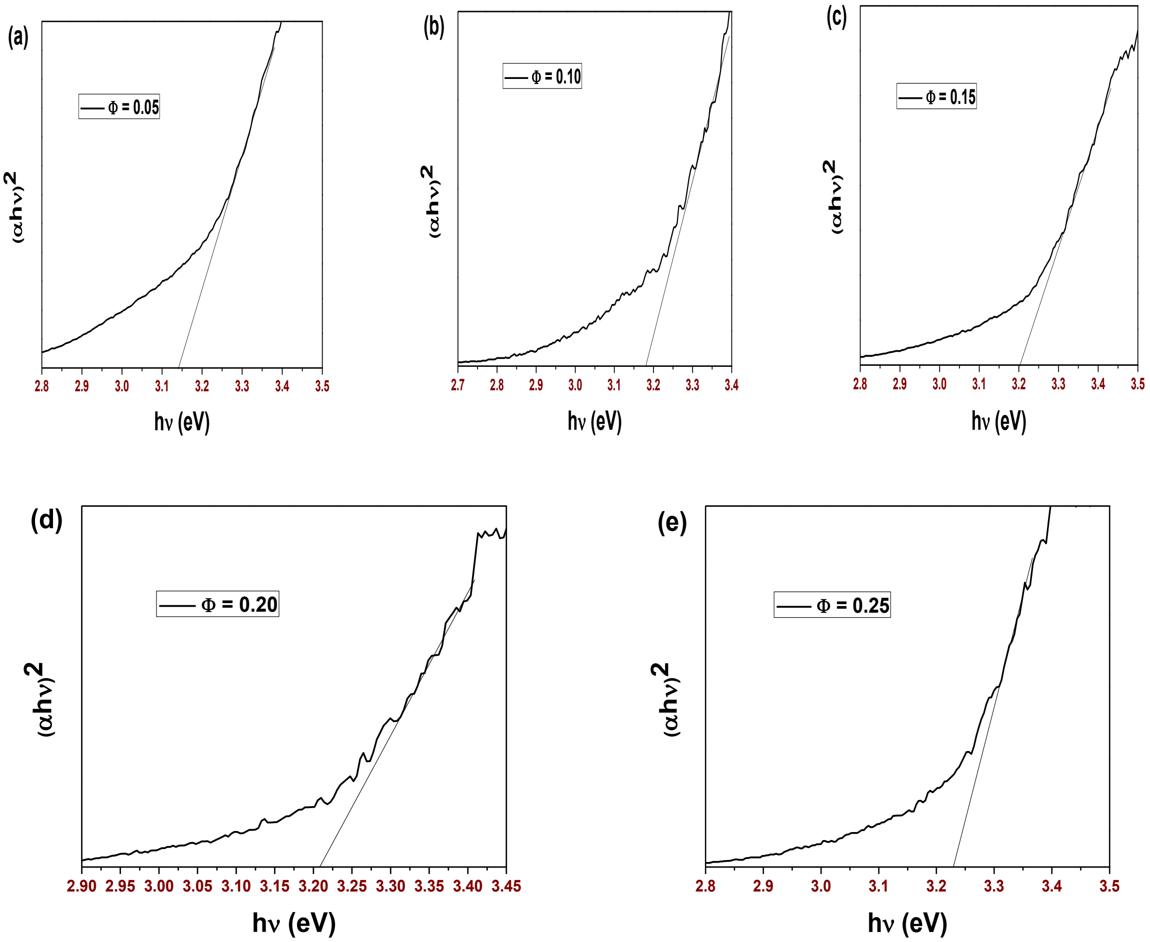

Fig. 5.8 The $(\propto h\nu)^2$ vs hν curves for Φ(BZT-BCT)-(1-Φ) epoxy composites with (a) Φ = 0.05, (b) Φ = 0.10, (c) Φ = 0.15, (d) Φ = 0.20 & (e) Φ = 0.25, respectively.

5.3 Morphological Studies

5.3.1 Morphological Studies of (BZT-BCT)-PVDF Composites

Fig. 5.9 shows the SEM micrographs with different volume fractions of (BZT-BCT) ceramics in the (BZT-BCT)-PVDF composites. The (BZT-BCT) particle distribution in the

PVDF polymer matrix is homogeneous with small agglomeration. In the SEM images of the (BZT-BCT)-PVDF composites, the bright region indicate (BZT-BCT) ceramic powder and the dark region indicates PVDF matrix. The ceramic powder is evenly distributed and surrounded by the PVDF matrix, which clearly indicates 0-3 connectivity (also confirmed from the cross-sectional SEM images) [8]. The uniform distribution increases with an increase in the (BZT-BCT) ceramic volume fractions in the ceramic-polymer composites.

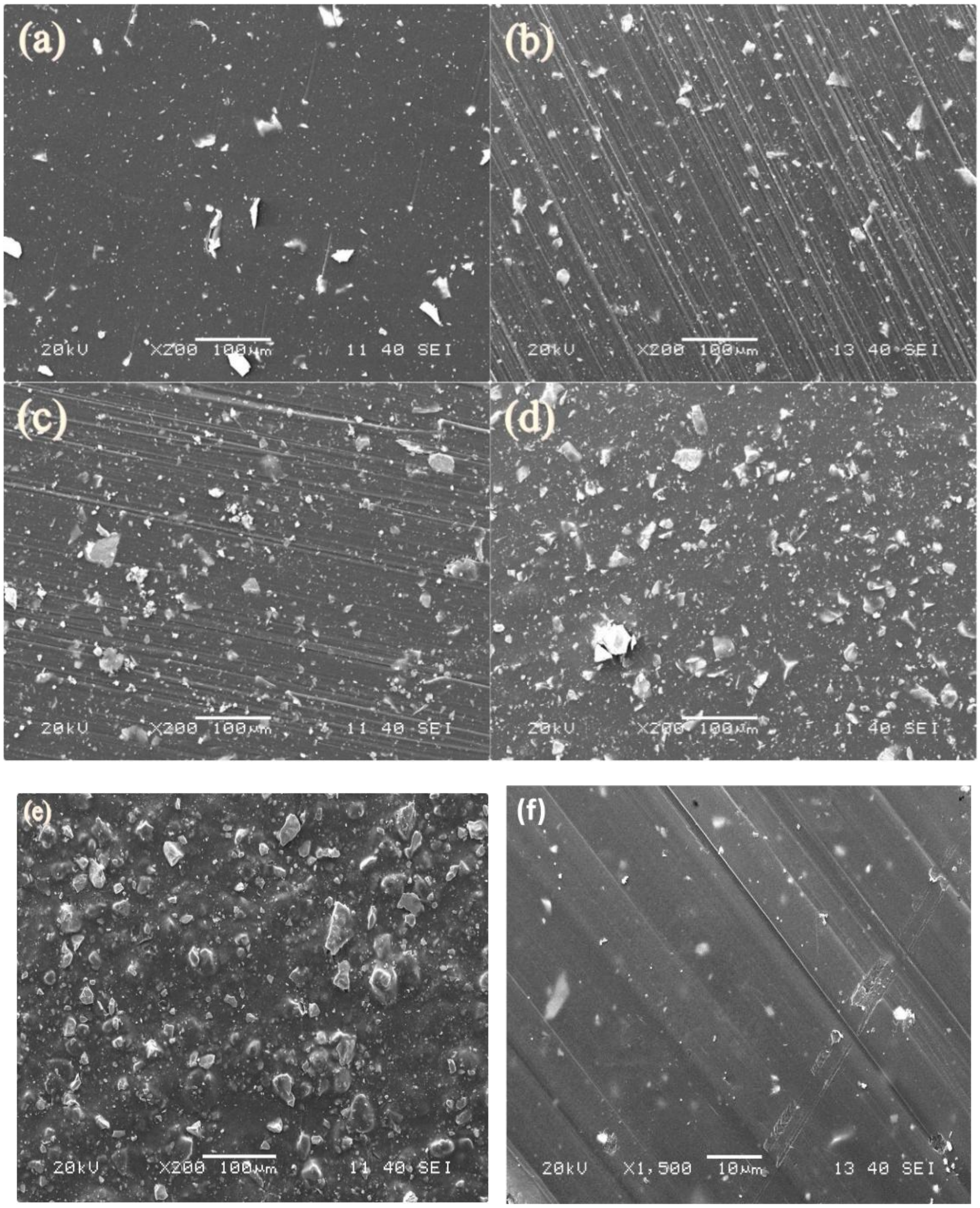

Fig. 5.9 SEM images of Φ(BZT-BCT)-(1-Φ)PVDF composites with (a) Φ = 0.05, (b) Φ = 0.10, (c) Φ = 0.15, (d) Φ = 0.20 & (e) Φ = 0.25, respectively and (f) Φ = 0.05 cross-sectional image.

Fig. 5.10 shows the density and porosity of the (BZT-BCT)-PVDF composites as a function of volume fractions of (BZT-BCT). The experimental densities of the composite samples increase from 2.01 to 2.48 g/cm^3 with an increase in volume fraction of the (BZT-BCT) in Φ(BZT-BCT)-(1-Φ)PVDF composites. The density and porosity of the composite samples are listed in Table – 5.1.

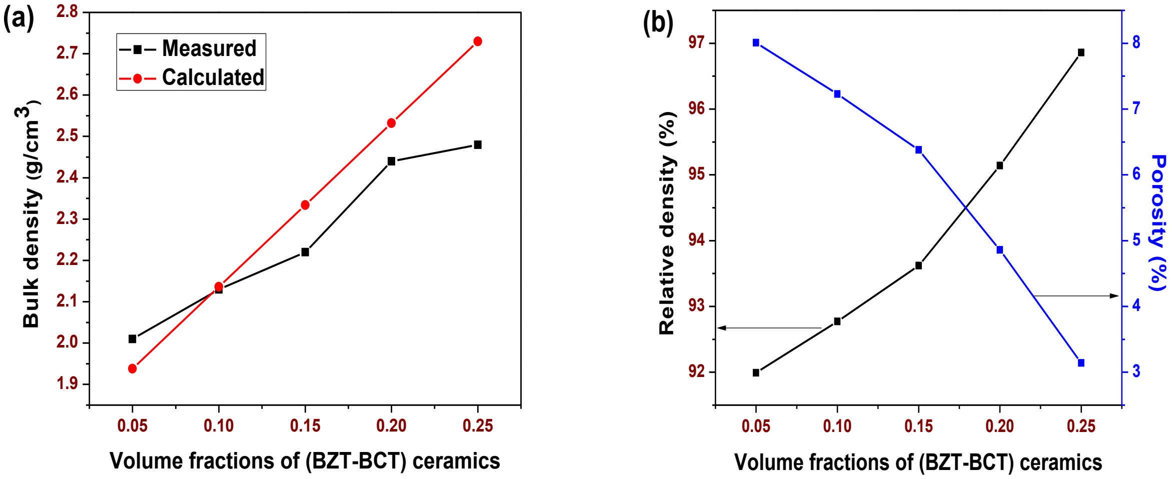

Fig. 5.10 (a) Bulk density, and (b) Porosity of (BZT-BCT)-PVDF composites as a function of volume fractions of (BZT-BCT).

5.3.2 Morphological Studies of (BZT-BCT)-epoxy Composites

Fig. 5.11 shows the SEM micrographs of the (BZT-BCT)-epoxy composites with different volume fractions of (BZT-BCT) ceramics. The black region is the epoxy and the white and gray particles are the sintered (BZT-BCT) ceramic powders. It can be seen that the (BZT-BCT) particle distribution is homogeneous with small agglomeration. The ceramic powder is evenly distributed and surrounded by epoxy matrix, which clearly indicates 0-3 type of connectivity (also confirmed from the cross-sectional SEM images) [8]. Uniform distribution increases with the increase in (BZT-BCT) ceramic volume fractions in the polymer matrix. Fig. 5.12 shows the density and porosity of the (BZT-BCT)-epoxy composites as a function of volume fractions of the (BZT-BCT) ceramics. The density of the composite samples is found to increase from 1.29 to 1.73 g/cm^3 with the increase of volume fractions of (BZT-BCT) powder from Φ = 0.05 to Φ = 0.20 in (BZT-BCT)-epoxy composites. But, the density decreases for Φ = 0.25 volume fraction of the (BZT-BCT) powder in the (BZT-BCT)-epoxy composites, which can be attributed to the limit of addition of ceramic powder in the composite. The values of density and porosity of composite samples are listed in Table – 5.1.

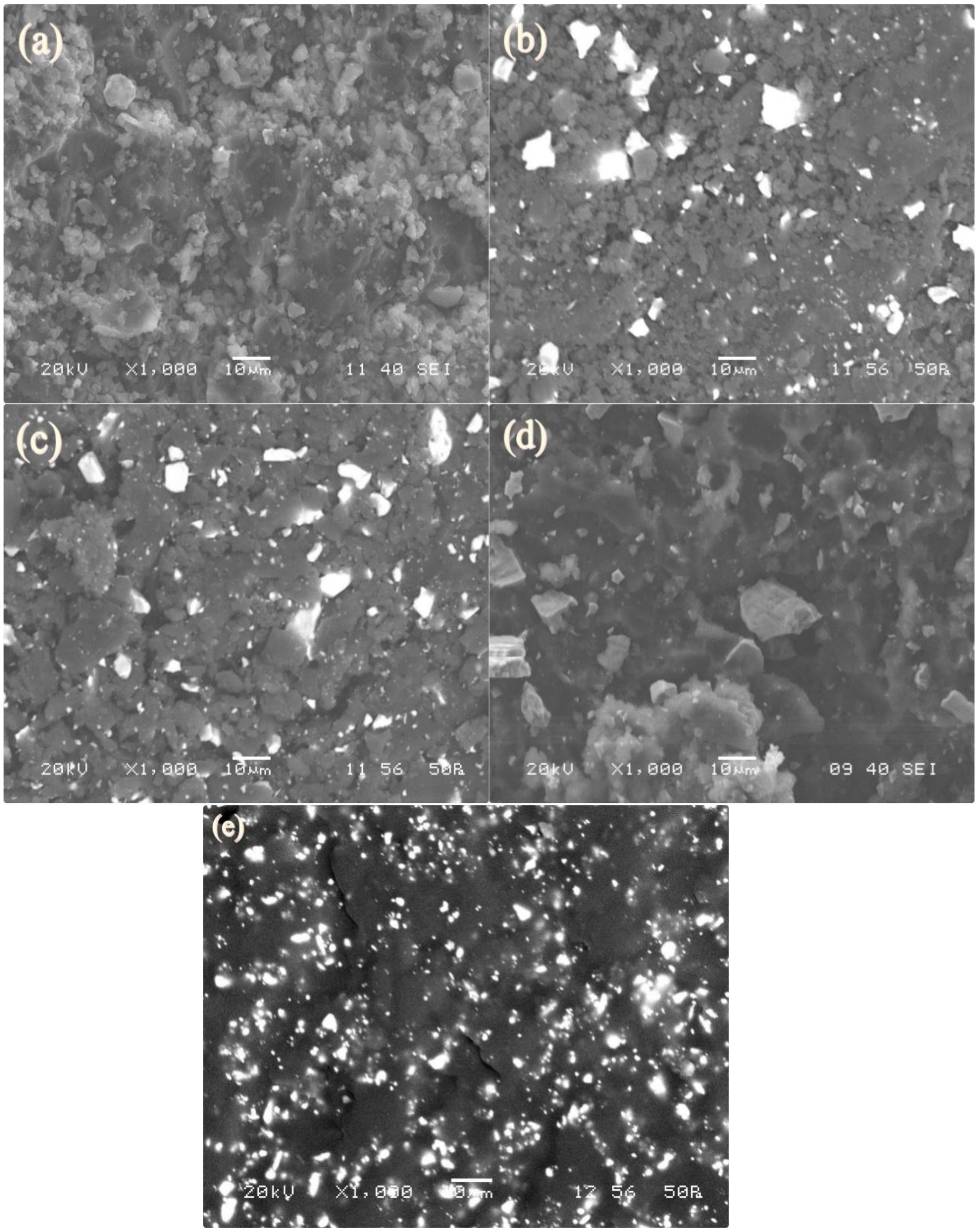

Fig. 5.11 SEM images of Φ(BZT-BCT)-(1-Φ)epoxy composites with (a) Φ = 0.05, (b) Φ = 0.10, (c) Φ = 0.15, (d) Φ = 0.20 & (e) Φ = 0.25, respectively.

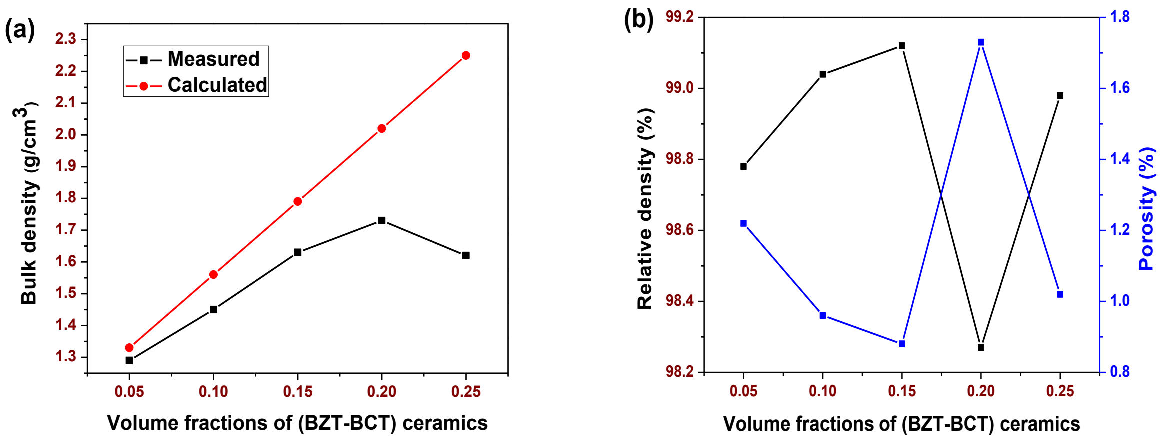

Fig. 5.12 (a) Bulk density, and (b) Porosity of (BZT-BCT)-epoxy composites as a function of volume fractions of (BZT-BCT).

Table – 5.1 E_g, Density & Porosity Values for (BZT-BCT)-PVDF & (BZT-BCT)-epoxy Composites with Different Volume Fractions of Ceramics

Materials	**Volume fractions of ceramics**	**Parameters**			
		Energy band gap (E_g) in eV	**Measured Density in gm/cc**	**Calculated Density in gm/cc**	**porosity of the composites in %**
Φ(BZT-BCT)-(1-Φ) PVDF composites	Φ = 0.05	2.96	2.01	1.93	8.01
	Φ = 0.10	3.07	2.13	2.13	7.23
	Φ = 0.15	3.09	2.22	2.33	6.38
	Φ = 0.20	3.22	2.44	2.53	4.86
	Φ = 0.25	3.24	2.48	2.73	3.14
Φ(BZT-BCT)-(1-Φ) epoxy composites	Φ = 0.05	3.14	1.29	1.33	1.22
	Φ = 0.10	3.18	1.45	1.56	0.96
	Φ = 0.15	3.20	1.63	1.79	0.88
	Φ = 0.20	3.21	1.73	2.02	1.73
	Φ = 0.25	3.23	1.62	2.25	1.02

5.4 Dielectric Studies

5.4.1 Frequency Dependent Dielectric Constant (ε_r) & Dielectric Loss (tanδ)

5.4.1.1 Φ(BZT-BCT)-(1-Φ)PVDF (where, Φ = 0.05, 0.10, 0.15, 0.20 & 0.25 Volume Fractions) Composites

The frequency dependence of ε_r for the (BZT-BCT)-PVDF composite samples with different volume fractions of (BZT-BCT) is shown in Fig. 5.13(a). As reported earlier [9], good dispersion along with homogeneous packing of the ceramic filler is likely to result in a high dielectric constant. A dielectric constant of ~ 41 at 1 kHz frequency and at RT is achieved for 0.25 volume fraction of the (BZT-BCT) in (BZT-BCT)-PVDF composites. As expected, ε_r values increases at all the frequencies under study with an increase in (BZT-BCT) volume content in the (BZT-BCT)-PVDF composites. In all the composites, the effective dielectric constants obtained are higher than for pure PVDF, but much lower than for pure (BZT-BCT). It is well known that PVDF has five different polymorphisms of which four phases designated as α, β, γ and δ are stable at room temperature (RT), apart from connectivity and particle size effects. Based on X-ray studies, it is confirmed that the PVDF is present in the mixed phases of α and β. The α phase of PVDF is non-polar and the constrained polymer chain hinders the contribution of electrical polarization; therefore, the value of ε_r is much lower than that of the (BZT-BCT) ceramics [10]. The low value of ε_r of the (BZT-BCT)-PVDF composites can also be accounted to porosity. The ε_r in vacuum is 1 and, with an increase in porosity, ε_r should decrease. In the (BZT-BCT)-PVDF composites, with an increase in ceramic volume fractions, both the porosity and ε_r increases. Here, the ceramic filler has a high ε_r; and, with an increase in ceramic volume fractions for the (BZT-BCT)-PVDF composites, the dielectric behavior of the ceramic particles dominates, which in turn increases ε_r.

The frequency dependence of tanδ for the (BZT-BCT)-PVDF composites with different volume fractions of (BZT-BCT) is shown in Fig. 5.13(b). It is observed that tanδ decreases in the 100 Hz-10 kHz frequency range and then subsequently increases at ~ 1 MHz frequency. It is known that the loss tangent (tanδ) is defined as $\varepsilon''/\varepsilon'$, where ε'' and ε' are the imaginary and real parts of relative permittivity. The value of ε'' first increases up to 1 kHz frequency and then starts decreasing up to 10 kHz frequency and beyond that again starts increasing for all the (BZT-BCT)-PVDF composites. The oscillatory behavior of ε'' suggest the presence of some relaxation processes, which usually occur in heterogeneous systems [11]. The variation of tanδ may again be ascribed to overlapping of the relaxation processes, which are attributed to some structural changes that takes place in the in the (BZT-BCT)-PVDF composites as a result of filler addition. The decrease in the tanδ values at low frequency region is attributed to interfacial polarization caused by the heterogeneous nature of the system, while the sharp increase of ε″ in the high frequency region is due to the onset of ohmic conductivity of the charge carriers [12-14]. The increase in loss at high frequency is also believed to be related to the glass transition relaxation of PVDF and the setting of the dielectric relaxation process [15,16]. Beyond 10 kHz frequency, the tanδ increases with the increase of ceramic volume fractions in the composites. This may be attributed to the interfaces present in the composites. The decrease of tanδ (below 10 kHz frequency) with an increase in ceramic volume fractions in the (BZT-BCT)-PVDF composites may be attributed to the low dielectric loss of the ceramic filler particles. These results suggest that the dielectric loss due to interfaces in the (BZT-BCT)-PVDF composites is frequency dependent. Therefore, in the (BZT-BCT)-PVDF composites, the (BZT-BCT) particles serve to increase the dielectric constant while retaining excellent dielectric loss properties up to 10 kHz. The same type of loss behavior has been reported earlier [17]. The RT values of ε_r and tanδ for the (BZT-BCT)-PVDF composite specimens at 1 kHz frequency are given in Table – 5.2.

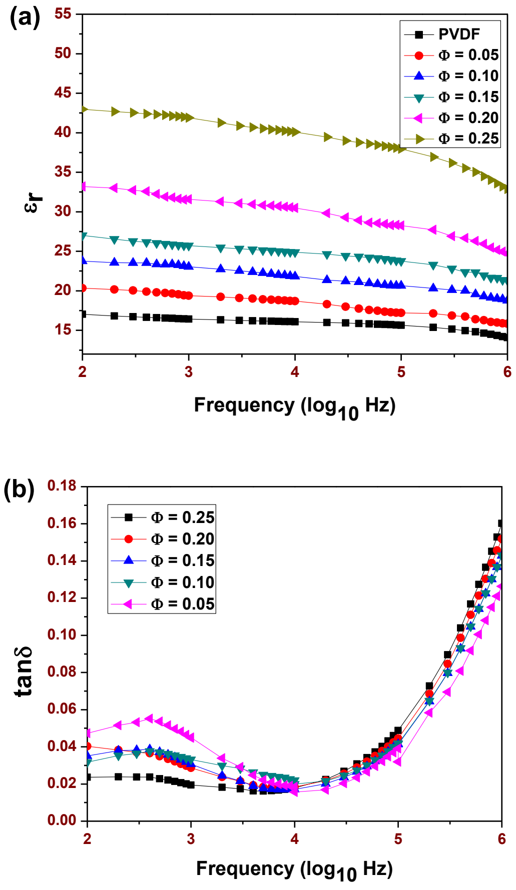

Fig. 5.13 Frequency dependence of (a) ε_r and (b) tanδ of PVDF, and Φ(BZT-BCT)-(1-Φ)PVDF composites with Φ = 0.05, 0.10, 0.15, 0.20, and 0.25, respectively.

5.4.1.2 Φ(BZT-BCT)-(1-Φ)epoxy (where, Φ = 0.05, 0.10, 0.15, 0.20, & 0.25 Volume Fractions) Composites

Fig. 5.14(a) shows the variation of ε_r with frequency for the (BZT-BCT)-epoxy composite samples. A maximum value of ε_r ~ 34 at 1 kHz frequency and at RT is achieved for 0.20 volume fractions of (BZT-BCT) ceramic fillers in the (BZT-BCT)-epoxy composites and beyond 0.20 volume fraction, the ε_r value starts decreasing. As expected, in all the cases, the effective dielectric constants obtained are higher than that of pure epoxy but much lower than that of pure (BZT-BCT) ceramics. The increase in ε_r values of the composites up to 0.20 volume fractions of (BZT-BCT) ceramic filler can be related to the increase in density and also increase in connectivity between the filler particles [18]. The decrease of ε_r in case of 0.25 volume fraction of the (BZT-BCT) ceramic filler in (BZT-BCT)-epoxy composites may be attributed to the decrease in density and increase in porosity of the composites. In all the (BZT-BCT)-epoxy composite samples, with the increase in frequency, ε_r decreases very fast up to 10^4 Hz, and in the frequency range from 10^4 to 10^6 Hz, it is almost constant. This can be related to the intermolecular cooperative motions and hindered dielectric rotations in the composite samples [19].

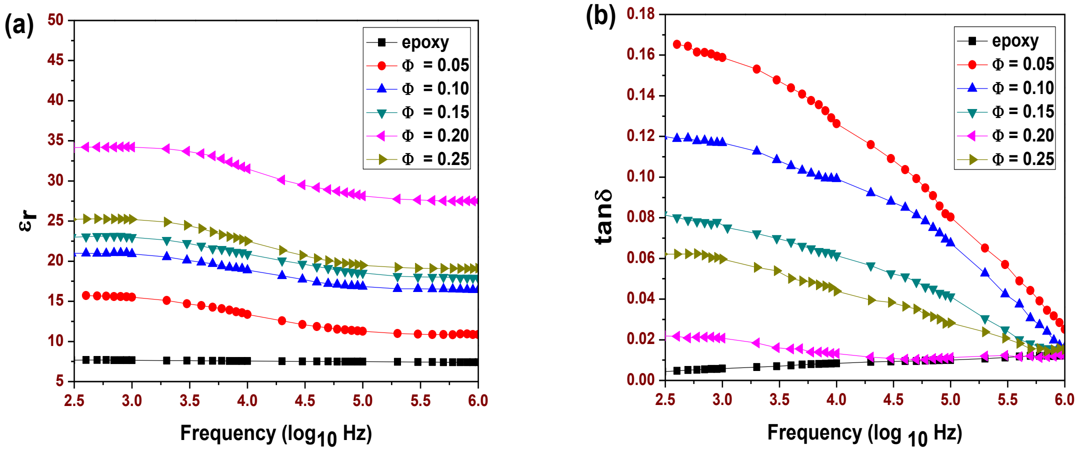

Fig. 5.14 Frequency dependence of (a) ε_r and (b) tanδ of epoxy, and Φ(BZT-BCT)-(1-Φ)epoxy composites with Φ = 0.05, 0.10, 0.15, 0.20, and 0.25, respectively.

The frequency dependence of tanδ for the (BZT-BCT)-epoxy composites with different volume fractions of (BZT-BCT) is shown in Fig. 5.14(b). Dielectric loss value decreases with the increase in frequency for all the compositions and become almost constant in the higher frequency range. This decrease in dielectric loss with the increase of frequency can be due to the decrease of space charge polarization [20]. The decrease in tanδ with frequency can also be ascribed to the decrease in electrical conductivity of the composites with the increase in frequency [21]. The tanδ also decreases with the increase in ceramic loading in the (BZT-BCT)-epoxy composites, but, with 0.25 volume fractions of ceramic filler in the composite, the tanδ value again increases. This can be explained in terms of percolation threshold [22]. It is known that percolation threshold varies depending upon the matrix, filler, particle size, shapes, spatial orientation, and processing parameters. In case of (BZT-BCT)-epoxy composites, the percolation limit of the composite (in terms of (BZT-BCT) ceramic particles) may be around 0.20 volume fractions. ε_r and tanδ values at RT and 1 kHz frequency of the (BZT-BCT)-epoxy composite samples are given in Table – 5.2.

5.4.2 Temperature Dependent Dielectric Constant (ε_r) & Dielectric Loss (tanδ)

5.4.2.1 Φ(BZT-BCT)-(1-Φ)PVDF (where, Φ = 0.05, 0.10, 0.15, 0.20, & 0.25 Volume Fractions) Composites

Fig. 5.15(a) shows the temperature dependence of dielectric constant of the Φ(BZT-BCT)-(1-Φ)PVDF 0-3 composites at an applied frequency of 1 kHz. The value of ε_r at RT increases with an increase of (BZT-BCT) ceramic content in the (BZT-BCT)-PVDF composites. Moreover, the value of ε_r increases continuously to a certain temperature for the (BZT-BCT)-PVDF composites. With an increase in the (BZT-BCT) ceramic content for the (BZT-BCT)-PVDF composites, the temperature corresponding to the maximum ε_r is similar to that of the pure (BZT-BCT) ceramics. This increase in ε_r with the increase in (BZT-BCT) ceramic content in the (BZT-BCT)-PVDF composites is a measure of polarization at RT. The reason may be ascribed to electronic, ionic and dipolar polarizations of the (BZT-BCT) ceramics in addition to a contribution of dipolar orientation polarization of the PVDF polymer. A maximum ε_r of ~ 41 at RT and 1 kHz is obtained for 0.25 volume fractions of the (BZT-BCT) ceramic in the (BZT-

BCT)-PVDF composites. This agrees with earlier reports [11,23]. When a high-permittivity ceramic is minor and forms a dispersed phase in a composite, the major contribution to the dielectric response comes from the continuous matrix instead from the minor ceramic phase. The T_c for the ceramic filler, (BZT-BCT), is ~ 110 ^oC [24]. Therefore, with an increase in the volume fractions of the ceramic filler in the (BZT-BCT)-PVDF composites, the effect of the ceramic filler starts appearing and, hence, there is a dependence of T_c or T_{max} on the ceramic content. There is no systematic variation of T_{max} (Table – 5.2), corresponding to ε_{rmax} at 1 kHz, for the composites. This can be accounted on the basis of existence of three different dielectric responses with temperature in the ceramic-polymer composites [25]. These dielectric responses are (i) the segmental mobility of polymer, which increases with the increase of temperature and increases the dielectric constant, (ii) the disruption of contacts between the filler particles, caused by the thermal expansion of the resin and ceramic and decreases the dielectric constant, and (iii) the change in the dielectric response of the ceramic particles with temperature. The value of ε_r at RT and at 1 kHz frequency increases with the increase in the volume fractions of the (BZT-BCT) ceramic fillers in the (BZT-BCT)-PVDF composites. However, the content of the (BZT-BCT) ceramic has been restricted to 0.25 volume fractions in the (BZT-BCT)-PVDF composites. This is as per the earlier reports on the ceramic-polymer composites; i.e., when the volume fraction of the ceramic filler is > 0.30, the flexibility of a specimen becomes too weak to be used in flexible devices. A high dielectric constant at RT and a low temperature coefficient of capacitance from RT to 70 ^oC makes the 0.25 volume fraction ceramic filled (BZT-BCT)-PVDF composite suitable for flexible capacitors devices.

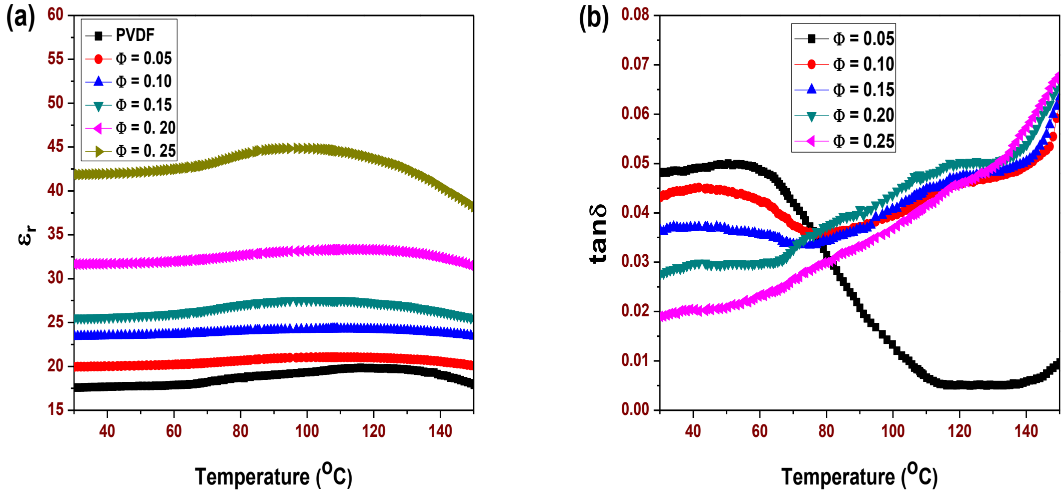

Fig. 5.15 Variation of (a) ε_r and (b) tanδ with temperature at 1 kHz frequency of PVDF, and Φ(BZT-BCT)-(1-Φ)PVDF composites with Φ = 0.05, 0.10, 0.15, 0.20, and 0.25, respectively.

Fig. 5.15(b) shows the temperature dependence of dielectric loss of the Φ(BZT-BCT)-(1-Φ)PVDF 0-3 composites at an applied frequency of 1 kHz. The loss curves of the composite samples do not follow a particular trend. The dielectric loss values are almost constant in the 30 – 80 ^{o}C temperature range and then suddenly it starts increasing. This change in loss values can be attributed to the presence of different types of polarizations in the composites.

5.4.2.2 Φ(BZT-BCT)-(1-Φ)epoxy (where, Φ = 0.05, 0.10, 0.15, 0.20, & 0.25 Volume Fractions) Composites

Fig. 5.16(a) shows the temperature dependence of ε_r at 1 kHz frequency of the (BZT-BCT)-epoxy composite samples. The increase of ε_r from RT to 60 ^{o}C is very small, suggesting the low value of temperature coefficient of capacitance. ε_r value increases continuously to a certain temperature ($T_{\max}$) corresponding to $\varepsilon_{r\max}$ for the composite samples. With the increase in volume fractions of the ceramic filler in the composites, the effect of ceramic filler starts appearing. There is no systematic variation of $T_{\max}$ (shown in Table – 5.2) corresponding to $\varepsilon_{r\max}$ at 1 kHz for the composites. This can be ascribed to the mobility of polymers, the disruption of contacts between the filler particles caused by the thermal expansion of the matrix and ceramic, and the change in the dielectric response of the ceramic particles with temperature [26].

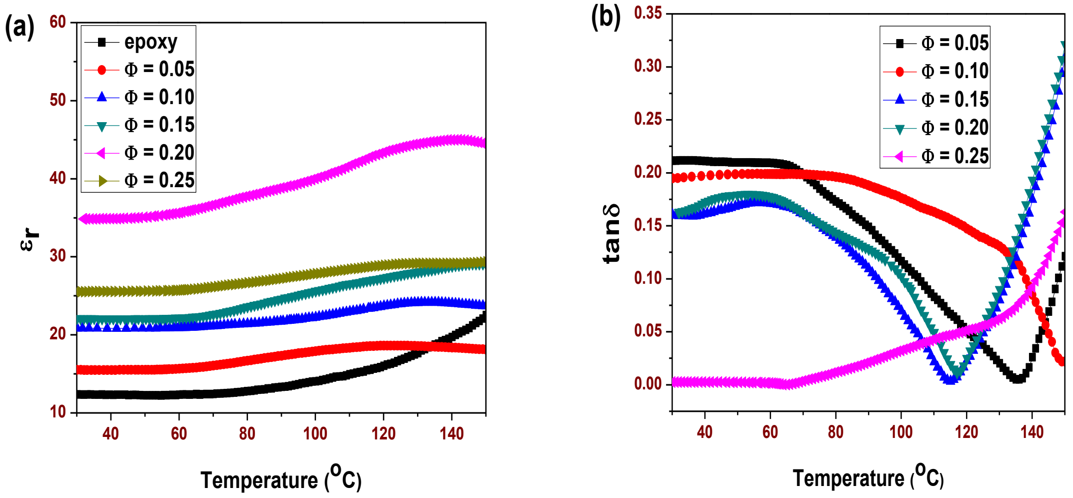

Fig. 5.16 Temperature dependence of (a) ε_r and (b) tanδ of epoxy, Φ(BZT-BCT)-(1-Φ)epoxy composites with Φ = 0.05, 0.10, 0.15, 0.20, and 0.25, respectively.

Fig. 5.16(b) shows the temperature dependence of tanδ of the (BZT-BCT)-epoxy composite samples at 1 kHz frequency. There is a decrease in tanδ with the increase in volume fractions (up to x = 0.15) of (BZT-BCT) ceramic filler content in the (BZT-BCT)-epoxy composite samples. The tanδ values sharply decreases, attaining minima in the temperature range 110–150^{o}C and then suddenly starts increasing with the increase of temperature. The dielectric properties of polymers depend upon the charge distribution and the thermal motion of the polar groups. The minima in the dielectric loss curves correspond to the glass transition regions (T_g) of the polymers. At higher temperature, the thermal oscillation intensifies and the degree of order of orientation diminishes, showing the sudden increase in loss values [26].

Table – 5.2 Different Dielectric Parameters & d_{33} Values for (BZT-BCT)-PVDF & (BZT-BCT)-epoxy Composites with Different Volume Fractions of Ceramics

Materials	**Volume fractions of ceramics**	**Parameters**				
		ε_r at RT at 1 kHz	**tanδ at RT at 1 kHz**	**ε_{rmax} at 1 kHz**	**T_{max} at 1 kHz**	**d_{33} in pC/N**
Φ(BZT-BCT)-(1-Φ) PVDF composites	Φ = 0.05	20	0.04	21	118	8
	Φ = 0.10	23	0.04	24	112	9
	Φ = 0.15	25	0.03	27.5	112	15
	Φ = 0.20	31	0.02	33	116	29
	Φ = 0.25	42	0.01	44	97	31
Φ(BZT-BCT)-(1-Φ) epoxy composites	Φ = 0.05	14	0.15	18.62	123	6
	Φ = 0.10	20	0.11	24.16	133	8
	Φ = 0.15	22	0.07	29.07	148	11
	Φ = 0.20	34	0.01	44.97	142	16
	Φ = 0.25	25	0.05	29.34	150	9

5.5 Dielectric Mixing Models

Experimental dielectric data were fitted to several theoretical equations to find the equation useful for the prediction of the effective dielectric constant of the studied composites. Several quantitative rules of mixture models had been proposed for predictions of the dielectric constant of heterogeneous two component systems on the basis of dielectric properties of each component. The different types of dielectric mixing rules are already discussed in Chapter-1.

5.5.1 Dielectric Mixing Rules for (BZT-BCT)-PVDF Composites

Among the different dielectric mixing models, the Lichtenecker model accounts better for the observed ε_r of the composites. The ε_r of the (BZT-BCT)-PVDF composites were calculated with a modified Lichtenecker logarithmic law (Eqn 5.2) [27].

$$\log \varepsilon_r = \log \varepsilon_p + v_b(1-k)\log\left(\frac{\varepsilon_b}{\varepsilon_p}\right) \tag{5.2}$$

Where, k is a fitting constant of the composite, v_b is the volume fraction of ceramic, ε_p and ε_b are the dielectric constants of the pure polymer and ceramic, respectively. For our composites, k = 0.438 was used, and the variations of ε_r, as per Lichtenecker logarithmic law equation and the measured one, with volume fraction of ceramic in the (BZT-BCT)-PVDF composites are shown in Fig. 5.17. The best fit of the Lichtenecker equation up to 0.20 volume fractions of ceramics in the (BZT-BCT)-PVDF composites show its usefulness for the prediction of the effective dielectric constant. The large mismatch of the fitted and experimental relative permittivities at 0.25 volume fractions of ceramic fillers can be ascribed to the limitations of Eqn 5.2. The Lichtenecker equation can be applied only if the dielectric constant of polymer matrix differs slightly from the dielectric constant of the particle inclusions. With an increase in volume fractions of the ceramic fillers in the (BZT-BCT)-PVDF composites, the dielectric constant of the pure polymer matrix starts differing greatly from the dielectric constant of the ceramic particle inclusions and, hence there starts deviation at 0.25 volume fraction of (BZT-BCT) filler. The calculated/fitted ε_{eff} values are given in Table – 5.3.

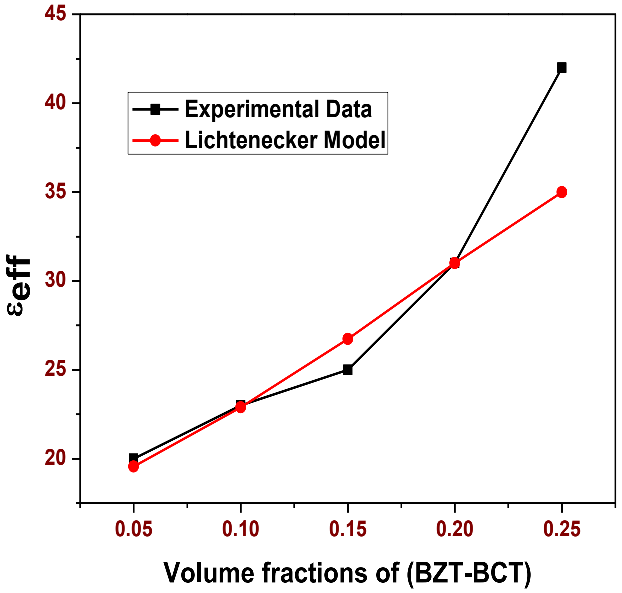

Fig. 5.17 Variation of effective dielectric constant (ε_{eff}) (measured at RT and 1 kHz frequency) of (BZT-BCT)-PVDF composites as a function of volume fractions of (BZT-BCT) ceramics.

5.5.2 Dielectric Mixing Rules for (BZT-BCT)-epoxy Composites

Fig. 5.18 shows the comparison of the RT ε_r values of the (BZT-BCT)-epoxy composites at 1 kHz (experimental), for different volume fractions of (BZT-BCT), with the ε_r values, calculated based on various models. For the (BZT-BCT)-epoxy composites, the most commonly used dielectric mixing models, the Lichtenecker model [27], Maxwell's model [28] and the Clausius-Mossotti model [29], are not fitting properly.

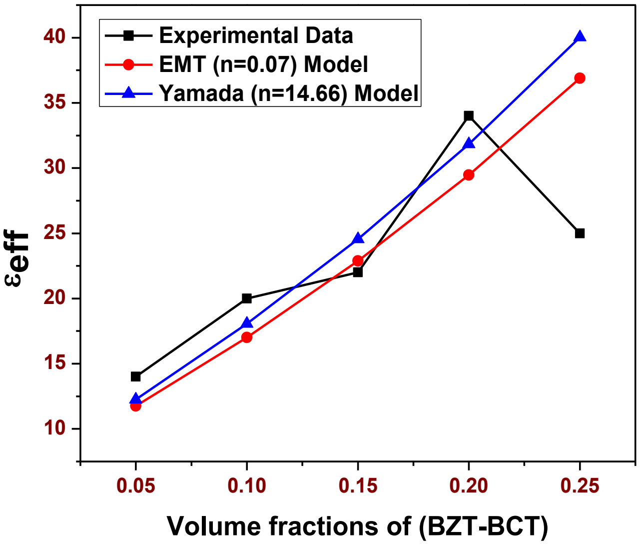

Fig. 5.18 Variation of ε_{eff} of (BZT-BCT)-epoxy composites as a function of volume fractions of (BZT-BCT) ceramics.

Effective Medium Theory (EMT) [30] model is used for calculating the ε_{eff} of the composites. As per this model, the effective dielectric constant is given by

$$\varepsilon_{eff} = \varepsilon_p \left[1 + \frac{f_c\,(\varepsilon_c - \varepsilon_p\,)}{\varepsilon_p + n\,(1 - f_c\,)(\varepsilon_c - \varepsilon_p)}\right] \tag{5.3}$$

Where, f_c is the volume fraction of the dispersed ceramic, ε_p, ε_c and n are the dielectric constants of the ceramic particle, polymer and the ceramic morphology fitting factor, respectively in the ceramic-polymer composites. n takes the value 0 (prolate), 1/3 (sphere), 1 (oblate) and intermediate values for intermediate shapes [31].

The parameter 'n' is calculated by using Eqn 5.3 to fit the experimental and theoretical values of the (BZT-BCT)-epoxy composites. The calculated/fitted ε_{eff} values are given in Table – 5.3. The experimental ε_r values fit well into the EMT model with n = 0.07 for the volume fractions (≤ 0.20) of the (BZT-BCT) ceramics.

The model, developed by Yamada *et al.* [32] is also used to predict ε_{eff} of the presently studied composites. As per this model, considering the binary system, composed of ellipsoidal particles dispersed in a continuous medium, the permittivity of the composite is given by

$$\varepsilon_{eff} = \varepsilon_1 \left[1 + \frac{n f_{ceramic}(\varepsilon_2 - \varepsilon_1)}{n\varepsilon_1 + (\varepsilon_2 - \varepsilon_1)(1 - f_{ceramic})}\right] \tag{5.4}$$

Here ε_1 and ε_2 are the dielectric constant of the polymer and ceramics, respectively. n and $f_{ceramic}$ are the parameter related to the geometry of the ceramic particles and the volume fraction of the ceramic phase in the matrix, respectively.

As per this model, the parameter 'n' is evaluated such that the mismatch between the theoretical and observed values is minimum. The experimental results are comparable to those obtained using this model for 0.20 volume fractions of the (BZT-BCT) ceramic filler, when the parameter 'n' is ~ 14.66 (given in Table – 5.3).

The mixing rule application of the composites to predict dielectric properties depends on several factors. As in Fig. 5.17 or 5.18, the best fit of the Lichtenecker equation is up to 0.20 volume fractions of the ceramics. The mismatch of the fitted and experimental relative permittivities at 0.25 volume fraction of the ceramic filler can be ascribed to the limitations of addition of filler. With the increase in volume fractions of the ceramic fillers in the composites, the dielectric constant of the pure polymer starts differing greatly from the dielectric constant of the ceramic particles, hence there starts the deviation. Another problem in predicting the effective dielectric constant of ceramic-polymer composites using theoretical equations is the fact that the dielectric constant of ceramic powders is not available. The dielectric constant of polymer can be easily obtained by capacitance measurement of the polymer film, but there is no direct method to measure the dielectric constant of ceramic powders. Because of this problem, in most of literatures the dielectric constant of bulk ceramics has been used instead of the dielectric constant of ceramic powders. Therefore the predicted dielectric constant values deviate from measured values at high powder loading [33].

5.6 Piezoelectric Studies

5.6.1 Piezoelectric Studies of (BZT-BCT)-PVDF Composites

The piezoelectric constant (d_{33}) of the (BZT-BCT)-PVDF composite samples are given in Table – 5.2. Maximum d_{33} value ~ 31 pC/N is obtained in case of 0.25(BZT-BCT)-0.75PVDF composite. It is known that the piezoelectric constant is strongly dependent on the domain orientation during poling. In our case, the domain orientation during poling process appears to be enhanced due to the improved connectivity [8].

The performance of a piezoelectric material for energy harvesting applications can be expressed as the figure of merit (FOM) presented in the following Eqn:

$$\mathrm{FOM}\left(\mathrm{pm}^2/\mathrm{N}\right) = d_{33} * g_{33} = \frac{(d_{33})^2}{\varepsilon} \tag{5.5}$$

Fig. 5.19 shows the FOM of (BZT-BCT)-PVDF composites as a function of the content of (BZT-BCT) ceramics for energy harvesting application. The FOM reaches maximum when the volume fraction of (BZT-BCT) ceramics is 0.25. g_{33} values are greatly affected by the volume fractions of ceramic filler. Therefore the maximum FOM for 0.25 volume fraction of ceramics can be attributed to the effect of g_{33} on the ceramic concentration. This phenomenon can also be explained by counteracting effects of density on the d_{33} [34].

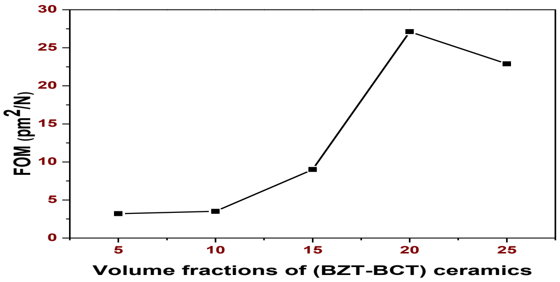

Fig. 5.19 FOM for energy harvesting application for (BZT-BCT)-PVDF composites as a function of the volume fractions of (BZT-BCT) ceramics.

5.6.2 Piezoelectric Studies of (BZT-BCT)-epoxy Composites

Piezoelectric constant (d_{33}) values of (BZT-BCT)-epoxy composite samples are listed in Table – 5.2. The maximum value of d_{33} was found for 0.20 volume fractions of filler content in the (BZT-BCT)-epoxy composites. The value of d_{33} decreases for 0.25 volume fraction of filler content in the composites. This can be related to the maximum loading of the ceramic fillers in the (BZT-BCT)-epoxy composites.

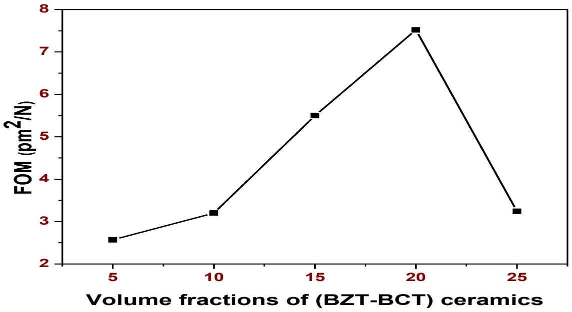

Fig. 5.20 FOM for energy harvesting application for (BZT-BCT)-epoxy composites as a function of the volume fractions of (BZT-BCT) ceramics.

The performance of a piezoelectric material for energy harvesting is expressed as the figure of merit (FOM) as given in the Eqn (5.5). Fig. 5.20 shows the FOM of (BZT-BCT)-epoxy composites for energy harvesting applications as a function of the content of (BZT-BCT) ceramic fillers. The FOM reaches maximum when the volume fraction of the (BZT-BCT) ceramics is 0.20 volume fraction in the (BZT-BCT)-epoxy composites, which can be related to the maximum density of these composite samples. Hence, it can be concluded that the mechanical strength of the (BZT-BCT)-epoxy composite specimens over 0.20 volume fraction becomes too weak to be used as flexible devices.

Table – 5.3 Comparison of Experimental and Theoretical Values of ε_{eff} of (BZT-BCT)-PVDF & (BZT-BCT)-epoxy Composites with Different Volume Fractions of Ceramics

Materials	**Volume fractions of ceramics**	**Experimental values of ε_r (at 1 kHz and at RT)**	**Theoretical values of ε_r (at 1 kHz and at RT) according to different models**		
			Lichtenecker model	**Yamada model**	**EMT model**
Φ(BZT-BCT)-(1-Φ) PVDF composites	Φ = 0.05	20	19.56	-	-
	Φ = 0.10	23	22.89	-	-
	Φ = 0.15	25	26.74	-	-
	Φ = 0.20	31	31	-	-
	Φ = 0.25	42	35	-	-
Φ(BZT-BCT)-(1-Φ) epoxy composites	Φ = 0.05	14	-	12.25	11.75
	Φ = 0.10	20	-	18.07	17.01
	Φ = 0.15	22	-	24.56	22.88
	Φ = 0.20	34	-	31.82	29.46
	Φ = 0.25	25	-	40.03	36.89

5.7 Summary

The structural, optical, morphological, dielectric and piezoelectric properties of the Φ(BZT-BCT)-(1-Φ)PVDF and Φ(BZT-BCT)-(1-Φ)epoxy 0-3 ceramic-polymer composites with (Φ = 0.05, 0.10, 0.15, 0.20 & 0.25 volume fractions) have been studied. The XRD patterns of all the composite samples showed the presence of peaks corresponding to both polymer and ceramics phases, respectively. The optical band gap value increases with the increase in the (BZT-BCT) ceramic filler concentration in both the (BZT-BCT)-PVDF and (BZT-BCT)-epoxy composites. Morphological studies confirmed the 0-3 connectivity of ceramic filler particles in the PVDF and epoxy polymer matrix, respectively. Dielectric studies of the composites illustrated the increase in the value of ε_r at RT with the increase in ceramic filler content. Finally, 0.25(BZT-BCT)-0.75(PVDF) composite showed the highest relative permittivity (ε_r) ~ 42 with low temperature coefficient of capacitance and highest d_{33} ~ 31 pC/N. Whereas, 0.20(BZT-BCT)-0.80(epoxy) composite showed the highest relative permittivity (ε_r) ~ 34 with low temperature coefficient of capacitance and highest d_{33} ~ 16 pC/N. Hence, it can be concluded that both 0.25(BZT-BCT)-0.75(PVDF) and 0.20(BZT-BCT)-0.80(epoxy) ceramic-polymer composites are suitable for flexible capacitors devices and also for energy harvesting piezoelectric applications.

References:

[1] Z. Cui-Hua, Z. Bo-Ping and S. Peng-Peng, Chinese Physics B. 18, (2009) 5539.

[2] U. Kreibig and C. V. Fragstein, Z. Phys. 224, (1969) 307.

[3] E. I. Awad, Journal of Kerbala University. 10, (2012) 1.

[4] H. G. Tompkins and E. A. Irene, Handbook of Ellipsometry (William Andrew, Inc. 2005).

[5] J. C. Sczancoski, L. S. Cavalcante, M. R. Joya, J. A. Varela, P. S. Pizani and E. Longo, Chemical Engineering Journal. 140, (2008) 632.

[6] S. Muthukumaran and M. Muthusamy, J Mater Sci: Mater Electron. 23, (2012) 1647.

[7] Z. M. Gibbs, A. L. Londe and G. J. Snyder. New J. Phys. 15, (2013) 075020.

[8] D. T. Le, N. B. Do, D. U. Kim, I. Hong, I. W. Kim and J. S. Lee, Ceram. Int. 38, (2012) S259.

[9] C. J. Dias and D. K. Das-Gupta, IEEE Trans. Electr. Insul. 5, (1996) 706.

[10] B. Hilczer, J. Kulek, M. Polomska, M. Kosec, B. Malic and L. Kepinski, Ferroelectrics. 338, (2006) 159.

[11] R. Popielarz, C. K. Chiang, R. Nozaki and J. Obrzut, Macromolecules. 34, (2001) 5910.

[12] V. S. Yadav, D. K. Sahu, Y. Singh and D. C. Dhubkarya, Proceedings of the International Multi Conference of Engineers and Computer Scientists, Newswood Limited, Hong Kong, 17–19 March, 2010.

[13] M. A. Habeeb, A. Hashim and A. R. K. Abid Ali, Eur. J. Sci. Res. 61, (2011) 367.

[14] P. K. C. Pillai and Rashmi, Int. J. Polym. Mater. 8, (1980) 255.

[15] R. J. Gregorio and M. J. Cestari, Polym. Sci. Part B. 32, (1994) 859.

[16] Y. Bai, Z. Y. Cheng, V. Bharti, H. S. Xu and Q. M. Zhanga, Appl. Phys. Lett. 76, (2000) 3804.

[17] S. H. Choi, I. D. Kim, J. M. Hong and S. G. Oh, Macromol. Symp. 249, (2007) 241.

[18] G. Zhang and M. S. Wu, International Journal of Engineering Science. 48, (2010) 37.

[19] C. V. Chanmal and J. P. Jog, Express Polymer Letters. 2, (2008) 294.

[20] C. Basavaraja, Y. M. Choi and H. T. Park, Bulletin of the Korean Chemical Society. 28, (2007) 1104.

[21] R. Gregorio Jr. and E. M. Ueno, Journal of Materials Science. 34, (1999) 4489.

[22] K. Osinska, A. Lisinska-Czekaj, H. Bernard, J. Dzik, M. Adamczyk and D. Czekaj, Archives of Metallurgy and Materials. 56, (2011) 1093.

[23] G. Wang, Appl. Mater. Interfaces. 2, (2010) 1290.

[24] P. Mishra, Sonia and P. Kumar, J. Alloy. Compd. 545, (2012) 210.

[25] L. Ramjo, M. Robredo and M. Castro, Composites A. 36, (2005) 1267.

[26] G. K.Williamson and W. H. Hall, Acta Metallurgica. 1, (1953) 22.

[27] A. V. Goncharenko, V. Z. Lozovski and E. F. Venger, Optics Communications. 174 (2000) 19.

[28] P. Thomas, K. T. Varughese, K. Dwarakanath and K. B. R. Varma, Composites Science and Technology. 70 (2010) 539.

[29] M. Dinulovic and B. Rasuo, Composite Structures. 93 (2011) 3209.

[30] Y. Rao, J. Qu, T. Marinis and C. P. Wong, IEEE Trans. Compon. Packag. Technol. 23, (2000) 680.

[31] H. Zewdie, Bull. Chem. Soc. Ethiop. 12 (1998) 159.

[32] T. Yamada, T. Ueda and T. Kitayama, J. Appl. Phys. 53, (1982) 4328.

[33] S. Cho, S. Lee, J. Hyun, K. Paik, J. Mater. Science: Mater. in Electronics 16 (2005) 77– 84

[34] C. R. Bowen, A. Perry, A. C. F. Lewis and H. Kara, Journal of the European Ceramic Society. 24, (2004) 541.

******

Chapter – 6

STRUCTURAL & ELECTRICAL PROPERTIES OF (BZT-BCT)-(PVDF-CCTO) AND (BZT-BCT)-(EPOXY-CCTO) CERAMIC-POLYMER COMPOSITES

In this chapter, the structural, optical, morphological, dielectric and piezoelectric properties of $0.25\{0.50[Ba(Zr_{0.2}Ti_{0.8})O_3]-0.50[(Ba_{0.7}Ca_{0.3})TiO_3]\}-0.75\{(1-x)PVDF-xCaCu_3Ti_4O_{12}\}$/[(BZT-BCT)-(PVDF-CCTO)] & $0.20\{0.50[Ba(Zr_{0.2}Ti_{0.8})O_3]-0.50[(Ba_{0.7}Ca_{0.3})TiO_3]\}-0.80\{(1-x)epoxy-xCaCu_3Ti_4O_{12}\}$/[(BZT-BCT)-(epoxy-CCTO)] ($x = 0.02$, 0.04, 0.06, 0.08 & 0.10 volume fractions) ceramic-polymer composites with 0-3 connectivity are discussed. (BZT-BCT)-(PVDF-CCTO) composites are prepared by hot uniaxial press method, whereas the (BZT-BCT)-(epoxy-CCTO) composites are prepared by cold press followed by hand lay-up technique. The detailed description of the preparation and the experimental procedure of these composite samples are mentioned in Chapter-3.

6.1 XRD Studies

6.1.1 XRD Studies of (BZT-BCT)-(PVDF-CCTO) Composites

Fig. 6.1 shows the XRD patterns of the (BZT-BCT)-(PVDF-CCTO) composite samples. These XRD patterns show the presence of peaks corresponding to all the three constituent components. However, the XRD patterns of the (BZT-BCT)-(PVDF-CCTO) composites resembles more with the pure (BZT–BCT) and CCTO ceramics as the volume fraction of the CCTO increases from $x = 0.02$ to $x = 0.10$.

6.1.2 XRD Studies of (BZT-BCT)-(epoxy-CCTO) Composites

Fig. 6.2 shows the XRD patterns of the (BZT-BCT)-(epoxy-CCTO) composites as a function of the volume fractions of the CCTO powder. The XRD patterns of these composites reveal mainly the presence of crystal phases of the (BZT-BCT) & CCTO ceramics. The intensities of the CCTO crystalline peaks increases and in the low angle range (20-30 ^{o}C) the relative intensities of the (BZT-BCT)-(epoxy) composites decreases with the increase of CCTO content in the composites [1]. This is because; with the increase of CCTO ceramic powder in the (BZT-BCT)-(epoxy-CCTO) composites, CCTO phase starts dominating the crystal properties of the (BZT-BCT)-epoxy composites. Again, there is a shifting observed in the maximum intensity peak of the composites with the increase in the CCTO ceramic content which follows no particular trends, but the values of 2θ are found in between 2θ values of (BZT-BCT) & CCTO.

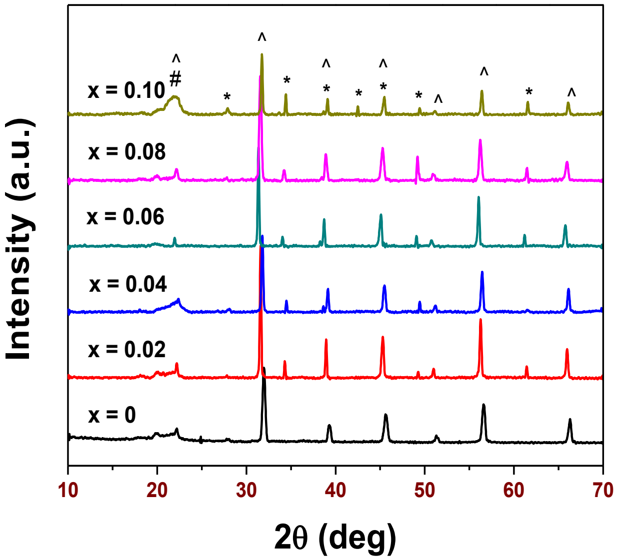

Fig. 6.1 XRD patterns of 0.25(BZT-BCT)-0.75[(1-x)PVDF-xCCTO] composites, where #, ^ and * represent PVDF, (BZT-BCT) and CCTO phases, respectively.

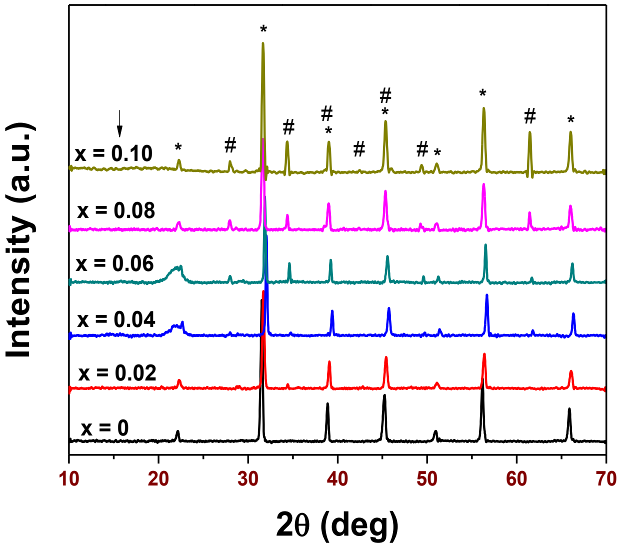

Fig. 6.2 XRD patterns of 0.20(BZT-BCT)-0.80[(1-x)epoxy-xCCTO] composites, where, ↓, * and # represents epoxy, (BZT-BCT) and CCTO phases, respectively.

6.2 UV–Visible Absorption Spectroscopy Studies

6.2.1 UV–Visible Absorption Spectroscopy Studies of (BZT-BCT)-(PVDF-CCTO) Composites

Fig. 6.3 depicts the UV absorption spectra of the (BZT-BCT)-(PVDF-CCTO) composite samples recorded in the 200 to 800 nm wavelength range. The absorption spectra of the composites show no particular trend in the peak intensity. The intensity of the absorption peak increases by increasing the CCTO ceramic content up to x = 0.08, but decreases as the CCTO content is more than x = 0.08. This weakened peak at high CCTO ceramic content (x = 0.10) in the composites may be due to the highly dispersed ceramics [2]. Also, the spectra of the composites show broadening which may be ascribed to the mean free path effect as well as the influence of conduction electron collisions with the particle surfaces [3]. Again, the broad peaks of the composites show blue shift with the increase in the ceramic content. The reason for this blue shift may be ascribed to the large electric field due to the spontaneous and piezoelectric polarization [4]. The piezoelectric polarization in a composite arises from the biaxial strain remaining in the hetero structures due to the lattice mismatch. The electric field tilts the energy bands and separates the electron hole pairs and the overlapping of the electron hole wave function results in a blue shift of the emission peaks [4]. Thus the blue shift can be attributed to the band filling of localized states at minimum potential.

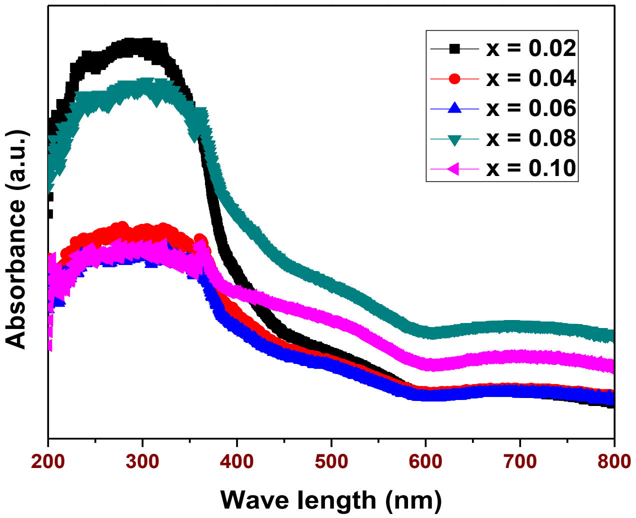

Fig. 6.3 UV-Visible absorption spectra of 0.25(BZT-BCT)-0.75[(1-x)PVDF-xCCTO] composites.

The absorption coefficient ($\propto$) values of the (BZT-BCT)-(PVDF-CCTO) composites are < 10^4 cm^{-1}, which indicates the presence of the indirect electronic transition. The relation proposed by Tauc, Davis & Mott [5] is used to find out the optical band gap (E_g). Since in this experiment, the indirect allowed transition is used, we can take the value of n=2. The E_g values of the (BZT-BCT)-(PVDF-CCTO) composite samples can be obtained by plotting $(\propto h\nu)^2$ vs hν graphs and by extrapolating the linear portion of the absorption edge to find the intercept with energy axis. The energy gap estimated by plotting $(\propto h\nu)^2$ vs hν is shown in Fig. 6.4 and the individual graphs of each composition are shown in the Fig. 6.5 (a)-(e).

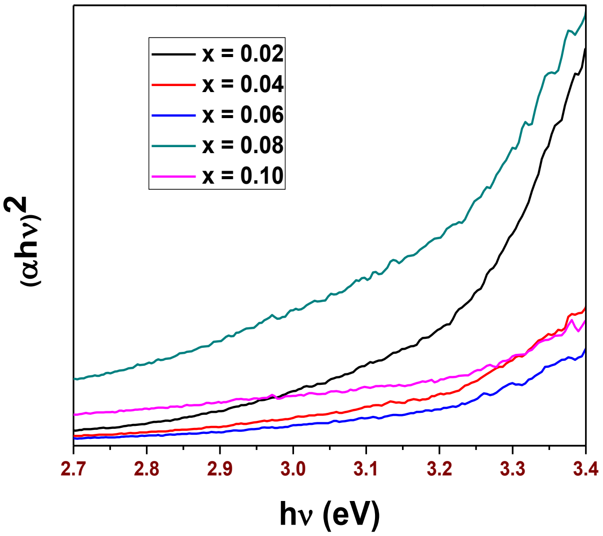

Fig. 6.4 The $(\propto h\nu)^2$ vs hν curves for 0.25(BZT-BCT)-0.75[(1-x)PVDF-xCCTO] composites.

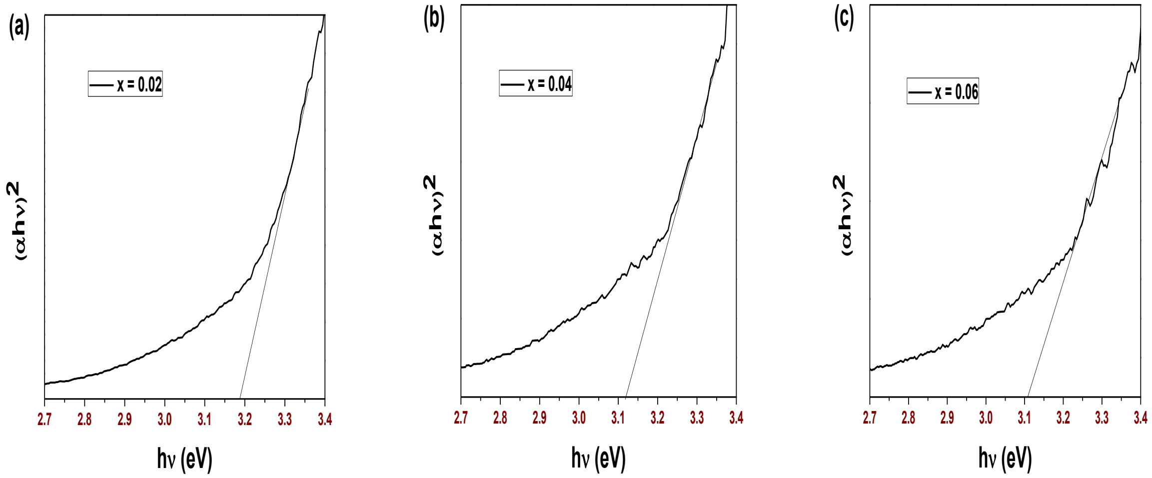

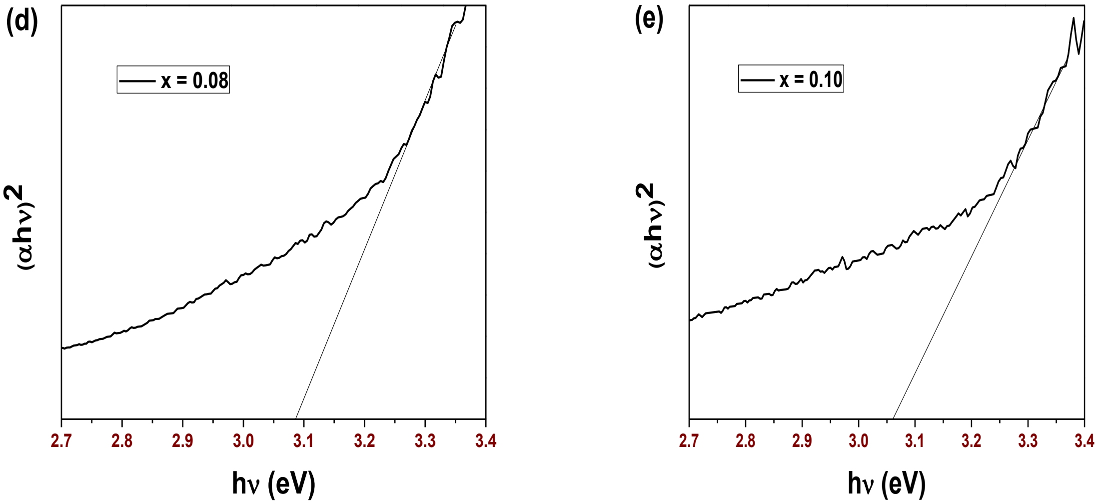

Fig. 6.5 The $(\propto h\nu)^2$ vs hν curves for 0.25(BZT-BCT)-0.75[(1-x)PVDF-xCCTO] composites with (a) x = 0.02, (b) x = 0.04, (c) x = 0.06, (d) x = 0.08 & (e) x = 0.10, respectively.

The band gap values of the composite samples are found to decrease from 3.19 to 3.06 eV with the increase of the (CCTO) ceramic concentrations from x = 0.02 to 0.10. This may be due to certain structural changes occurring in the composite materials with changing composition. The increase in CCTO ceramic concentration may localize some states in the deep energy levels to cause a decrease in the energy gap [6]. Table – 6.1 gives the values of the band gap energy of the (BZT-BCT)-(PVDF-CCTO) composite samples.

6.2.2 UV–Visible Absorption Spectroscopy Studies of (BZT-BCT)-(epoxy-CCTO) Composites

The absorption spectra of the (BZT-BCT)-(epoxy-CCTO) composite samples have been recorded in the 200 to 800 nm wavelength range and shown in Fig. 6.6. The absorption spectra show the increase in the absorbance intensities with the increase in the CCTO concentration from x = 0.02 to 0.10 in the composites [7]. Fig. 6.6 also shows that with the increase in volume fractions of the CCTO ceramics there is no change of the chemical structure of the composites but a new physical mixture has been formed. There is no shift in the peak positions, but the intensity of the peaks increases with the increase in the CCTO ceramic concentrations in the composites [8].

The energy band gap of the (BZT-BCT)-(epoxy-CCTO) composites is obtained by plotting $(\propto h\nu)^2$ versus hν and by extrapolating the linear portion of the absorption edge to find the intercept with the energy axis. The energy band gap is estimated by plotting $(\propto h\nu)^2$ versus hν as shown in Fig. 6.7. The band gap values of the composite samples is increased from 3.10 to 3.21 eV with the increase of CCTO ceramic concentrations from x = 0.02 to 0.10. This increase in the E_g values can also be related to the Burstein–Moss effect [9]. Table – 6.1 gives the values of the optical band gap for the different (BZT-BCT)-(epoxy-CCTO) composites.

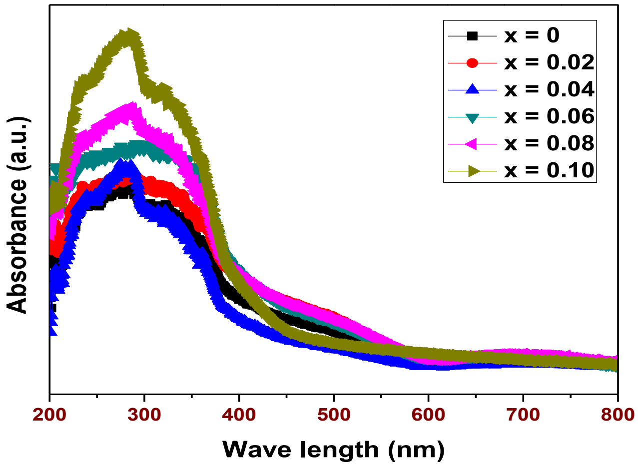

Fig. 6.6 UV-Visible absorption spectra of 0.20(BZT-BCT)-0.80[(1-x)epoxy-xCCTO] composites.

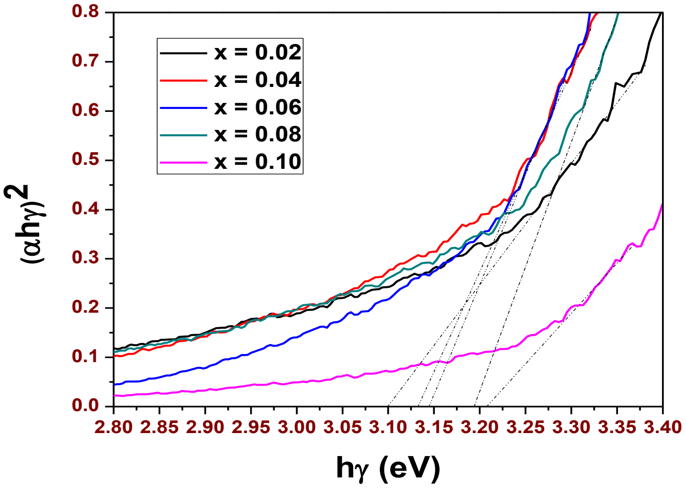

Fig. 6.7 The $(\propto h\nu)^2$ vs hν curves for 0.20(BZT-BCT)-0.80[(1-x)epoxy-xCCTO] composites with x = 0.02, 0.04, 0.06, 0.08 & 0.10, respectively.

6.3 Morphological Studies

6.3.1 Morphological Studies of (BZT-BCT)-(PVDF-CCTO) Composites

Fig. 6.8 shows the SEM micrographs of the (BZT-BCT)-(PVDF-CCTO) composite samples with different volume fractions of the CCTO ceramics. It can be seen that the ceramic particles are distributed randomly in the PVDF matrix. The even distribution of ceramic powders in the PVDF matrix clearly indicates the 0–3 connectivity pattern (also confirmed from the cross-sectional SEM images) [10]. The experimental densities (given in Table – 6.1) are found to increase from 2.85 to 2.93 g/cm^3 with the increase in volume fractions of the CCTO ceramics in the composites from x = 0.02 to 0.08 and it decreases for x = 0.10. The density and porosity of the composite samples are listed in the Table – 6.1. The decrease of the density for x = 0.10 volume fraction of CCTO ceramics in (BZT-BCT)-(PVDF-CTO) composites suggest the limit of addition of the CCTO in the composites.

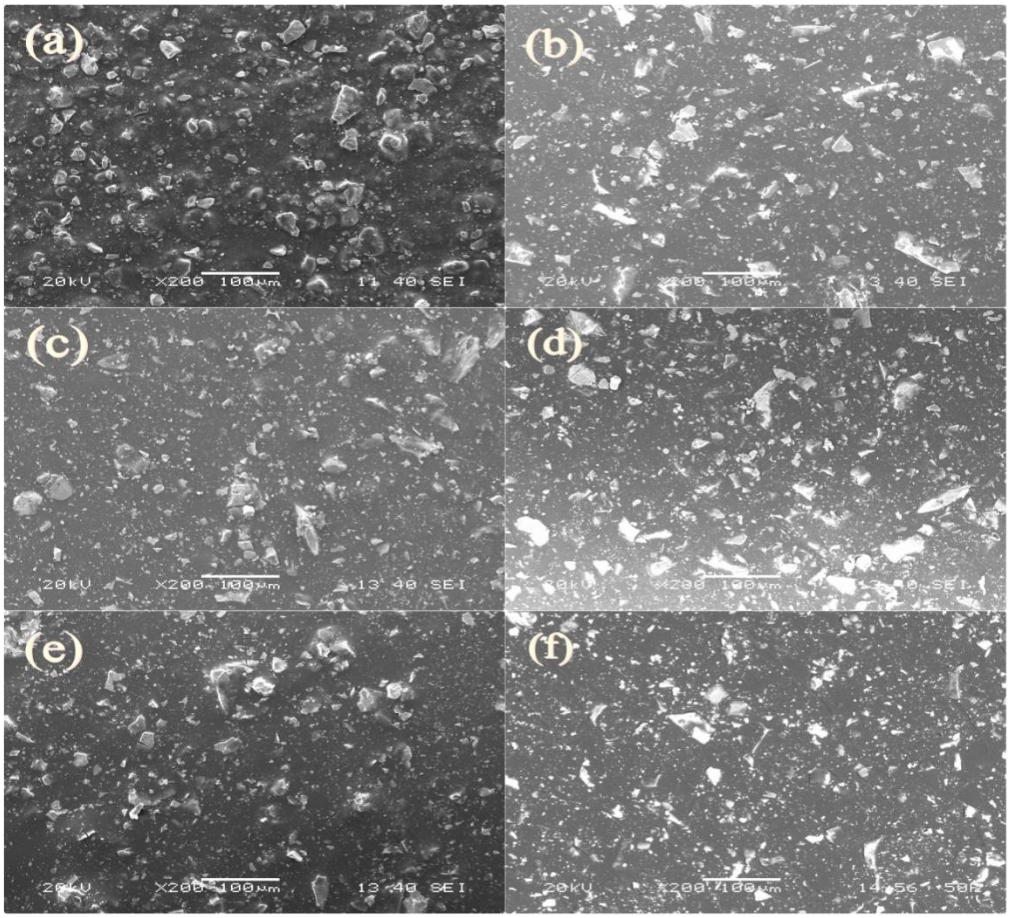

Fig. 6.8 SEM images of 0.25(BZT-BCT)-0.75[(1-x)PVDF-xCCTO] composites with x = (a) 0, (b) 0.02, (c) 0.04, (d) 0.06, (e) 0.08 & (f) 0.10, respectively.

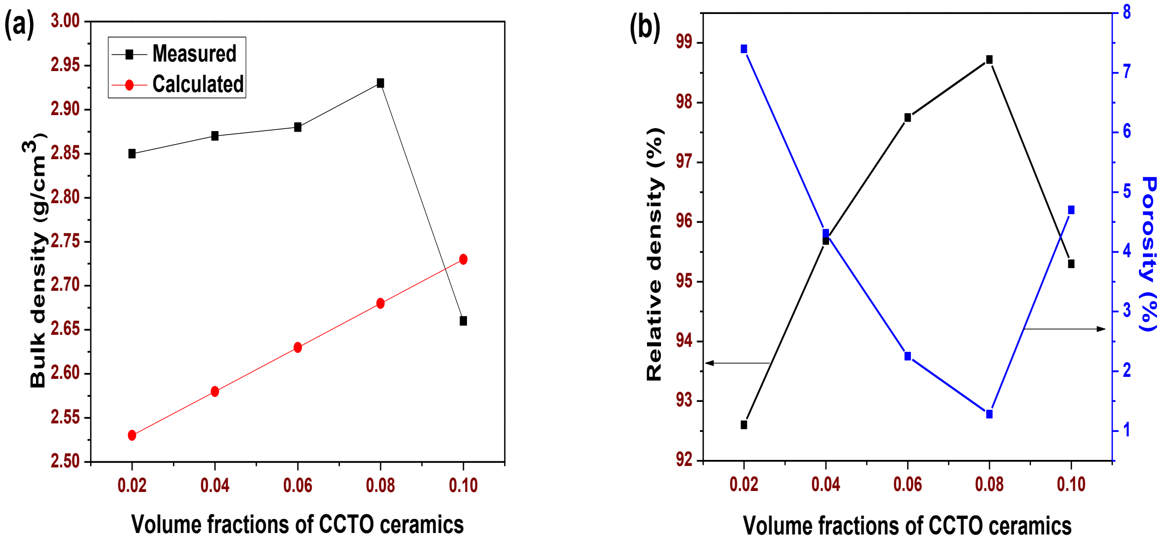

Fig. 6.9 (a) Bulk density, and (b) porosity of (BZT-BCT)-(PVDF-CCTO) composites as a function of volume fractions of CCTO.

6.3.2 Morphological Studies of (BZT-BCT)-(epoxy-CCTO) Composites

Fig. 6.10 shows the SEM micrographs of the (BZT-BCT)-(epoxy-CCTO) composites with different volume fractions of the CCTO ceramics. Fig. 6.10 shows the random distribution of the CCTO ceramic particles in the epoxy polymer, which increases with the increase in the volume fractions of the CCTO ceramics. This random distribution of ceramic particles in the polymer matrix confirms the 0-3 connectivity pattern of the composite samples (also confirmed from the cross-sectional SEM images) [10]. The density and porosity of the (BZT-BCT)-(epoxy-CCTO) composite samples are listed in Table – 6.1. Fig. 6.11 shows the density and porosity of the (BZT-BCT)-(epoxy-CCTO) composite samples as a function of the volume fractions of the CCTO ceramics. The experimental density of the composite samples is found to increase from 1.80 to 2.19 g/cm^3 with the increase of volume fractions of the CCTO ceramics from x = 0.02 to 0.08 in the composites and it decreases for x = 0.10 of the CCTO ceramics. Further addition of the CCTO ceramics beyond x = 0.08 volume fraction reduces the flexibility of the composite samples and the decrease in the density at x = 0.10 volume fraction of CCTO ceramics suggests the limit of addition of the ceramics in the composites.

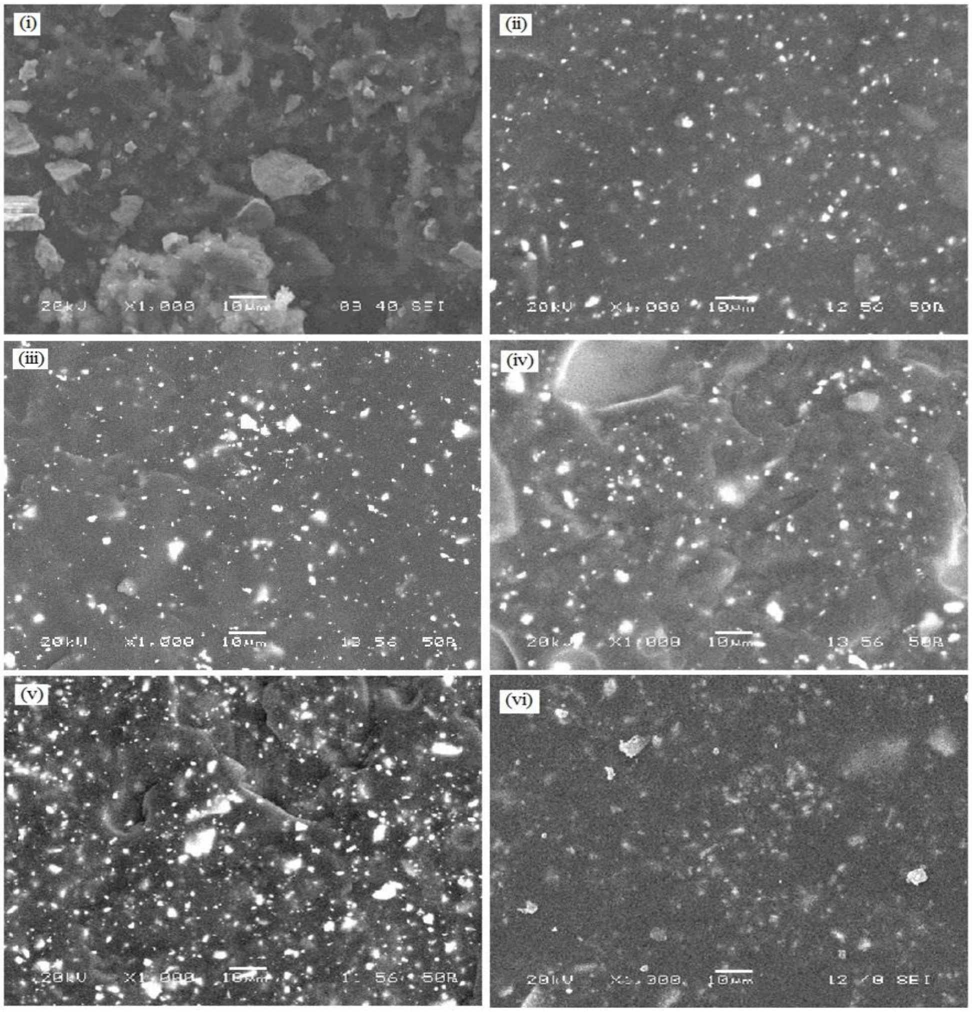

Fig. 6.10 SEM images of 0.20(BZT-BCT)-0.80[(1-x)epoxy-xCCTO] composites with x = (i) 0, (ii) 0.02, (iii) 0.04, (iv) 0.06, (v) 0.08 and (vi) 0.10, respectively.

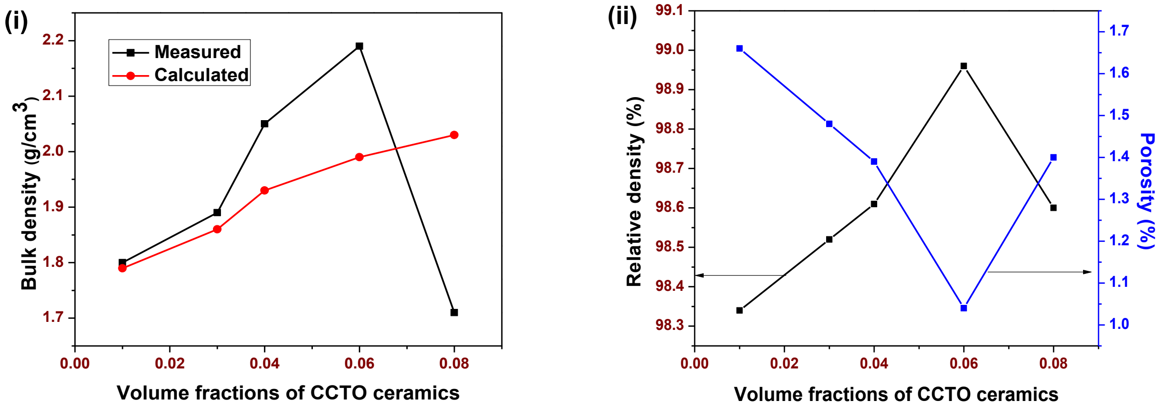

Fig. 6.11 (i) Bulk density and (ii) porosity of (BZT-BCT)-(epoxy-CCTO) composites as a function of volume fractions of CCTO.

Table – 6.1 E_g, Density & Porosity Values for (BZT-BCT)-(PVDF-CCTO) & (BZT-BCT)-(epoxy-CCTO) Composites with Different Volume Fractions of Ceramics

Materials	**Volume fractions of ceramics**	**Parameters**			
		Energy band gap (E_g) in eV	**Measured Density in gm/cc**	**Calculated Density in gm/cc**	**porosity of the composites in %**
0.25(BZT-BCT)-0.75[(1-x)PVDF-xCCTO] composites	x = 0.02	3.19	2.85	2.53	7.40
	x = 0.04	3.12	2.87	2.58	4.31
	x = 0.06	3.11	2.88	2.63	2.25
	x = 0.08	3.08	2.93	2.68	1.28
	x = 0.10	3.06	2.66	2.73	4.70
0.2(BZT-BCT)-0.8[(1-x)epoxy-xCCTO] composites	x = 0.02	3.10	1.80	1.79	1.66
	x = 0.04	3.13	1.89	1.86	1.48
	x = 0.06	3.14	2.05	1.93	1.39
	x = 0.08	3.19	2.19	1.99	1.04
	x = 0.10	3.21	1.71	2.03	1.40

6.4 Dielectric Studies

6.4.1 Frequency Dependent Dielectric Constant (ε_r) & Dielectric Loss (tanδ)

6.4.1.1 (BZT-BCT)-(PVDF-CCTO) Composites

The frequency dependence of ε_r of the (BZT-BCT)-(PVDF-CCTO) composite samples with different volume fractions of CCTO ceramics is shown in Fig. 6.12(a). A maximum dielectric constant of ~ 90 at 1 kHz frequency and at RT is achieved for x = 0.08 volume fraction of CCTO ceramics in the (BZT-BCT)-(PVDF-CCTO) composites. As expected, ε_r increases with the increase in CCTO volume content up to x = 0.08 in the (BZT-BCT)-(PVDF-CCTO) composites and beyond x = 0.08, ε_r value starts decreasing. In all the cases, the obtained effective dielectric constants of the composites are higher than that of 0.25(BZT-BCT)-0.75(PVDF) composites, but much lower than that of pure (BZT-BCT) and CCTO ceramics, respectively. Apart from the connectivity and particle size effects, the low value of ε_r of the (BZT-BCT)-(PVDF-CCTO) composites as compared to that of the (BZT-BCT) and CCTO ceramics individually can be ascribed to the following facts. Based on the X-ray studies, it is confirmed that in the composites, the PVDF is present in the mixed α and β phases. α phase of PVDF is non-polar and the corresponding constrained polymer chain is hindering the contribution of electrical polarization, therefore the value of ε_r is lower than that of the (BZT-

BCT) and CCTO ceramics [11]. The value of ε_r of the (BZT-BCT)-(PVDF-CCTO) composites can also be related to its porosity. In the (BZT-BCT)-(PVDF-CCTO) composites (up to x = 0.08 volume fraction of the CCTO ceramics) the porosity decreases and ε_r increases. Here, the CCTO ceramic filler has a high ε_r and with the increase in CCTO ceramic volume fraction, the dielectric behavior of the ceramic particles starts dominating, which in turn increases the ε_r of the composites. The decrease of ε_r in case of x = 0.10 volume fraction of the CCTO ceramics in the (BZT-BCT)-(PVDF-CCTO) composites can be related to the decrease of density of the corresponding composite. Also, some broadening of the XRD peaks ~ 22^o is observed in the composite for x = 0.10 volume fraction of the CCTO ceramic filler. This implies that in the corresponding composite some structural change is taking place, which may also be responsible for the lowering of the dielectric constant.

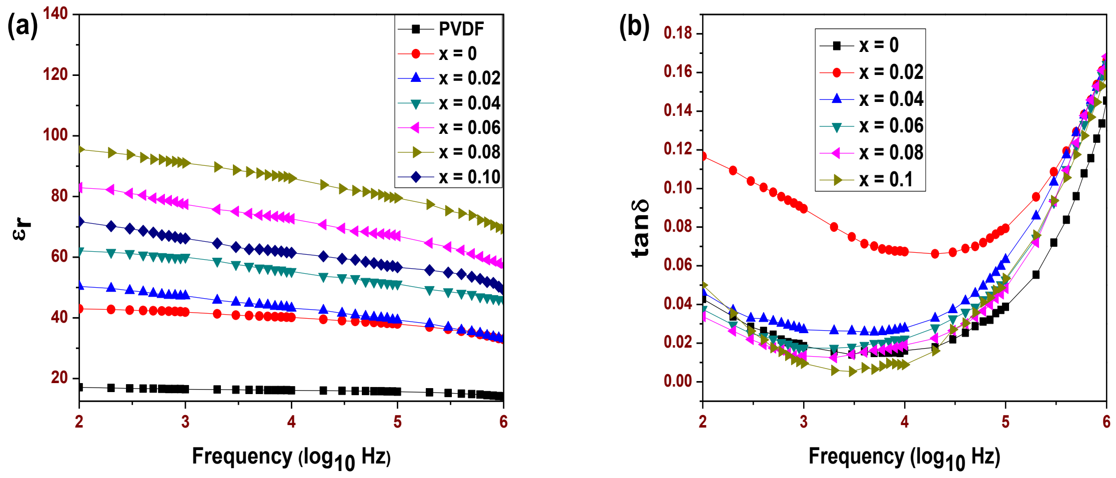

Fig. 6.12 Frequency dependence of (a) ε_r and (b) tanδ of PVDF & 0.25(BZT-BCT)-0.75[(1-x)PVDF-xCCTO] composites with x = 0.02, 0.04, 0.06, 0.08 and 0.10, respectively.

The frequency dependence of tanδ for the (BZT-BCT)-(PVDF-CCTO) composite with different volume fractions of the CCTO ceramic filler is shown in Fig. 6.12(b). It is observed that tanδ value for all composites decreases in the 100 Hz–10 kHz frequency range and then subsequently increases. This variation of tanδ can be due to the relaxation processes, which usually occur in a heterogeneous system. The reason may also be attributed to some structural changes that are taking place in the composite as a result of filler addition. The decrease of loss in the low frequency region is attributed to the interfacial polarization caused by the heterogeneous nature of the system, while the sharp increase of tanδ in the high frequency region may be related to the onset of the ohmic conductivity of the charge carriers [12]. The increase in tanδ at high frequency is also believed to be related to the glass transition relaxation of PVDF and the setting of the dielectric relaxation process [13]. Again the dielectric loss decreases with an increase in CCTO ceramic volume fractions in the composites up to 10 kHz frequency. Beyond 10 kHz frequency, the dielectric loss again increases with the increase of CCTO ceramic volume fractions in the composites. This may be attributed to the increase in interfaces with the increase of CCTO ceramic volume fractions in the composites [14]. The RT values of ε_r and tanδ for the (BZT-BCT)-(PVDF-CCTO) composite specimens at 1 kHz frequency are given in Table – 6.2.

6.4.1.2 (BZT-BCT)-(epoxy-CCTO) Composites

Fig. 6.13(a) shows the RT variation of ε_r with frequency of the (BZT-BCT)-(epoxy-CCTO) composite samples. From Fig. 6.13(a), it is clear that ε_r value increases with the increase in the CCTO ceramic content up to x = 0.08 volume fraction in the (BZT-BCT)-(epoxy-CCTO) composites and beyond that ε_r value starts decreasing. The maximum value of ε_r ~ 61 at 1 kHz frequency and at RT is obtained for x = 0.08 volume fraction of the CCTO ceramics in the composite samples. For all additions of the CCTO ceramics, the values of the dielectric constant of the composite samples is higher than that of the 0.20(BZT-BCT)-0.80(epoxy) composites and lower than that of pure (BZT-BCT) and CCTO ceramics individually. As expected, since the CCTO ceramic has the higher value of ε_r and therefore with the increase in the volume fractions of this ceramic filler, the effective dielectric constant value of the composites increases. The increase of the ε_r value with the increase of CCTO ceramic filler in the composites can also be related to the increase in connectivity between the ceramic fillers. Whereas, the decrease of ε_r for x = 0.10 volume fraction of the CCTO ceramic fillers in the (BZT-BCT)-(epoxy-CCTO) composites can be related to the decrease in density of this composites. Again, in all the (BZT-BCT)-(epoxy-CCTO) composite samples, ε_r is almost constant in the 10^4 to 10^6 Hz frequency range, which can be related to the intermolecular cooperative motions and hindered dielectric rotations in the composite samples [15].

Fig. 6.13(b) depicts the variation of tanδ with frequency of the (BZT-BCT)-(epoxy-CCTO) composite samples. For all the composites, it is observed that the tanδ value decreases with the increase in frequency and is almost constant in the 10^4 to 10^5 Hz frequency range and then starts increasing. The reason for this oscillatory behaviour of tanδ may be due to some relaxation processes which usually occur in a heterogeneous system [16]. This can also be related to the structural changes which takes place due to the addition of CCTO ceramic filler in the (BZT-BCT)-(epoxy-CCTO) composites. The decrease in the tanδ values in the lower frequency range can be related to the interfacial polarization. While the sharp increase in the tanδ value at higher frequency region can be due to the dielectric relaxation processes and also due to the increase in connectivity between the CCTO ceramic particles [13,17]. Again the tanδ value decreases with the increase in the CCTO ceramic content in the (BZT-BCT)-(epoxy-CCTO) composites up to x = 0.08 volume fraction and beyond that it start increasing. This increase in the tanδ value for x = 0.10 volume fraction of the CCTO ceramic fillers can be due to percolation threshold [18]. ε_r and tanδ values at RT and 1 kHz frequency of the (BZT-BCT)-(epoxy-CCTO) composite samples are given in Table – 6.2.

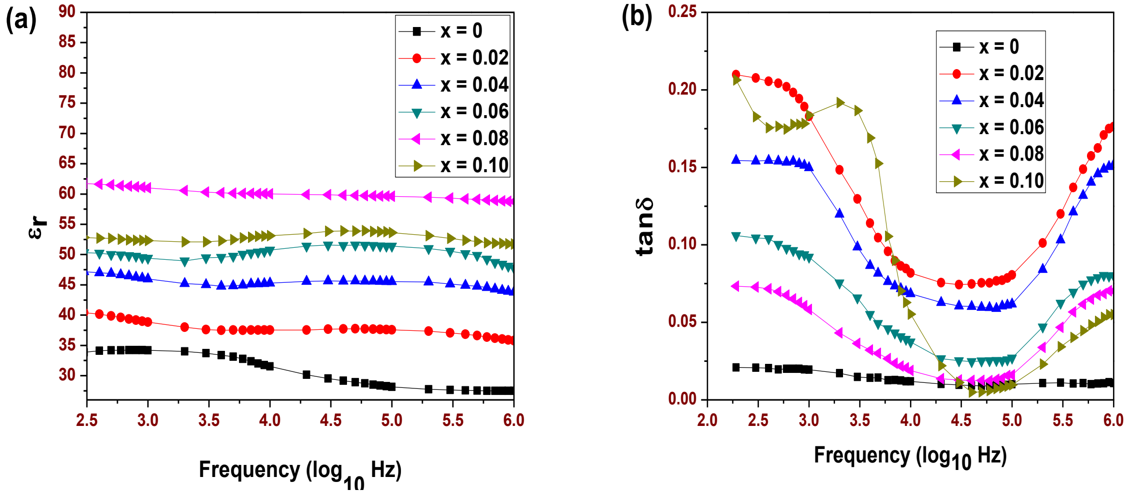

Fig. 6.13 Frequency dependence of (a) ε_r and (b) tanδ of 0.20(BZT-BCT)-0.80[(1-x)epoxy-xCCTO] composites with x = 0, 0.02, 0.04, 0.06, 0.08 and 0.10, respectively.

6.4.2 Temperature Dependent Dielectric Constant (ε_r) & Dielectric Loss (tanδ)

6.4.2.1 (BZT-BCT)-(PVDF-CCTO) Composites

Fig. 6.14(a) shows the temperature dependence of dielectric constant at 1 kHz frequency of the (BZT-BCT)-(PVDF-CCTO) 0-3 composites. The RT value of ε_r increases with the increase in the CCTO ceramic content up to x = 0.08 volume fraction in the composites. The increase in ε_r is related to the increase in density of the composites with the increase of CCTO volume fractions. Since, the dielectric constant of the CCTO ceramics is very high, therefore with the increase of CCTO volume fractions in the composites the increase in dielectric constant of the composites is justified. But, for x = 0.10 volume fraction of the CCTO ceramics in the composites the dielectric constant starts decreasing. This can be related to the decrease of the density of this composites, which also suggests the limit of CCTO addition in the (BZT-BCT)-(PVDF-CCTO) composites. Again, the value of ε_r of all the composite samples increases continuously to a certain temperature. The T_c for the composites is related to the (BZT-BCT) ceramic filler, which has T_c ~ 110 ^oC. Therefore, with the increase in the volume fractions of CCTO ceramics in the (BZT-BCT)-(PVDF-CCTO) composites, the dielectric abnormality near the (BZT-BCT) T_c starts decreasing. The maximum RT value of ε_r at 1 kHz frequency is ~ 90 for the x = 0.08 volume fractions of the CCTO ceramics in the (BZT-BCT)-(PVDF-CCTO) composites. This dielectric behavior is almost temperature independent in the 30 - 70 ^oC temperature range, which suggests the usefulness of this composite for the embedded capacitor applications.

Fig. 6.14(b) shows the temperature dependence of dielectric loss at 1 kHz frequency of the (BZT-BCT)-(PVDF-CCTO) 0-3 composites. The nature of the curves for different composites is approximately similar. The tanδ value sharply decreases and attains minima in the 110 – 130 ^oC temperature range and beyond it suddenly starts increasing. The dielectric properties of a polymer are determined by the charge distribution and also by the statistical thermal motion of its polar groups. In case of a dielectric material, the polarization is contributed by all the ionic, electronic and dipole polarizations. The electronic polarization occurs during a very short interval of time of the order of 10^{-10} s, but the process of ionic polarization occurs for longer time i.e. 10^{-3} to 10^{-2} s. The dipole polarization requires still longer time. In case of polar polymers, the dielectric constant starts decreasing at a certain frequency. The dipole molecules cannot orient themselves at lower temperature regions. As the temperature increases, the orientation of dipoles is facilitated which increases the dielectric constant. As expected, the tanδ values near minima correspond to the T_g region of the polymers. With the further increase in temperature, the thermal oscillation in the composites intensifies and the degree of order of orientations starts diminishing leading to the increase in dielectric loss [19].

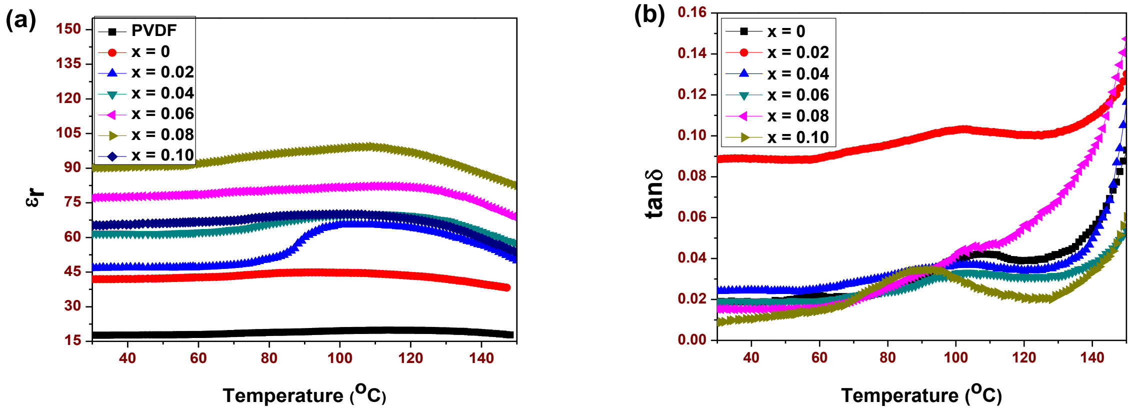

Fig. 6.14 Variation of (a) ε_r and (b) tanδ with temperature at 1 kHz frequency of PVDF, and 0.25(BZT-BCT)-0.75[(1-x)PVDF-xCCTO] composites with x = 0.02, 0.04, 0.06, 0.08 and 0.10, respectively.

6.4.2.2 (BZT-BCT)-(epoxy-CCTO) Composites

The temperature dependence of dielectric properties at 1 kHz frequency of the (BZT-BCT)-(epoxy-CCTO) composites are shown in the Fig. 6.15(a). ε_r value increases slowly with temperature up to 70 ^{o}C and appear to be almost constant. This corresponds to the low temperature co-efficient of capacitance, which makes these composites suitable for capacitor applications. There is a sudden increase in the ε_r value of the (BZT-BCT)-(epoxy-CCTO) composites at higher temperature. This sudden increase in the ε_r value of the (BZT-BCT)-(epoxy-CCTO) composites at high temperature can be attributed to the (i) development of the contact between ceramic filler particles due to the thermal expansion between the polymer matrix and ceramic particles and (ii) the dielectric response of the ceramic filler particles with the change in temperature [20].

Fig. 6.15(b) shows the temperature dependence of tanδ at 1 kHz frequency of the (BZT-BCT)-(epoxy-CCTO) composites. The tanδ values of all most all the composite samples appear constant up to 70 ^{o}C, and then suddenly it starts increasing. The minimum value of the tanδ corresponds to the glass transition temperature of the polymer in the composites. Again, the dielectric properties of the polymers depend upon the motion of the polar groups. The sudden increase in the loss curve at higher temperatures can again be related with the thermal motion of the polar groups [21].

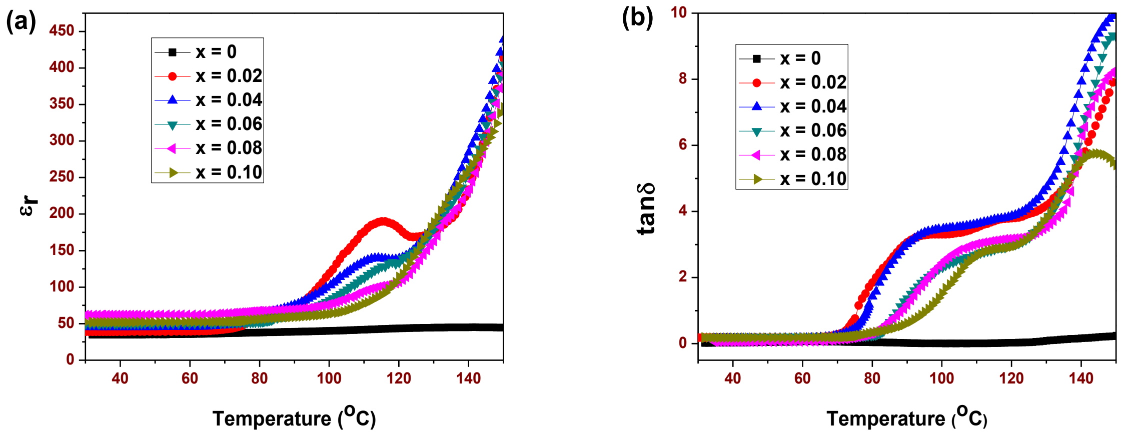

Fig. 6.15 Temperature dependence of (a) ε_r and (b) tanδ of 0.20(BZT-BCT)-0.80[(1-x)epoxy-xCCTO] composites with x = 0, 0.02, 0.04, 0.06, 0.08 and 0.10, respectively.

Table – 6.2 Different Dielectric Parameters & d_{33} Values for (BZT-BCT)-(PVDF-CCTO) & (BZT-BCT)-(epoxy-CCTO) Composites with Different Volume Fractions of Ceramics

Materials	**Volume fractions of ceramics**	**Parameters**				
		ε_r at RT at 1 kHz	**tanδ at RT at 1 kHz**	**ε_{rmax} at 1 kHz**	**T_{max} at 1 kHz**	**d_{33} in pC/N**
0.25(BZT-BCT)-0.75[(1-x)PVDF-xCCTO] composites	x = 0.02	47	0.08	-	-	7
	x = 0.04	59	0.02	-	-	8
	x = 0.06	77	0.01	-	-	13
	x = 0.08	90	0.01	-	-	19
	x = 0.10	66	0.009	-	-	10
0.2(BZT-BCT)-0.8[(1-x)epoxy-xCCTO] composites	x = 0.02	38	0.18	-	-	5
	x = 0.04	45	0.14	-	-	7
	x = 0.06	49	0.09	-	-	10
	x = 0.08	61	0.05	-	-	15
	x = 0.10	52	0.18	-	-	13

6.5 Dielectric Mixing Models

6.5.1 Dielectric Mixing Models for (BZT-BCT)-(PVDF-CCTO) Composites

Variation of effective dielectric constant (ε_{eff}) (measured at RT and 1 kHz frequency) of (BZT-BCT)-(PVDF-CCTO) composites as a function of volume fractions of CCTO ceramics are shown in Fig. 6.16.

Fitting to Lichtenecker Model

As reported earlier, among the different dielectric mixing models, the Lichtenecker model is found to be the best for (BZT-BCT)-PVDF composites [22]. But, the Lichtenecker model is not fitting properly for the (BZT-BCT)-(PVDF-CCTO) composites while considering the composite as three phase system [23]. We also tried to fit the Lichtenecker logarithmic eqn. with the experimental data by considering the [(BZT-BCT)-PVDF)] as polymer phase and CCTO as the ceramic phase. With this consideration, it is found that in the lower volume fraction (< 0.04) substitution of the CCTO ceramics in the (BZT-BCT)-(PVDF-CCTO) composites the experimental results are comparable with those obtained using the modified Lichtenecker logarithmic law. But at higher volume fractions ($x > 0.04$) substitution of the CCTO ceramics in the composites the deviation between the theoretical and experimental values increases.

Fitting to Yamada Model

The parameter ‘n’ is evaluated to fit the theoretical and the experimental values of dielectric constant [24]. This model is valid for the $x = 0.04$ volume fraction substitution of CCTO ceramics with $n \sim 9.6$. The mismatch for higher volume fraction substitution of CCTO ceramics may be attributed to the ceramic filler morphology.

Fitting to EMT Model

As per this model, the parameter ‘n’ is calculated to fit the experimental and theoretical values of the dielectric constant of the (BZT-BCT)-(PVDF-CCTO) composites. The theoretical and experimental dielectric constants values matches exactly for $x = 0.02$ & 0.04 volume fraction substitution of the CCTO ceramics in the composites (given in Table – 6.3). The experimental dielectric constant values fit well into the EMT model with the shape parameter $n = 0.12$ for the low volume fractions $\leq x = 0.04$ volume fractions of the CCTO ceramics substitution in the (BZT-BCT)-(PVDF-CCTO) composites. The obtained morphology fitting factor n (= 0.12) is closer to that of the reported (= 0.13), which is further related to the irregular shaped particles [25]. Therefore, the close agreement between the experimental and theoretical values of the dielectric constant can be attributed to the morphology of the dispersed particles.

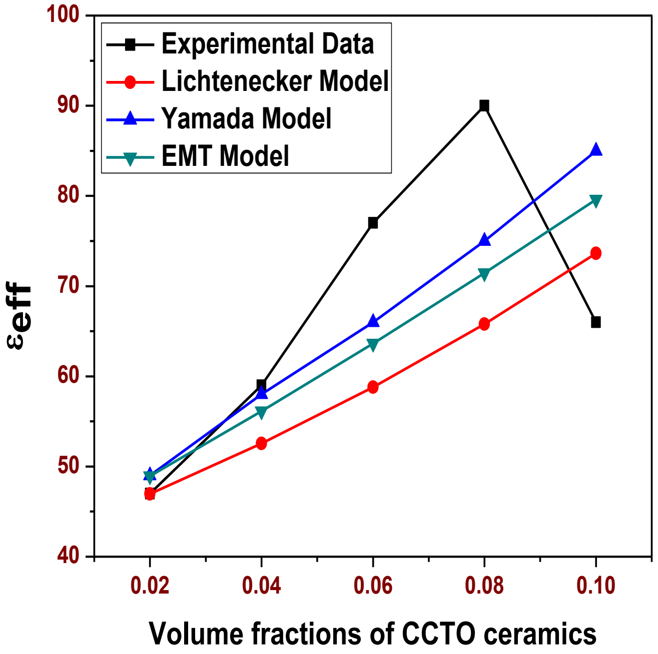

Fig. 6.16 Variation of ε_{eff} of (BZT-BCT)-(PVDF-CCTO) composites as a function of volume fractions of CCTO ceramics.

6.5.2 Dielectric Mixing Models for (BZT-BCT)-(epoxy-CCTO) Composites

In order to predict the effective dielectric constant (ε_{eff}) of the (BZT-BCT)-(epoxy-CCTO) composites, various dielectric models are used. Fig. 6.17 shows the comparison of the RT experimental and theoretical (calculated based on various models) ε_r values of the composites for different volume fractions of the CCTO ceramics. For the (BZT-BCT)-(epoxy-CCTO) composites, the most commonly used dielectric mixing models: the Lichtenecker model [23], Maxwell's model [26] and the Clausius-Mossotti model [27] are not fitting properly. Therefore, dielectric mixing models other than these are tried.

Fitting to Yamada Model

As per this model [24], the parameter 'n' is evaluated to fit the theoretical values with the experimental values of the dielectric constant. This model is valid up to x = 0.04 volume fraction substitution of the CCTO ceramics in the (BZT-BCT)-(PVDF-CCTO) composites with n ~ 8.64. The mismatch for higher volume fraction substitution of the CCTO ceramics may be attributed to the ceramic filler morphology.

Table – 6.3 Comparison of Experimental and Theoretical Values of ε_{eff} of (BZT-BCT)-(PVDF-CCTO) & (BZT-BCT)-(epoxy-CCTO) Composites with Different Volume Fractions of Ceramics

Materials	**Volume fractions of ceramics**	**Experimental values of ε_r (at 1 kHz and at RT)**	**Theoretical values of ε_r (at 1 kHz and at RT) according to different models**		
			Lichtenecker model	**Yamada model**	**EMT model**
0.25(BZT-BCT)-0.75[(1-x)PVDF-xCCTO] composites	x = 0.02	47	46.97	49	48.92
	x = 0.04	59	52.55	58	56.13
	x = 0.06	77	58.81	66	63.63
	x = 0.08	90	65.79	75	71.46
	x = 0.10	66	73.62	85	79.61
0.20(BZT-BCT)-0.80[(1-x)epoxy-xCCTO] composites	x = 0.02	38	-	39.84	38.53
	x = 0.04	45	-	45.93	43.24
	x = 0.06	49	-	52.26	48.16
	x = 0.08	61	-	58.87	53.28
	x = 0.10	52	-	65.76	58.63

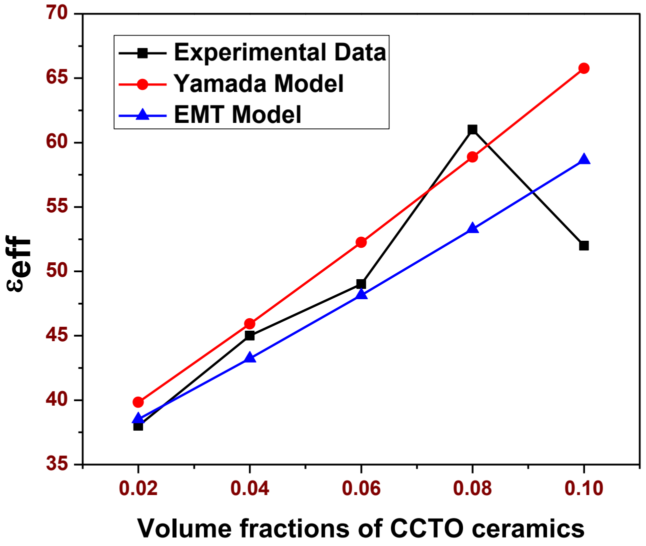

Fig. 6.17 Variation of ε_{eff} of (BZT-BCT)-(epoxy-CCTO) composites as a function of volume fractions of CCTO ceramics.

Fitting to EMT Model

As per this model [25], the parameter 'n' is calculated to fit the experimental and theoretical values of the dielectric constant of the (BZT-BCT)-(epoxy-CCTO) composites. The experimental dielectric constant values fit well into the EMT model with the shape parameter, n = 0.15 for the low volume fractions (x = 0.02-0.08) of the CCTO ceramic substitution in the composites. The obtained morphology fitting factor n (=0.15) is closer to that of the reported (=0.13), which is further related to the irregular shaped particles. Therefore, the close agreement between the experimental and the theoretical values can be attributed to the morphology of the dispersed particles. The calculated ε_{eff} values of the (BZT-BCT)-(epoxy-CCTO) composites using different dielectric mixing models are given in Table – 6.3.

6.6 Piezoelectric Studies

6.6.1 (BZT-BCT)-(PVDF-CCTO) Composites

The piezoelectric constant (d_{33}) of the (BZT-BCT)-(PVDF-CCTO) composite samples are given in Table – 6.2. Maximum d_{33} value ~ 19 pC/N is obtained in case of x = 0.08 volume fraction substitution of CCTO ceramics in the (BZT-BCT)-(PVDF-CCTO) composites. The poling field cannot be sufficiently elevated due to the reduced breakdown voltage which may be due to the pores trapped between the ceramic particles [28]. When the substituted CCTO ceramic volume fraction is above x = 0.08 in the composites, then the mechanical strength of the composites becomes weak to be used as flexible devices.

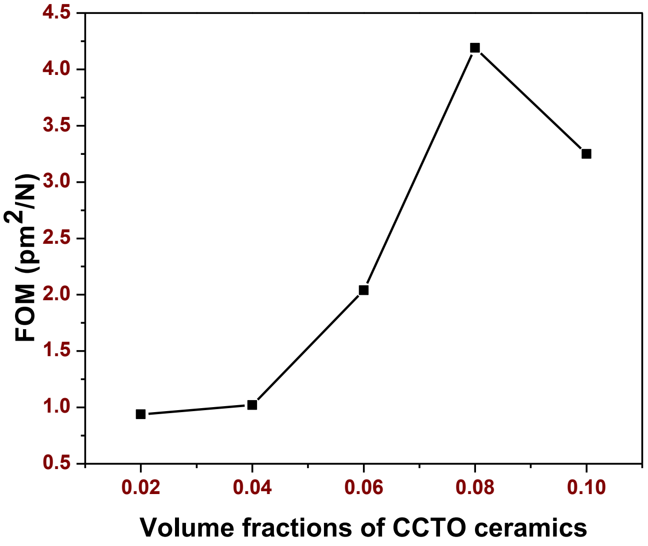

Fig. 6.18 FOM for energy harvesting application of (BZT-BCT)-(PVDF-CCTO) composites as a function of the volume fractions of CCTO ceramics.

Fig. 6.18 shows the FOM as a function of the content of CCTO ceramics of the (BZT-BCT)-(PVDF-CCTO) composites for energy harvesting applications. The FOM reaches maximum when the volume fraction of the CCTO ceramics is x = 0.08. As given in Table – 6.2, that with the increase of the content of the CCTO ceramics in the composite over x = 0.08 volume fractions, the physical property dependent d_{33} is relatively less increased. This shows that for the samples over x = 0.08 volume fraction substitution of the CCTO ceramics in the composites, the mechanical strength becomes too weak to be used as flexible devices.

6.6.2 (BZT-BCT)-(epoxy-CCTO) Composites

The piezoelectric constant (d_{33}) of the (BZT-BCT)-(epoxy-CCTO) composite samples are given in Table – 6.2. Maximum d_{33} value ~ 15 pC/N is obtained in case of [0.2(BZT-BCT)-0.736(Epoxy)-0.064(CCTO)] composite samples. It is known that the piezoelectric constant is strongly dependent on the domain orientation during poling. In the present case, the domain orientation during poling process appears to be enhanced due to the improved connectivity [28]. However, the poling field cannot be sufficiently elevated due to the reduced breakdown voltage which may be due to the pores trapped between the ceramic particles [27]. When the volume fractions of the CCTO ceramics in the composite is over x = 0.08, the mechanical strength of the specimen becomes weak to be used as flexible devices.

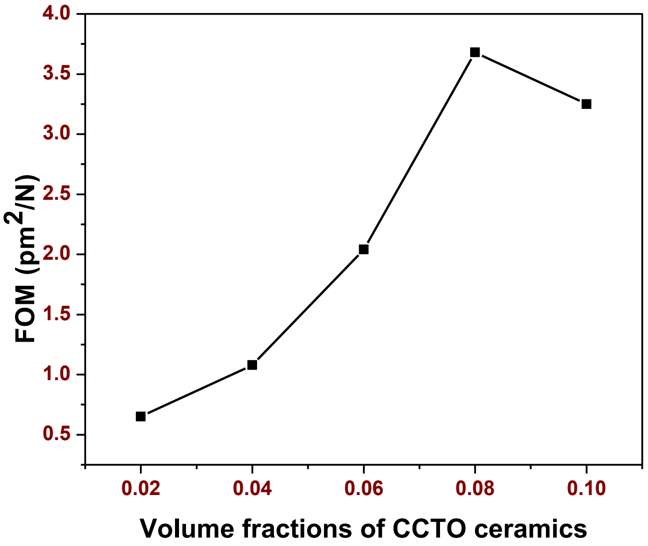

Fig. 6.19 FOM for energy harvesting application of (BZT-BCT)-(epoxy-CCTO) composites as a function of the volume fractions of CCTO ceramics.

Fig. 6.19 shows the FOM for energy harvesting application as a function of the volume fractions of the CCTO ceramics. The FOM reaches maximum when the volume fractions of the CCTO ceramics is $x = 0.08$. This phenomenon can be explained by counteracting effects of density on the d_{33} and ε. As can be seen in Table – 6.2, that with the increase of the volume fractions of the CCTO ceramics over $x = 0.08$ in the (BZT-BCT)-(epoxy-CCTO) composites, the physical property dependent d_{33} is relatively less increased, which shows that the mechanical strength of the (BZT-BCT)-(epoxy-CCTO) composite specimen over $x = 0.08$ volume fractions becomes too weak to be used as flexible devices.

6.7 Summary

Both the 0.25(BZT-BCT)-0.75[(1-x)PVDF-xCCTO)] and 0.20(BZT-BCT)-0.80[(1-x)epoxy-xCCTO)] 0-3 ceramic-polymer composites with ($x = 0.02$, 0.04, 0.06, 0.08 & 0.10, respectively) were fabricated and characterized. The structural, optical, morphological, dielectric and piezoelectric properties of the composite samples have been studied. The XRD patterns of all the composite samples showed the presence of peaks corresponding to both polymer and ceramics phases, respectively. The E_g value decreases with the increase in the (CCTO) ceramic concentration in the (BZT-BCT)-(PVDF-CCTO) composites, while the E_g increase with the increase in the (CCTO) ceramic concentration in the (BZT-BCT)-(epoxy-CCTO) composites samples. Morphological studies confirmed the 0-3 connectivity of the ceramic particles in the PVDF and epoxy polymer matrix. Dielectric studies of the composites illustrated the increase in the value of ε_r at RT with the increase in CCTO ceramic content. [0.25(BZT-BCT)-0.69(PVDF)-0.06(CCTO)] composite showed the highest values of $\varepsilon_r \sim 90$ and $d_{33} \sim 19$ pC/N. And also [0.2(BZT-BCT)-0.736(Epoxy)-0.064(CCTO)] composite showed the highest values of $\varepsilon_r \sim 61$ and $d_{33} \sim 15$ pC/N. Hence it can be concluded that both the (BZT-BCT)-(PVDF-CCTO) and the (BZT-BCT)-(epoxy-CCTO) ceramic-polymer composites are suitable for flexible capacitors devices and also for energy harvesting piezoelectric applications.

References:

[1] C. C. Wu, Y. C. Chen, C. F. Yang, C. C. Su and C. C. Diao, Journal of the European Ceramic Society**.** 27, (2007) 3839.

[2] Y. Zhang, B. P. Zhang, L. S. Jiao, H. L. Zhang and X. Y. Li, Acta Phys. Sin. 55, (2006) 3730.

[3] G. Cao and Y. Wang, Nanostructures and Nanomaterials – Synthesis, Properties and Applications (2nd Edition, World Scientific Publishing Co. Pte. Ltd. 2011).

[4] F. Neumark, I. L. Kuskovsky and H. Jiang, Wide band gap light emitting materials and devices (Wiley-VCH, Verlag GmbH & Co, KGaA, Weinheim. 2007).

[5] H. G. Tompkins and E. A. Irene, Handbook of Ellipsometry (William Andrew, Inc. 2005).

[6] M. Altaf and M. A. Chaudhry, Journal of the Korean Physical Society. 36, (2000) 265**.**

[7] S. Muthukumaran and M. Muthusamy, J Mater Sci: Mater Electron. 23, (2012) 1647.

[8] S. Hadi, A. Hashim and A. Jewad, Australian Journal of Basic and Applied Sciences. 5, (2011) 2192.

[9] Z. M. Gibbs, A. LaLonde and G. J. Snyder, New Journal of Physics. 15, (2013) 075020.

[10] A. P. Ramireza, M. A. Subramanian, M. Gardela, G. Blumberga, D. Li and T. Vogt, Solid State Commun. 115, (2000) 217.

[11] H. A. Avila, L. A. Ramajo, M. S. Goes, M. M. Reboredo, M. S. Castro and R. Parra, ACS Appl Mater Inter. 5, (2013) 505.

[12] B. Hilczer, J. Kulek, E. Markiewicz, M. Kosec and B. Mali, J Non-Cryst Solids. 305, (2002) 167.

[13] R. Gregorio and M. Cestari, J Polym Sci, Part B:Polym Phys. 32, (1994) 859.

[14] P. Thomas, K. T. Varughese, K. Dwarakanath and K. B. R. Varma, Compos. Sci. Technol. 70, (2010) 539.

[15] C. V. Chanmal and J. P. Jog, Express Polymer Letters. 2, (2008) 294.

[16] A. S. Ayesh and R. Abdel-Rahem, Bull Mater Sci. 33, (2010) 589.

[17] B. Hilczer, J. Kułek, E. Markiewicz, M. Kosec and B. Mali, J Non-Cryst Solids. 305, (2002) 167.

[18] K. Osinska, A. Lisinska-Czekaj, H. Bernard, J. Dzik, M. Adamczyk and D. Czekaj, Archives of Metallurgy and Materials**.** 56, (2011) 1093.

[19] E. Q. Huang, J. Zhao, J. W. Zha, L. Zhang, R. J. Liao and Z. M. Dang, J. Appl. Phys. 115, (2014) 194102.

[20] F. G. Garcia, C. R. Foschini, J. A. Varela, E. Longo, F. Moura and A. Z. Simoes, Processing and Application of Ceramics. 5, (2011) 205.

[21] M. A. Islam, Z. Farhat and J. Bonnell, Journal of Surface Engineered Materials and Advanced Technology. 1, (2011) 112.

[22] P. Kumar, P. Mishra and S. Sonia, J. Inorg. Organomet. Polym. 23, (2013) 539.

[23] A. K. Zak, W. C. Gan, W. H. Abd. Majid, M. Darroudi and T. S. Velayutham, Ceramic International. 37, (2011) 1653.

[24] S. George, V. N. Deepu, P. Mohana and M. T. Sebastian, Polymer Engineering & Science. 50, (2010) 570.

[25] A. Tiwari and S. Valyukh, Advanced Energy Materials (Scrivener Publishing, Beverly, MA. 2014).

[26] M. Dinulovic and B. Rasuo, Composite Structures. 93, (2011) 3209.

[27] C. Xin, H. Shifeng, C. Jun, X. Ronghua, L. Futian and L. Lingchao, J of European Ceram. Soc. 25, (2005) 3223.

[28] D. T. Le, N. B. Do, D. U. Kim, I. Hong, I. W. Kim and J. S. Lee, Ceram. Int. 38, (2012) S259.

******

Chapter – 7

CONCLUSIONS & FUTURE WORKS

In this chapter, the major conclusions drawn from the present research work carried out are summarised. The need and scope of extending the present research work are also presented.

The overall work of the present thesis has four parts: (i) to synthesize and suggest an effective lead free ferroelectric system, (ii) by using this effective lead free ferroelectric system as fillers, prepare the 0-3 ferroelectric ceramic-polymer composites for embedded capacitor (ε_r ~ 30 at RT and at 1kHz frequency) and piezoelectric (d_{33} ~ 20 pC/N) applications, (iii) for improving the dielectric properties of the effective ceramic-polymer composite system to synthesize and suggest an effective lead free system with good dielectric properties (ε_r >10,000 at RT and at 1kHz frequency) and (iv) by using this high dielectric constant system as fillers particles further improving the dielectric properties (ε_r > 30 at RT and at 1kHz frequency) of the effective ceramic-polymer composite system. Considering all this proposed objectives it can be concluded that there are mainly four parts of this thesis. The major conclusions of each part, which is related to the previous one, are given as:

7.1 Conclusions

7.1.1 Conclusions from the Studies on (BZT-BCT) System

- The optimized calcination and sintering temperatures for all the MPB compositions of the studied (BZT-BCT) ceramics was 1300°C for 4 h and 1400°C for 6 h, respectively.
- The maximum relative density ~ 97% was found in the 0.50BZT-0.50BCT ceramics at optimized sintering temperature.
- The co-existence of the tetragonal and monoclinic structures was found in the 0.50BZT-0.50BCT composition, which confirmed about its MPB nature.
- Maximum value of ε_r ~ 3888 at 1kHz and at RT and piezoelectric coefficient (d_{33}) ~ 281 pC/N were obtained in the 0.50BZT-0.50BCT ceramics samples.

- The excellent dielectric and piezoelectric results (comparable to lead based systems) in this study indicated that 0.50BZT-0.50BCT ferroelectric system can be a suitable candidate to replace the lead-based materials for piezoelectric applications.

7.1.2.1 Conclusions from the Studies on Φ(0.50BZT-0.50BCT/BZT-BCT)-(1-Φ)PVDF Ceramic-polymer Composites

- Φ(BZT-BCT)-(1-Φ)PVDF ceramic-polymer composite thick films with (Φ = 0.05, 0.10, 0.15, 0.20 & 0.25 volume fractions) were synthesized by hot uniaxial press.
- The XRD patterns of the composite specimens showed the presence of crystalline peaks corresponding to both PVDF polymer and (BZT-BCT) ceramic separately.
- Morphological studies confirmed the 0-3 connectivity and homogeneity of the ceramic powder distribution with the increase of (BZT-BCT) ceramic particles content in the Φ(BZT-BCT)-(1-Φ)PVDF composites.
- Dielectric studies illustrated the increase in the value of ε_r at RT with the increase in ceramic content in the composites.
- The Φ(BZT-BCT)-(1-Φ)PVDF composite with Φ = 0.25 volume fraction exhibited the highest values of the $\varepsilon_r \sim 42$ at 1kHz and at RT and $d_{33} \sim 31$ pC/N.
- The obtained results are better than the earlier reports (given in chapter 1) and suggested the suitability of Φ(BZT-BCT)-(1-Φ)PVDF composite with Φ = 0.25 for embedded capacitor and piezoelectric applications.

7.1.2.2 Conclusions from the Studies on Φ(0.50BZT-0.50BCT/BZT-BCT)-(1-Φ)epoxy Ceramic-polymer Composites

- Φ(BZT-BCT)-(1-Φ)epoxy ceramic-polymer composites with (Φ = 0.05, 0.10, 0.15, 0.20 & 0.25 volume fractions) were synthesized by hand lay-up techniques followed by cold pressing.
- The XRD patterns of the composite specimens showed the presence of both amorphous phase of epoxy polymer and crystalline phase of the (BZT-BCT) ceramic.
- Morphological studies confirmed 0-3 connectivity pattern of the composites with the homogeneous distribution of the (BZT-BCT) ceramic particles in the epoxy polymer.
- The Φ(BZT-BCT)-(1-Φ)epoxy composite with Φ = 0.20 volume fraction exhibited highest values of the $\varepsilon_r \sim 34$ at 1kHz and at RT and $d_{33} \sim 16$ pC/N.

- The obtained results are better than the earlier reports (given in chapter 1) and suggested the suitability of Φ(BZT-BCT)-(1-Φ)epoxy composite with $\Phi = 0.20$ for embedded capacitor and piezoelectric applications.

7.1.3 Conclusions from the Studies on CCTO Systems

- The optimized calcination and sintering temperatures for the CCTO ceramic systems was 1050^{o}C for 4 h and 1100^{o}C for 8 h, respectively.
- The maximum relative density ~ 94% was found in CCTO ceramics at optimized sintering temperature.
- The RT values of ε_r and tanδ at 1 kHz frequency of the CCTO ceramic samples sintered at 1100^{o}C were found to be ~ 11,537 and 0.21, respectively.
- The dielectric constant of CCTO ceramics was comparatively higher than the (BZT-BCT) ceramic system and almost temperature independent in the temperature range of 30-70^{o}C.

7.1.4.1 Conclusions from the Studies on 0.25(BZT-BCT)-0.75[(1-x)PVDF-xCCTO] Ceramic-polymer Composites

- 0.25(BZT-BCT)-0.75[(1-x)PVDF-xCCTO] ceramic-polymer composite thick films with (x = 0.02, 0.04, 0.06, 0.08 & 0.10 volume fractions) were synthesized by hot uniaxial press.
- The XRD patterns of the composite specimens showed the presence of crystalline peaks corresponding to PVDF polymer and (BZT-BCT), CCTO ceramics separately.
- Morphological studies confirmed the homogeneous distribution of the ceramic particles in the PVDF polymer matrix with good connectivity, confirming the 0-3 pattern.
- 0.25(BZT-BCT)-0.75[(1-x)PVDF-xCCTO] composite with x = 0.08 volume fraction exhibited highest value of ε_r ~ 90 at 1kHz and at RT and d_{33} ~ 19 pC/N.
- The obtained results are better than the earlier reports (given in chapter 1) and suggested the suitability of 0.25(BZT-BCT)-0.75[(1-x)PVDF-xCCTO] composite with x = 0.08 for embedded capacitor and piezoelectric applications.

7.1.4.2 Conclusions from the Studies on 0.20(BZT-BCT)-0.80[(1-x)epoxy-xCCTO] Ceramic-polymer Composites

- 0.20(BZT-BCT)-0.80[(1-x)epoxy-xCCTO] ceramic-polymer composite samples with (x = 0.02, 0.04, 0.06, 0.08 & 0.10 volume fractions) were synthesized by hand lay-up techniques followed by cold pressing.
- The XRD patterns of the composite specimens showed the presence of amorphous phase of epoxy polymer and the crystalline phases of the (BZT-BCT) & CCTO ceramics.
- Morphological studies show homogeneous dispersion of the ceramic particles in the polymer matrix with small agglomerations.
- 0.20(BZT-BCT)-0.80[(1-x)epoxy-xCCTO] composite with x = 0.08 volume fraction exhibited highest value of ε_r ~ 61 at 1kHz and at RT and d_{33} ~ 15 pC/N.
- The obtained results are better than the earlier reports (given in chapter 1) and suggested the suitability of 0.20(BZT-BCT)-0.80[(1-x)epoxy-xCCTO] composite with x = 0.08 for embedded capacitor and piezoelectric applications.

Overall Summary:

The (BZT-BCT) system near MPB was successfully synthesized in single perovskite phase. The co-existence of the tetragonal and monoclinic structures was found in the 0.50BZT-0.50BCT composition, which confirmed about its MPB nature. Maximum values of ε_r ~ 3888 at RT and at 1kHz frequency and d_{33} ~ 281pC/N (comparable to lead based effective ferroelectric systems) were obtained in the 0.50BZT-0.50BCT ceramic samples. 0.50BZT-0.50BCT system sintered at 1400^{o}C showed better structural, microstructural, dielectric, ferroelectric and piezoelectric properties and can be considered as suitable candidate to replace the lead-based materials. Using 0.50BZT-0.50BCT/BZT-BCT system ceramic particles as fillers and PVDF and epoxy as matrices, 0-3 ceramic-polymer composites were successfully prepared for embedded capacitor and piezoelectric applications. The 0.25(BZT-BCT)-0.75(PVDF) composite showed the highest ε_r ~ 42 at RT and at 1kHz frequency and highest d_{33} ~ 31 pC/N, whereas the 0.20(BZT-BCT)-0.80(epoxy) composite showed the highest ε_r ~ 34 at RT and at 1kHz frequency and highest d_{33} ~ 16 pC/N. Both the 0.25(BZT-BCT)-0.75(PVDF) and 0.20(BZT-BCT)-0.80(epoxy) ceramic-polymer composites are suitable for capacitor and energy harvesting piezoelectric applications. For improving the dielectric properties of the 0.25(BZT-BCT)-0.75(PVDF) and 0.20(BZT-BCT)-0.80(epoxy) composites, CCTO ceramics were successfully synthesized in single phase. The RT values of ε_r and tanδ at 1kHz frequency of the CCTO samples sintered at 1100^{o}C were found to be ~ 11,537 and 0.21, respectively. Finally the dielectric properties of the 0.25(BZT-BCT)-0.75(PVDF) and 0.20(BZT-BCT)-0.80(epoxy) composites were further improved by using CCTO ceramic particles as the fillers. [0.25(BZT-BCT)-0.69(PVDF)-0.06(CCTO)] composite showed the highest value of ε_r ~ 90 at RT and at 1kHz frequency and d_{33} ~ 19 pC/N, whereas the [0.20(BZT-BCT)-0.736(Epoxy)-0.064(CCTO)] composite showed the highest value of ε_r ~ 61 at RT and at 1kHz frequency and d_{33} ~ 15 pC/N. The obtained dielectric and piezoelectric properties of these ceramic-polymer composites are better than the reports in the literature (Chapter 1) and suggested their suitability for flexible capacitor devices and for energy harvesting piezoelectric applications.

7.2 Future Works

- Poling of the sintered ceramics and composites was carried out at a particular field and temperature. The piezoelectric properties generally depend on the poling conditions. Therefore effect of poling temperature and poling field on piezoelectric properties of these ceramics and composites can be studied.
- Different synthesis techniques like combustion synthesis, sol gel processing, mechano chemical synthesis, are found to reduce the processing temperatures with enhanced properties. Therefore, the studied composites can also be prepared by these techniques and their properties can be investigated.
- Thin films of these composites can also be prepared and their properties can be investigated.
- Other characterizations like strain vs electric field and pyroelectric measurements of the composites can also be carried out.

******

Bio – Data of the Author

Name : Punyatoya Mishra

DOB : 16-11-1981

Educational Qualifications :

10 th : Salipur High School, Cuttack, Odisha.

+ 2 Sc : Salipur Collge, Cuttack, Odisha.

B. Sc (Physics Hons.) : Salipur Collge, Cuttack, Odisha.

M. Sc in Physics : Ravenshaw University, Cuttack, Odisha.

Ph. D in Physics : Thesis Submitted to National Institute of Technology Rourkela, Odisha.

Publications :

1. **P. Mishra**, Sonia, P. Kumar. Effect of sintering temperature on dielectric, piezoelectric and ferroelectric properties of BZT-BCT 50/50 ceramics. Journal of Alloys and Compounds, 545, 210-215 **(2012)**.
2. P. Kumar, **P. Mishra**, S.Sonia. Synthesis and characterization of lead-free ferroelectric $0.5[Ba(Zr_{0.2}Ti_{0.8})O_3]-0.5[(Ba_{0.7}Ca_{0.3})TiO_3]$ - Polyvinylidene Difluoride 0-3 composites. Journal of Inorganic and Organometallic Polymers, 23, 539-545 **(2013)**.
3. **P. Mishra**, P. Kumar. Dielectric properties of 0.25(BZT-BCT)-0.75[(1-x)PVDF-xCCTO] (x = 0.02, 0.04, 0.06, 0.08 and 0.1) composites for embedded capacitor applications. Composites Science and Technology, 88, 26-32 **(2013)**.

4. **P. Mishra**, P. Kumar. Dielectric properties of Φ(BZT-BCT)-(1−Φ) Epoxy composites with 0-3 connectivity. Hindawi Publishing Corporation Advances in Condensed Matter Physics, 2013, 1-8 **(2013)**.
5. **P. Mishra**, Sonia, P. Kumar. Enhanced Dielectric and Piezoelectric Properties of BZT-BCT System near MPB. Ceramic International, 40, 14149-14157 **(2014)**.
6. **P. Mishra**, P. Kumar. Enhancement of dielectric properties of 0.2[BZT-BCT]-0.8[(1-x)Epoxy-xCCTO] (x = 0.02, 0.04, 0.06, 0.08 & 0.1) composites for embedded capacitor and energy harvesting applications. Journal of Alloys and Compounds, 617, 899-904 **(2014)**.
7. **P. Mishra**, P. Kumar. Structural and optical properties of 0.2[BZT-BCT]-0.8[(1-x)EPOXY-xCCTO] (x = 0.02, 0.04, 0.06, 0.08 & 0.1) composites. Ceramic International, **(2014)** (In Press).

Papers in Symposiums/Conferences :

1. **P. Mishra**, P. Kumar and N.K. Singh. Synthesis and Characterizations of BZT-BCT ceramics by conventional and microwave processing routes. NSFD-XVII- The 17th National Seminar On Ferroelectric and Dielectrics. Organised by Department of Physics, ITER, Bhubaneswar. 17-19 December **2012**. **(Poster presentation)**
2. **P. Mishra**, P. Kumar. Lead free ferroelectric Φ(BZT-BCT)-(1-Φ)Epoxy composites for capacitor applications. ENMEA, oganised by Department of Mechanical Engineering, VSSUT Burla. 19-20 January **2013**. **(Oral presentation)**
3. **P. Mishra**, P. Kumar. Sintering Temperature Effect on Structural and Dielectric Properties of CCTO Ceramics. Condensed Matter Days.

Organised by Department of Physics, N.I.T., Rourkela. 29-31 August **2013**.
(Poster presentation)

Permanent Address : Punyatoya Mishra
C/O - Debendra nath Mishra
Chitrakara Sahi (New Colony)
At/Po - Puri
Odisha – 752001
